TECHNISCHE
UNIVERSITÄT
WIEN
Vienna University of Technology

Dissertation

Characterisation of Defects in Carbon Fibre Reinforced Polymer (CFRP) Laminates and Pultruded Profiles

ausgeführt zum Zwecke der Erlangung des akademischen Grades eines Doktors
der technischen Wissenschaften unter der Leitung von

Ao.Univ.Prof. Dipl.-Ing. Dr. mont. Vasiliki-Maria Archodoulaki
E 308
Institut für Werkstoffwissenschaft und Werkstofftechnologie

und

Em.O.Univ.Prof. Dipl.-Ing. Dr.techn. Hans-Peter Degischer
E 308
Institut für Werkstoffwissenschaft und Werkstofftechnologie

eingereicht an der Technischen Universität Wien
Fakultät für Maschinenwesen und Betriebswissenschaften

Marta Rodríguez-Hortalá
Matrikelnummer: 0701389

Guglgasse 8/2/9/82
1110 Wien

Wien, am 25.01.2013   _____

La science, la nouvelle noblesse !
Le progrès. Le monde marche !
Pourquoi ne tournerait-il pas ?
C'est la vision des nombres.
Nous allons à l'Esprit.
C'est très certain, c'est oracle, ce que je dis.
Je comprends, et ne sachant m'expliquer sans paroles païennes, je voudrais me taire.

Science - The new aristocracy!
Progress - The world is on the march!
Why shouldn't it turn too?
It's the vision of numbers.
We are moving towards the Spirit.
Certainly deserted: It's the voice of the oracle, what I say.
Understand, and not knowing how to express myself without using pagan words.
I prefer to remain silent.

(Excerpt from Arthur Rimbaud's (1873) "Mauvais sang")

Acknowledgements

Abstract

This work focuses on the microstructural characterisation of carbon fibre reinforced polymer composites (CFRP) with special regard to defects and their impact on the mechanical and thermal properties. For the structural characterisation, a wide variety of classical and innovative destructive and non destructive testing and imaging methods are applied to detect relevant defects. These are used to correlate defect types with mechanical and thermal properties of different types of CFRPs.

The differences between studied materials included the production process used, the nature of their constituents, the reinforcement arrangement within the structure and the thermal history of the products, which affects matrix related properties.

These materials are very sensitive to manufacturing conditions, yielding completely different composite materials for a given matrix-fibre combination if for instance the curing temperature or the compaction pressure is modified. Therefore, comparisons are made between: a) prepreg laminates with different ply sequences and produced with different curing cycles, b) impregnated laminates produced using different resin systems and compaction pressures and c) pultruded profiles with tubular and cylindrical cross sections with and without mineral filler particles.

Special emphasis is put on non-destructive 3D visualisation techniques such as X-ray computed tomography (CT, comprising conventional X-rays and synchrotron radiation) and in-situ observations during deformation. Different techniques are combined to characterize the samples on different scales, down to individual fibre level. CT offers more than just structural characterisation, it provides quantification of fibre orientation and porosity volume fraction. Failure processes can also be studied, not only at the surface but also internally within the bulk material at the relevant micromechanical length-scales down to the sub micrometer range.

The internal structure and the different damage mechanisms are investigated for the different CFRP under different loading conditions (bending, torsion, tension) using a combination of in-situ 3D imaging and acoustic emission with post-mortem fractography. The damage accumulation of all samples is similar. Fibre fracture is the dominant strength controlling mechanism. Matrix crack growth is observed to occur prior to extensive fibre breakage. Also filler particle agglomerations have a detrimental effect in pultruded profiles. This knowledge could be applied to the interpretation of failures of more complex components if the loading conditions are comparable.

Manufacturing dependant differences in the microstructure, e.g. porosity content, fibre volume fraction are correlated to thermal and mechanical properties. Although in non-fully cured composites additional crosslinkig and changes in the thermal properties of the matrix are observed, the overall mechanical properties of the composites are not affected. Thermal properties, such as the glass transition temperature of the matrix, are not influenced by defects present in the composite. Furthermore, the defects in each type of composite are classified and their effect on mechanical properties is assessed.

Kurzfassung

Die Gefügecharakterisierung von Kohlenstofffaser verstärkten Kunststoffen (CFRP) steht im Mittelpunkt dieser Arbeit, wobei besonderes Augenmerk auf die Defekte und deren Auswirkungen auf mechanische und thermische Eigenschaften gelegt wird. Eine breite Palette klassischer und neuerer, zerstörender und zerstörungsfreier Prüf- und Abbildungsmethoden wird eingesetzt, um relevante Gefügefehler zu beschreiben. Darüber hinaus werden diese Methoden genützt, um die Art der Fehler mit den mechanischen und thermischen Eigenschaften verschiedener CFRP-Materialien in Beziehung zu setzen.

Die untersuchten Verbundwerkstoffe werden nach deren Herstellungsprozess, der Art ihrer Bestandteile, der Anordnung der Verstärkungsfasern und der Wärmebehandlung der Produkte unterschieden. Mit einem bestimmten Matrix-Faser System können sehr unterschiedliche Materialien erzeugt werden, wenn beispielsweise die Aushärtetemperatur oder der Konsolidierungsdruck verändert werden. Deshalb werden Vergleiche angestellt zwischen a) Prepreg-Laminaten in unterschiedlicher Stapelfolge und mit verschiedenen Wärmebehandlungen; b) Laminate, die mit verschiedenen Harzen imprägniert und unterschiedlichen Drücken konsolidiert wurden; c) Pultrusionslangprodukte unterschiedlicher Geometrie, nämlich Rundstäbe bzw. Rohre, mit oder ohne mineralischen Füllstoffen.

Ein spezieller Schwerpunkt wird auf den Einsatz von zerstörungsfreien 3D Abbildungstechniken gelegt: Röntgen-Computer-Tomografie (CT) mit konventionellen Röntgenstrahlen und mit Synchrotron Strahlquellen, sowie In-situ Beobachtungen während der Verformung. Verschiedene Techniken werden kombiniert, um die Proben in unterschiedlichen Größenskalen bis zu den Faserdurchmessern herab zu charakterisieren. CT bietet nicht nur eine Methode zur Gefügecharakterisierung, wie Faserorientierung und Porenvolumenanteil, sondern erlaubt über die Oberflächenbeobachtung hinaus auch Versagensmechanismen im Inneren der Proben in den mikromechanischen Vorgängen entsprechenden Längenskalen bis in den Submikrometerbereich zu untersuchen.

Das innere Gefüge und die verschiedenen Schädigungsmechanismen werden an verschiedenen CFRP untersucht, die unterschiedlichen Belastungen (Biegung, Torsion, Zug) unterworfen werden, wobei die Proben in-situ 3D abgebildet und die emittierten, akustischen Signale analysiert, sowie nach dem Bruch fraktografisch untersucht werden. Faserbruch begrenzt die Festigkeit aller CFRP, obwohl die Ausbreitung von Matrixrissen dem Faserbruch vorausgeht. Die Füllstoffteilchen bilden in den Pultrusionsprodukten lokale Anhäufungen, die vorzeitiges Versagen auslösen. Diese Erkenntnisse können für die Erklärung des Versagens komplexer Komponenten unter vergleichbaren Belastungen herangezogen werden.

Obwohl sich die Vernetzung in unvollständig ausgehärteter Matrix durch Temperaturbelastung verändert wird, beeinflusst dies die mechanischen Eigenschaften des Verbundwerkstoffes nicht. Andererseits werden die thermischen Eigenschaften der Matrix, wie die Glasübergangstemperatur, durch Verbundwerkstoffdefekte nicht beeinflusst. Schließlich werden die quantifizierten Defekte in den untersuchten Verbundwerkstoffen klassifiziert und ihr Einfluss auf die mechanischen Eigenschaften bewertet.

1. Introduction

Carbon fibre reinforced polymers (CFRP) are composites consisting of at least two components, a matrix and an uniformly embedded second reinforcement phase, yielding a specific property profile. In CFRP the matrix is a polymer, most often a thermoset epoxy with continuous C- fibres as the reinforcement. The key properties of the fibres are their longitudinal stiffness and tensile strength, while the matrix transfers the load between fibres by their bonding to the matrix and holds them together, giving shape to the overall composite. For continuous fibre reinforced composites, the material in its final structure and the final product is generally made at the same time.

These materials have found applications as structural parts in many fields (Fig. 1) because of their interesting properties such as high specific stiffness, extremely high strength, low density, low thermal expansion, excellent damping and high impact resistance [1] [2]. Due to their anisotropic nature CFRP components can be designed for a particular purpose by choosing the appropriate matrix system, fibre type and the disposition of the reinforcement within a structure. The best mechanical performance is achieved by a continuous unidirectional fibre reinforcement. The desired mechanical properties and other predefined properties may be achieved by controlling the fibre type, orientation and to a limited extent by adapting the volume fraction throughout the structural component. The external geometrical shape of a structural component can also be adapted and designed to a particular application [3] [4], predominantly for long products or components consisting of shells.

Different processes can be used for the manufacture of semi-finished products and final products, depending on the geometry and requirement profile involved. The many diverse manufacturing techniques influence the properties of the finished component and determine the type and distribution of defects. For load transfer, the bonding between matrix and fibres as well as the effect of the microstructure of the materials (including defects within it) are decisive for their mechanical performance [2] [5].

Fig. 1: Race car made mostly of CFRP exhibited at the 15th European conference on composite materials.

History: first composites

Composite materials have been popular in construction since prehistoric times (Fig. 2). Mud and straw bricks, cob and adobe have been used for centuries over the world. Likewise, the wattle and daub method of construction has been used as far back as the Iron Age. Essentially longitudinal, tensile fibres i.e. straw, are bound together in a matrix, i.e. mud, with the baked material having the beneficial structural properties of both materials. In our days, fibre reinforced polymers use glass, aramid or carbon fibres in an epoxy matrix which binds them together in specific directions. The fibres are strong in tension but weak in compression. The epoxy matrix protects the fibres and transfers and spreads the shear forces between them [6].

Fig. 2: Composites have been used as construction materials since time immemorial. Here we can observe the walls of a building in a reconstructed roman city in Petronell-Carnuntum (Bruck an der Leitha, Austria). These ancient composites were made of cooked mud reinforced with tree branches in unidirectional or 0°/90° weave disposition.

"There is nothing new under the sun": natural composites

Composite materials are not a 20th century invention but occur naturally. Nature produces composite structures since the beginning of time. Structures made of natural composites usually exhibit lower strength and stiffness than their synthetic counterparts. However, their advantage lies in their greater flexibility of design and manufacturing, their adaptation to exposure during growth and curing ability. Natural composites, e.g. wood or bones can adapt their structural design to changes in environmental conditions; such behaviour cannot be currently expected from synthetic composites [7].

Structural applications and actual markets

Lighter than aluminium, stronger than iron and with higher stiffness than titanium, CFRP are becoming the material of choice for a broad spectrum of applications requiring high specific stiffness and strength. These include space structures, planes, racing cars, boats, ships, energy production (particularly wind energy turbines), pressure vessels and increasingly in other areas such as sports (bicycles, skis, etc.) and even in civil engineering (bridges, buildings, tunnels, etc.), particularly for uniaxially loaded components produced in relative small series.

In the aerospace and sport cars industries CFRP has been used regardless of cost and so the material performance to cost relation has become a key factor for further market penetration. Improving productivity and performance of these composites has therefore become the objective of many research and development efforts. Technological improvements have led to a decrease in the costs of raw materials and of composite production. CFRP became an alternative to conventional materials for many other applications, see Fig. 3 left diagram.
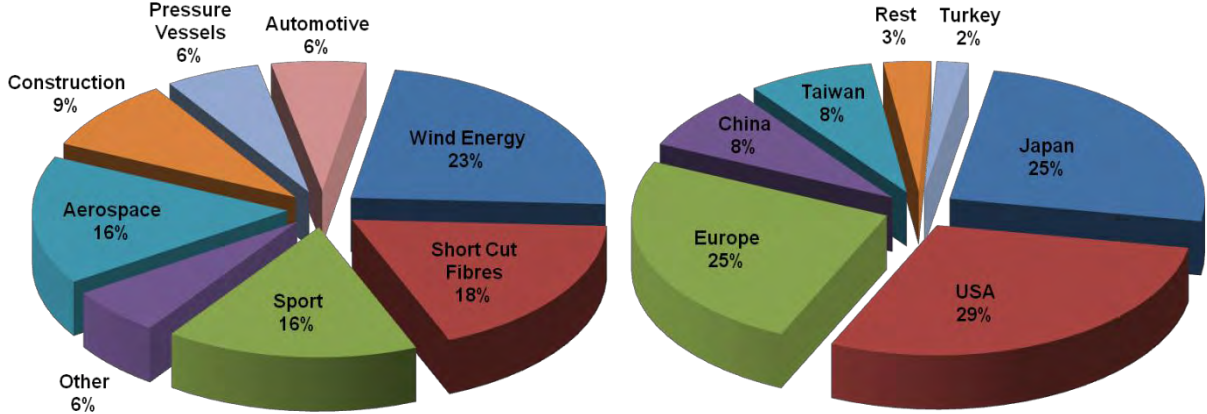
Fig. 3: Global CFRP consumption by application & carbon fibre production capacity by region (2011) [8].

As shown by the right diagram in Fig. 3, carbon fibre production is dominated by Japan and the USA, followed closely by Europe (Germany). The Global and China Carbon Fibre Industry Report 2010-2011 [9] published by Research in China (RIC) ranked the four global leaders. They are in the order of production capacity Toray (Japan), Toho Tenax (Japan), Zoltek (USA) and Mitusubishi Rayon (Japan). Carbon fibre production is dominated by small-tow (<10K) PAN-based fibres, which are produced by Toray, Toho Tenax and Mitsubishi Rayon. Zoltek, the report notes, deals primarily with large-tow (>10K) PAN-based materials with nearly half the total global capacity. China has embarked on the industrialisation of carbon fibre technology and has 8% of the total global capacity.

Strong signs of recovery in the USA and Germany signal a positive growth in the global demand for carbon fibre materials, as observed by Acmite Market Intelligence in its July 2010 report, World Carbon Fiber Composite Market [10]. The strongest demand is expected in aircraft/aerospace and wind energy. Researchers at Lucintel relate that supply has increased to the point that some manufacturers now have ample supply of carbon fibre with relatively short lead times to consumers. In its April 2010 report, Growth Opportunities in Carbon Fiber Market 2010-2015 [11], Lucintel predicted that the global carbon fibre market will grow 13% per year through 2015, when the market is expected to reach US $2.3 billion in value [12].

The market for CFRP continues to grow strongly. According to an October 2012 study by the Carbon Composites e.V. (CCeV) [8] a high growth, with rates of 13-17%, is expected (Fig. 4 and Fig. 5). Currently, the global demand for carbon fibres accounts 37.000t (compared to $250 \cdot 10^6$ t annual polymer production), from which 98% flow into the CFRP production. In 2012, a demand of 42.000t is predicted, for 2014, 73.000t requiring approximately the same amount of polymer matrix.

The largest consumer is the wind power market with 23%, the 6% share in vehicle manufacturing is still relatively small, but promises the biggest growth potential.

The crux of the success of the composite materials, particularly CFRP, is their suitability for automated mass production. This would make the materials attractive for economically viable new applications. This challenge has been studied by the VDMA Forum Composites in cooperation with Roland Berger Strategy Consultants, under the project name: "Mass production of high-strength fibre composite parts - Perspectives for the German plant and mechanical engineering". According to the initial results, the costs of fibre composite components will be reduced by 30% by 2020 [13].
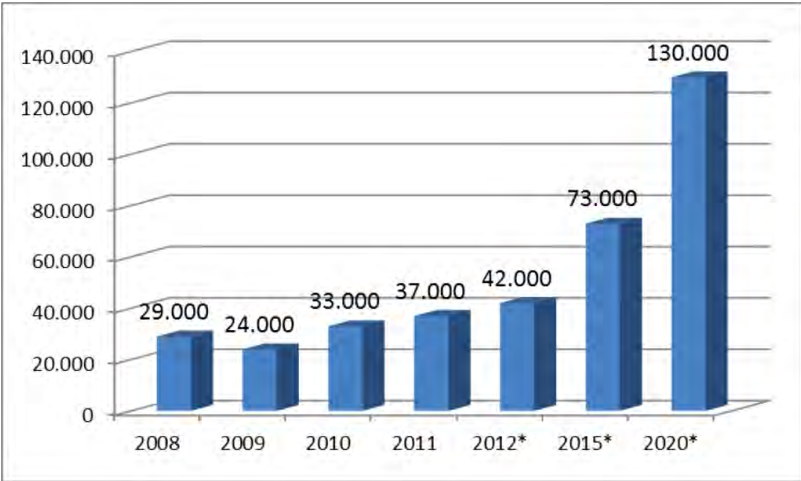
Fig. 4: Global demand for carbon fibre in tonnes 2008-2020 (*estimates) [8]. These highly optimistic forecasts reflect the declared intent of a number of companies to expand their production capacity.
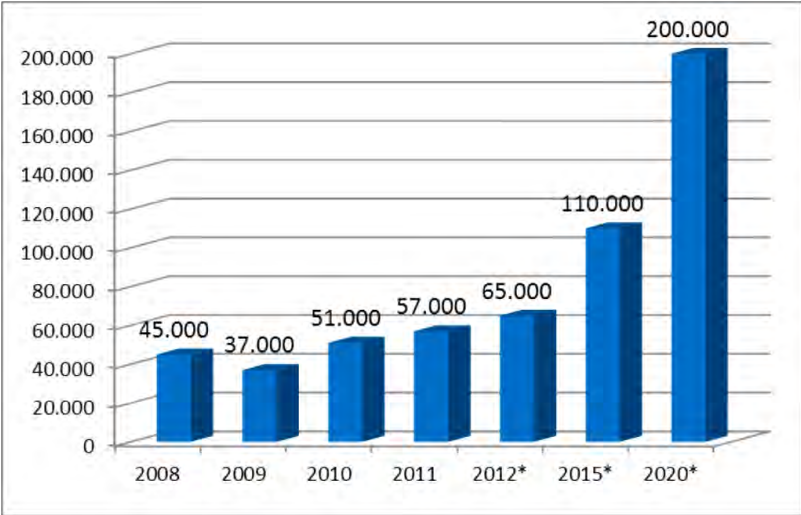
Fig. 5: Global demand for CFRP in tonnes 2008-2020 (*estimates) [8]. As the vast majority of carbon fibre produced (over 98%) is processed into composite materials of all types, the carbon composite market develops at the same pace as the carbon fibre market. The tonnage of CFRP is naturally much higher, due to the addition of the matrix component.

Analysts see the CFRP as a solid market with high growth potential. The consensus is for growth of at least 13% annually. For sectors such as aerospace, construction and particularly automotive huge growth rates are forecasted [8].

2. State of the Art

2.1 Components of advanced polymer composites

2.1.1 Epoxy systems classification

Resin is a generic term used to designate the polymer, polymer precursor material, and/or mixture or formulation thereof with various additives or chemically reactive components. The chemical composition and physical properties of the resin, fundamentally affect the processing, fabrication and ultimately the properties of composite materials. Variations in the composition, physical state, or morphology of a resin and the presence of impurities or contaminants in a resin may affect handleability and processability, laminate properties, composite material performance and long-term durability [14].

Epoxies are polymerizable thermosetting resins consisting of a blend of major (Fig. 6) and minor epoxies, with different epoxide groups curable by reaction with amines, acids, amides, alcohols, phenols, acid anhydrides, or mercaptans. They are characterised by the presence of the epoxide group, an oxirane structure, consisting of a three-member ring with one oxygen and two carbons. The cure of epoxy resins is based on the oxirane ring opening and crosslinking with the curing agent. The epoxide group has unfavourable bond angles, which makes it chemically reactive with a variety of substances that can easily open the ring to form a highly crosslinked structure. Aromatic epoxy resins are the most common matrix material for high-performance CFRP composites [5].

Diglycidyl ether of Bisphenol A (DGEBA)

Tetraglycidyl methylene dianiline (TGMDA)
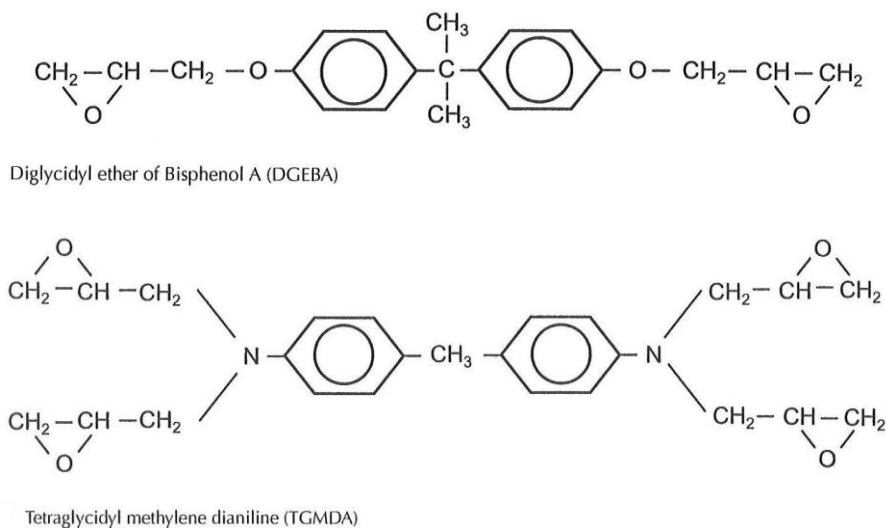
Fig. 6: Two main major epoxies are DGEBA (diglycidyl ether of Bisphenol A), which is used extensively in filament winding and pultrusion and TGMDA (tetraglycidyl-4-4"-diaminodiphenylmethane), which is used frequently for commercial composite matrix systems [5].

Minor epoxies are frequently added to improve processability (viscosity), elevated temperature performance or other properties of the cured resin. Typical minor epoxies include amine-based phenols, novolacs, cycloaliphatics and others.

Diluents are sometimes added to epoxy resin systems to reduce viscosity, improve shelf and pot life, lower the exothermic heat and reduce shrinkage. They are used in small amounts of up to 5%, because higher concentrations degrade the mechanical and thermal properties of the cured system.

There are a wide variety of curing agents that can be used with epoxies; the most common include aliphatic and aromatic amines, anhydrides and catalytic agents, such as BF_3. Aliphatic amines are very reactive, producing enough exothermic heat given off by the reaction to cure at room or slightly elevated temperatures. However, since these are room-temperature curing systems, their elevated temperature properties are lower than those of the aromatic amine systems cured at elevated temperatures. The elevated temperature performance of aliphatic amine systems can be improved by initially curing at room temperature followed by a second curing at elevated temperature to increase crosslinking density. Aromatic amines require elevated temperatures, usually 120° to 175°C, to obtain full cure. Aromatic amines produce structures with greater strength, lower shrinkage and better temperature capability but are less tough than aliphatic amines. Dyaminodiphenyl sulfone (DDS) is by far the most common curing agent used in epoxy composite matrices.

Epoxy resins for composite matrices are truly engineered systems to yield the best combination of processability and final properties. The principal epoxy in most systems is TGMDA, two or more minor epoxies are added to control viscosity or influence the final cured properties. The major curing element is DDS, catalytic curing agents can be added to reduce flow and accelerate the cure. Higher cure temperatures and long cure times give the highest glass transition temperatures (Tg). When these are combined with high functionality, for example four reactive groups, the highest possible crosslinking densities are achieved, yielding strong, stiff but somewhat brittle structures. The resin is frequently toughened by a number of different means, but this often results in lower temperature resistance. The use of flexibilizing units gives higher elongation and impact strength at the expense of Tg, tensile and compression strength and Young's modulus of the resin [5].

A classification of epoxy resins can be made in terms of their thermal stability:

HT: High temperature epoxy   LT: Low temperature epoxy.

2.1.2   C-Fibres classification

Carbon fibres are available in many grades and forms with wide-ranging properties. Their most attractive attributes are their longitudinal properties: high modulus of elasticity, good strength and fatigue properties, excellent creep resistance, low thermal expansion coefficient, high thermal conductivity, and low electrical resistivity; combined with orientation independent properties: low density (giving good specific properties), good thermal stability in the absence of oxygen, good chemical resistance and biocompatibility. The disadvantages are: relatively high cost, low strain to failure, lower compressive than tensile strength, poor mechanical properties in transverse direction. Care is required while handling carbon fibres, since they are electrically conductive, oxidize in air at temperatures above 450°C and exhibit high anisotropy of physical and mechanical properties in the axial and transverse directions (see Fig. 7).

$E_\perp = 36.000 \text{ N/mm}^2$

$E_\| = 1.050.000 \text{ N/mm}^2$

fibre direction

$\dfrac{E_\|}{E_\perp} \sim 28$

strong covalent bonding   weak van der Waals interaction
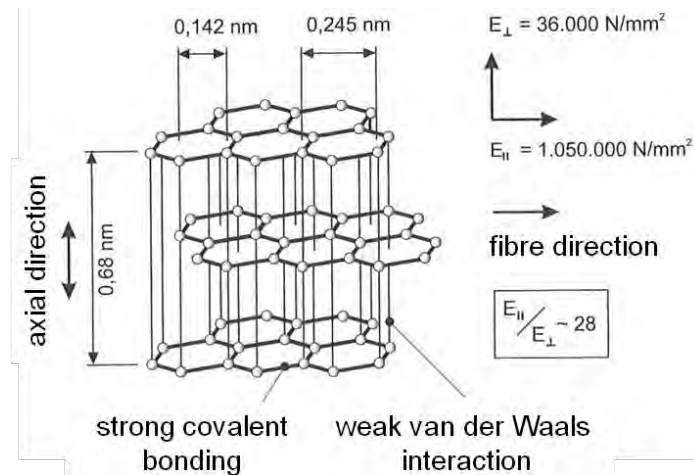
Fig. 7: The graphite structure of C-fibres explains their anisotropy. In fibre direction there is strong covalent bonding, whereas in the axial direction only secondary van der Waals forces are responsible for the bonding between graphitic layers [2].

Carbon fibres can be prepared from polymeric precursor materials such as polyacrylonitrile (PAN), cellulose, pitch and polyvinylchloride. PAN based carbon fibres predominate and have longitudinally good strength and high stifness, whereas pitch based fibres have a higher longitudinal Young's modulus, but a lower longitudinal strength. The ideal requirements for a precursor are that it should be easily converted to carbon fibre, give a high carbon yield and allow to be processed economically [15]. The production of the precursor, or white fibre consists of the following processes: polymerization, spinning, drawing and washing (**Fehler! Verweisquelle konnte nicht gefunden werden.**). The characteristics of the white fibre influence the processing of the resulting black fibre. The black fibre process consists of several steps: oxidation, pyrolysis, surface treatment and sizing. For the oxidation process the fibre diameter is limited by waste gas diffusion. In pyrolysis, which is performed under an inert atmosphere, most of the non-carbon material is expelled. In the surface treatment step the fibre may be etched in either gas or liquid phase by oxidizing agents such as chlorine, bromine, nitric acid or chlorates. This together with the sizing improves the wettability by the resin and encourages formation of a strong durable bond. Carbon fibres are often treated with solutions of unmodified epoxy resin or other products as a size. The sizing prevents fibre abrasion, improves handling and can provide an epoxy matrix compatible surface [14].
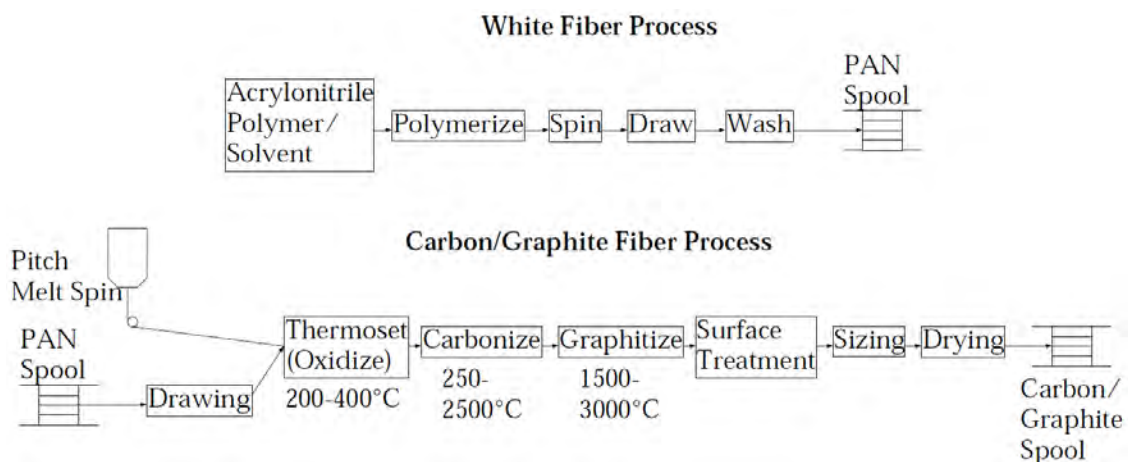
Fig. 8: Flow diagram for carbon fibre processing [14].

PAN precursors: The PAN polymer has a continuous carbon backbone and the nitrile groups are ideally placed for cyclization reaction to occur, producing a ladder polymer, believed to be the first stage towards the carbon structure of the final fibre. The carbon content of acylonitrile ($CH_2=CHCN$) is 67.9%, this precursors have a carbon yield of 50-55%.
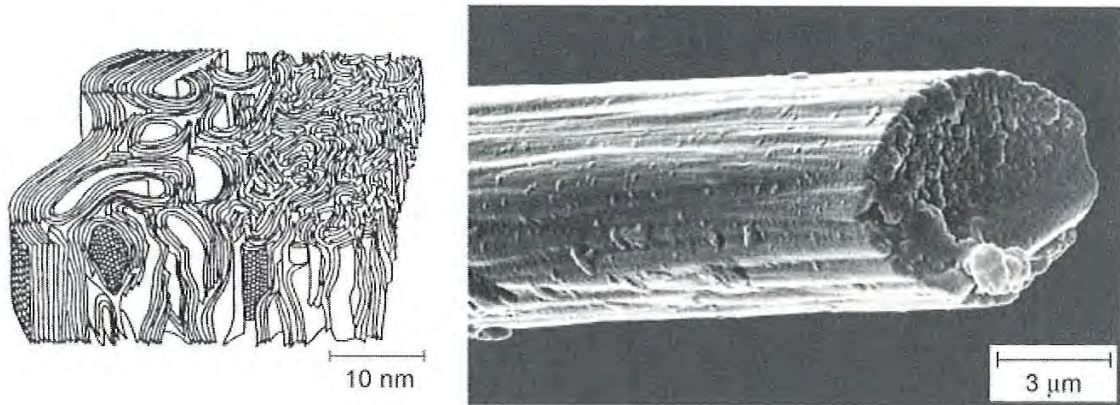
Fig. 9: Typical onion skin microstructure of a PAN based C-fibre and SEM micrograph of a fibre [2].

Cellulosic precursors: A cellulosic precursor ($C_6H_{10}O_5$) has a carbon content of 44.4% but, unfortunately, in practice, the reaction is more complicated than just simple dehydration and the carbon yield is only of the order of 25-30%.

Pitch precursors: Pitch based carbon fibres have a higher yield of 85% with a high resultant Young's modulus but, due to their more graphitic nature, they will have poorer compression and transverse properties as compared to PAN based carbon fibres [15].

X4000   X8000   X50000
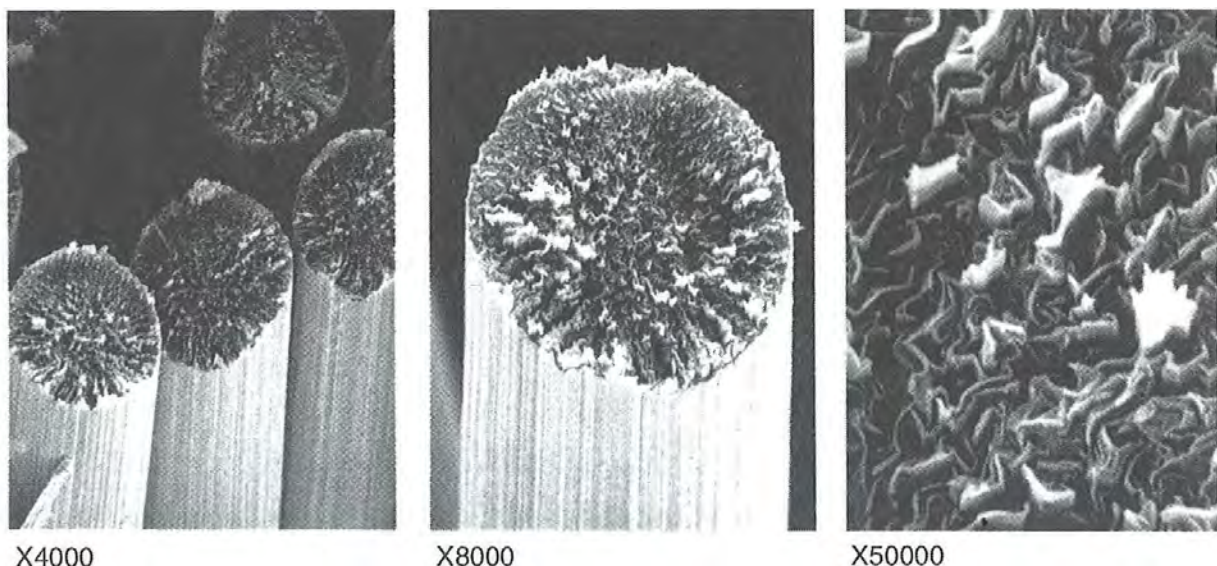
Fig. 10: SEM micrographs at different magnifications of a pitch based C-fibre showing its typical radial foiled microstructure [15].

Fibres are produced as tows consisting of 1K to 60K fibres of about 7 μm in diameter each in a bundle wound on bobbins. Another way of classifying C-fibres is by their tensile properties [2]: HT: high tenacity; IM: intermediate modulus; HM: high modulus; UHM: ultra-high modulus; UMS: ultra-modulus strength. See Fig. 11.
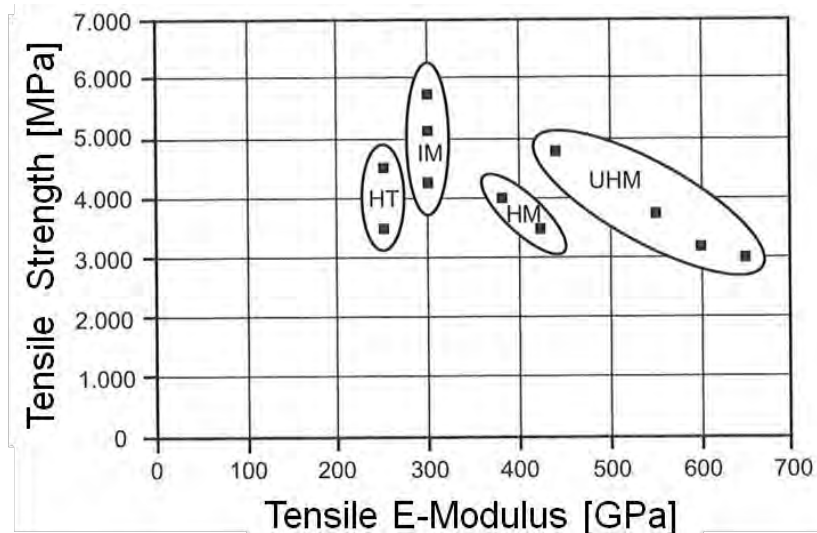
Fig. 11: Fibre strength as function of the E-modulus for the different carbon fibre types [2].

2.2 Processing of CFRP components

As broad are the applications, so are the manufacturing methods, but not all of these can be controlled to assure the quality needed for performance requirements [15]. The main industrial requirements are: high performance, reproducibility, cost and energy efficiency.

Besides material composition, manufacturing parameters such as temperature, time, pressure, etc. play a decisive role for the quality and performance of the CFRP component. Depending on the size, desired application and complexity of the part being produced, an adequate production process must be found. An overview of the possible combinations is shown in Fig. 12. Big complex components e.g. wind energy rotor blades are produced from laminates using established techniques such as autoclave or resin injection. Smaller parts with an easy geometry, like unidirectional tubes for sport applications are made by pultrusion.
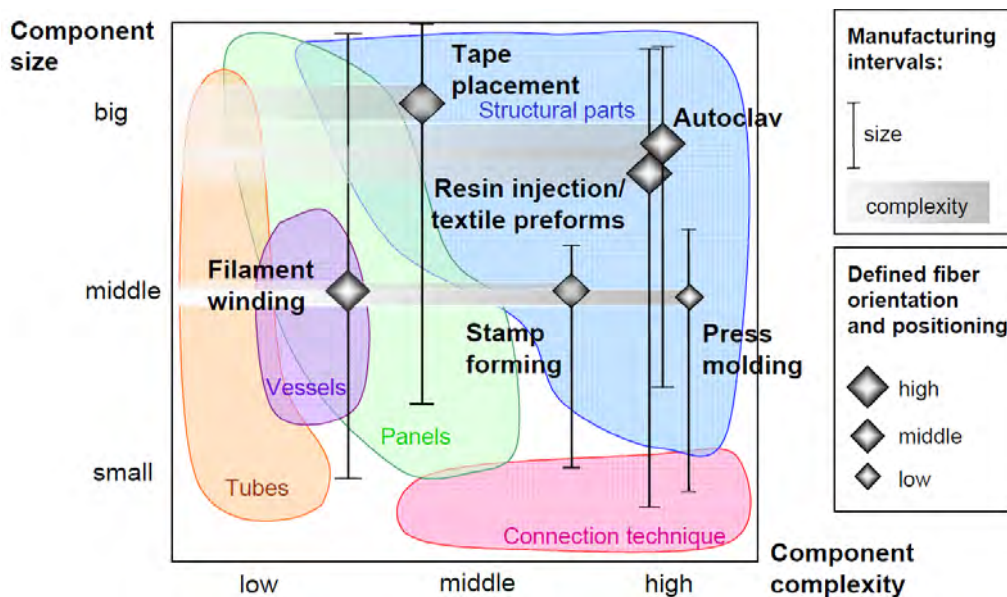
Fig. 12: Relationship between manufacturing process and CFRP component size and complexity [17].

The three manufacturing techniques relevant for this work are presented here.

Prepreg moulding. When applied to aircraft structures, carbon composites are generally supplied in unidirectional (UD) form: thin sheets or tapes (~0.125 – 0.25 mm thick) of parallel fibres that have been pre-impregnated with resin that has yet to set. This form of the material is ideal for the manufacturing of thin plates that are used so extensively in airframe structures. The production of prepregs begins with the pre-impregnation of the reinforcement fibres with a resin or binder. The composite processing by combining of these two materials occurs prior to the moulding process and therefore enables a very accurate reinforcement to resin ratio to be achieved. Prepregs are pliable and therefore able to be cut into various shapes or patterns prior to processing into moulded products. Manufacturers use tape-laying machines to lay down layers, or plies, of this material, one on top of the other, to form single piece sub-components. By laying successive plies in different directions, the strength and stiffness of the component can be tailored to match the demands of the engineer, allowing adequate structural properties to be attained for minimum weight [18].

Bag press moulding. The elimination of autoclave curing of CFRP materials, while delivering the same performance and material characteristics of autoclave-cured parts, is an industry priority. Autoclaves for large parts are expensive to build and operate and require huge amounts of electrical energy. Plus, the process is slow, resulting in long queues of parts awaiting final cure. Out-of-autoclave (OOA) processing promises a much less expensive alternative with shorter cycle times. The low-temperature, vacuum-bag or press moulding offer the mechanical performance equivalent to autoclave-cured, toughened epoxy prepreg systems [12].

Pultrusion combines the composite processing with the production of long products. Therefore it is particularly useful for producing unidirectional structural profiles with constant cross sections. Developed in the 1950s by the person considered by many to be "the father of composites" W. Brandt Goldsworthy, it is the process of "pulling" raw composites through a heated die to create a continuous composite profile. The term pultrusion combines the words, "pull" and "extrusion". Extrusion is the pushing of material, such as a billet of aluminium, through a shaped die. Pultrusion is the pulling of carbon fibres impregnated in a yet to cure resin, through a shaped die. It enables the easy production of long products with constant wall-thicknesses such as rods, tubes and other hollow cross sections [19]. Due to the pulling, the fibres are in tension and thus better aligned and compacted achieving a higher volume fractions providing higher longitudinal strength of the composite [20].

2.3 Mechanical and thermal properties of CFRP composites

CFRP can be tailored for a particular application. The mechanical properties of the composite are determined by the appropriate single constituents, whereas the stacking of the plies offers the possibility of designing shells for structural parts with the desired mechanical properties in a given direction such as to fulfil the needs of a particular loading condition (see Fig. 13). The architecture, that is, the configuration of the reinforcement phase within the matrix phase, dictates the composite's anisotropy, mechanical and physical characteristics, therefore different stacking sequences are used depending on the required composite performance.
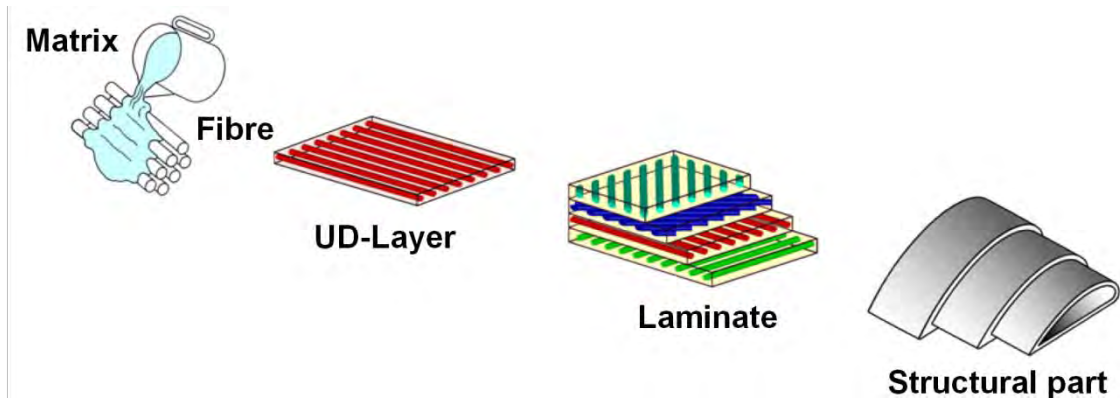
Fig. 13: Design parameters: components, single layer (ply), laminate, and structural component. The mechanical properties of CFRP composites can be designed depending on the design requirements [7].

Fig. 14 illustrates how unidirectional fibres, which lie parallel to each other, provide the highest stiffness and strength in the direction the fibres are laid (anisotropic material). Creating a weave or mat formation of fibres (0°, 90°, 45° etc.) could distribute the mechanical properties in certain directions (planar quasi-isotropic material). Shortening fibre length and arranging them in a 2D random order, results in equal stiffness and strength in all directions within a plane (planar isotropic material).
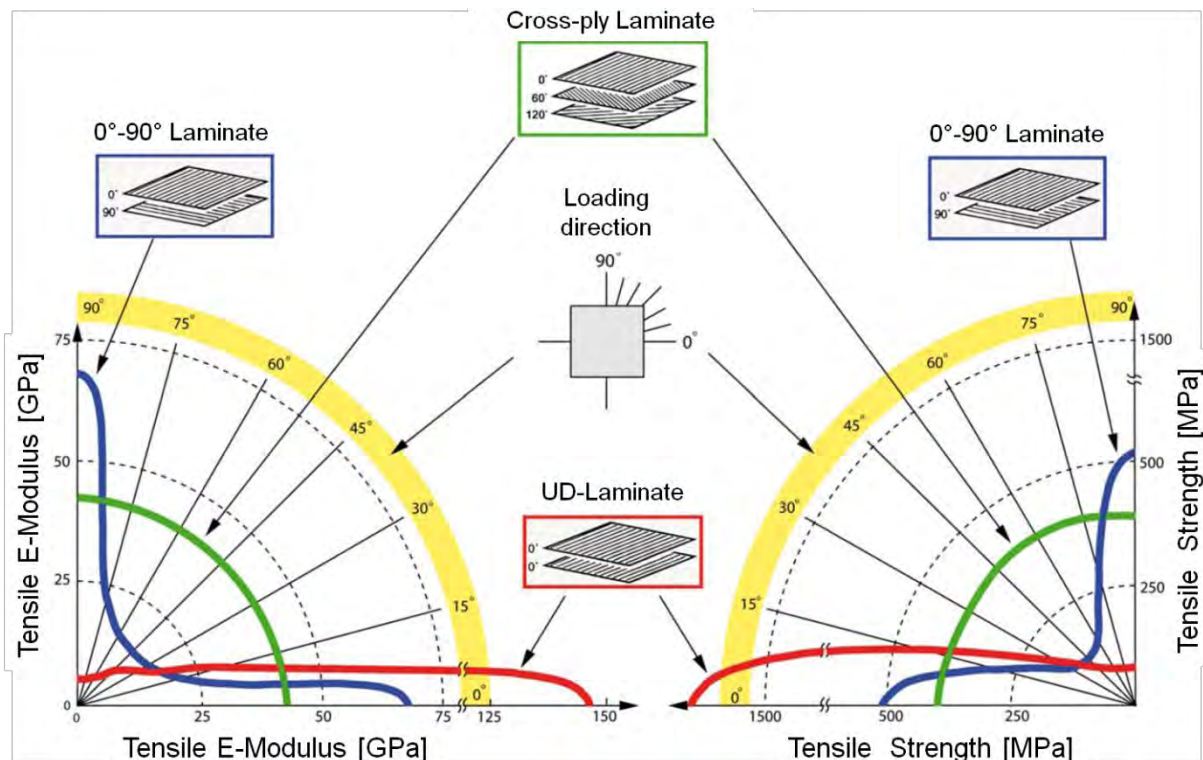
Fig. 14: Mechanical properties of laminates with different reinforcement dispositions plotted in a polar diagram show how fibre direction influences stiffness and strength dramatically [7].

The different packing of carbon fibres and the symmetry planes of a UD laminate (1: longitudinal, 2: in-plane-transversal and 3: out-of-plane) are described in Fig. 15. Taking into account real fibre packing in UD layers, the 1-2 and 1-3 planes can be considered statistically isotropic. Therefore, the assumption of a transversely isotropic material behaviour for UD layers or laminates is justified. Furthermore, out-of-plane and in-plane properties are poor.

15
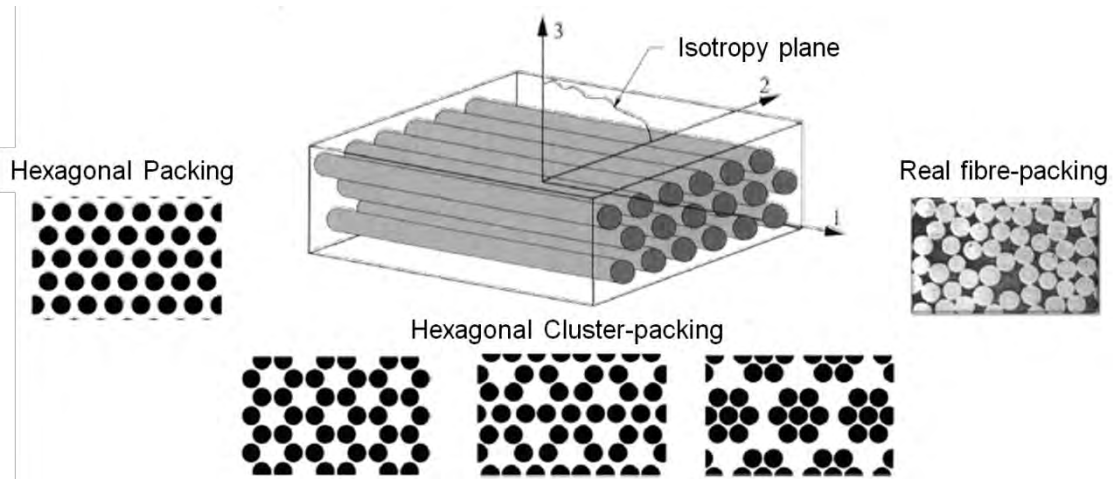
Fig. 15: Symmetry planes of a orthotropic UD laminate. Mechanical properties in 1 direction are much higher than in 2 or 3, due to C-fibre anisotropy. The transversal isotropy is explained by the irregular packing of the cylindrical fibres in real CFRP laminates [7].

Ashby diagrams like the one presented in Fig. 16 allow us to compare several materials at once [21]; for instance in terms of specific 0° stiffness, CFRP can be compared to other light weight construction materials used for similar applications, like aluminium or titanium alloys.
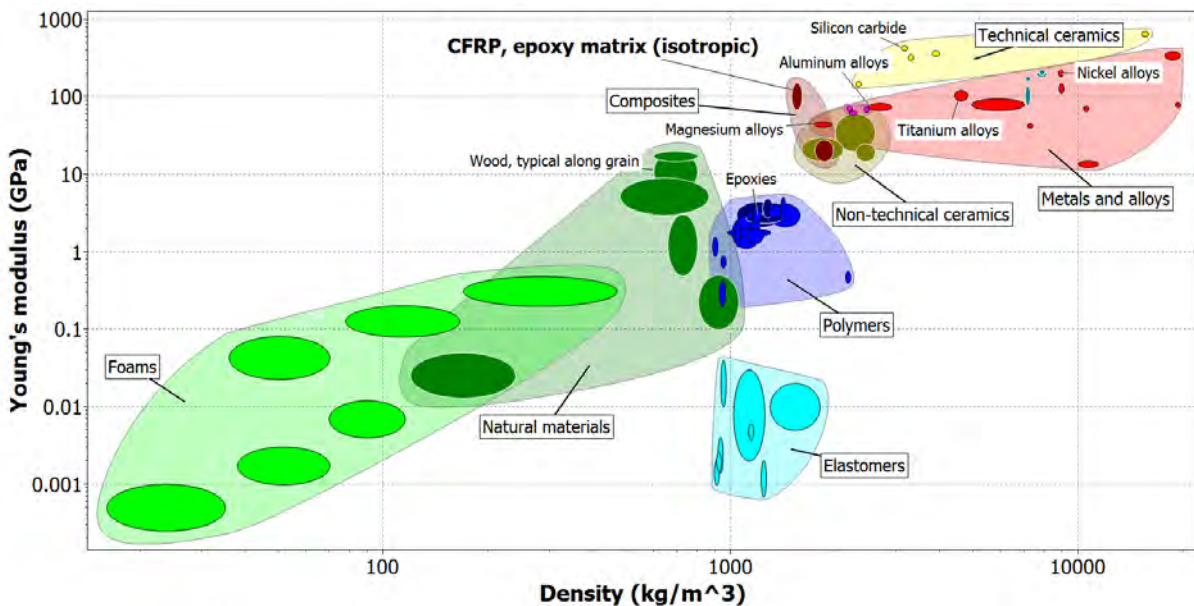
Fig. 16: Ashby diagram Young modulus versus density [22].

By applying the rule of mixtures (ROM) theoretical values for composites properties can be obtained [23]. The mismatch between theoretical and experimental results can be explained in terms of defect density, uniformity of reinforcement distribution and fibre misorientation.

$$E_{0°} = f_F E_F + (1 - f_F) E_M$$

$$\sigma_{0°} = f_F \sigma_F + (1 - f_F) \sigma_M$$

E_F ... Young's Tensile modulus of the fibres [GPa] E_M ... Young's modulus of the matrix [GPa]

σ_F ... Longitudinal Tensile strength of the fibres [MPa] σ_M ... Tensile strength of the matrix [MPa]

f_F ... Fibre volume fraction [%]

Thermal analysis is a branch of materials science where the properties of materials are studied as they change with temperature. Techniques such as differential scanning calorimety (DSC), thermal mechanical analysis (TMA; DMA) and thermogravimetric analysis (TGA) are used to determine the degree of cure, the rates of cure, heats of reactions, melting points of thermoplastics and thermal stability.

The cured glass transition temperature (Tg) of a polymeric material is the temperature at which it changes from a rigid glassy solid into a softer, viscous material. At this point, the polymer structure is still intact but the cross-links are no longer locked in position. The Tg determines the upper temperature limit for a composite, above which the material will exhibit significantly reduced mechanical properties. Since most thermoset polymers will absorb moisture, which can severely depresses the Tg, the actual service temperature should be about 30°C lower than the wet or saturated Tg [5].

The glass transition temperature can be determined by several methods, such as TMA; DSC and DMA, all of which give different results because each measures a different property of the resin [24] [25]. Fig. 17 shows idealized schematic outputs from these three methods.
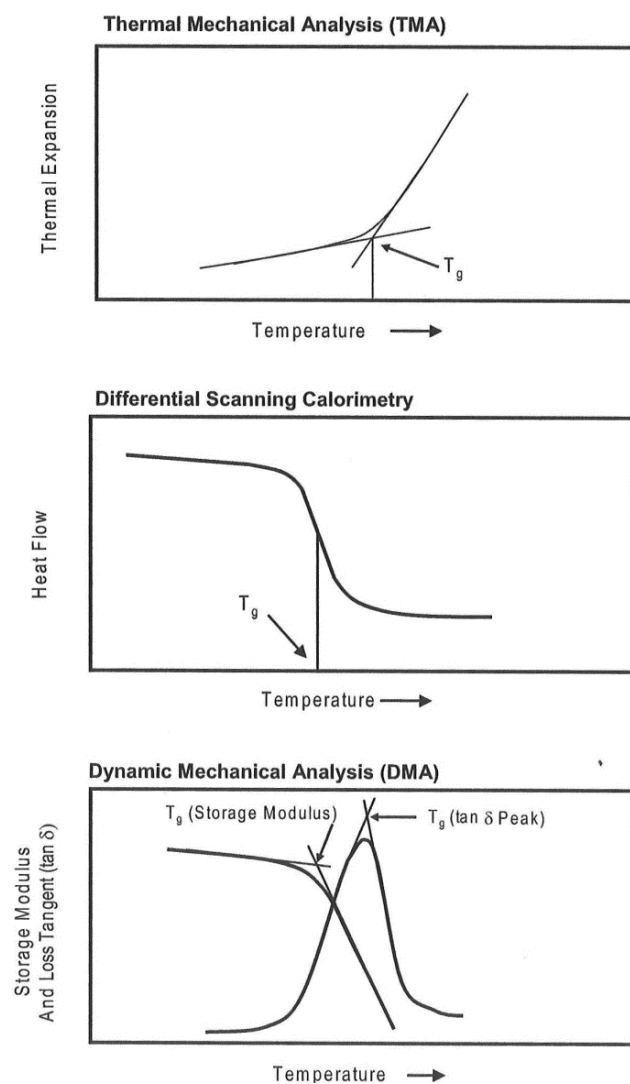
Fig. 17: Schematic thermal analysis curves showing how glass transition temperature (Tg) can be determined on each case [5].

2.4   Defects in composite structures

Theoretical design relies upon a firm understanding of the physical and mechanical properties of the three important constituents of a composite: the reinforcement fibre, the matrix resin and the interface between fibre and resin. Equations defining how a composite structure responds to an applied load are typically governed by a number of physical assumptions, these often are pretty universal in developing failure criteria. An assumption is made that a) fibre and resin are perfectly bonded together, b) individual layers are also perfectly bonded together and homogeneous in nature, with fibres homogeneously packed within the matrix. Failure criteria are developed without regard to the presence of manufacturing defects which can contribute significantly to the premature failure of a structural part.

Environmental and processing conditions such as: temperature, pressure, moisture, shelf-life, out-time and contamination, can often create manufacturing defects that must be accounted for in the design of a composite structure. The typical defects found in composite structures are: porosity, voids, delaminations, fibre-matrix debonding, misaligned fibres, fibre/bundle waviness, fibre bridging, resin rich areas and inclusions (foreign objects).

Processing flaws can occur at almost any stage of the composite manufacturing. Foreign objects are the most serious issue during ply collation. Other irregularities are ply misorientation, gaps/overlaps at ply edges and ply wrinkling. The cure process can also result in defects, the most serious being porosity and voids. Incorrect fibre volume fraction and matrix microcracking are other possible consequences, as well as the presence of over/under cured parts. If an adhesive bonding operation is involved, adhesive unbonds are some of the most serious damages. Delaminations are one of the most serious types of defect encountered during machining, assembly and in service. It is therefore important to be able to reliably find and characterise these relevant defects [5].

Methods used to describe composites' microstructure and to asses defects can be classified in terms of sample integrity in destructive and non-destructive methods [26] [15] [27] [28] [29] and in terms of visualisation in 2D and 3D methods (see Tab. 1).

	2D	3D
Destructive Methods	Light optical microscopy (LOM)	Light optical tomography (LOT)
	Scanning electron microscopy (SEM)	FIB-Tomography
Non-destructive methods	X-ray Radiography	Computed Tomography
	Acoustic emission	Laminography
	Laser ultrasonics	Infrared Thermography
	Visual inspection	Sampling phased array

Tab. 1: Summary of destructive and non destructive methods applied for CFRP characterisation and quality control.

2.5   Effect of defects

The traditional "effects of defects" approach, practiced a few decades ago, relied on testing with simulated defects, e.g. artificially induced delamination, and analyses where defects were embedded in a homogenized composite [30] [31] [32]. Today, experimental techniques have advanced to the extent that images of defects such as voids can be generated in three-dimensional geometry [33], and computational methods can analyze local stress fields around

defects with high accuracy [34] [35] [36]. These advances call for a "defect engineering" approach that can produce a cost/performance trade-off based design strategy. This makes it possible to investigate the effects of defects in ways that are compatible with physical observations of real products. The classical "effects of defects" approach based in introducing artificial defects and characterising them, must be replaced by realistic real structural components studied and analyzed with the help of coherent physically justified models [37].
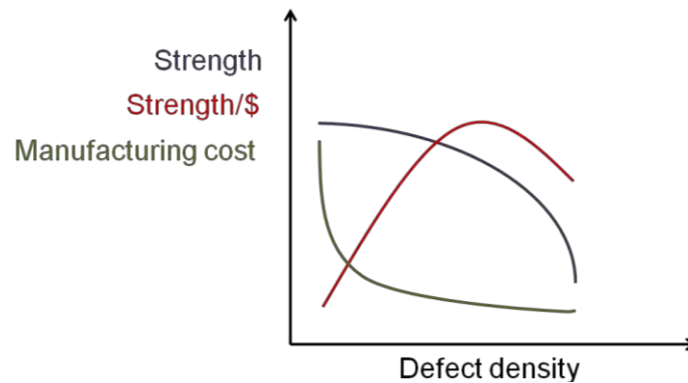
Fig. 18: The role of defects in cost/performance trade off [38].

Cost-effective manufacturing is a design limiter in most non-aerospace structures (see Fig. 18). The conventional approach to accept or reject a composite part based on detection of manufacturing defects, e.g. voids of a certain volume fraction or delaminations of a certain size, by ultrasonic or other inspection techniques, is not viable except in the high end of aerospace applications. Many applications today, particularly wind turbine rotor blades, would be prohibitive in cost if designed on the basis of only negligible defects. In these structures significant amounts of manufacturing defects are inevitable, and a sound engineering approach would be to account for their effects rather than apply arbitrarily large factors of safety and conduct expensive full-scale tests as proof of safety [38].

Manufacturing defects cannot be avoided, they must be analyzed. Most relevant defects have been intensively investigated in the last few years. Fibre misalignment and bundle waviness, an intrinsic property of continuous C-fibres, have a detrimental influence on the mechanical performance of CFRP composites and have to be carefully characterized [39] [40] [41]. Porosity content, distribution and void shape and size affect properties such as the interlaminar shear strength [42] [43]. Damage mechanism assessment [44] in order to understand failure initiation and evolution as well as fatigue properties [45] is a fundamental line of research, that has not been fully explored yet.

Most conventional experimental methods for micromechanical analysis suffer from either being destructive and, thus, limited to the surface observations or being of limited spatial resolution. Consequently, X-ray tomography is increasingly being employed to study the micromechanical response when assumptions are made in fibre failure based models of strength. Moffat et al. [46] [47] [48] [49] used synchrotron X-ray microtomography to study ply splits in a $[90/0]_S$ CFRP laminate during loading of notched samples. Scott et al. [50] [51] carried out a more detailed analysis by incremental straining of notched specimens to failure.

3. Motivation

The main objective of the present work is to assess the effect of defects on the mechanical and thermal performance of carbon fibre reinforced polymer composites (CFRP). The knowledge gained should help to increase reliability and to decrease rejections in the course of the production of composites for structural applications. The interaction between relevant factors is summarized in Fig. 19.
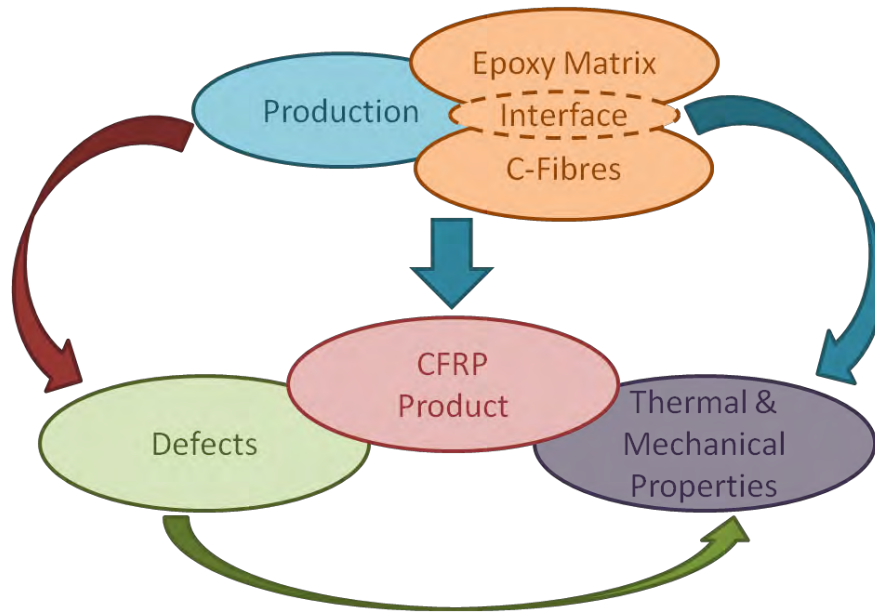
Fig. 19: Effect of defects. The selection of constituents and the choice of processing determine the formation of characteristic defects in the final CFRP product influencing its thermal and mechanical properties. These properties are also influenced by the nature of the single components, their mutual interface, volume fraction and spatial arrangement.

Initially, a structural characterisation of the composites' architecture will be carried out in order to characterise the inner architecture and presence of unavoidable defects within the composite. Characteristics such as fibre orientation highly influence the mechanical properties (e.g. the Young's modulus can be more than ten times lower in the transverse direction compared to the longitudinal direction). Furthermore, the degree of cure of the epoxy matrix determines the temperature resistance of the final product. Therefore a mechanical and thermal characterisation of the materials follows. A correlation can be made between the mechanical and thermal properties and the defect parameters found during the previous structural investigations.

The architecture of a composite is intrinsically linked to the manufacturing processing route. The forming process affects: the degree of cure, the glass transition temperature, fibre orientation and alignment, uniformity of the fibre to resin ratio, void volume fraction and residual stresses. It also determines the dimensional tolerances and final properties (Fig. 20). Besides processing induced defects, certain defects may be caused by the chosen constituents, for instance a poor interfacial adhesion. Defect characterisation by classification and quantification does not necessarily give an insight regarding the origin of each particular defect, but forms the basis for the evaluation of their influence on the material properties in

terms of defect-related parameters. This work aims to evaluate which factors (i.e. selection of constituents, production parameters, thermal history) are more relevant for premature failure. Therefore, during the whole work, it is of paramount importance to consider the factors influencing the observed properties while trying to achieve concluding statements on the causality of an observed behaviour. These phenomena are all interconnected and sometimes, it is not possible to study them separately to quantify their individual contribution to an actual property.

Defect definition: A defect is an undesirable deviation from the intended microstructure introduced by the processing steps either when the components are brought together or is inherent in one of the constituents. Some typical defects are, for example, porosity, inclusions, fibre misorientation, waviness and heterogeneous distribution of constituents, since they represent deviations from the idealized homogeneous UD distribution (shown in Fig. 15). Primarily, the effect of the defects with respect to application and mechanical performance will be quantified and assessed. Which defects affect which property and how large is their influence? Is it possible to introduce threshold values and safety factors? How does the fibre-matrix interface influence the mechanical and thermal properties of the composite? Furthermore, an assessment of the different techniques available for the detection and quantification of defects is intended. In addition, this work tries to associate the different kinds of defects with the matrix or the fibres or the composite manufacturing steps.
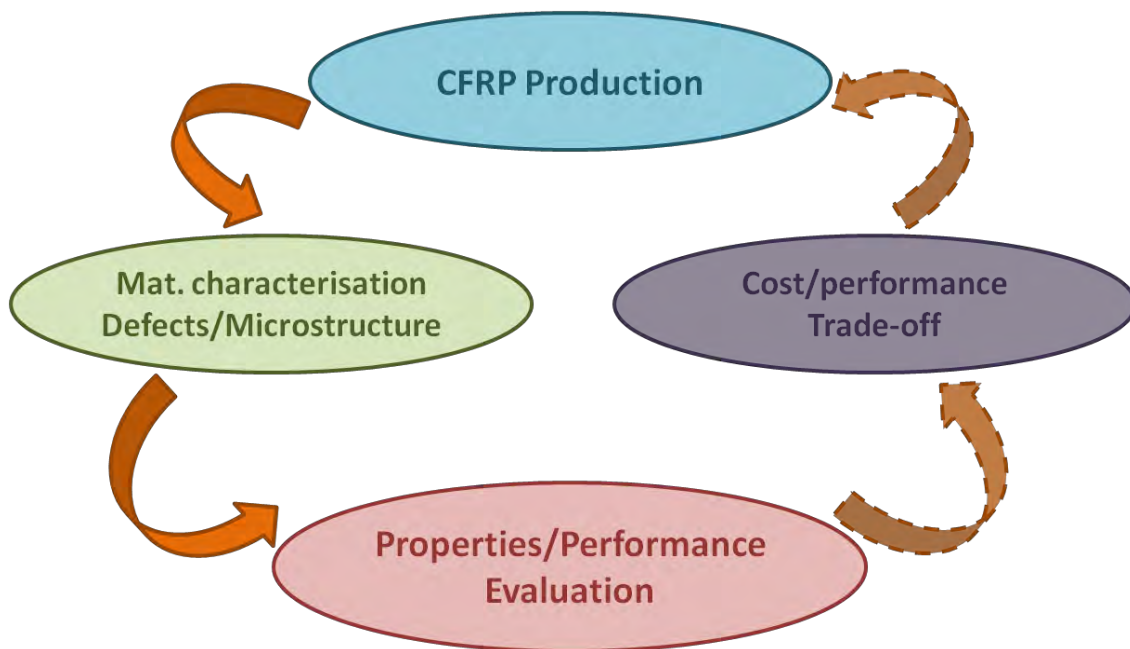
Fig. 20: Characterisation of composites' architecture reveals the causality of its service performance to be considered as a trade-off on processing costs and eventually as a source of production improvements.

The designers apply relatively large safety factors to the specified properties owing to limited reliability. If the most degrading defects are identified and means are applied to reduce their effect then a narrower scatter of properties can be achieved. It is assumed that correlations between the mechanical properties of CFRP and their internal inhomogeneities are necessary to develop more reliable CFRP products with knowledge based safety factors.

4. Experimental

4.1 Materials

The materials investigated are Carbon Fibre Reinforced Polymers (CFRP) composites. For this work the polymer matrix is always an epoxy system and the fibres are PAN based carbon fibres. Some of the studied CFRPs contain filler particles as well, introduced as additional reinforcement to the matrix. The studied materials can be classified in many ways.

Regarding their geometry, two groups can be distinguished:

➢ Laminates
➢ Pultruded profiles

Regarding reinforcement orientation:

➢ Unidirectional continuous reinforcement (UD)
➢ Multidirectional reinforcement with different fibre orientations(0°/90° and ± 45°)

Regarding production process:

➢ Prepreg compression moulding
➢ Vacuum-bag moulding
➢ Pressurized chamber
➢ Pultrusion

In the following sections, materials are presented in two subchapters; 4.1.1 for laminates and 4.1.2 for pultruded profiles, within each one of them manufacturing process and nomenclature of the studied composites are presented in two separate sections. Sections 4.1.3 to 4.1.5 are dedicated to each particular component (carbon fibres, epoxy matrix and prepregs) separately.

4.1.1 Laminates

4.1.1.1 *Laminates manufacturing Process*

The different studied CFRP laminates can be classified into three groups according to their production route. Six different manufacturing processes can be distinguished considering the actual conditions applied. These are listed in detail in Tab. 2.

<u>Prepreg compression moulding:</u>

The different steps used are summarized in Fig. 21. Step1: Lay-up or stack multiple plies of preimpregnated fabrics (prepreg) inside a vacuum bag. Step2: Packaging, the shape of the mould determines the laminate final geometry. The moulded product is wrapped with a polypropylene or nylon tape prior to heat curing. Step3: The sealed mould undergoes curing in a hot press under a controlled temperature program at a constant pressure. Heat curing gives a permanent hard, cross linked composite structure. Following curing the tape is removed and if necessary the completed moulded form can be post cured.
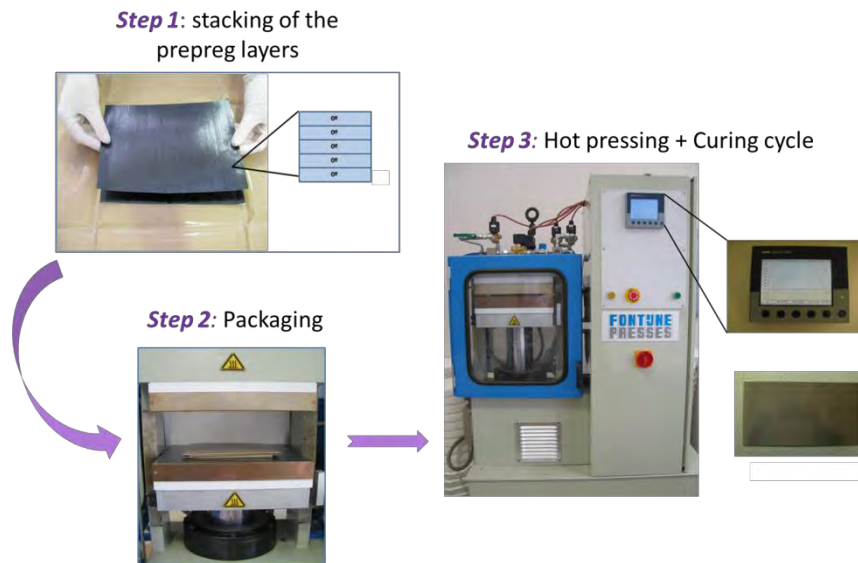
Fig. 21: Prepreg compression moulding (corresponding to processes P1 and P2).

The two different curing cycles used to process the prepreg laminates are shown schematically in Fig. 22. The difference between them is the temperature of the first isothermal plateau, this leads to different end products.
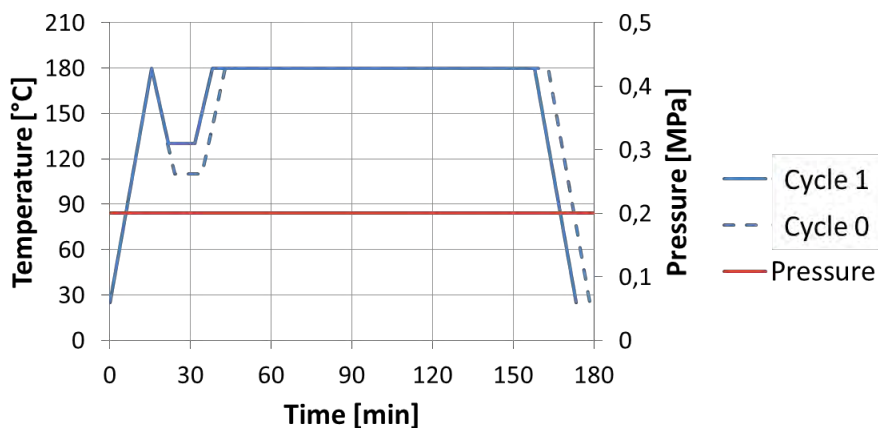
Fig. 22: Curing cycles 0 and 1. The only difference between cycle 0 and 1 is the temperature plateau at 110°C or 130°C (10 minutes 30% or 40% under the curing temperature: 180°C).

Vacuum-bag moulding:

Fig. 23 shows the steps involved in the process. It starts with the impregnation of the reinforcement (UD and multidirectional carbon fibre woven fabrics). The impregnated reinforcements are then guided through pressing and guiding rolls and the desired composite lay-up is formed. The rolls also help to get rid of air bubbles trapped between layers. The structure consists of several reinforcement layers or plies. Curing of the laminate is made at room temperature under constant pressure to get the final dimensions.

The thickness of the laminate is constantly monitored during the process. Post curing is carried out at a constant controlled temperature for a given time as specified by resin provider.
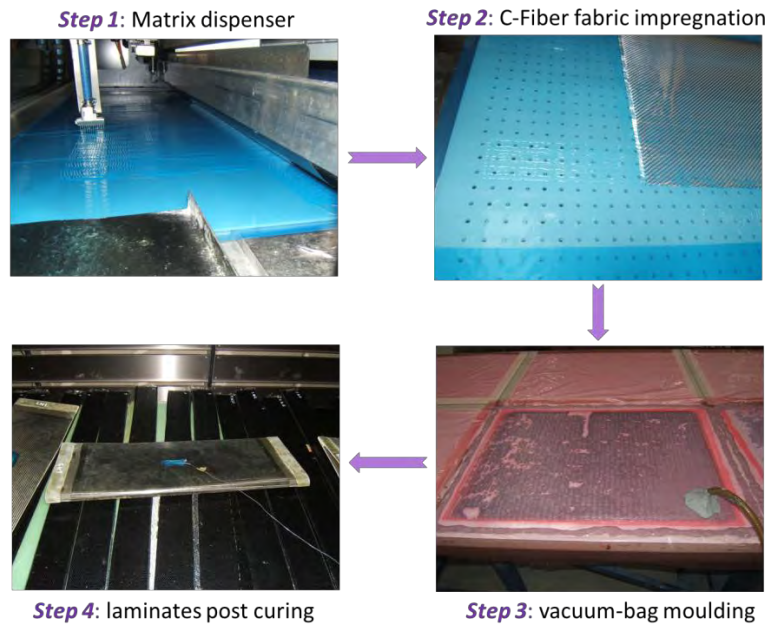
Fig. 23: Vacuum-bag moulding production schema (corresponding to processes P3 and P5).

Pressurized chamber:

This is not an autoclave. The curing of the stacked impregnated layers takes place at room temperature and under a constant pressure above atmospheric. Afterwards the cured form undergoes post-curing at a higher temperature.

Process	Name	Pressure (MPa)	Curing Temp (°C)	Post-curing T (°C)-t (h)	T_{MIN} (°C)	Cycle Nr
P 1	Compression moulding	0.2	180°	No	130°	Cycle 0
P 2	Compression moulding	0.2	180°	No	110°	Cycle 1
P 3	Vacuum-bag moulding	0.1	RT	120°-8h	-	-
P 4	Pressurized chamber	0.3	RT	120°-8h	-	-
P 5	Vacuum-bag moulding	0.1	RT	140°-15h	-	-
P 6	Pressurized chamber	0.3	RT	140°-15h	-	-

Tab. 2: Parameters of the different manufacturing processes for the studied laminates.

4.1.1.2 *Laminates Nomenclature*

The studied laminates are designated as follows:

Matrix/C-Fibres/PlySequence-Vf/Pressure/Process

The first term is for the matrix designation, followed by fibre type, stacking sequence and volume fraction of fibres as well as manufacturing pressure and production process P between 1 and 6, depending on the manufacturing process, if different materials were produced by several routes, as indicated in Tab. 2.

- GF=glass fibres   PES-F= polyester fibres
- CF=carbon fibres   UD=unidirectional

CFRP	Matrix	C-Fibre	Ply Sequence	N^r of plies	Nominal thickness (mm)	Process	Nominal V$_f$ (vol %)
HexPly8552/HSAS4/UD58f/0.2MPa/1	HexPly 8552	HS AS4	UD 0°	10	2	P 1	58
HexPly8552/HSAS4/UD58f/0.2MPa/2			UD 0°	10	2	P 2	
HexPly8552/HSAS4/± 45-58f/0.2MPa/2			± 45°	6	1.14		
Sik/FT300B/0-90°/1bar/3	Sika Biresin CR132	Torayca FT 300B	0°/90° CF-fabric	23	5.9	P 3	n.a.
Sik/HTA40/UD/1bar/3		Toho Tenax HTA 40	UD fabric: 95% CF 0° 05% GF 90°	19	5.3	P 3	n.a.
Sik/HTS5631/UD/1bar/3		Toho Tenax HTS 5631	UD CF-band + PES-F	13	4.7	P 3	n.a.
Sik/HTS5631/UD/3bar/4				13	4.5	P 4	n.a.
Hex/FT300/0-90°/1bar/5	Hexion L418	Torayca FT 300B	0°/90° CF-fabric	23	5.3	P 5	n.a.
Hex/HTA40/UD/1bar/5		Toho Tenax HTA 40	UD fabric: 95% CF 0° 05% GF 90°	19	5.1	P 5	n.a.
Hex/HTS5631/UD/1bar/5		Toho Tenax HTS 5631	UD CF-band + PES-F	13	4.3	P 5	n.a.
Hex/HTS5631/UD/3bar/6				13	4.2	P 6	n.a.

Tab. 3: Eleven different laminate composites. The difference between the different laminates can be the constituents (to compare two matrix systems), the ply orientation (to see the influence of reinforcement orientation), the manufacturing pressure or the curing temperature (to compare different porosity contents).

4.1.2 Pultruded profiles

4.1.2.1 *Pultruded profiles manufacturing Process*

Pultrusion (a combination of the words "pull" and "extrusion") is a continuous manufacturing process for composite materials with constant cross-section whereby the continuous fibres are pulled through a liquid resin and into a preforming system and a heated die, where the resin undergoes polymerization at a constant temperature.

Different cross sections are achievable by changing the geometry of the die in the pulling head. The finished profiles are cut by a saw at the end of the line. Afterwards post curing at a lower temperature is carried out if the used epoxy system requires it. Fig. 24 shows details of the pultrusion production line. The process starts with racks or creels holding spools of bundled continuous fibre (roving). This raw fibre is pulled off the racks and guided through a resin bath or resin impregnation system. The raw resin is a thermosetting resin, and is sometimes combined with fillers, catalysts, and pigments. The fibre reinforcement becomes fully impregnated (wetted-out) with the resin such that all the fibre filaments are thoroughly saturated with the resin mixture. As the resin rich fibre exits the resin impregnation system, the un-cured composite material is guided through a series of tools. This custom tooling helps arrange and organize the fibre into the correct shape, while excess resin is squeezed out, also known as "debulking". This tooling is known as a "pre-former".

Fig. 24: Different steps during pultrusion process.

Once the resin impregnated fibre is organized and excess resin removed, the composite passes through a heated steel die. Precisely machined and often chromed, the die is heated to a constant temperature, and may have several zones of temperature throughout its length, which will cure the thermosetting resin. The profile that exits the die is a cured pultruded composite. This profile is pinched and pulled by a "gripper" system. Either caterpillar tracks or hydraulic clamps are used to pull the composite through the pultrusion die on a continuous basis. At the end of the pultrusion machine there is a cut-off saw. The pultruded profiles are cut to the specific length and stacked for delivery.

4.1.2.2 *Pultruded profiles Nomenclature*

The studied pultruded profiles presented in Tab. 4 are designated as follows:

G/Matrix/C-Fibres/Orientation-Vf

The first term (G) is for the geometry of the profile: T for tubes or R for rods, followed by matrix and fibre type designation, nominal fibre direction and volume fraction of fibres.

CFRP	Matrix	C-Fibre	Filler	Orient.	Nominal thickness (mm)	Process	Nominal V_f (vol %)
T/L20-T/HTSTS/UD65f	L20	HT Tenax STS	mineral	UD	Do = 10 Di = 8	Pultrusion	65
R/L20-T/HTSTS/UD65f	L20	HT Tenax STS	mineral	UD	D = 10	Pultrusion	65
R/Sika/Sigrafil-T700SC/UD65f	Sika Biresin CR141	Sigrafil C + Torayca T700 SC	-	UD	D = 10	Pultrusion	65

Tab. 4: Pultruded profiles. The difference between the different pultruded profiles is the geometry (tubes and rods) on one side and also the matrix system, which in one case contains additional mineral fillers.

26

4.1.3 Prepreg Hexply 8552 HS AS4

HexPly AS4/8552 RC34 AW194 is a UD High Strength Carbon Epoxy prepreg, whereby 8552 is the resin type; 34% is the resin content by weight; AS4 AW194 is the reinforcement reference and AS4 represents High Strength Carbon fibre. Details are listed in Tab. 5.

Prepreg Data	AS4/8552 RC34 AW194
Nominal Areal Weight	294 g/m²
Nominal Resin Content	34 w%
Volatiles	≤1% w%
Tack level	High
Matrix Data	**8552**
Glass transition temperature (dry)	200 °C
Glass transition temperature (wet)	154 °C
Nominal resin density	1.3 g/cm³
Tensile Strength	121 MPa
Tensile Modulus	4670 MPa
Colour	Yellow
Reinforcement Data	**AS4 AW194**
Nominal Areal Weight [0°]	194 g/m²
Nominal Areal Weight [90°]	-
Composition	UD
Fibre Type	High Strength Carbon
Nominal Fibre Density	1.79 g/cm³
Filament count/tow	12K
Nominal fibre diameter	7.1 μm
Tensile Strength	4400 MPa
Tensile Modulus	231 GPa
Nominal cured UD laminate properties	$V_f = 60\%$ **(dry)**
Nominal Cured Ply Thickness	0.130 mm
Nominal Fibre Volume	57.42 %
Nominal Laminate density	1.58 g/cm³
Tensile Strength [0°] RT	2207 MPa
Tensile Strength [90°] RT	81 MPa
Tensile Modulus [0°] RT	141 GPa
Tensile Modulus [90°] RT	10 GPa
Compression Strength [0°] RT	1531 MPa
Compression Mudulus [0°] RT	128 GPa
ILSS [0°] RT (short beam shear)	128 MPa
In-plane shear strength RT	114 MPa

Tab. 5: Properties of the HexPly AS4/8552 RC34 AW194 prepregs, their components and nominal values for a cured UD laminate with 60% fibre volume fraction. Values taken from [52].

4.1.4 Epoxy Matrices

Properties of the four epoxy matrices used to manufacture the impregnated fabric laminates and the pultruded profiles are summarized in Tab. 6.

Manufacture	Vacuum-bag moulding Laminates		Pultruded profiles	
Property	Biresin CR 132	Laminating resin L418	L20	Biresin CR 141
Manufacturer	Sika	Hexion	Rutapox	Sika
Tensile strength	78 MPa	75-90 MPa	68 MPa	78 MPa
E-Modulus	2.7 GPa	3.3-3.6 GPa	3.4 GPa.	3.20 GPa
Ultimate strain	5.7 %	5-6 %	n.a.	3.3 %
Density	n.a.	1.15 g/cm³	1.15 g/cm³	1.20 g/cm³
Glass transition temperature	135 °C	120-125 °C	n.a.	139 °C

Tab. 6: Properties of the studied matrix systems. Values taken from [53], [54], [55] and [56].

4.1.5 C-Fibres

Properties of the three carbon fibre types used to manufacture the impregnated fabric laminates and the pultruded profiles can be found on Tab. 7 and Tab. 8 respectively.

Fibre description	FT300B-3000-40B	Tenax-E HTA40 E13	Tenax-E HTS 5631
Producer	Torayca	Toho Tenax	Toho Tenax
Tensile strength	3811 MPa	3813 MPa	4627 MPa
E-Modulus	235 GPa	236 GPa	239 GPa
Ultimate strain	1.62 %	1.7 %	1.79 %
Density	1.75g/cm³	1.76 g/cm³	1.77 g/cm³
Fibre diameter	7 µm	7 µm	7 µm
Fabric identifier	98141	CCC 796	KDU 1034
Textile producer	Porcher Industries	C. Cramer & Co	vom Baur
Nominal Areal Weight	204 g/m²	280 g/m²	382 g/m²
Linking	Body 2/2	UD cloth	UD cloth
Warp	Carbon fibre	Carbon fibre	Carbon fibre
Weft yarn	Carbon fibre	Glass fibre	PES fibre
Nominal thickness per layer	0.295 mm	0.28 mm	0.4 mm

Tab. 7: Properties of the carbon fibre textiles used to produce the impregnated fabric laminates [57].

Fibre description	Tenax-STS40 F13 24K	Torayca-T700 SC	Sigrafil C40 T024 EPY
Producer	Toho Tenax	Toray Carbon Fibers America, Inc.	SGL Group Fibers Ltd.
Tensile strength	4000 MPa	4900 MPa	4800 MPa
E-Modulus	240 GPa	230 GPa	240 GPa
Ultimate strain	1.5-1.7 %	2.1 %	2.0 %
Density	1.77 g/cm³	1.8 g/cm³	1.82 g/cm³
Fibre diameter	7 µm	7 µm	7 µm
Number of filaments	24000	24000	24000
Nominal linear density	1600 tex	1650 tex	1600 tex
Running length per kg	625 m/kg	-	-
Sizing properties	F13 - approx. 1.0 % sizing based on polyurethane	-	approx. 1.0 % sizing based on epoxy

Tab. 8: Properties of the fibres used to produce the different studied pultruded profiles [58], [59], [60].

4.2 Experimental methods

Light optical microscopy (LOM), scanning electron microscopy (SEM) as well as X-ray (XCT) and synchrotron computed tomography (SCT) were used for structural characterisation and to assess manufacturing defects present in each composite.

Thermogavimetric analysis (TGA) was performed to estimate components volume fraction and to study thermal degradation of the composites.

Differential scanning calorimetry (DSC), dynamic mechanical analysis (DMA) and thermomechanical analysis (TMA) were carried out to study the influence of thermal treatments on the matrix systems; to compare the different studied epoxy systems and to assess the possible effect of the found production defects on the composites thermal and thermomechanical properties.

Mechanical tests such as bending tests, torsion tests, interlaminar fracture toughness, and interlaminar shear strength (short beam shear) test were carried out to compare all different composites regarding their mechanical properties and interfacial fibre-matrix adhesion.

In-situ acoustic emission, in-situ synchrotron tomography and post mortem SEM fractography were carried out to assess damage initiation and evolution, as well as XCT scans on selected specimens prior and after mechanical testing.

Tab. 9 presents an overview of all applied methods and studied properties.

Material Property	Method										
	Materialography			Thermal Analysis				Mechanical Testing			In-situ
Morphology	LOM		XCT								
Porosity volume fraction	LOM		XCT	TGA							
Fibre volume fraction	LOM			TGA							
Defects (inclusions, pores)	LOM		XCT/SCT								
Fibre orientation	LOM		XCT/SCT								SCT
Fibre diameter	LOM										
Fractography		SEM									
Glass transition temperature					DSC	TMA	DMA				
Thermal expansion coefficient (CTE)						TMA					
Stiffness (E', E'')							DMA				
Bending strength, E-modulus								4P-Bending			
Mode of failure			XCT/SCT					4P-Bending			SCT
Torsion strength, Shear modulus								Torsion			AE
Damage initiation			XCT/SCT					4P-B & Torsion Tensile test			AE/SCT
Interlaminar fracture toughness									IFT		
Interlaminar shear strength										SBS	

Tab. 9: Material properties studied with each one of the experimental methods applied.

4.2.1 2D Microscopy

4.2.1.1 *LOM*

Optical micrographs were made on a Zeiss Axioplan microscope. All samples were embedded in an Araladit® epoxy cylinder with fibre orientation of 0° and 90° for cross section and longitudinal views and subsequently ground and polished at a Struers Tegra Doser-5 machine using the steps indicated in Tab. 10.

Step	Polishing Cloths	Lubricant	Suspension	Time (min)	Force (N)	Rotational speed (rpm)	Level
1	SiC 320	Water	-	2	10/30	300	AN
2	MD-largo	Struers blue	DP-9μm	8	30/180	150	5/11 5/11
3	MD-dur	Struers blue	DP-3μm	8	30/180	150	5/10 3/11
4	MD-nap	Struers blue	DP-1μm	10	30/180	150	5/10 7/11
5	MD-chem	Water	OP-S	2	10/30	150	5/11
6	OP-chem	Water	-	2	10/30	150	-

Tab. 10: Polishing program for surface preparation of the samples for materialography

Image processing was done using the free software ImageJ [61] and the program provided with the microscope AxioVision [62], both offering different advantages and disadvantages. ImageJ was used to determine the fibre diameter and the fibre volume fraction of the samples. AxioVision was used to analyze the porosity area fraction. To verify the nominal fibre diameters, single fibre diameters were measured. By using binarized LOM micrographs, fibre and matrix volume content could be also studied; these results will be compared in some cases with results obtained by other methods (TGA, XCT).

4.2.1.2 *SEM*

Secondary (SE) and back-scatter electron (BSE) images were produced by a Philips XL 30 scanning electron microscope (SEM) at accelerating voltage between 12 and 15kV. All samples were embedded into an Araladit® epoxy cylinder and subsequently ground and polished using a Struers Tegra Doser-5 machine. SEM samples were first made electrically conductive by coating with a thin layer of gold in an Agar Sputter Coater machine. Energy dispersive X-ray spectrometry (EDS) was performed to carry out the elemental analysis of the filler particles within the matrix of a sample.

After mechanical testing until fracture the fracture surfaces of some specimens were imaged by SEM microscopy. Prior to examination, the fracture surfaces were vacuum-sputter-coated with a thin layer of gold. Thermosets, like epoxy resins, are brittle because of their high degree of cross-linking. Typical features to be found on a delaminated fracture surface are cusps and scallops. Micrographs of the fracture surface give us insight into the origin of failure and possible failure mechanisms involved. The fibre pull out lengths are indications of the bonding strength. The presence of bare fibres and matrix debris are indicatives of the quality of the fibre-matrix bonding as well [63] [64] [65].

4.2.2 Materialography 3D

The aim of the materialographic investigations was to gain insight into the inner architecture and the microstructure of each composite family with special regard to constituent distribution and interfacial properties. A systematic characterisation of the observed defects was carried out, in order to be able to correlate them to the mechanical and thermal characterisation of the materials, which is the ultimate aim of this work.

Different approaches for 3D imaging of CFRP materials were taken, the different applied methods are explained in the following subchapters.

4.2.2.1 *X-ray computed tomography (XCT)*

A 3D-Computertomograph consists of three components, the x-ray source, a turntable on which the sample is mounted and a digital detector, as shown in Fig. 25. The x-ray source emits a cone-shaped x-ray beam. As the x-ray beam penetrates the sample the intensity is attenuated depending on sample thickness, the density and atomic number of the material. The digital detector converts the x-ray intensity into a digital 2D projection image. To obtain a 3D image of a sample, a full rotation of the sample within the x-ray beam is essential, so the rotary table stops every angle <1° to collect a further projection-image. From the series of 2D projections the reconstruction software provides a 3D-dataset using a filtered back-projection algorithm. Depending on the sample and the desired quality of the 3D-dataset, between 1000 and 2000 projections are needed to create a 3D-dataset (also called voxel-dataset) [66] [67].

The different grey values of each voxel correspond to the material density, with high density giving a bright representation and low density a dark one [68] [69]. To analyse a voxel-dataset special software is needed. This software splits the volume-data into axial, frontal and sagittal slices displaying the results on screen, similar to a metallographic preparation. These three slices are orientated to the global coordinate system of the 3D-dataset. Axial means a slice in XY, frontal in XZ and sagittal in ZY direction. By different rendering-algorithms, the software can also display a 3D-Image of the measured sample.
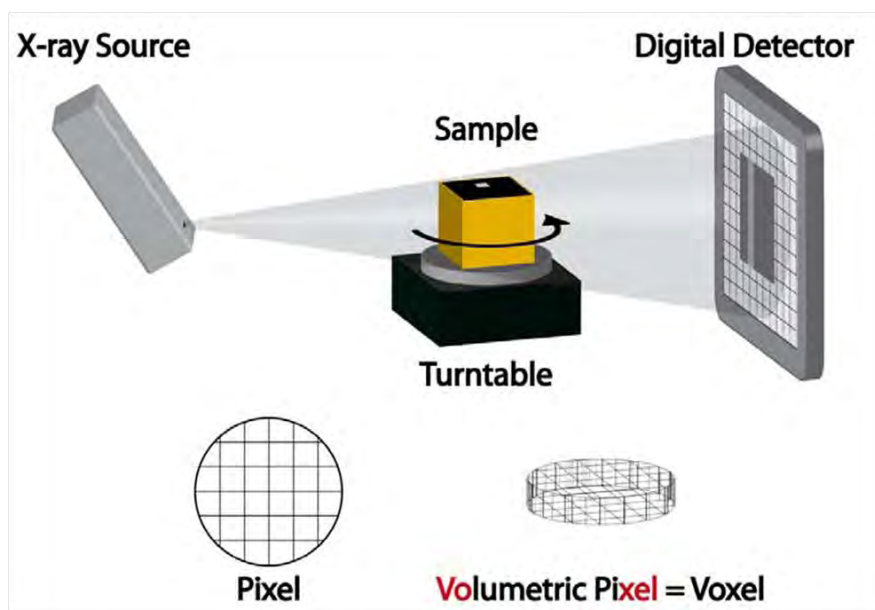
Fig. 25: Set-up for XCT measurements [66].

To archive a high resolution, the sample has to be positioned as close to the tube as possible; this means that the diameter of the sample determines the maximum voxel-size of the XCT measurement (Resolution = Diameter / 2300). In Fig. 26 the dependency of spatial resolution and sample diameter is shown.

For the Nanotom CT-device, the maximum length of the sample is limited by the size of the chamber in the device and is about 370 mm in height for cylindrical samples with a diameter smaller than 14 mm. For samples with the maximum length only one measurement is possible since the object cannot be moved in axial direction. For smaller samples several measurements can be carried out in axial direction [66] [67].
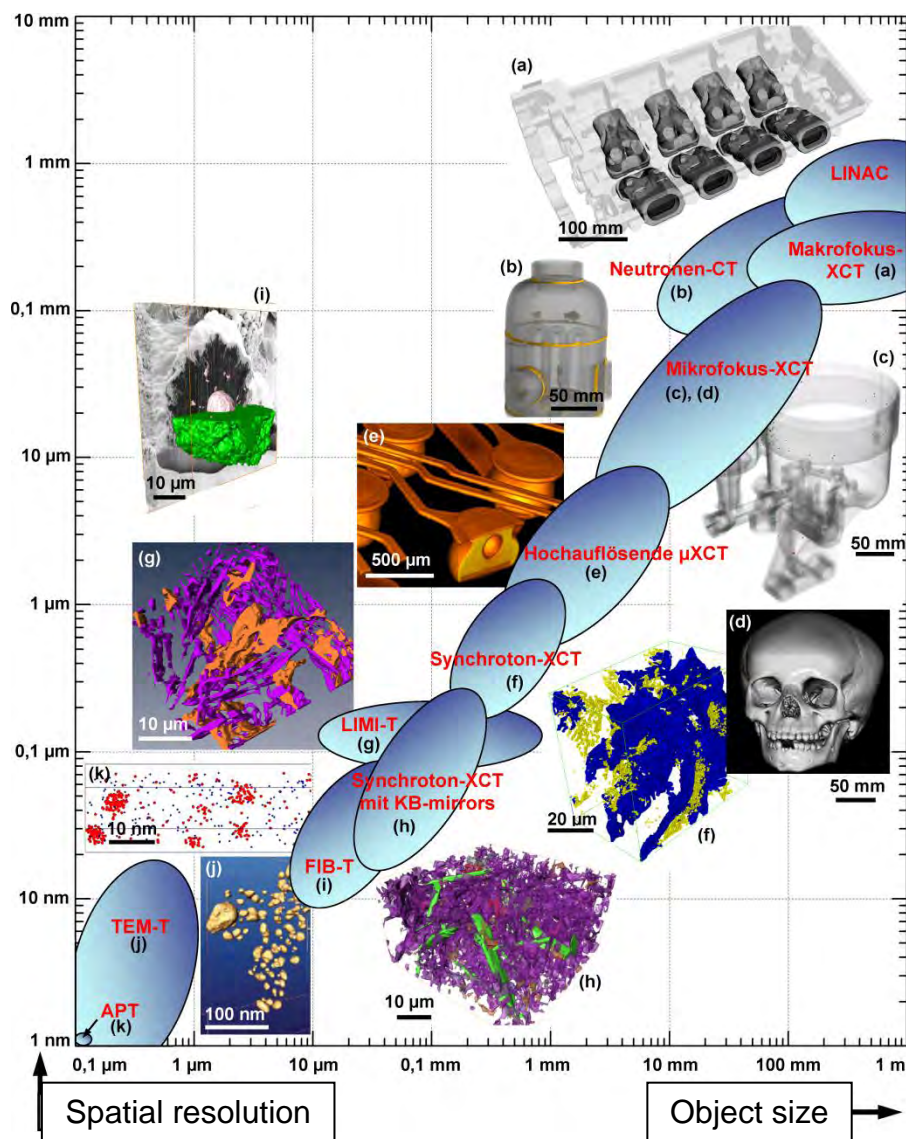
Fig. 26: Compromise between spatial resolution and sample size, the tomography dilemma [70].

CT Scans were performed in cooperation with FHOÖ using a Sub-µm-XCT device Nanotom (GE Phoenix|x-ray, Wunstorf, Germany) applying a voltage between 50-70kV, a current intensity of 150-350µA for 1500 or 1700 projections. The resolution achieved depends on the size of the specimens and of the analyzed volume; voxel size was variable depending on the actual specimen and its geometry. For details see Tab. 11.

CFRP	U [kV]	I [µA]	Tint [ms]	Time [min]	Detector distance	Voxelsize [µm]^3	Scanned Vol [mm]	N^{er} Projec
HexPly8552/ HSAS4/UD58f	50	350	750	122	215	11	24 × 24 × 22	1500
Sik/HTS5631/ UD/3bar/4	60	350	750	309	250	16	35 × 35 × 64	1700
T/L20-T/HTSTS/ UD65f	60	220	750	115	300	11	12 × 12 × 20	1800
	70	220	750	122	300	5	11 × 11 × 10	1500
	70	220	1000	368	300	1.5	6.6 × 6.6 × 3	1700
R/L20-T/HTSTS/ UD65f	60	280	500	96	250	12	26 × 26 × 24	1700
	70	220	1000	160	300	2.5	5.1 × 5.1 × 4.4	1700
R/Sika/Sigrafil-T700SC/UD65f	70	160	900	144	300	2.5	5.5 × 5.5 × 3.7	1500

Tab. 11: Parameters used for the different tomographic scans on each type of composite.

4.2.2.2 *Light optical tomography (LOT)*

Light optical tomography (LOT) is a serial sectioning technique that combines subsequent mechanical polishing, acquisition of images using a light microscope and three dimensional reconstruction. Two dimensional sections are acquired after a gradual controlled removal of material layers and stack afterwards to a three dimensional volume. This is a destructive method, but it can be performed with regular laboratory equipment: a light optical microscope and a semi-automatic polishing machine. The principle is to steadily polish the sample taking pictures of each slice. The XY resolution of the stack depends on the objective used. It can be higher than the one obtained by XCT but the distance between two slices (resolution in Z direction) is less constant and the technique is in general more time consuming.

Serial sectioning steps:
1) Embedding of small CFRP sample together with an aluminium piece (to enable Vickers hardness indentation)
2) Sample is ground and polished following the standard materialographic procedure (as for normal LOM materialography)
3) Two or more Vickers microindentations (HV5) close to the region of interest (ROI)
3.1 Locating region of interest
3.2 The sample is polished again to remove the plastic deformation on the aluminium surface around the indentations.
4) LOM micrographs
4.1 Sample ROI panorama (different magnifications)
4.2 Micrographs of all microindentations (for depth removal calculation)
4.3 Section alignment
5) Polishing step to remove one layer (controlled depth removal Tab. 12.)
6) Repeat steps 4-5 so many times as layers wished (eventually new indentations may be needed)
7) 2D micrographs aligned, assembled and segmented
8) Reconstruction of 3D volume
9) 3D visualisation of interesting feature (e.g. fibre orientation analysis)

The formula for the depth calculation is explained in Fig. 27. The height h of the pyramid corresponding to the lost depth can be related to the diagonal length of the indentation. Various indentations were monitored to assure proper h values.

$$\tan\frac{\propto}{2} = \frac{L}{h} \qquad\qquad L = \frac{D}{2\sqrt{2}}$$

$$h = \frac{D}{2\sqrt{2}\tan\frac{136}{2}}$$

$$h \approx \frac{D}{7}$$
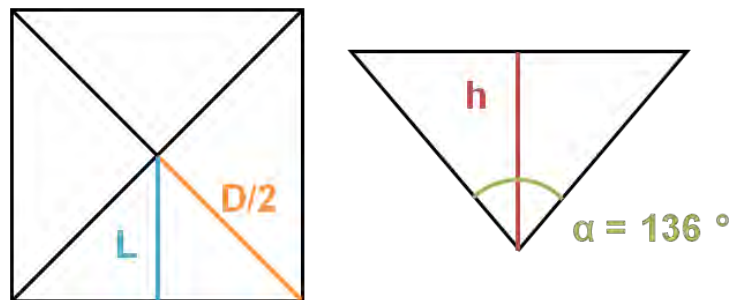
Fig. 27: Schematic drawing explaining the calculation of the hardness depth (h) from the Vickers indentation average diagonal (D) made on the aluminium.

Multiple HV5 (Hardness Vickers test force 5kp) indentations on an aluminium piece embedded together with the CFRP sample were used to measure the lost depth between steps. Fig. 28 shows a prepared sample and the LOM micrograph of an indentation with measured diagonals.
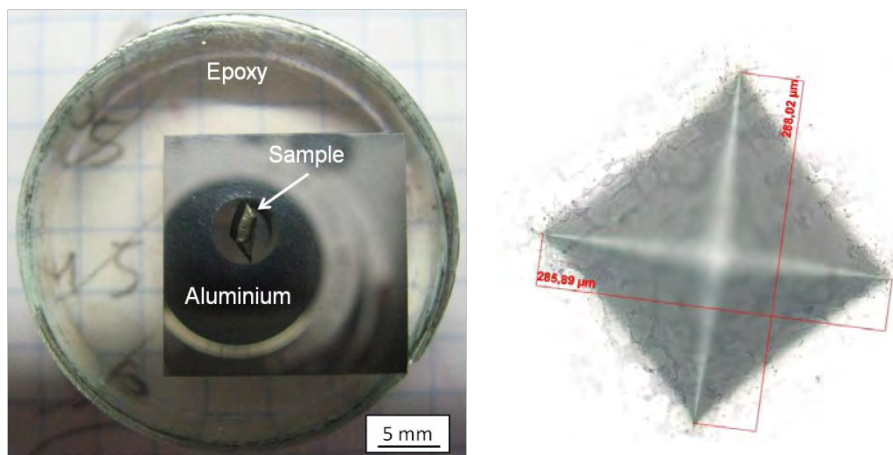
Fig. 28: Embedded CFRP sample surrounded by aluminium for LOT investigations (left). Micrograph of a Vickers indentation showing measured diagonals (right) made on the aluminium.

A UD-braided sample was imaged to define the applicability of LOT to CFRP structural characterisation and to optimize the parameters of serial sectioning on fibre reinforced composites; the three-dimensional reconstruction was satisfactory however the high misalignment of the reinforcement introduced some difficulties while aligning layers in the braided regions. The fibre orientation and fibre volume fraction were measured satisfactorily using the 3D reconstruction.

An important parameter is the polishing program. This program should be reproducible in order to always have the same distance between consecutive layers; this distance should not be bigger than the smallest feature that needs to be studied. Different polishing conditions have to be studied for each particular CFRP sample in order to optimize the polishing procedure.

In order to evaluate the effect of the polishing program on the depth removed, a series of tests were done to evaluate the influence of each single parameter. Time, suspension grain size and polishing cloths were systematically modified for each of the two steps. The influence of each factor on the removed depth did not show any logical tendencies. No direct correlation could be established between material removal and the modified parameters. Although it was observed that the moisture of the polishing cloths has a big influence on the amount of material removed. Also the nature of the composites gives rise to problems, since the hardness of the carbon fibres is much higher than the hardness of the matrix, the polishing rate is not the same one for each component. As a result, the surface of the specimen after a few steps is so uneven that it is impossible to obtain sharp micrographs of the region of interest.

Another issue is the viscoelastic behaviour of the epoxy matrix. Serial sectioning cannot be done in one session but it takes weeks to get enough layers (with a rate of about 6 layers per day). During the night the epoxy matrix tends to recover, which results in a very different polishing rate between one day and another. This problem has also been observed in similar works of serial sectioning on polymer based composites [71].

The polishing programs found to be more suitable for the samples studied in this work are shown in Tab. 12 and Tab. 13.

Step	Polishing Cloths	Lubricant	Suspension	Time (min)	Force (N)	Rotational speed (rpm)	Niveau
1	MD-nap	Struers blue	DP-1μm	5-8	30/180	150	5/10 7/11
2	OP-chem	Water	-	2	10/30	150	-

Tab. 12: Polishing program used for serial sectioning of pultruded profiles.

Step	Polishing Cloths	Lubricant	Suspension	Time (min)	Force (N)	Rotational speed (rpm)	Niveau
1	MD-nap	Struers blue	DP-3μm	1-12	30/180	150	5/10 7/11
2	MD-nap	Struers blue	DP-1μm	1-12	30/180	150	5/10 7/11

Tab. 13: Polishing program used for serial sectioning of impregnated fabric laminates.

With the volumes obtained after stacking of the layers obtained by serial sectioning, an analysis of the fibre orientation, fibre volume fraction, filler particle distribution was performed.

4.2.3 Thermal treatments

4.2.3.1 *Pultruded rods*

The pultruded rod: R/Sika/Sigrafil-T700SC/UD65f and R/L20-T/HTSTS/UD65f were delivered from the producer before undergoing the post-curing step. The epoxy matrix was therefore not completely cured. Different heat treatments were carried out in order to study the influence of the matrix curing degree on the mechanical and thermal performance of the composite materials. The different heat treatments are listed in Tab. 14. Also a temperature versus time schematic view is presented in Fig. 29.
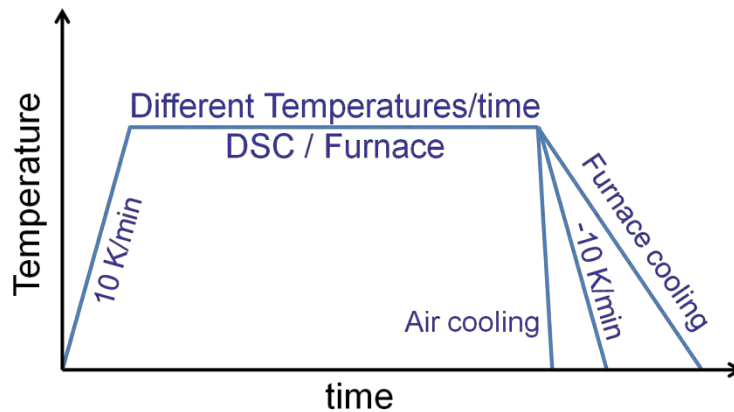
Fig. 29: Schematic temperature vs. time evolution during the heat treatments used on pultruded rods. Different holding times and temperature plateaus were used; the cooling at the end could be a) fast (air cooling), b) – 10K/min controlled cooling rate in the DSC or c) slow (furnace cooling).

CFRP	Where	Heating rate [K/min]	Holding Temp [°C]	Holding time [h]	Cooling
R/Sika/Sigrafil-T700SC/UD65f	furnace	n/a	70	4	Air
	furnace	n/a	90	4	Air
	furnace	n/a	120	3, 4, 5	Air
	in-situ DSC	5	140	3, 4	DSC
	in-situ DSC	5	150	3, 3.5, 4	DSC
	in-situ DSC	5	160	2, 2.5, 3, 3.5, 4	DSC
	in-situ DSC	5	165	1	DSC
	in-situ DSC	5	170	1.5	DSC
	in-situ DSC	5	175	2	DSC
	furnace	n/a	190	10	Air
	in-situ DSC	10	250	1, 2	DSC
R/L20-T/HTSTS/UD65f	furnace	n/a	100	2	furnace
	furnace	n/a	140	2	furnace
	furnace	n/a	170	1	furnace

Tab. 14: Heat treatments on pultruded rod samples.

4.2.4 Thermal Analysis

Thermal analysis yields mainly matrix properties, but information about matrix-fibre interaction can also be gained in terms of adhesion and interfacial bonding strength. Furthermore the stiffness and thermal stability of the composites can be assessed. The methods used and the corresponding properties studied are presented in Tab. 9 and briefly listed here.

- ➢ TGA: components volume fraction, thermal degradation
- ➢ DSC: glass transition temperature (Tg), curing degree (α)
- ➢ DMA: stiffness, Tg, viscoelastic properties of the matrix, interfacial adhesion
- ➢ TMA: CTE, Tg, anisotropy of thermal expansion

Evaluation of all thermal analysis results obtained was carried out using the software pack: Universal Analysis V4.4 from TA Instruments.

4.2.4.1 *Thermogravimetric Analysis (TGA)*

Objectives: determination of components volume fraction, thermal degradation.

Thermogravimetric analysis (TGA) is commonly used to characterise CFRP composites; to determine the components weight percentage and to estimate the composite's thermal resistance. A TGA set-up consists of a high-precision balance with an alumina ceramic pan where the sample is loaded. Analysis is carried out by raising the temperature of the sample gradually under a chosen atmosphere, which can be neutral or oxidative and plotting weight percentage against temperature. Set-up is shown in Fig. 30.
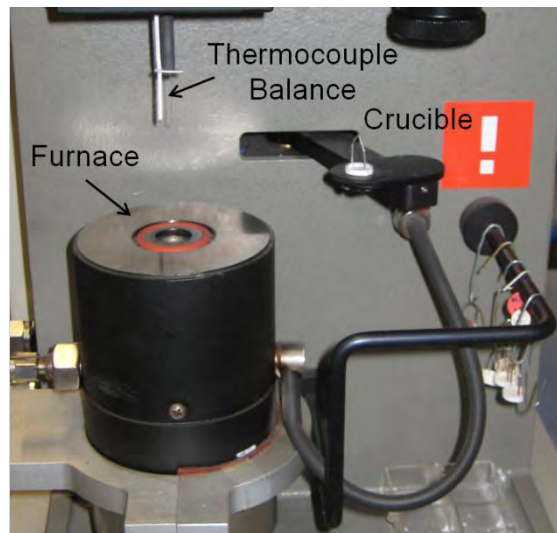
Fig. 30: TGA Set-up at the TU Wien facilities. Sample in a crucible attached to the balance is heated up in a furnace, the temperature is measured with a thermocouple [57].

All measurements were carried out on a TA-Instruments TGA 2050 device. Different conditions were applied for each studied sample. The most suitable method was chosen depending on the size of the studied sample, the nature of the epoxy matrix and whether filler was present or not. Different final temperatures, heating rates and types of atmosphere were applied. Isothermal steps were used for large specimens to ensure entire volatilisation of each component.

Sample weight was variable ranging between 20 and 450 mg. Samples were cut using a Discotom-2 cutting machine from Struers. The heating rates were 10K/min for samples smaller than 100 mg and 8K/min for larger ones.

The different atmospheres used were: N_2, air flow or a combination of both, starting with N_2 and changing to air at 600°C, to assure C-fibre combustion. Final temperature was variable: 850°C, 900°C or 1000°C. The alumina crucible was always cleaned between consecutive measurements with a gas burner. Details on the measurements are summarized in Tab. 15, classified according to the matrix system.

Sample type	Heating rate (K/min)	Temp range (°C)	Atmosphere	Size (mg)
HexPly 8552 UD	10	RT → 900°C	Air	70-170
HexPly 8552 ± 45°		RT → 630°C → 900°C	N_2-Air	25
Sika CR132	10	RT → 850°C	N_2	100-150
Hexion L148		RT → 850°C	N_2	100-150
L20 pultruded tubes	10	RT → 600°C → 1000°C	N_2-Air	60-70
	8	RT → 900°C	Air	
L20 pultruded rods	10	RT → 600°C → 900°C	N_2-Air	180-350
	8	900°C → 1000°C	Air	
Sika CR141 pultruded rods	10	RT → 600°C → 900°C	N_2-Air	250-450
	5	900°C → 1000°C	Air	

Tab. 15: Different methods used for TGA measurements for each composite type.

In order to detect the difference in fibres and matrix distribution through the cross section of the rod shaped profiles, two different sample types were studied: cubes cut from the centre of the profile and curved samples from the border (as indicated in Fig. 31).
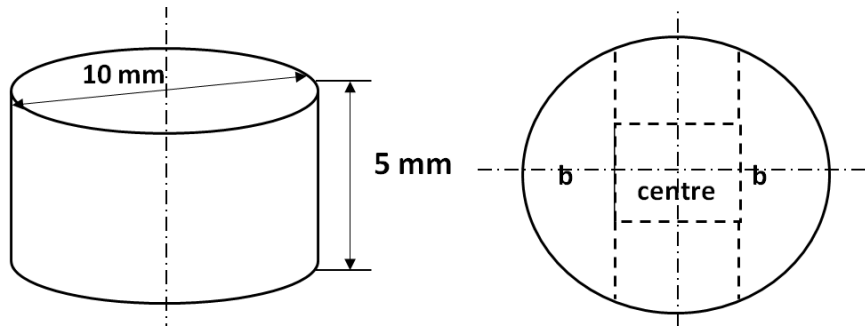
Fig. 31: Schematic drawing of the two kinds of samples prepared for TGA measurements. Centre samples and border samples (b) representative of the outer most side of the rods.

From the obtained weight fractions (W_m and W_f) the volume fractions of matrix, fibre and porosity (V_m, V_f, V_p) can be calculated using the following equations [57].

$$V_f = W_f \cdot \frac{\rho_c}{\rho_f} \qquad V_m = W_m \cdot \frac{\rho_c}{\rho_m} \qquad V_p = 1 - V_m - V_f$$

The values of density of each studied composite (ρ_c) were calculated experimentally [72] and for the single components (ρ_m, ρ_f) taken from the data provided in the data sheet.

4.2.4.2 *Differential Scanning Calorimetry (DSC)*

Objectives: determination of glass transition temperature (Tg) interval, degree of curing (α).

Differential scanning calorimetry (DSC) measures the change of the heat flow of the sample while it is subjected to a controlled temperature program. Hence endothermic and exothermic processes can be described and reversible and irreversible thermal events can be distinguished. Fig. 32 shows a generalized schematic curve of a DSC curve for polymer materials. Epoxy resins are thermoset polymers, a hard and stiff cross-linked material that does not soften or become mouldable when heated (thermoplastics on the contrary become mouldable when heated). Typical thermal transition points for epoxy resins are: an endothermic step corresponding to the glass transition interval, followed by an exothermal post-curing peak (this peak appears only if the resin is not 100% cured). At higher temperatures epoxy resins do not melt, but degrade irreversibly. The crystallisation and the melting peaks will only show up for polymers that can form crystals. Completely amorphous polymers do not show any crystallisation or any melting. But polymers with both crystalline and amorphous domains will show all three features [73].
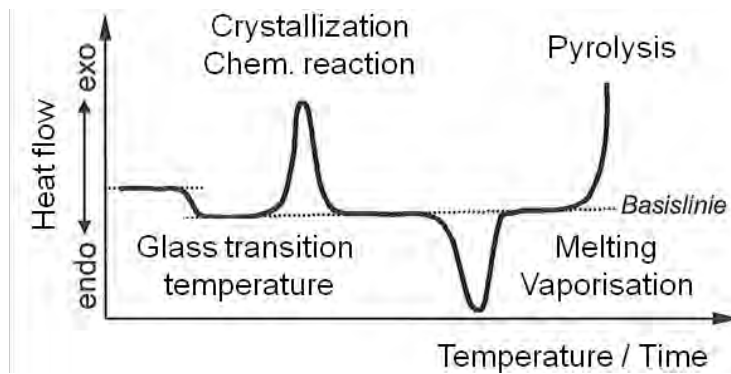
Fig. 32: Schematic DSC curve for polymers [73].

The system used was a TA Q2000 Calorimeter from TA Instruments, which gives the possibility of modulated measurements (MDSC). The heat flow can be separated into a reversible and a non-reversible part so facilitating the evaluation. this is because the step defining the glass transition temperature is more distinct in case of the reversible heat flow curve. Furthermore DSC offers the possibility of carrying out in-situ heat treatments by holding a constant temperature over a controlled time interval. These heat treatments are mentioned in chapter 4.2.3. The DSC curves also contain information about the enthalpy exchanged during the process, which can be used to assess the curing degree (alpha) of the materials in the as received state and also after the above mentioned heat treatments.

$$\alpha_{DSC} = \left(1 - \frac{\Delta H_r}{\Delta H_{tot}}\right) \cdot 100 \ (\%)$$

α_{DSC}: curing degree

ΔH_r: released enthalpy

ΔH_{tot}: total reaction enthalpy

40

Specimen weight was between 7-40 mg depending on the studied composite. Slices were cut out using a circular saw and were manually ground to be encapsulated in standard cylindrical aluminium pans with a diameter of approximately 5 mm. The reference was an empty pan and therefore air. Different test conditions were applied as summarized in Tab. 16. Some specimens undergo two consecutive DSC runs (referenced during this work as first and second cycle). The first cycle was in some case a heat treatment, the second one a DSC measurement. Measurements took place between room temperature (RT) and a maximum temperature shown in Tab. 16 depending on the actual matrix system. Three different heating rates were used: 3, 5 or 10 K/min, temperature modulation was always ± 1K/min.

Sample type	DSC in-situ HT	Heating rate [K/min]	Cooling rate [°C/min]	Max Temp [°C]
Laminates HexPly8552	No	3, 5, 10	No	300
Laminates Sika Birresin CR132	No	3	No	250
Laminates Hexion L418	No	3	No	250
Pultruded profile T/L20-T/HTSTS/UD65f	No	5	No	300
Pultruded profile R/L20-T/HTSTS/UD65f	No	5, 10	10	250
Pultruded profile R/Sika/Sigrafil-T700SC/UD65f	See Tab. 14	5, 10	10	350

Tab. 16: Different test conditions for DSC measurements of each kind of composite studied.

4.2.4.3 *Dynamic Mechanical Analysis (DMA)*

Objectives: stiffness, glass transition temperature (Tg) interval, cross linking, viscoelastic properties of the matrix, interfacial adhesion.

Dynamic mechanical analysis (DMA) is a technique used to study the viscoelastic behaviour of polymers. A sinusoidal stress is applied and the strain in the material is measured, allowing one to determine the Young's modulus. The glass transition temperature can also be estimated.
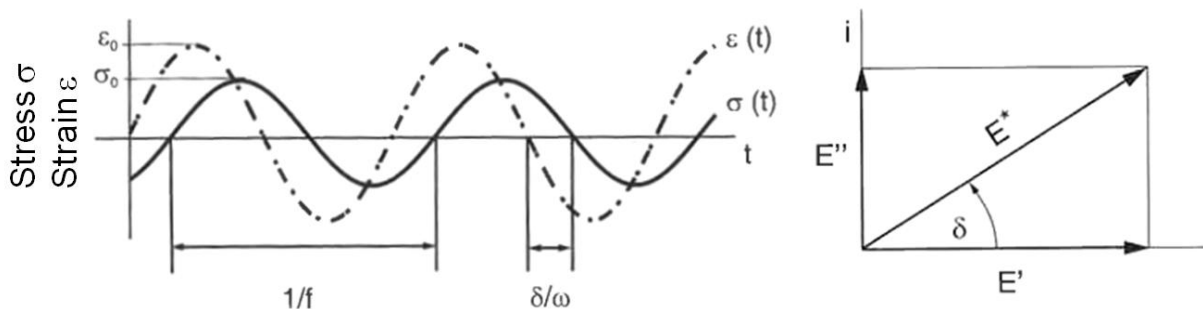
Fig. 33: DMA viscoelastic behaviour of CFRP, phase mismatch. Complex modulus (E*) vector [74].

Due to the viscoelastic behaviour of CFRP the frequency of the stress and strain curves are equal but a phase shift between them can be determined as seen inFig. 33. The lag of the strain ranges between 0°, for ideal elastic material, and 90°, for ideal viscous material. Thus the complex modulus E* and the loss factor tan δ are defined as followed, according to:

$$E^* = E' + iE''$$

$$\tan \delta = \frac{E''}{E'}$$

E': storage modulus (the real component)   E'': loss modulus (imaginary component)

The test method used was a three point bending test on a TA Instruments 2980 dynamic mechanical analyzer. Sample length is 60 mm, the support distance 50 mm, the width and height of the samples are selected not to exceed the maximum force of 15 N (as specify in Tab. 17). Heating rate is 3K/min, the amplitude of the deformation 70 μm and the loading frequency 1 Hz. Storage modulus, loss modulus and loss factor were recorded between 25°C and the maximal temperatures shown in Tab. 17.

Sample type	Sample geometry L × w × h [mm]	Final temp [°C]	Nr Cycles
Laminates HexPly8552	60×4×1.5	270-300	1
Laminates Sika Birresin CR132	60×6.5×2	200	1
	60×4.1×1.6		
Laminates Hexion L418	60×8.5×1.8	200	1
	60×4.8×2.1		
Pultruded profile R/L20-T/HTSTS/UD65f	60×4.5×1.5	210	2
Pultruded profile R/Sika/Sigrafil-T700SC/UD65f	60×4.5×1.5	290	2

Tab. 17: DMA conditions for each studied composite.

4.2.4.4 *Thermomechanical Analysis (TMA)*

Objectives: CTE, Tg interval (cross linking), anisotropy of thermal expansion.

The coefficient of thermal expansion (CTE) describes how the size of an object changes with a change in temperature. Specifically, it is the fractional change in size per degree change in temperature at a constant pressure. To a first approximation, the change in length of a specimen (linear dimension as opposed to, e.g., volumetric dimension) due to thermal expansion is related to temperature change by a linear expansion coefficient. It is the fractional change in length per degree of temperature change [75].

$$CTE = \frac{1}{L_i} \cdot \frac{dL}{dT}$$

L: Sample length [mm] L_i: Instantaneous sample length [mm]   T: temperature [°C]

Coefficient of linear expansion (CTE) measurement was done by TMA with the help of a TA Instruments TMA 2940 analyzer and a quartz glass holder. Sample dimensions for the different specimens are given in Tab. 18. Samples were loaded with a constant force of 0.1N; measurements were carried out to measure specimens dimensional change parallel (0°) and perpendicular (90°) to fibre orientation (see Fig. 34). The Sika CR132 laminates were measured in three directions, as shown in Fig. 35.

After cooling for 5 minutes at 0°C, the specimens were heated at 3K/min until the desired temperature was reached. According to the DIN EN ISO 53752 standard [76] measurements with two identical consecutive cycles were performed to ensure total curing of the samples, thus eliminating irreversible effects which may distort the results. The glass transition temperature was evaluated as the minimum of the CTE curve from each heating cycle. Regarding linear CTE values, only the second cycle was evaluated. Two CTE values, at room temperature before glass transition temperature (CTE_1) and above Tg (CTE_2) were obtained.

Sample type	Sample geometry L×w×h [mm]	Heating rate [K/min]	Temp range [°C]	Nr Cycles
Laminates HexPly8552	15×5×1.8		0° - 0-180	
			90° - 0-300	
Laminates Sika Birresin CR132	20×20×5	3	0-200	2
Pultrued profile T/L20-T/HTSTS/UD65f	0° - L=15		0° - 0-150°	
	90° - L=8		90° - 0-200°	

Tab. 18: TMA conditions for each studied composite.
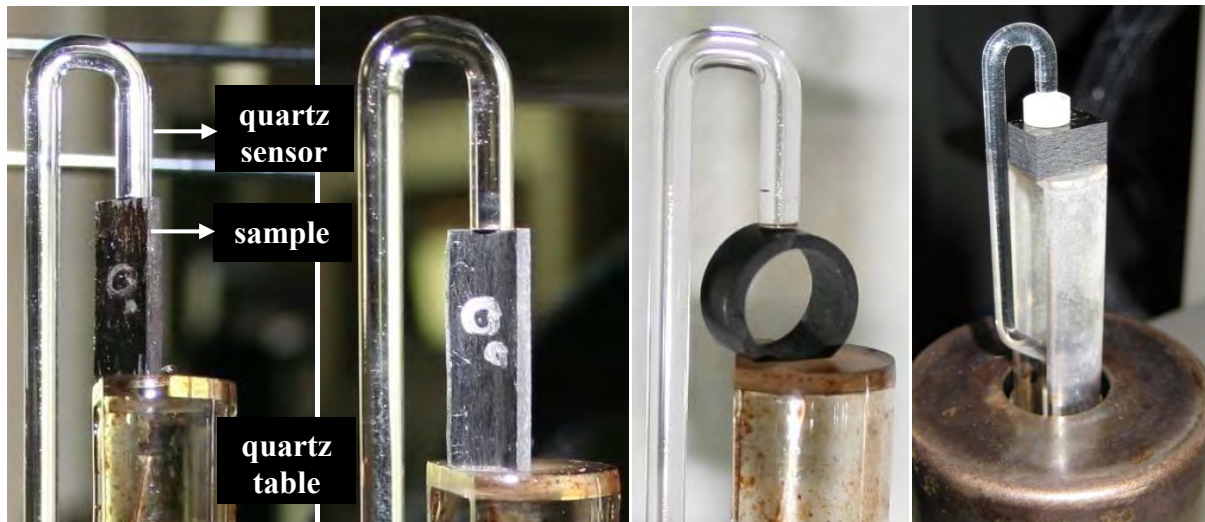
Fig. 34: Samples fixed for TMA dilatometry tests. From left to right: HexPly 8552 laminates for measurement parallel and perpendicular to the fibre direction have the same shape. Tube segment for measurements of dimensional change parallel to the fibre direction (0°). Tube circular specimen for measurements perpendicular to the fibre direction (90°). Sika CR132 laminates for measurement perpendicular to the fibre direction (90° I).
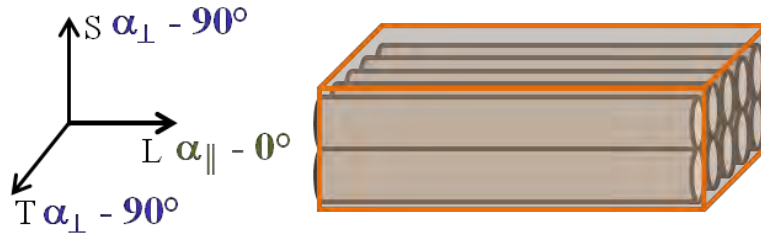
Fig. 35: TMA measurements were done in S, T and L direction for Sika CR132 laminates.

4.2.5 Mechanical Testing

4.2.5.1 *Torsion tests of pultruded materials*

Tubes T/L20-T/HTSTS/UD65f:

Torsion tests were carried out on a universal torsion test machine at the TVFA – TU WIEN facilities. Torsion samples with a length of L_t = 200 mm were cut perpendicular to the fibre direction from tubes pultruded several meters long with outer and inner diameters D_1 = 10 mm and D_2 = 8 mm, respectively.

A self-made clamp was applied to avoid damage of the samples by the grip of the torsion machine (see Fig. 36). It consisted of three parts: a Cu-tube (D_{Cu} = 12 mm, L_{Cu} = 40 mm) outside, an Al-plug (D_{Al} = 8 mm, L_{Al} = 25 mm) inside and a steel gripping screwed around for mounting in the sample holder. The resulting gauge length was L_1 = 120 mm. Tubes were twisted clockwise with a rotational speed of about 6°/min (1.7x10^{-3} rad/s).
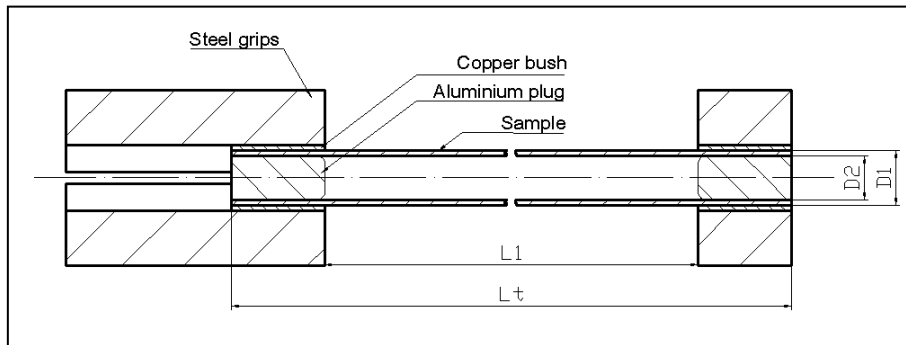
Fig. 36: Clamping used for torsion test of CFRP pultruded tubes [74].

A shear stress-strain curve is obtained from the recorded values of the torque and the angle of twist according to the following equations [77]:

$$\tau = \frac{16\,M_T\,D_1}{\pi\,(D_1^4 - D_2^4)}$$

$$\gamma = \frac{D_1\,\theta\,\pi}{180\,L_1}$$

τ: Torsion stress [MPa] M_T: Torque [Nm]

γ: Torsion strain [rad] θ: Twisting angle [°]

D_1: Outer diameter [mm] D_2: Inner diameter [mm] L_1: Gauge length [mm]

The shear modulus was calculated as the quotient of the differences of the shear stress and the strain between 0.0025 and 0.0045 rad of the shear strain or between the reversal points of the loading-unloading cycles according to the following equation:

$$G = \frac{\tau_f - \tau_0}{\gamma_f - \gamma_0}$$

G: Shear modulus [GPa]

τ_0, τ_f: Torsion stress [MPa] at lower (reversal) and at upper (reversal) point, respectively

γ_0, γ_f: Torsion strain [rad] at lower (reversal) and at upper (reversal) point, respectively

The ultimate torsional shearing strength or modulus of rupture τ_u is calculated using equation:

$$\tau_u = \frac{16\, M_{T\,max}\, D_1}{\pi\, (D_1^4 - D_2^4)}$$

Loading-unloading hysteresis cycles were carried out by twisting the specimens clockwise up to a particular angle at a constant rate of 1.7×10^{-3} rad/s, then unloading anticlockwise down to 0.5 Nm and loading again clockwise at the same rate up to a higher twist angle value. After three or four cycles, specimens were either twisted until failure or unloaded for microstructural characterisation by means of XCT; these results are presented in section 5.5.3.

Rods R/L20-T/HTSTS/UD65f and R/Sika/Sigrafil-T700SC/UD65f:

Torsion tests of pultruded rod samples were carried out on a universal TMM-04 torsion test machine at the Department of Materials Physics facilities at the Eötvös University in Budapest (Hungary).

Samples with a length between 100 and 105 mm were cut perpendicular to the fibre direction from several meters long pultruded rods with a diameter of 10 mm. The cut samples were machined to torsion specimens with a gauge length of L_1 between 60-66 mm and a constant diameter D = 5 mm. Three kinds of measurements were done: monotonic torsion test using different strain rates (1×10^{-3}, 3×10^{-3}, 5×10^{-3}, 7×10^{-3} and 10×10^{-3}), modulated torsion test with amplitudes 0.0005 and 0.001 and a constant strain rate of 5×10^{-3} rad/s. Low cycle fatigue tests with loading-unloading cycles were done to study damage evolution under torsion loading.

A shear stress-strain curve is obtained from the recorded values of the torque and the angle of twist according to the following equations [77]:

$$\tau = \frac{16\, M_T}{\pi\, D^3}$$

$$\gamma = \frac{D\,\theta}{L_1}$$

τ: Torsion stress [MPa] M_T: Torque [Nm]

γ: Torsion strain [%]   θ: Twisting angle [rad]

D: Diameter [mm] L_1: Gauge length [mm]

The ultimate torsional shearing strength or modulus of rupture τ_u is calculated using equation:

$$\tau_u = \frac{16\,M_{T\,max}}{\pi\,D^3}$$

4.2.5.2 *Four-point bending test*

The four point bending test has the advantage of a constant bending moment between the two pressure rams and consequently uniform shear forces and shear stresses. The test was done according to the DIN EN ISO 14125 standard [77] on a Zwick Z050 testing assembly using fixed supports, a 50kN load cell and a crosshead speed of 5mm/min. Sample geometry was variable and is shown in Tab. 19. The test configuration is shown in Fig. 37.

Sample type	Sample geometry L × w × h[mm]	Support span [mm]	Span length [mm]	Hysteresis cycles Reversal points
Laminates HexPly8552	100×15×1.8	81	27	Force-controlled
Laminates Sika Birresin CR132	180×20.2×5.9 220×20.1×5.3 220×20.2×4.7 220×20.2×4.5	150 190 190 190	50	Displacement-controlled
Laminates Hexion L418:	180×20.3×5.3 220×20.1×5.1 220×20.4×4.3 220×20.4×4.2	150 190 190 190	50	No
Pultrued profile T/L20-T/HTSTS/UD65f	80×10×1.4	60	20	No
Pultrued profile R/Sika/Sigrafil-T700SC/UD65f	80×10×1.4	60	20	No

Tab. 19: Four point bending test conditions for each composite, with and without hysteresis cycles.

In order to study the gradual damage evolution of the laminate samples during testing, loading-unloading cycles coupled with in-situ acoustic emission (AE) measurements were carried out. The loading-unloading hysteresis cycles varied from specimen to specimen, some laminates were tested with force-controlled increasing reversal points at 300, 600, 700, 750, 800, 850, 900, 950 and 1000 N; whilst other laminates were tested using displacement-controlled cycles with constant reversal points at deflection values corresponding to 90% of the observed maximum obtained for previously performed monotonic tests until failure.
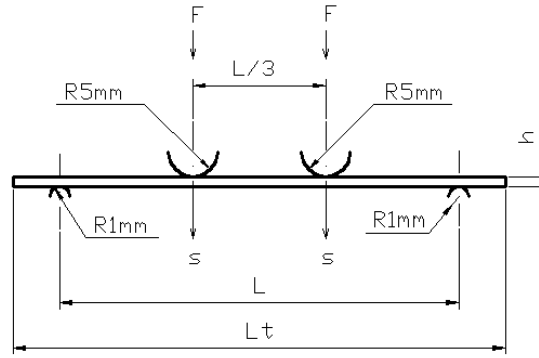
Fig. 37: Test configuration used for the four point bending test [74].

The applied force and the movement of the crosshead were measured and hence the flexural stress and strain were calculated using the following equations taken from the standard [78].

$$\sigma_f = \frac{FL}{wh^2}$$

$$\varepsilon = \frac{540sh}{L^2}$$

σ_f: Flexural stress [MPa]   F: Force [N]   L: Support span [mm]

ε: Flexural strain [%]   w: Sample width [mm]

h: Sample thickness [mm]   s: Crosshead displacement [mm]

As the formula for high strain leads to unrealistic results it was not employed in case of the four point bending test. The Young's modulus was either calculated as the quotient of the differences of the flexural stress and the strain of the outer fibre between 0.05% and 0.25% of the failure strain or as secant modulus between the reversal points considering testing with hysteresis loops.

$$E_b = \frac{\sigma_f - \sigma_0}{10(\varepsilon_f - \varepsilon_0)}$$

E_b: Young's modulus [GPa]

σ_f: Flexural stress at ε_f [MPa]

σ_0: Flexural stress at ε_0 [MPa]

ε_0: 0.05% of the failure strain, or strain at the lower reversal point considering loading with hysteresis loops

ε_f: 0.25% of the failure strain, or strain at the upper intersection point considering loading with hysteresis loops

47

4.2.5.3 *Interlaminar fracture toughness (Mode I&II)*

HexPly8552 laminates: These experiments were carried out in cooperation with IMDEA Materials in Madrid using a INSTRON 3384 universal testing machine.

Mode I:

This test was performed according to the ASTM D 5528 standard [79] on an INSTRON 3384 universal testing machine using a double cantilever beam (DCB). As the same samples were employed for mode I and II tests the original sample dimensions were $200 \times 25 \times 3$ mm^3. A 3µm thin and 25mm long PTFE foil was embedded in the middle of the 16 layers across the whole width of the specimen simulating an initial crack. Furthermore two loading blocks were adhesively bonded to the samples using Loctite Hysol® 9466 A&B two component epoxy based adhesive. The surface was roughened with adhesive paper to apply the glue and cured for at least 10 hours at room temperature. Moreover the specimen sides were painted white and a blue ink scale improved crack length measurements. Fig. 38 shows a drawing of the specimen ready for testing and the clamped specimen.
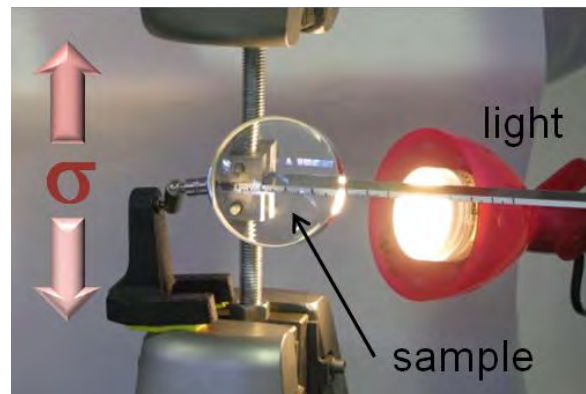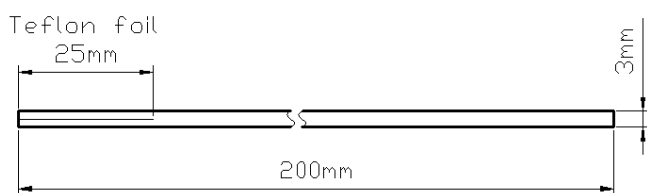
Fig. 38: Specimen geometry for Mode I (left). Picture of the set-up (right). To identify the crack growth more easily whilst loading, a magnification glass was used and a lamp was positioned behind the sample [74].

After mounting the sample in the test machine it was loaded until the crack reached a total length of 30mm. Subsequently the sample was unloaded and loaded again until the crack propagated another 10mm. The procedure was repeated four times resulting in a final crack length of 70mm. Testing speed was 1mm/min. To ensure easy handling and accurate precision of the crack propagation measurement a magnifying glass was used.

Load and displacement during the test were recorded and thus the critical interlaminar fracture toughness G_{Ic} was calculated according to the following equation. For each loading step, the area underneath the curve was approximated by a rectangle.

$$G_{Ic} = \frac{A}{a * w}$$

G_{Ic}: Critical interlaminar fracture toughness mode I [J/mm^2]

A: Total approximated area underneath a loop in the force-displacement diagram [J]

a: Total crack growth [mm]

w: Sample width [mm]

Mode II:

This experiment was also carried out using a INSTRON 3384 universal testing machine. The Interlaminar fracture toughness test mode II follows a three point bending test using an end notched flexure (ENF) specimen (see Fig. 39).
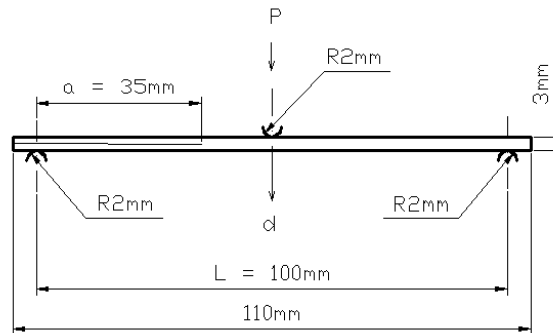
Fig. 39: Specimen geometry for Mode II [74].

Therefore samples from mode I test were cut in length to leave an initial crack of 40mm and were stressed continuously with a deformation speed of 1mm/min until crack propagation occurred. The flexural load and the displacement were recorded during the test and hence the critical fracture toughness G_{IIc} was calculated according to the following equation.

$$G_{IIc} = \frac{9Pa^2d}{2w(0.25L^3 + 3a^{3)}}$$

G_{IIc}: Critical fracture toughness mode II [J/mm^2]

P: Flexural load [N]

w: Sample width [mm]

a: Initial crack length [mm]

L: Span length [mm]

d: Displacement [mm]

4.2.5.4 *Short beam shear strength test (SBS)*

Sika CR132 and Hexion L418 Laminates:

Under bending loading, very short thick specimens undergo strong shear stresses. The apparent Interlaminar Shear Strength (ILSS) can be estimated using the short beam shear (SBS) test. This material property is directly related with the matrix-fibre interface properties. The F^{SBS} is a qualitative indication of the quality of resin, and the compatibility of the resin with the fibres. The set-up is basically like a 3-point bending test, but the clamping is in much smaller in relation to sample thickness, as shown in Fig. 40. Tests were performed in accordance with the ASTM D2344 standard [80] on a Zwick Z050 testing assembly using fixed supports, a 50kN load cell and a crosshead speed of 1mm/min. Sample thickness h, width w and span length L' were variable depending on the laminate, Tab. 20 summarizes them for all materials.
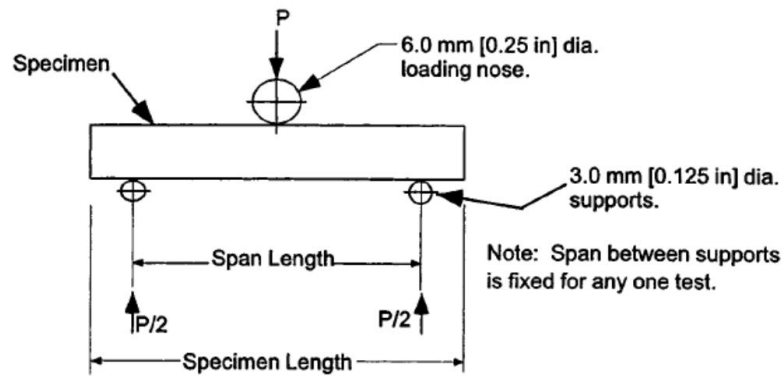
Fig. 40: Short beam shear set-up as specified in [80].

Material	h [mm]	w [mm]	L' [mm]
Sik/FT300B/0-90°/1bar/3	5.9	11.9	24
Sik/HTA40/UD/1bar/3	5.3	10.0	21
Sik/HTS5631/UD/1bar/3	4.7	9.9	19
Sik/HTS5631/UD/3bar/4	4.3	8.9	17
Hex/FT300/0-90°/1bar/5	4.8	12.3	20
Hex/HTA40/UD/1bar/5	4.9	11.2	20
Hex/HTS5631/UD/1bar/5	4.3	10.3	18
Hex/HTS5631/UD/3bar/6	4.1	8.9	16

Tab. 20: Sample geometries and span length used for each kind of laminate.

Afterwards the apparent short beam shear strength was estimated from the maximum force values obtained using the following equation.

$$F^{sbs} = 0,75 \cdot \frac{F_{max}}{w \cdot h}$$

F_{max}: Maximal force [N]

w: Sample width [mm]

h: Sample thickness [mm]

4.2.6 Damage Analysis

4.2.6.1 *In-situ acoustic emission during deformation*

A computer-controlled DAKEL-IPL acoustic emission system [81] based on four channels detection and continuous storage of AE signals with 2 MHz sampling frequency was used to monitor the AE activity. A miniaturized MIDI-410-2 piezoelectric transducer (diameter 6 mm [82]) was attached to the specimen surface with the help of silicon grease and a spring (see Fig. 41 and Fig. 42). A BNC input/output preamplifier with a gain of 35 dB was used. Each of the four channels has a different gain eliminating under/overflows of recorded data.
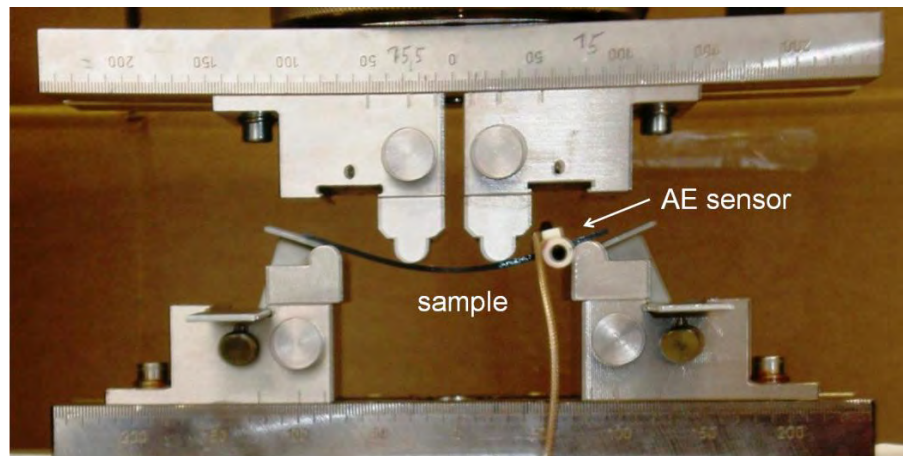
Fig. 41: AE measurement during four point bending test. The piezoelectric sensor attached to a sample on one side is connected to the DAKEL-IPL acoustic emission detector.
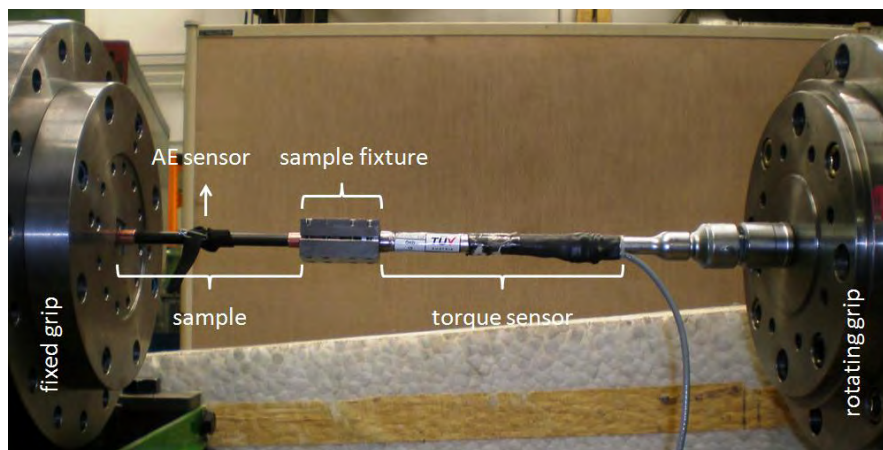
Fig. 42: AE measurement during torsion test. The piezoelectric sensor attached to the sample is hidden under an elastic band.

After the measurement, threshold-level detection of recorded AE signals was set for each channel to achieve a comprehensive set of AE parameters. The threshold voltage for the AE count rate dN_C/dt (number of counts per second [83]) was 15 % of the maximum voltage of each channel. This eliminated the lowest signals which presumably originate from disturbing noise in the test system.

4.2.6.2   *In-situ synchrotron tomography during tensile deformation*

The aim of this measurements is to identify and follow in situ the formation and evolution of damage and the change in fibre orientation, in a cross-ply carbon fibre reinforced laminate, during tensile loading. The composite, was manufactured by compression moulding of six HexPly 8552 prepreg plies with a nominal thickness of 0.19 mm. The plies were stacked with a [+45/-45/+45]$_S$ lay-up. The manufacturing conditions correspond to P2 in Tab. 2.

Synchrotron microtomography was carried out in-situ during tensile deformation of a sample at the ID15A beamline of the European Synchrotron Radiation Facility (ESRF, Grenoble). During the investigation a pink beam was used provided by an U22 undulator with energy maximum at ~ 30 keV. The experimental set-up is shown in Fig. 43.
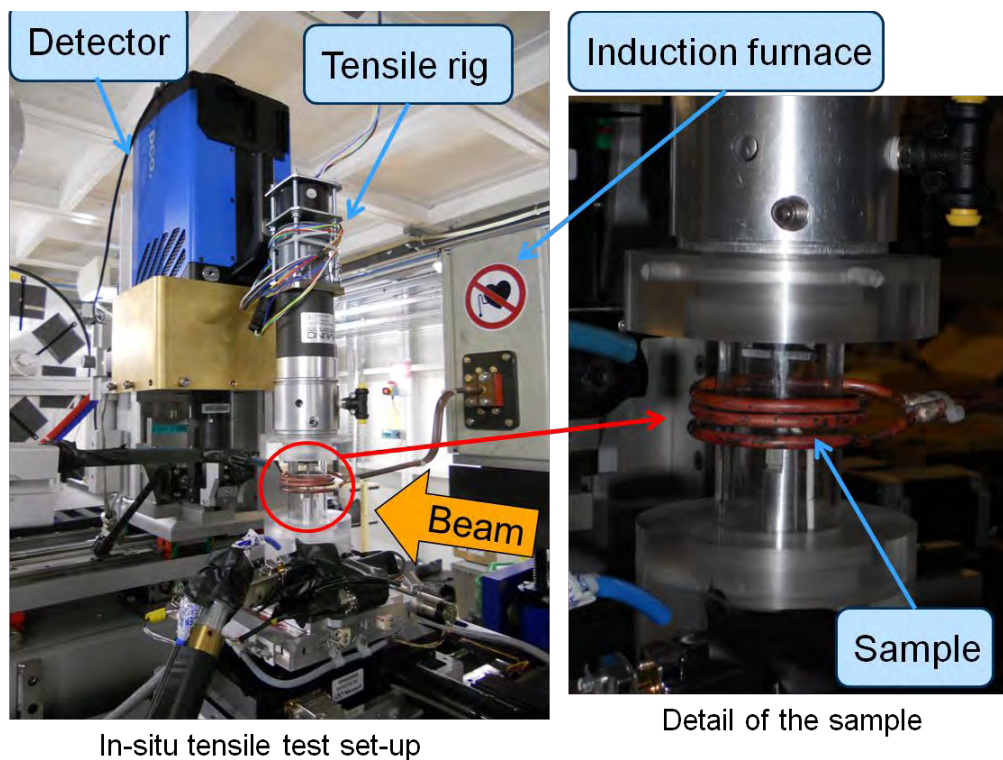
Fig. 43: Experimental set-up at ID15A at the ESRF and sketch [84]. The detector shown in the upper picture (PCO) is not the one used during the experiments described in this work (FReLoN).

On each measurement 600 projections were taken between 0-180° by the FReLoN (fast readout low noise) detector of the ESRF [85] using an acquisition time of 100 ms/projection with an effective pixel size of 1.4 µm. 3D data sets were reconstructed using a filtered back-projection algorithm under various combinations of experimental parameters. Phase contrast is necessary to distinguish between the polymer matrix and carbon fibres owing to their low contrast in absorption. The size of the reconstructed 32 bit volumes is (1019×1019×801) voxel, each voxel having a size of $(1.4 \ \mu m)^3$.

Tensile specimen geometry is shown in Fig. 44, the notch radius was 1 mm, sample thickness was 1.14 mm, and its cross section about $\sim 1 \ mm^2$. The in situ tensile rig was provided by the colleagues at INSA-Lyon. The first tomographic scan was performed using a preload of ~ 4.5 MPa. Then, the sample was deformed stepwise using constant deformation steps at a strain rate of 5 µm/s. Tomographic scans were carried out after each deformation step, yielding a total of ten scans. Each scan took approximately two minutes. The region observed in the tomography scans contained the whole sample cross section in the centre of the specimen (notch region) as shown in Fig. 44.
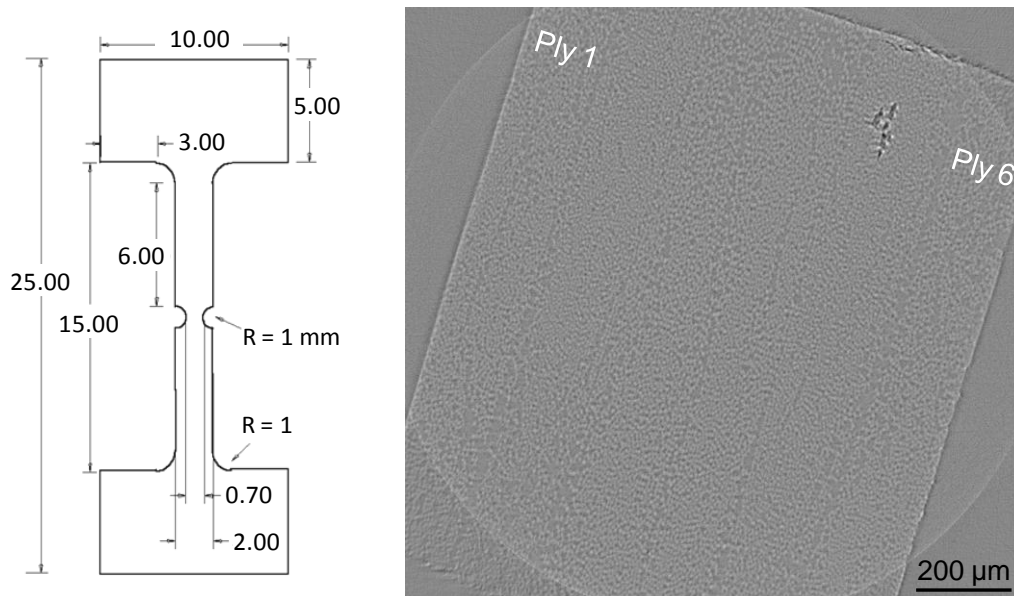
Fig. 44: Tensile specimen geometry. XY Slice of the first tomographic scan (sample at pre load) in its original size (1019x1019 pixel^2) after reconstruction. Sample thickness = 1.14 mm.

The image processing of reconstructed volumes consisted of three main steps. Registration of all ten obtained volumes in order to make possible a comparison of results between them; this was done using the free software MedINRIA [86]. Fibre orientation analysis on each single ply was performed afterwards using the ImageJ plug-in OrientationJ [87]. Finally crack and porosity segmentation was carried out using Avizo Fire 6.1 software [88].

Registration:

Reconstructed 32 bit volumes with a size of (1019×1019×801) voxel were converted to 8 bit using the software ImageJ [61] in order to achieve a file size which caould be computationally handled. 8 bit volumes were rotated without interpolation, and then cropped to avoid sample-air boundaries that may interfere in further analysis. The volumes were all registered in

MedINRIA using a manual landmarks rigid body algorithm using the plies 3 and 4 in the centre of the sample as reference and registering them consecutively. This means, the second scan referred to the first and then the third scan referred to the registered second one and so on. After registration, all volumes were cropped simultaneously using the Sync Windows plug-in, the resulting size was (660×676×653) voxel for all ten volumes, which is a cube with a volume of approximately ~ 0.8 mm^3.

Orientation Analysis:

The ten registered cropped volumes were resliced in ImageJ prior to orientation analysis. The OrientationJ [87] plug-in was applied on each ply individually; the algorithm is based on the evaluation of the structure tensor in a local neighbourhood of 5×5 pixels within each 2D resliced slice. Afterwards a volumetric histogram can be exported with the normalized frequency for each one of the orientations found. A colour map can also be plotted to help visualization, as shown in Fig. 45.
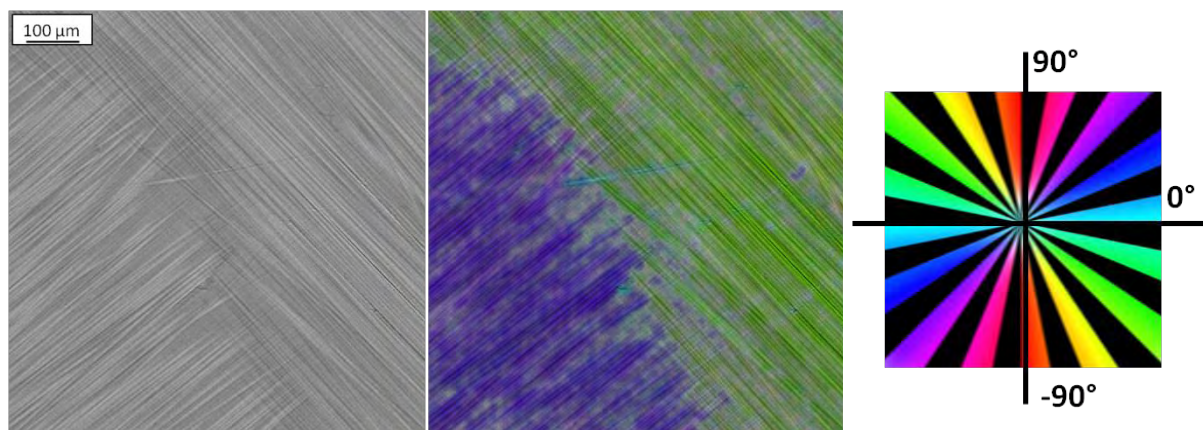
Fig. 45: Exemplary XY resliced slice and the colour map obtained after orientation analysis. To interpret the colours the angle legend shown on the right is used.

Cracks and porosity segmentation:

The cracks and porosity have similar grey values. They were segmented individually for each volume. Porosity was found only in one of the six plies, therefore it was segmented by hand after applying a global threshold. To segment the cracks, the ImageJ and Avizo software were required. The 8 bit segmented cropped volumes were filtered before thresholding by means of a 3D median filter with a mask radius of 1 in ImageJ. The filtered volumes were further analyzed using Avizo Fire 6.1 software. A global threshold was applied, the resulting binary image was edited to remove segmented porosity manually. Afterwards the segmented objects were quantified with a global labelling. In order to avoid the consideration of tomographic artefacts, only the objects larger than 27 voxels in volume were considered. Therefore the binarized labelled phase was filtered again using a min volumetric size as constraint. The imaging of the segmented cracks in 3D as well as the individual quantification of characteristic parameters such as area and volume of each object found followed. The results are presented in section 5.5.2.

5. Results

5.1 Materialography 2D

For each of the eleven different laminates and three different pultruded profiles studied a microstrutural description with special regard to irregularities and found defects will be presented in a separated subchapter. Light optical (LOM) and scanning electron (SEM) micrographs for the laminates are presented in chapter 5.1.1 and for the pultruded profiles in chapter 5.1.2. Properties such as components distribution, fibre volume fraction, fibre diameter, manufacturing defects, internal architecture of the composite, quality of fibre-matrix interface can be assessed with 2D materialography. Defects observed for each composite, classified by composite geometry will be listed separately in chapter 6.7. In light optical micrographs, porosity appears as the darker areas, the matrix can be distinguished from pores because of its brighter contrast and smoother surface. The fibres are the brightest features observed. In longitudinal samples cut parallel to fibre direction, fibres appear as elongated sections; whereas in cross-section samples, as circular or rather ellipsoidal shapes. Cross sectional fibre-shapes provide information about fibre orientation within the composite and waviness degree. Although this does not apply to some of the materials studied containing non-cylindrical fibres with a kidney-like cross section.

5.1.1 Laminates

In the following sections characteristic features observed for the different studied laminates are highlighted and indicated in the corresponding figure captions.
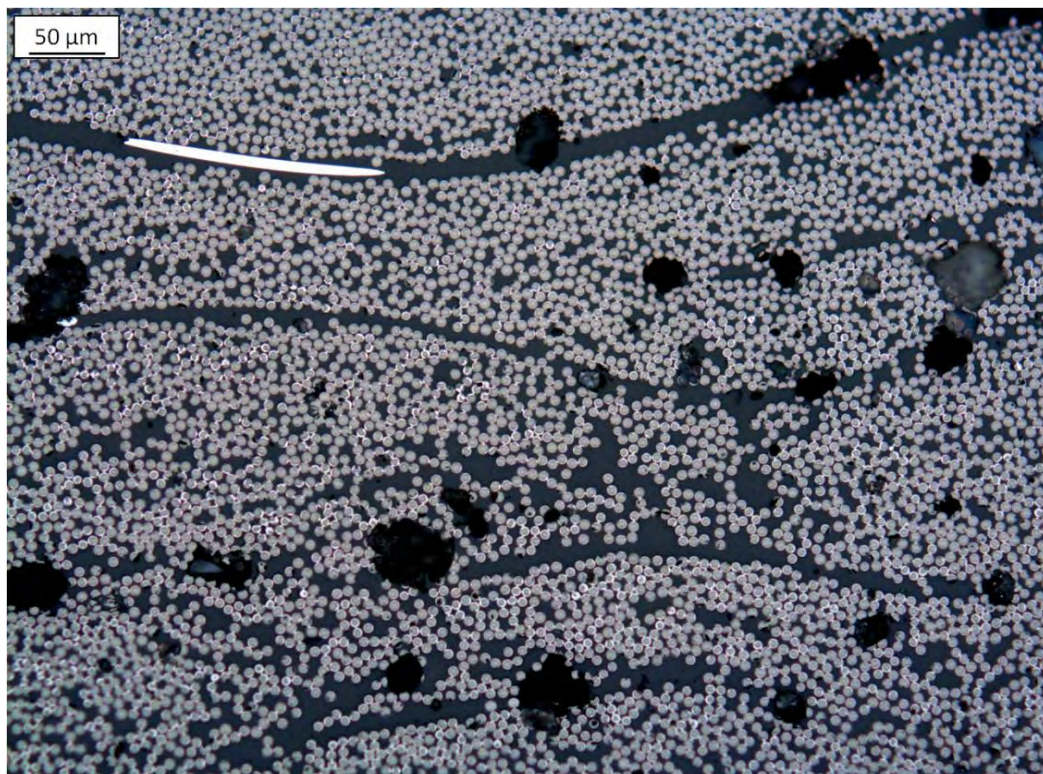
Fig. 46: Cross section of sample HexPly8552/HSAS4/UD58f/0.2MPa/1. Interply macro porosity, intraply micro porosity, fibre bundles shape and matrix-rich regions with a misaligned fibre within are observed.

5.1.1.1 *Laminates HexPly8552/HSAS4/UD58f/0.2MPa/1&2*

Fig. 47: Longitudinal section of sample HexPly8552/HSAS4/UD58f/0.2MPa/1. Long porosity channels in matrix-rich regions are observed, especially between consecutive plies.
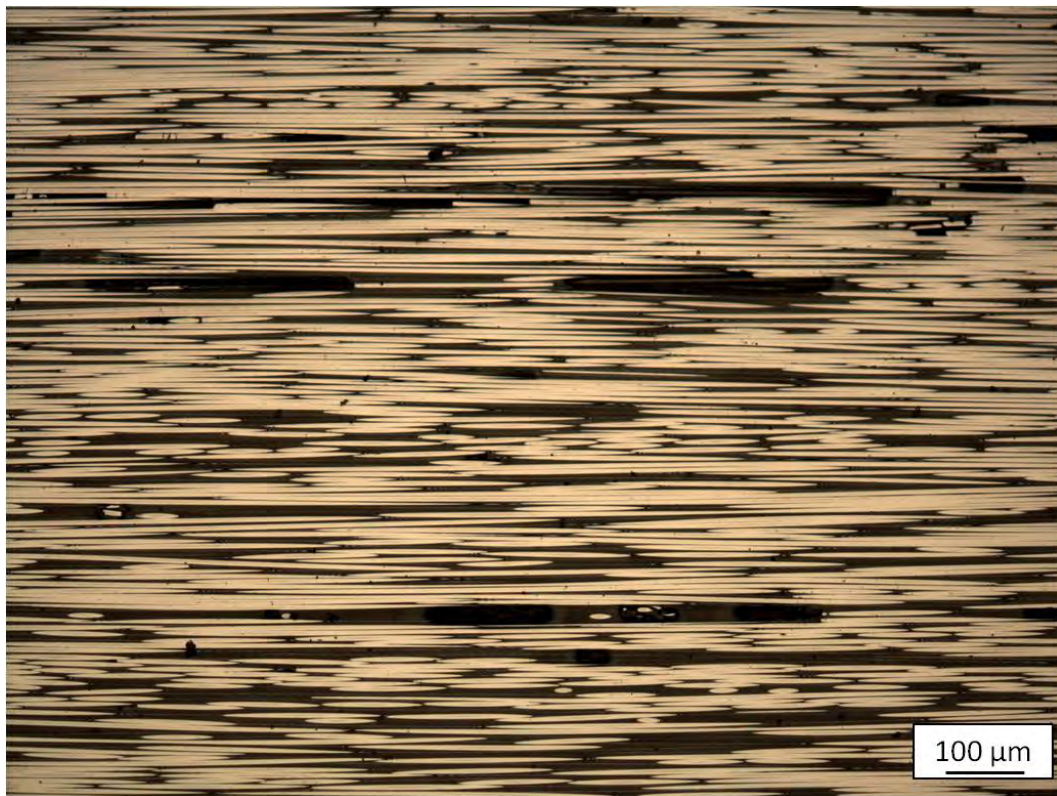
Fig. 48: Longitudinal section of sample HexPly8552/HSAS4/UD58f/0.2MPa/2. Long porosity channels are also observed, although smaller than for the laminates produced with P1 cycle.

Fig. 49: Sample HexPly8552/HSAS4/UD58f/0.2MPa/2 cross section through the whole laminate thickness (~ 2 mm). Voids are smaller than those observed in laminates produced with P1. The ten stacked UD plies composing the material are recognizable due to matrix-rich regions at the interface between them. The shape of fibre bundles within a ply is also visible. Two kinds of pores can be observed: pores within bundles (intraply porosity) and pores between stacked layers (interply porosity). Along the laminate thickness: the largest matrix-rich regions are close to the surfaces, whereas porosity concentrates within the central plies of the laminate.

5.1.1.2 *Laminates HexPly8552/HSAS4/± 45-58f/0.2MPa/2*
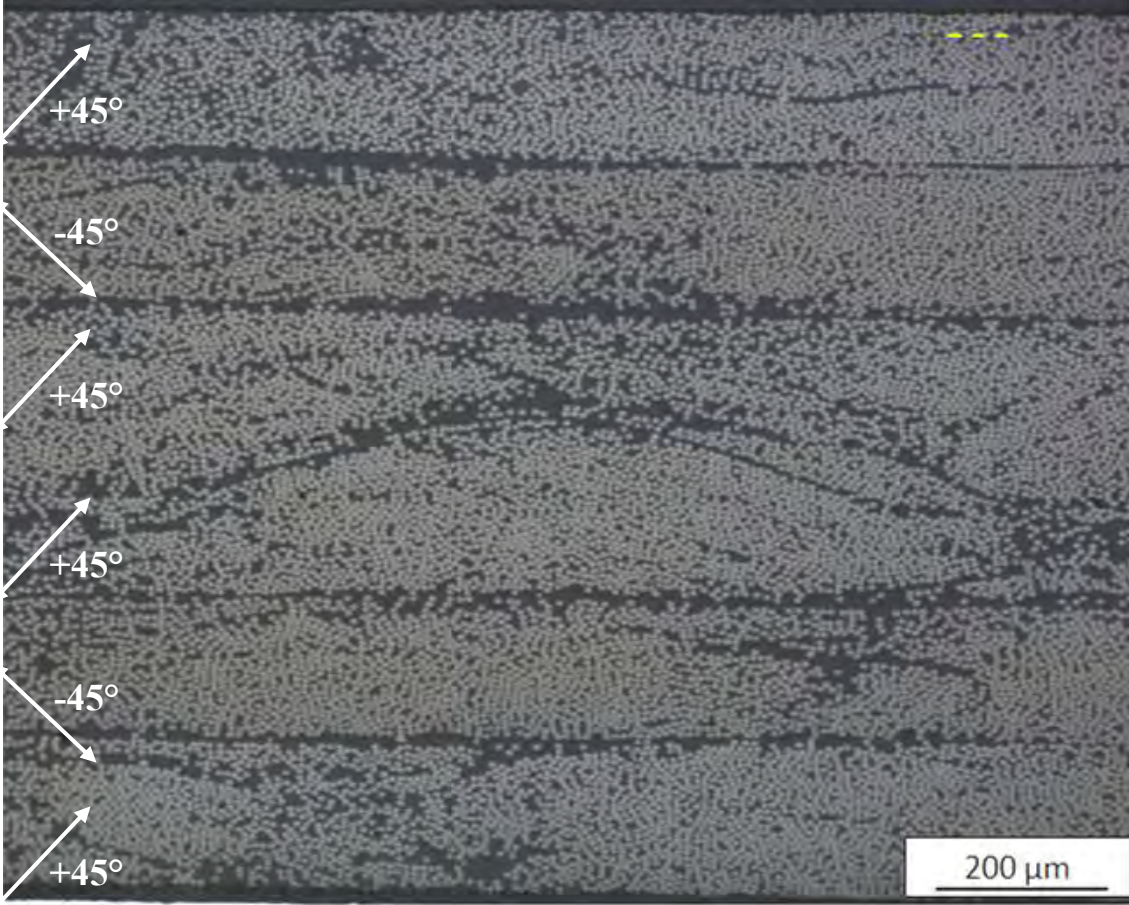
Fig. 50: Cross section of a HexPly8552/HSAS4/± 45-58f/0.2MPa/2 sample showing the six stacked plies across the whole thickness of the laminate. Matrix-rich areas between plies are observed. No porosity observed. In the centre of the laminate, the two central +45° layers merge and no boundary is observed between them. Fibre bundles within a ply can be recognized.

Fig. 51: Cross section of a HexPly8552/HSAS4/± 45-58f/0.2MPa/2 sample showing, matrix-rich areas between plies and bundles boundaries within the -45° ply. Oval fibre cross section is due to the 45° ply orientation.

58

5.1.1.3 *Laminates Sik/FT300B/0-90°/1bar/3*
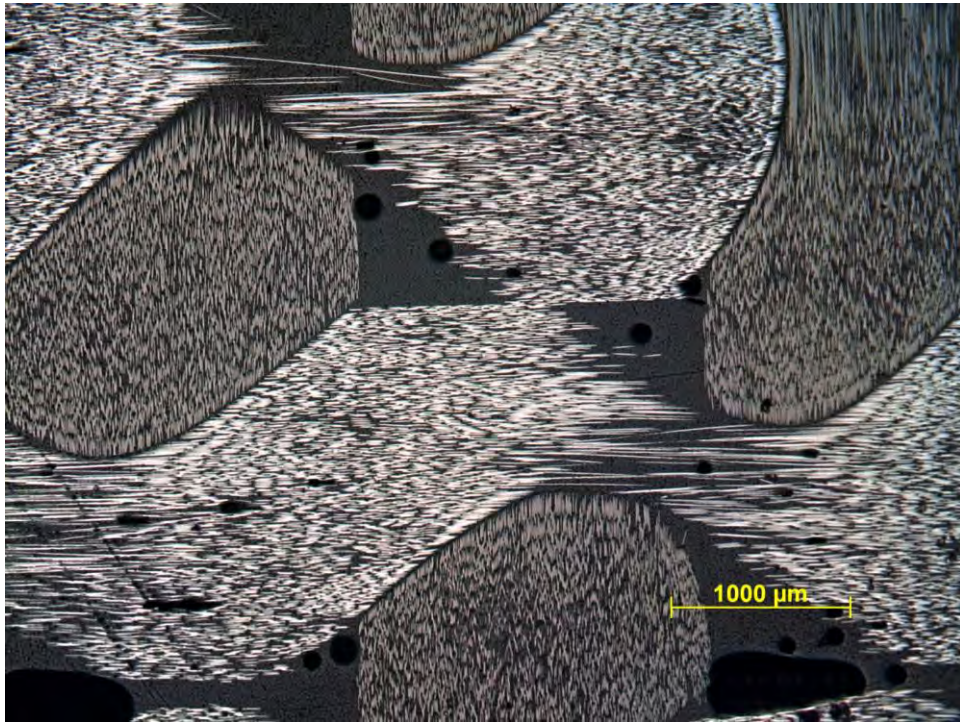
Fig. 52: Top section of the laminates Sik/FT300B/0-90°/1bar/3 showing a view perpendicular to the textile surface, where fibre tows oriented in 0° and 90° direction cross. Small round pores as well as very large voids are observed within the matrix-rich areas formed at the cross points of the fibre tows. The woven nature of the fabric induces a high degree of fibre waviness.
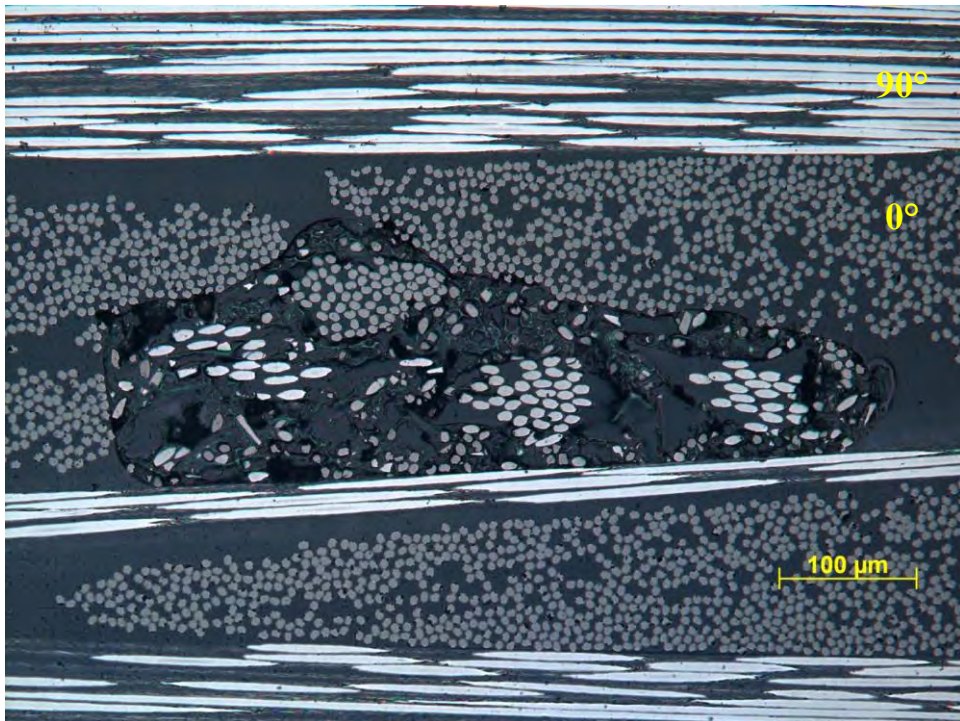
Fig. 53: Section of the laminates Sik/FT300B/0-90°/1bar/3 showing the end of a textile tape, which originated a cluster of broken and wrong aligned fibres associated to a very dry and porous matrix. Furthermore on the 0° layers the shape of fibre bundles can be recognized. The short length of the longitudinal 90° fibre fragments is also indicative of their high degree of waviness.
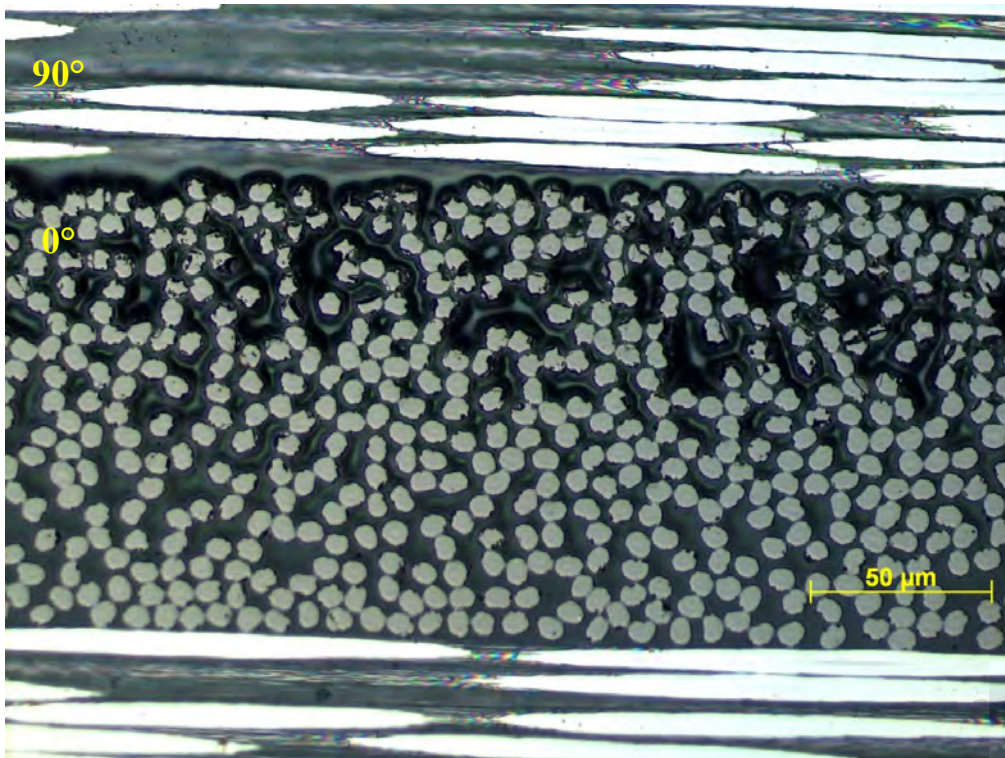
Fig. 54: Section of the laminates Sik/FT300B/0-90°/1bar/3 showing a nonimpregnated area within the sample in between a 0° and a 90° layer.
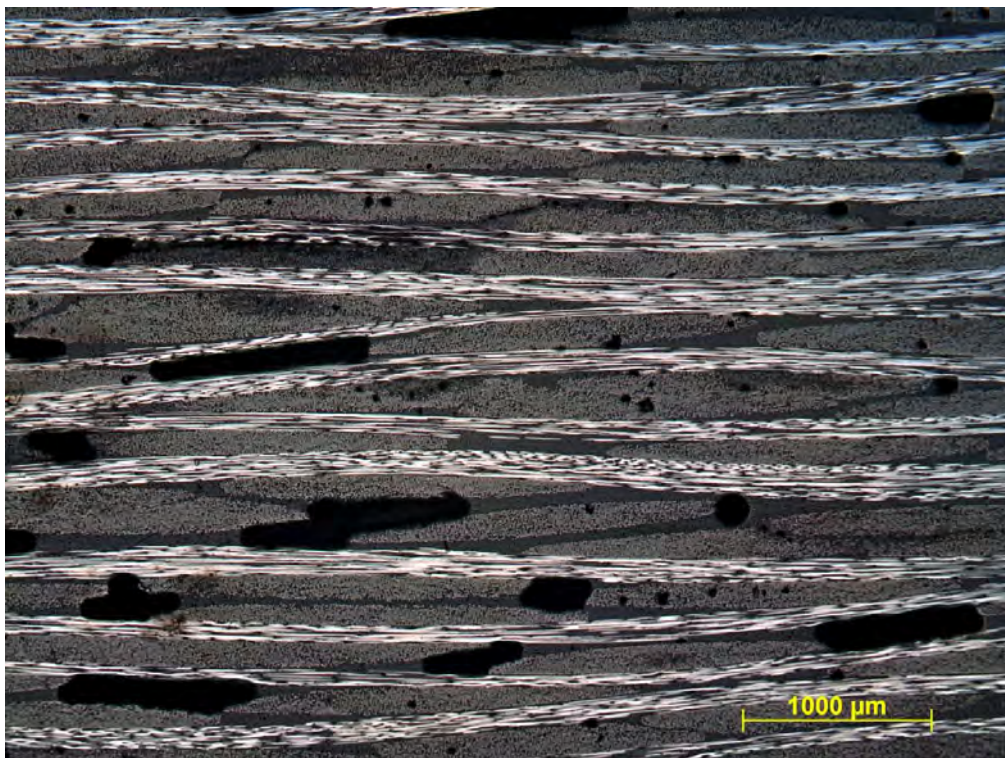
Fig. 55: Overview section of the laminates Sik/FT300B/0-90°/1bar/3 where many of the defects found can be seen. Very large interply pores within textile layers as well as matrix-rich areas can be clearly recognised. Small pores at the interface between neighbour bundles are observed within some of the 0° plies.

5.1.1.4 *Laminates Sik/HTA40/UD/1bar/3*
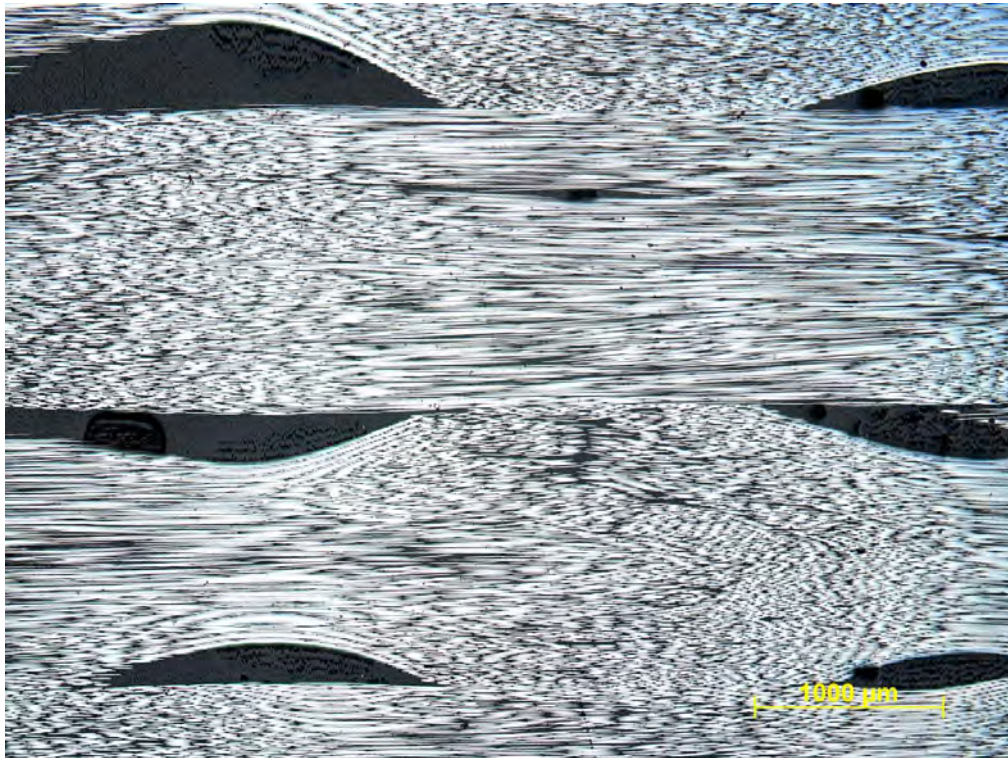
Fig. 56: Top section of a Sik/HTA40/UD/1bar/3 laminate showing a view perpendicular to the textile surface, where the UD tapes exhibit a curvy tendency which might be explained by the presence of glass fibres (weft yarn) perpendicular to them.

Fig. 57: Overview cross section of a Sik/HTA40/UD/1bar/3 laminate. Micro porosity within bundles as well as large voids between layers are observed. Matrix-rich regions around bundles with glass fibres embedded in them have a brighter contrast.
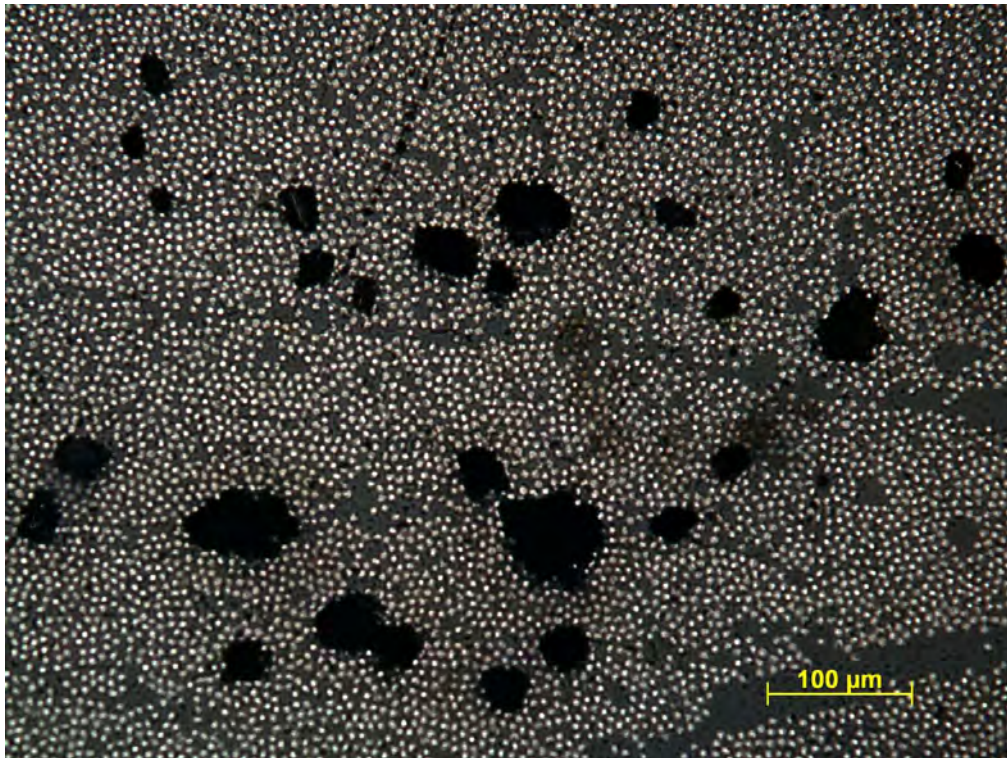
Fig. 58: Cross section of a Sik/HTA40/UD/1bar/3 laminate. Micro porosity within two bundles as well as large matrix-rich regions between them are observed.
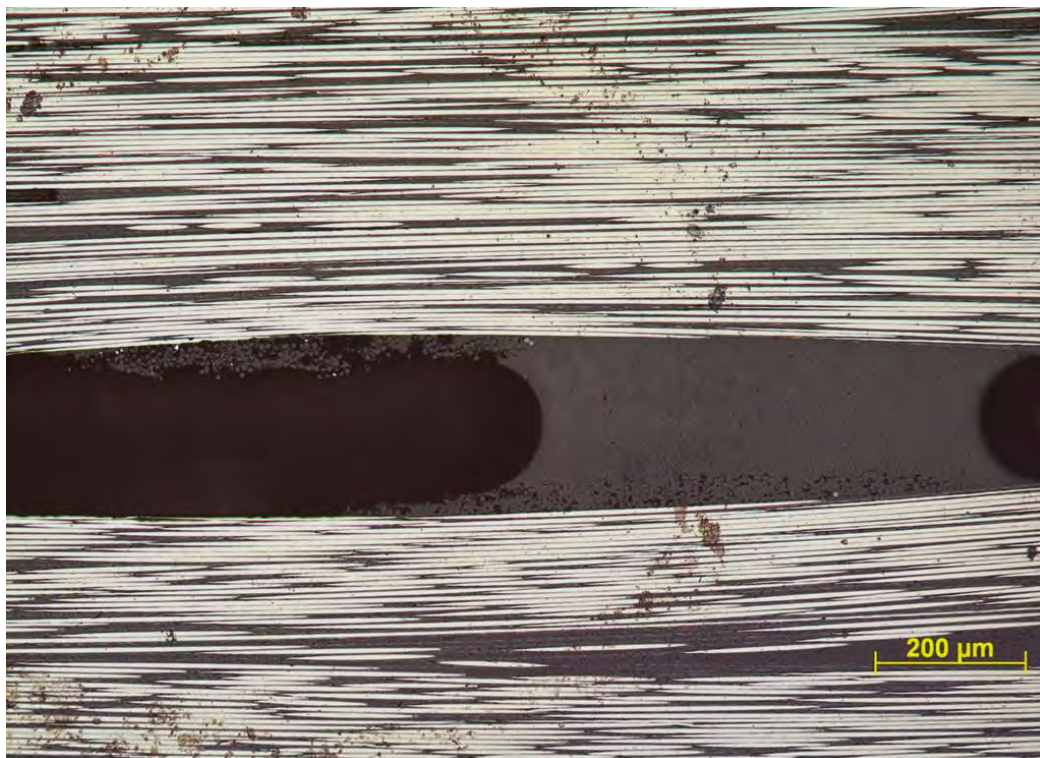
Fig. 59: Longitudinal section of a Sik/HTA40/UD/1bar/3 laminate. Macro porosity within matrix-rich regions associated to glass fibres (weft fibres) can be observed, as well as fibre waviness induced by the presence of these large wormhole-like pores.

5.1.1.5 *Laminates Sik/HTS5631/UD/1bar/3*

Fig. 60: Top section of a Sik/HTS5631/UD/1bar/3 laminate showing a view perpendicular to the textile surface, waviness of the tape is clearly seen, as well as some voids within matrix rich regions.
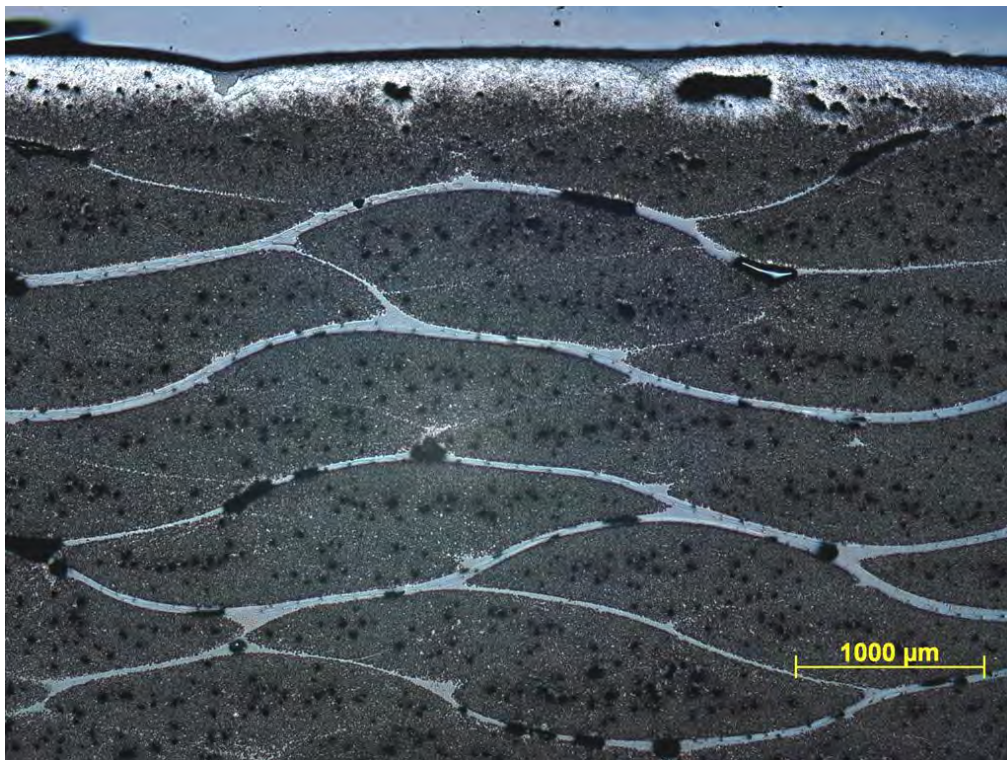
Fig. 61: Overview cross section of a Sik/HTS5631/UD/1bar/3 laminate. On the surface of the laminate large pores are observed, formed around gases which could not escape during resin consolidation.

Fig. 62: Cross section of a Sik/HTS5631/UD/1bar/3 laminate. Macro und micro porosity within bundles as well as large matrix-rich regions between bundles within the same ply. PES support fibres embedded in matrix-rich interply regions are observed.
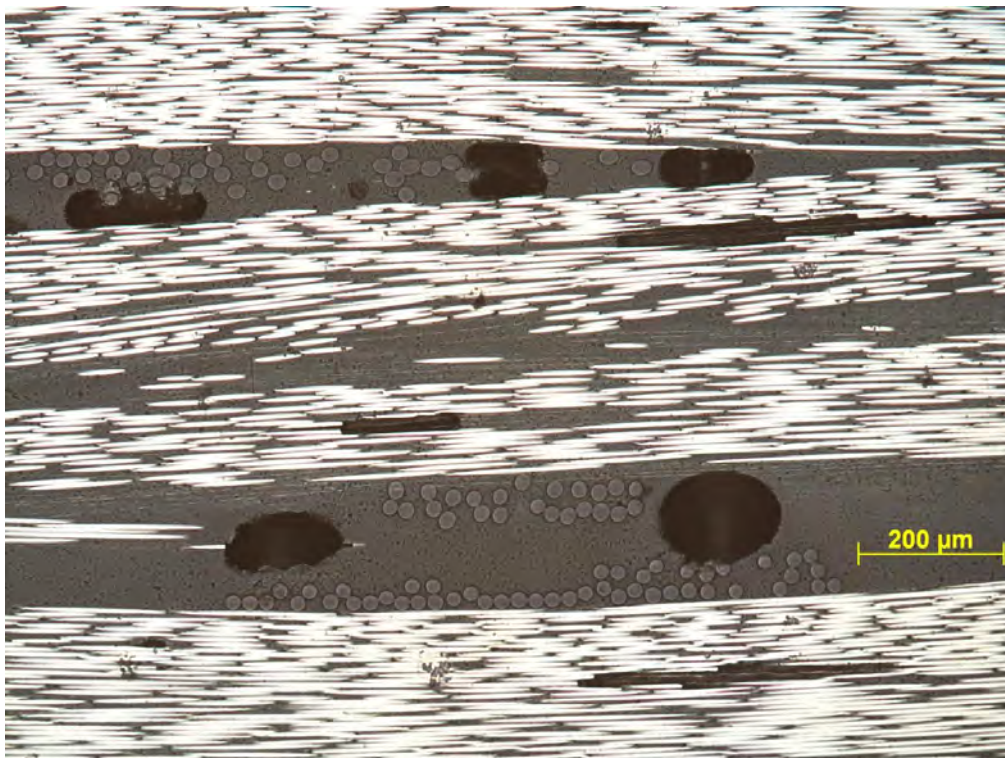
Fig. 63: Longitudinal section of a Sik/HTS5631/UD/1bar/3 laminate. Large pores associated to PES support fibres are formed in matrix rich-regions between plies. Higher misalignment of the fibres can be observed close to these regions.

5.1.1.6 *Laminates Sik/HTS5631/UD/3bar/4*
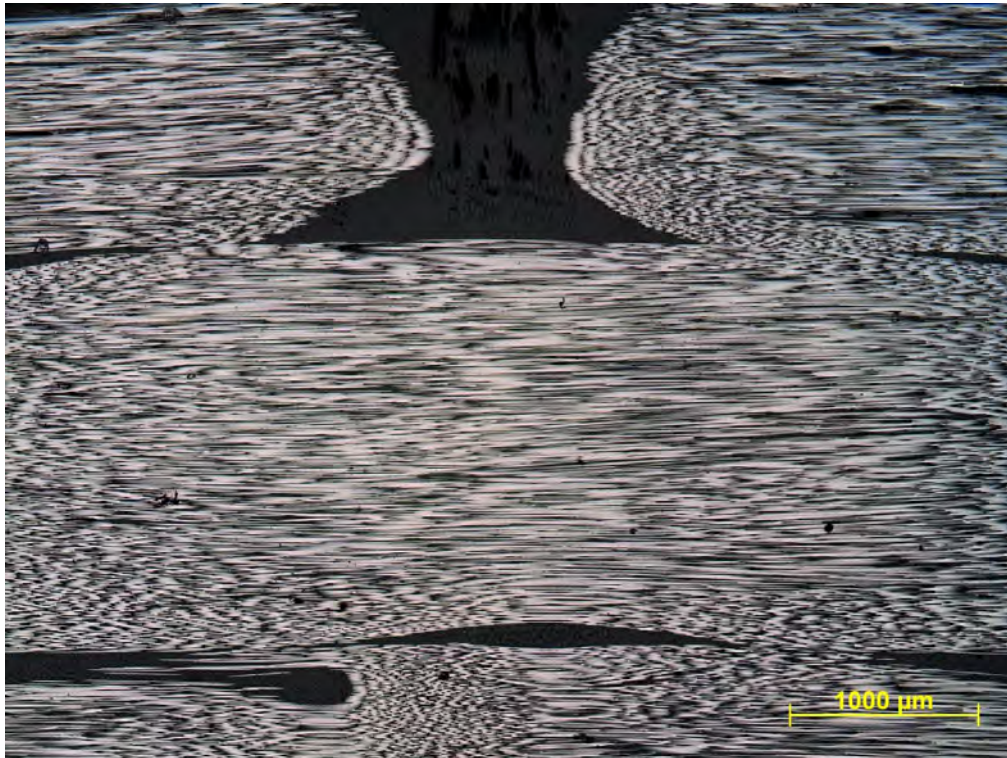
Fig. 64: Top section of a Sik/HTS5631/UD/3bar/4 laminate showing a view perpendicular to the textile surface, waviness of the tape is clearly seen, as well as some voids within matrix-rich regions.

Fig. 65: Cross section of a Sik/HTS5631/UD/3bar/4 laminate. During production a human hair was trapped between two textile layers. It is surrounded by a matrix-rich region. Porosity is localized in the centre of the bundles.
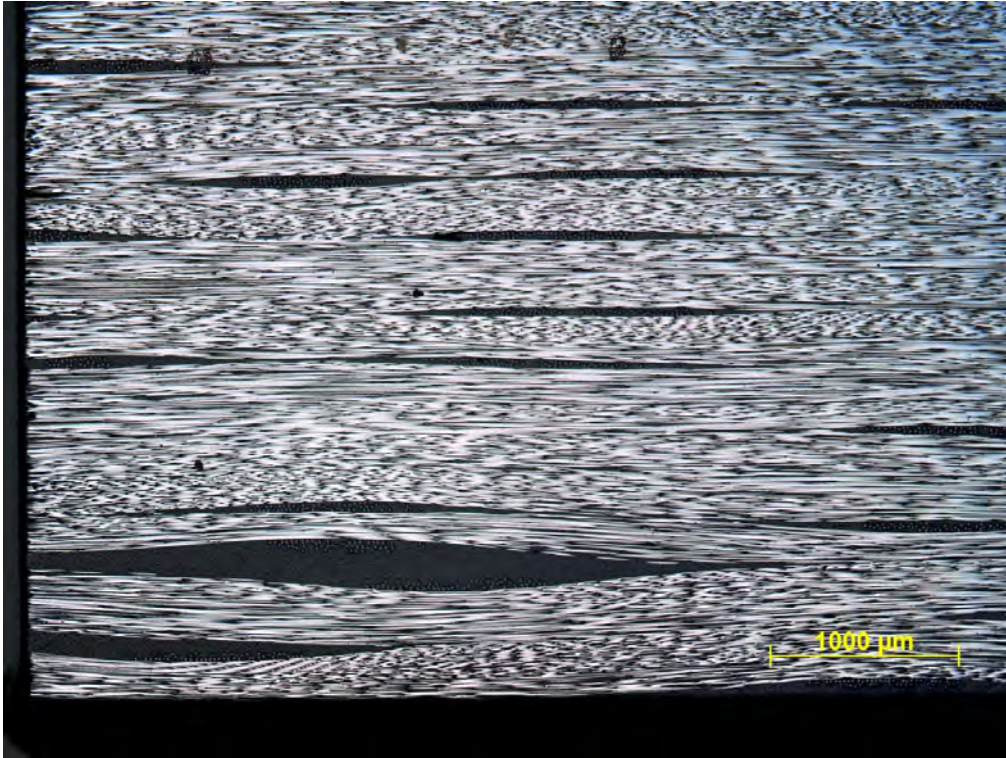
Fig. 66: Longitudinal section of a Sik/HTS5631/UD/3bar/4 laminate. Waviness of plies is more accentuated at the edges of the laminates, where larger matrix-rich areas can be observed.
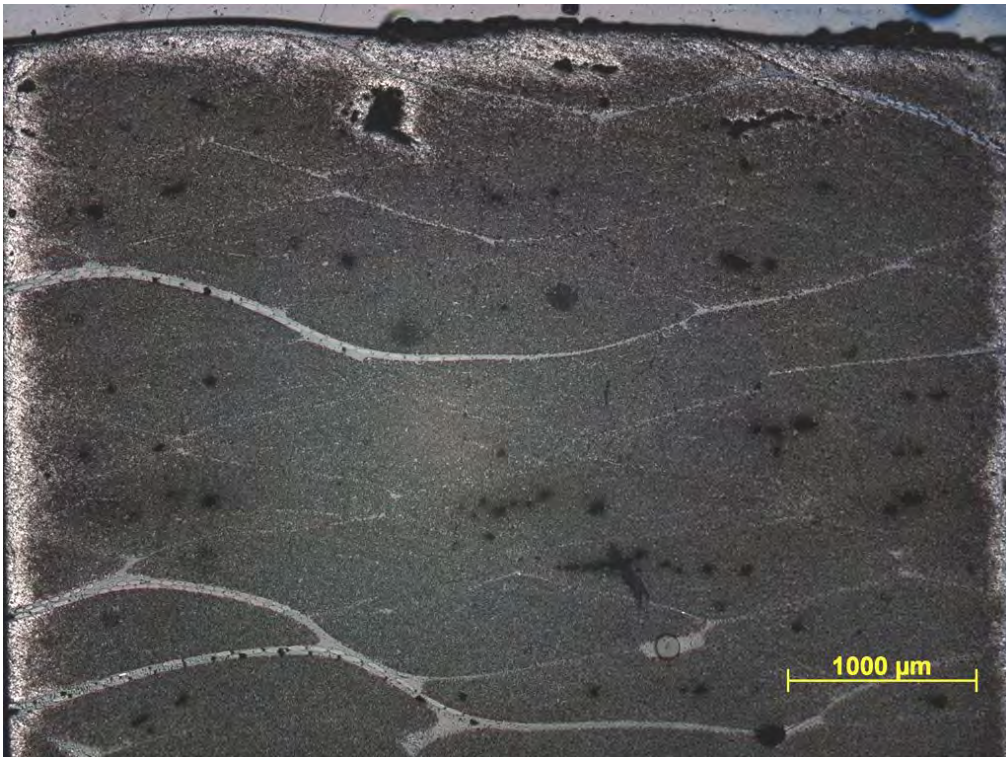
Fig. 67: Overview cross section of a Sik/HTS5631/UD/3bar/4 laminate. Large pores accumulations are observed near the surface of the laminate. This can be a consequence of bad impregnation or be originated by trapped gases that could not escape the resin during consolidation. Matrix-rich regions between plies with embedded PES support fibres are observed.
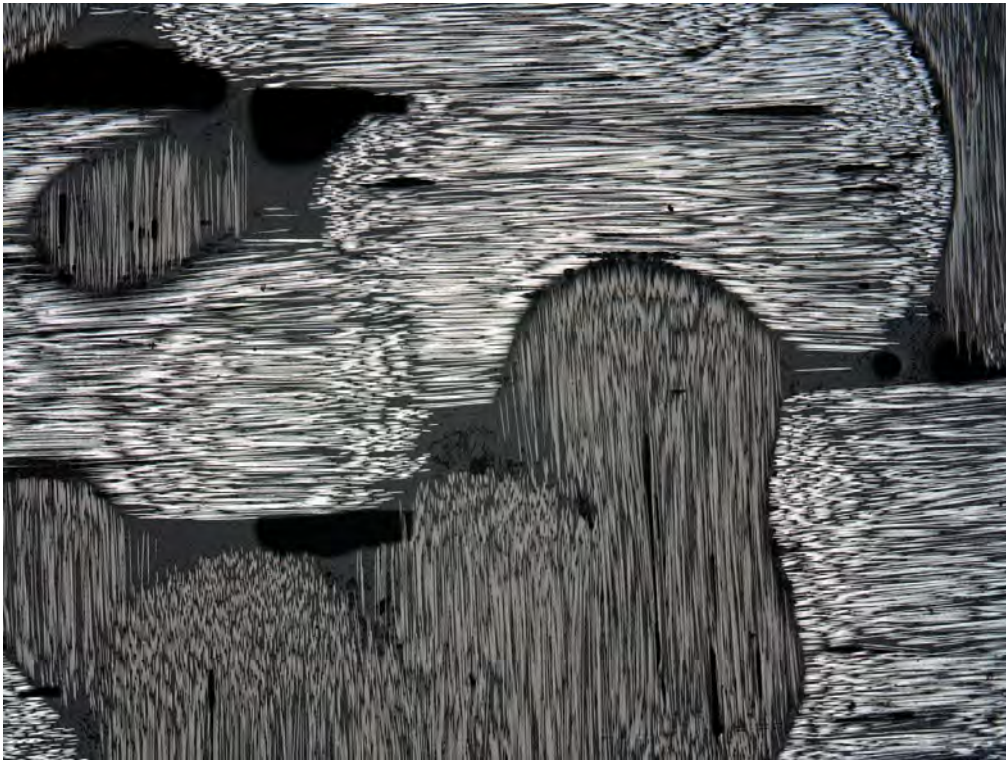
Fig. 68: Top section of a Hex/FT300B/0-90°/1bar/5 laminate perpendicular to the textile surface. Small round pores and very large voids are observed within the matrix-rich areas formed at the cross points of the 0° and 90° oriented fibre tows. The woven nature of the fabric induces a high degree of fibre waviness


Fig. 69: Overview section of a Hex/FT300B/0-90°/1bar/5 laminate. Through the whole laminate thickness very large pores between textile layers as well as matrix-rich areas can be recognised. Small pores are observed within some of the 0° plies and also at the interface between neighbour bundles.
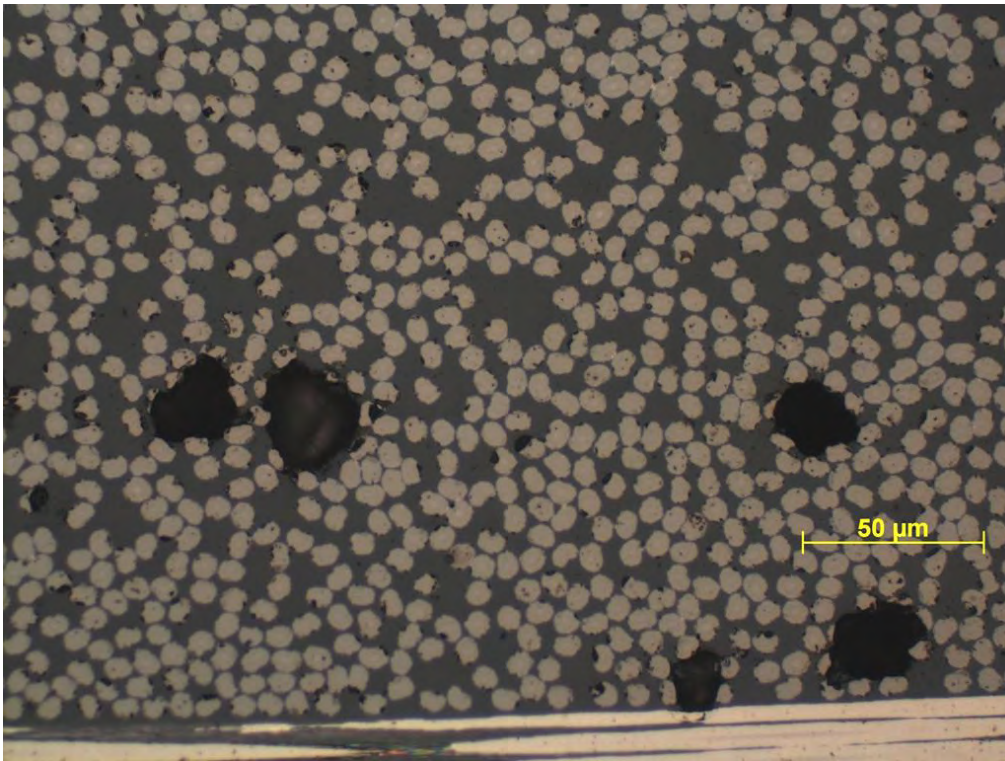
Fig. 70: Cross section of a Hex/FT300B/0-90°/1bar/5 laminate. The cross section of the Torayca FT 300B fibres is not circular but bean-shaped. Micro porosity within a bundle can be observed close to the transition to a 90° ply.
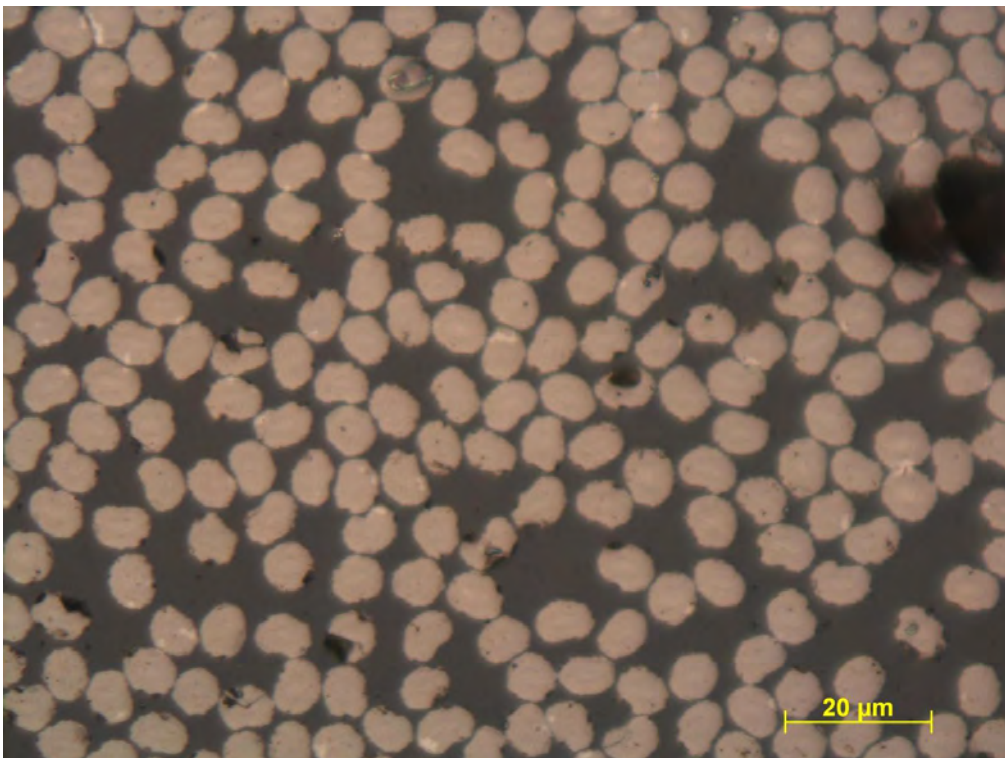
Fig. 71: Zoom on cross section of a Hex/FT300B/0-90°/1bar/5 laminate. Bean-shaped fibre cross section. The packing of bean-shaped fibres is less effective than for cylindrical ones. Numerous matrix-rich regions and non-touching fibres are observed through the whole imaged cross section. The cross sectional area of a fibre is between 34-39 μm^2 (circular fibres cross section area is 38 μm^2). Broken fibres are observed.

5.1.1.8 *Laminates Hex/HTA40/UD/1bar/5*
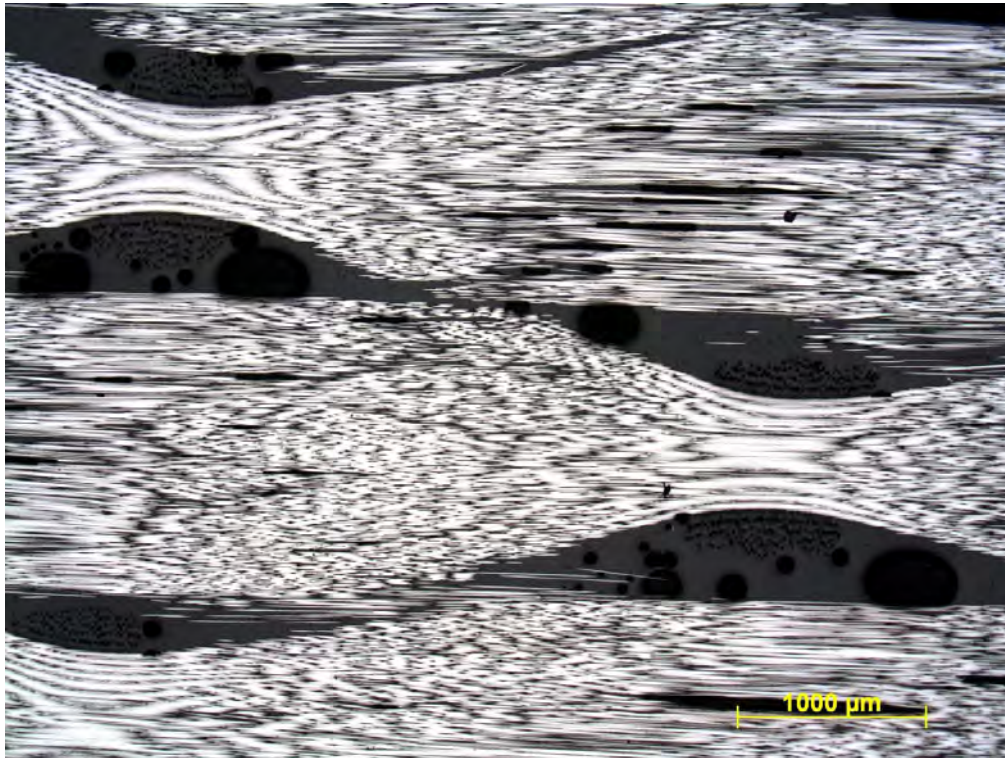
Fig. 72: Top section of a Hex/HTA40/UD/1bar/5 laminate showing a view perpendicular to the textile surface. Waviness of the UD tapes can be observed. Underneath the curved regions matrix-rich areas are present, with gas porosity and weft yarn glass fibres embedded in them.
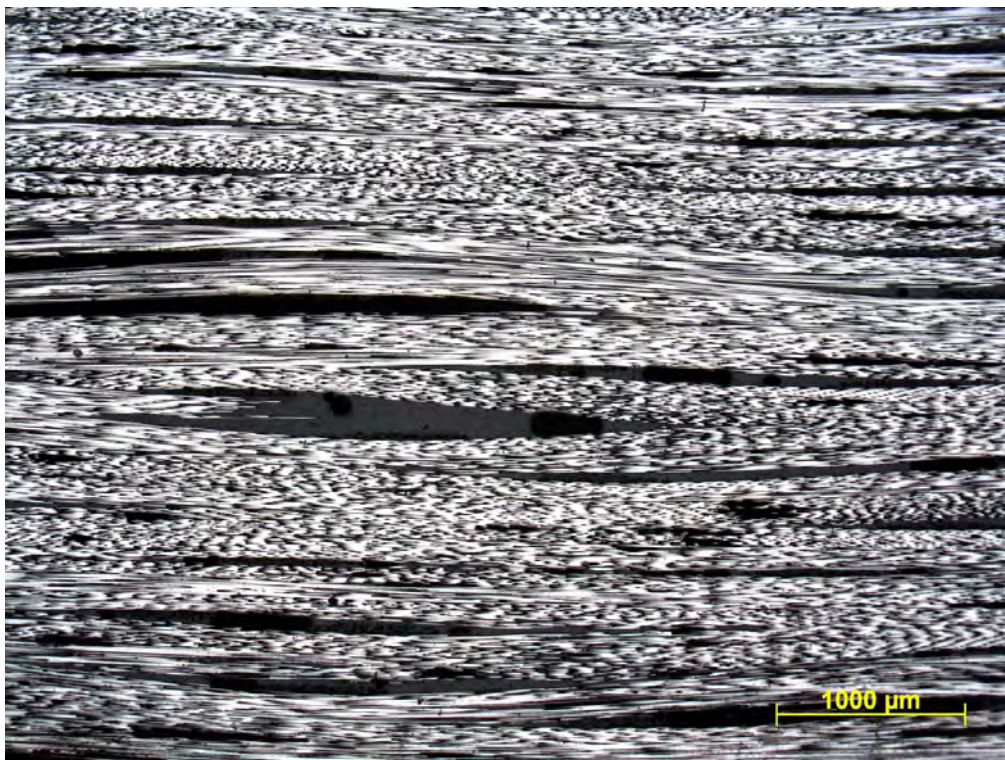
Fig. 73: Longitudinal section of a Hex/HTA40/UD/1bar/5 laminate. Waviness is observed. A large resin-rich area as well as stacking faults with large wormhole-like pores can be observed.
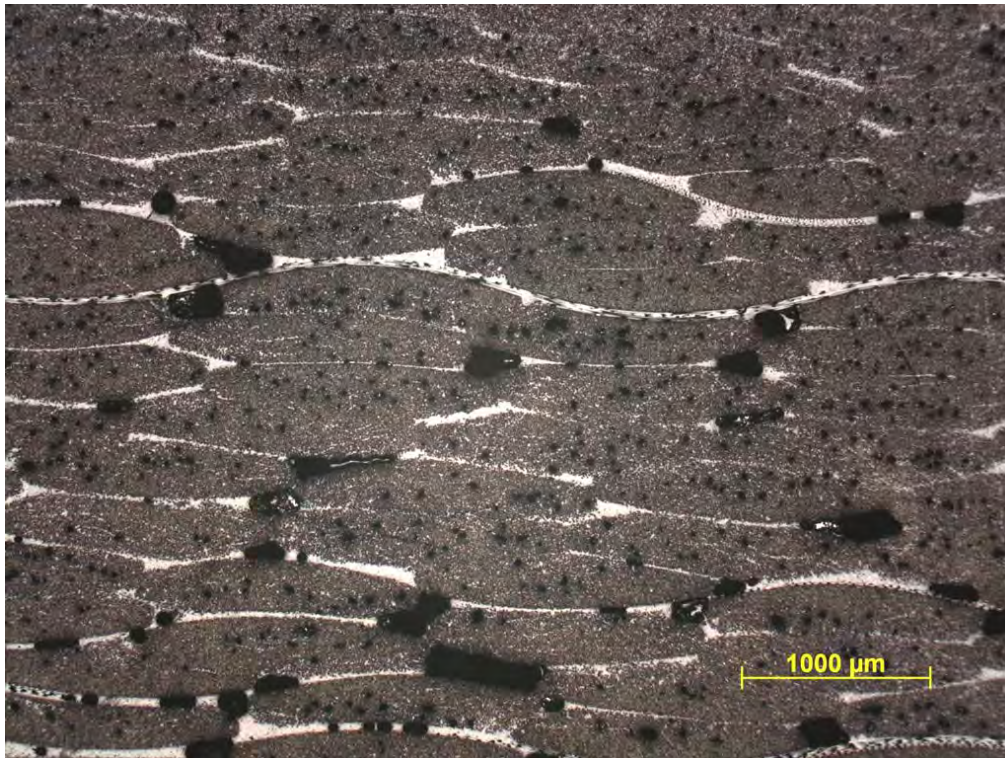
Fig. 74: Overview cross section of a Hex/HTA40/UD/1bar/5 laminate. Micro porosity within bundles as well as large voids between layers can be observed. Glass fibres embedded in matrix-rich regions around carbon bundles have a brighter contrast than the rest.

Fig. 75: Cross section of a Hex/HTA40/UD/1bar/5 laminate. At the end of a textile tape, pores and broken fibres are observed. At the edge of a bundle a large pore between plies can be seen surrounded by the PES supporting fibres. Within the same bundle micro pores can be observed.

5.1.1.9 Laminates Hex/HTS5631/UD/1bar/5

Fig. 76: Overview cross section of a Hex/HTS5631/UD/1bar/5 laminate. Micro porosity within bundles as well as large voids between layers can be observed. Dry nonimpregnated regions are observed on both the upper and the lower surface.

Fig. 77: Cross section of a Hex/HTS5631/UD/1bar/5 laminate. Porosity is homogeneously distributed across the whole imaged surface. Both micro and macro pores are observed both in the matrix boundary between bundles and within them.
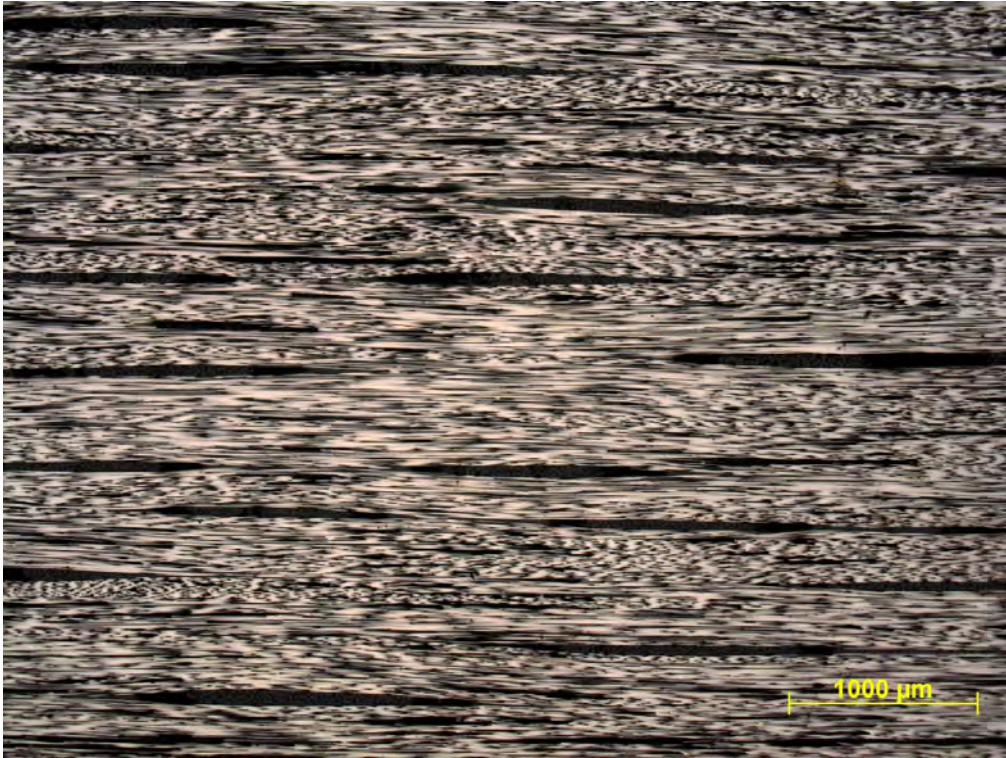
Fig. 78: Longitudinal section of a Hex/HTS5631/UD/1bar/5 laminate. Waviness and longitudinal pores are observed. Each different ply can be recognised due to the matrix-rich regions between them.

5.1.1.10 *Laminates Hex/HTS5631/UD/3bar/6*
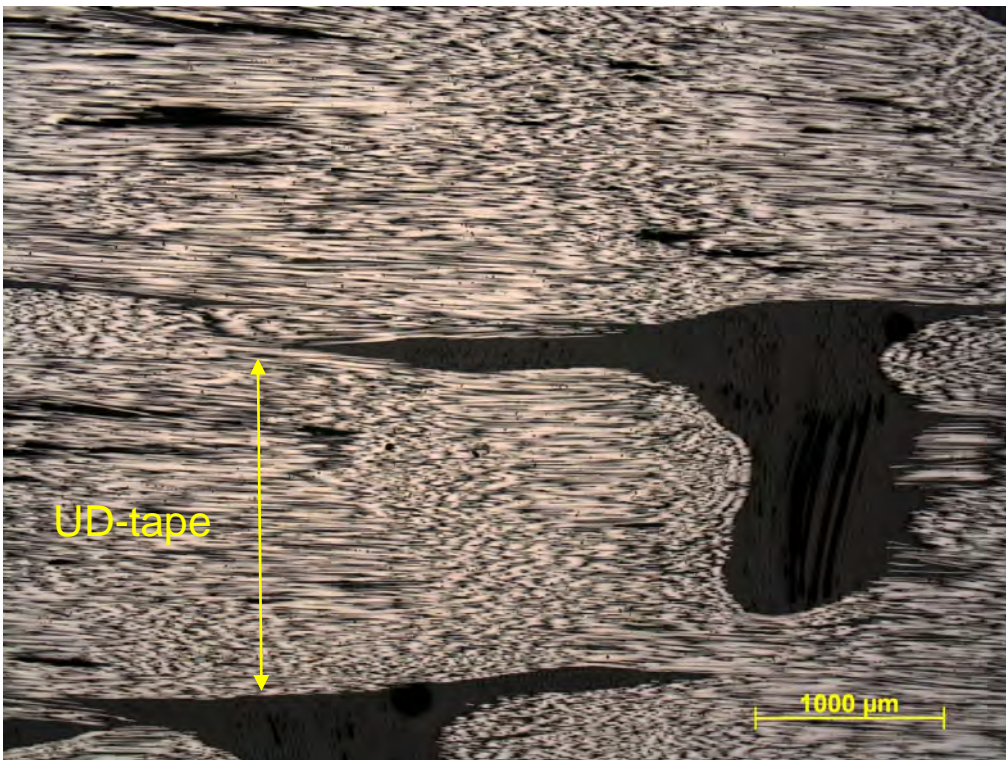
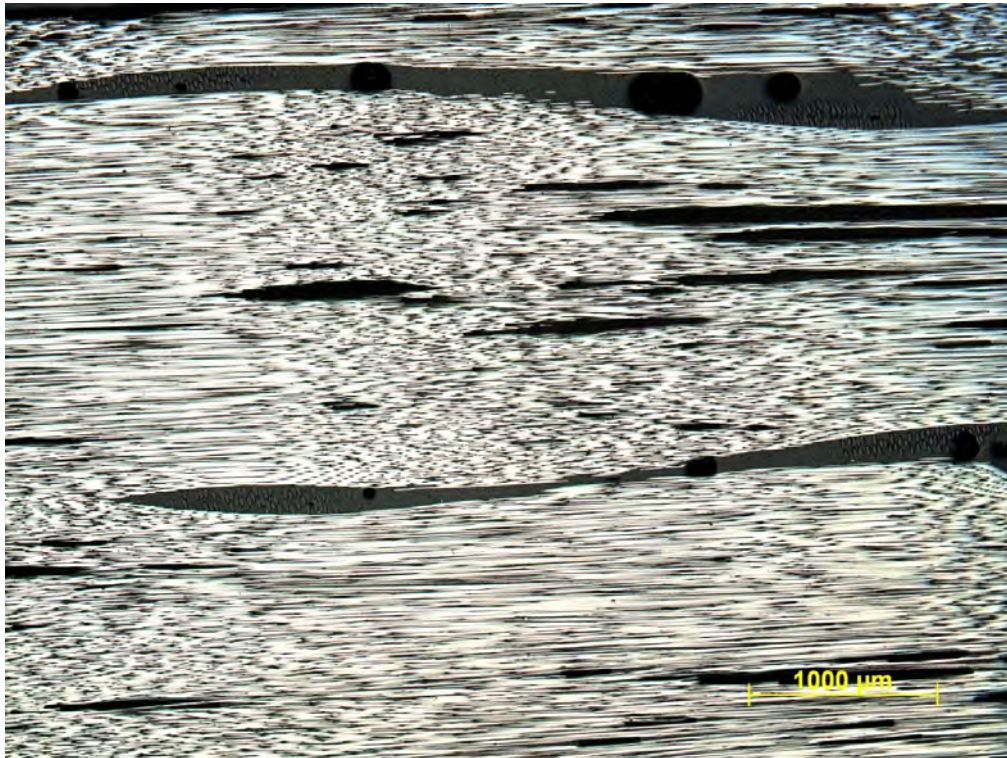**Fig. 79: Top section of a Hex/HTS5631/UD/3bar/6 laminate showing a view perpendicular to the textile surface. Waviness of the UD tape associated to a huge resin nest, with PES support fibres embedded in it is highlighted.**
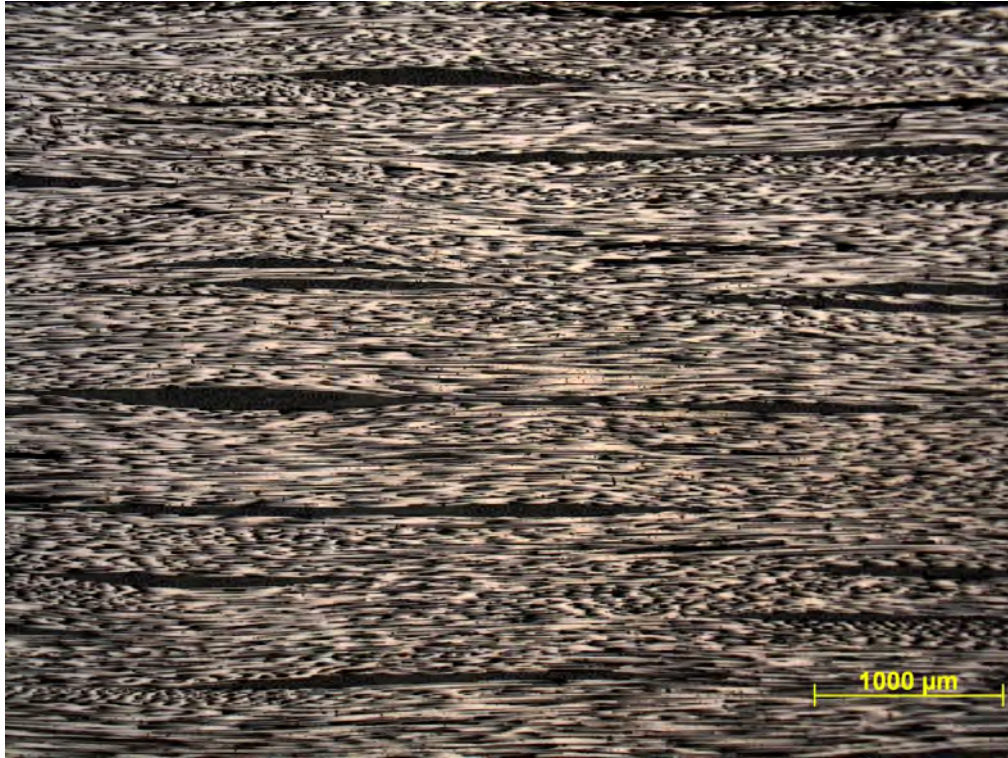
**Fig. 80: Longitudinal section of a Hex/HTS5631/UD/3bar/6 laminate. Waviness and longitudinal pores are observed. Each different ply can be recognised due to the matrix-rich regions between them, as it was observed for the corresponding laminates cured at a lower pressure.**

Fig. 81: Cross section of a Hex/HTS5631/UD/3bar/6 laminate. The laminates cured at 3 bar contain less and smaller pores than the ones cured at 1 bar. Both exhibit matrix-rich areas between textile layers. The bundle structure of the carbon-textiles can be recognized. The larger pores are in the laminates centre.

5.1.2 Pultruded profiles

In the following subchapters the features observed for the different studied pultruded profiles are highlighted and indicated in the corresponding figure caption. First the LOM micrographs followed by SEM pictures.

5.1.2.1 *Pultruded profile T/L20-T/HTSTS/UD65f*

<u>Light optical micrographs:</u>

At high magnifications (x1000) mineral filler particles are visible, as shown in Fig. 82.
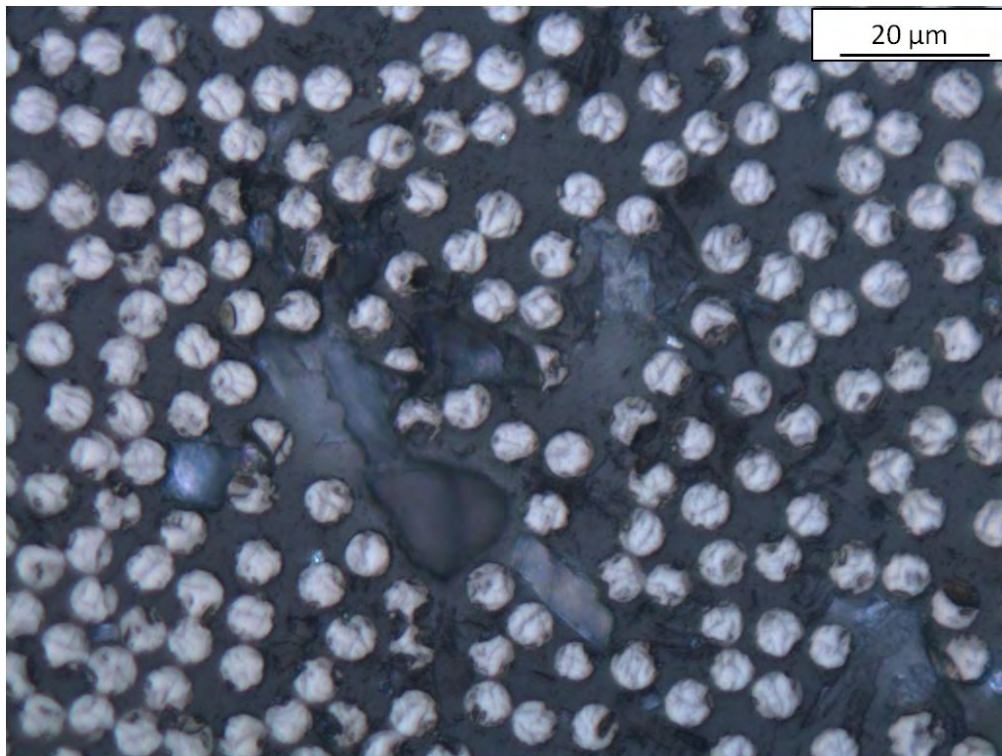
Fig. 82: Cross section of a T/L20-T/HTSTS/UD65f pultruded tube. Mineral filler particles embedded in the epoxy resin and porosity associated to them is observed. The cross section of the fibres is circular indicating UD reinforcement.

Fig. 83 presents a panorama picture obtained by combining four single micrographs. This way the whole wall thickness of a pultruded tube in cross section can be observed. In general, an homogeneous distribution of fibres within the cross section is observed. Although, clusters of touching fibres are found scattered over the whole imaged surface The porosity (dark regions) tends to accumulate in the centre, pores are present mainly in matrix-rich regions.
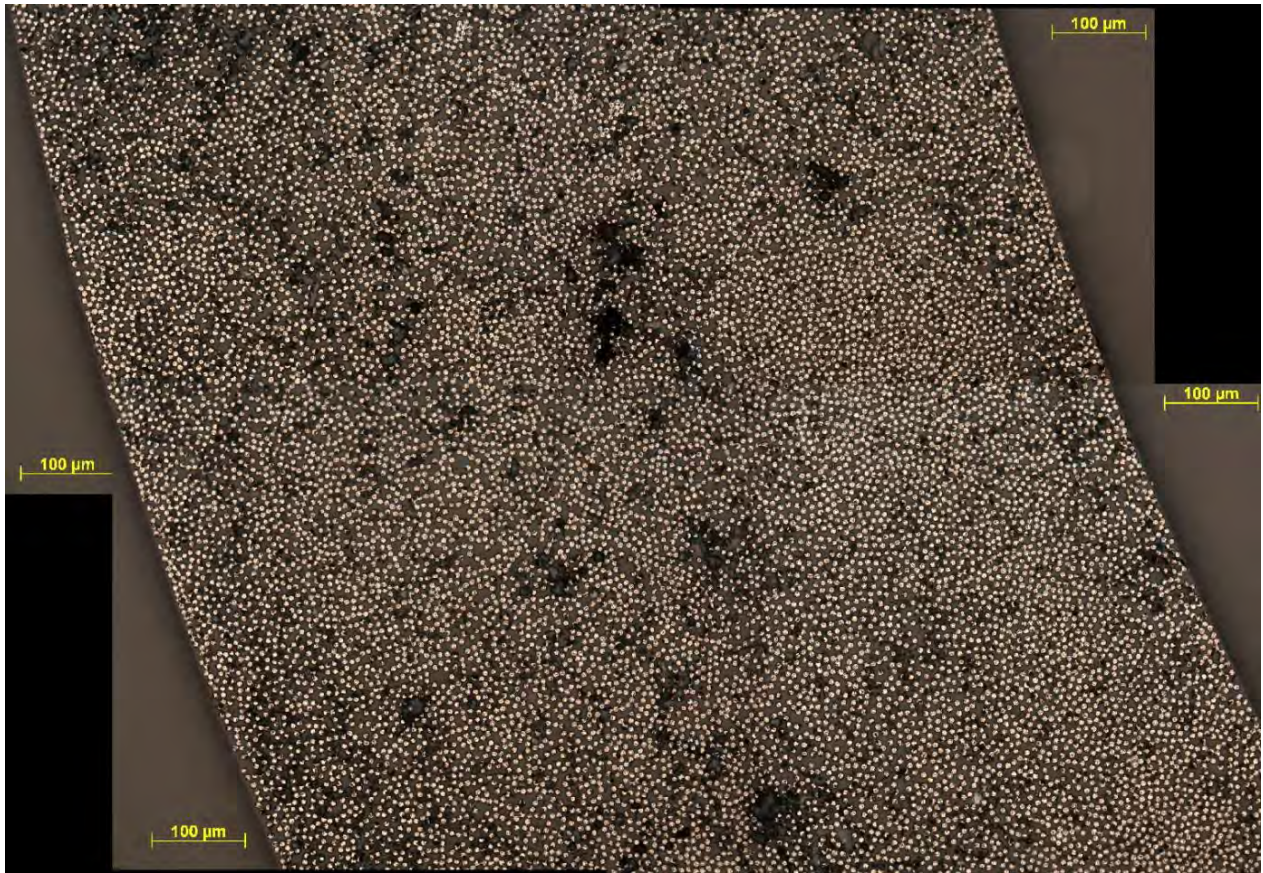
Fig. 83: Cross section panorama of a T/L20-T/HTSTS/UD65f pultruded tube. Dark areas correspond to porosity and filler particle agglomerations. The distribution of the reinforcement is not perfectly homogeneous, touching fibres as well as some matrix-rich regions containing porosity are observed.

On scanning electron micrographs with secondary electron detector (SE), the contrast between mineral filler particles containing heavy atoms in comparison to epoxy and C-fibres is very high. It is also sufficient to distinguish fibre from surrounding matrix. Filler particle size being mostly under 8μm, with some seldom large ones ~40μm. The distribution is very inhomogenous, tending to form agglomerations ($V_{agg} < 120000$ μm^3) as shown in Fig. 85. EDS analysis on some particles yielded the following elements: C, O, Na, Mg, Al, Si, Ca. Such chemical composition corresponds to aluminosilicates, minerals such as clay or talc.
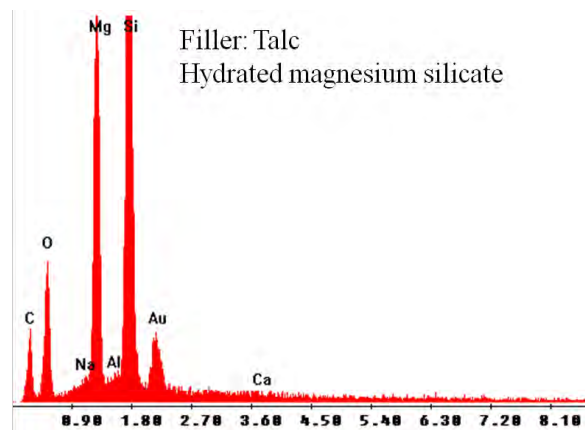
Fig. 84: EDS analysis result for a particle from Fig. 86. The volume fraction of the filler particles was between 2 - 2.5 vol.% (obtained from TGA analysis, see section 5.3.1.)

75
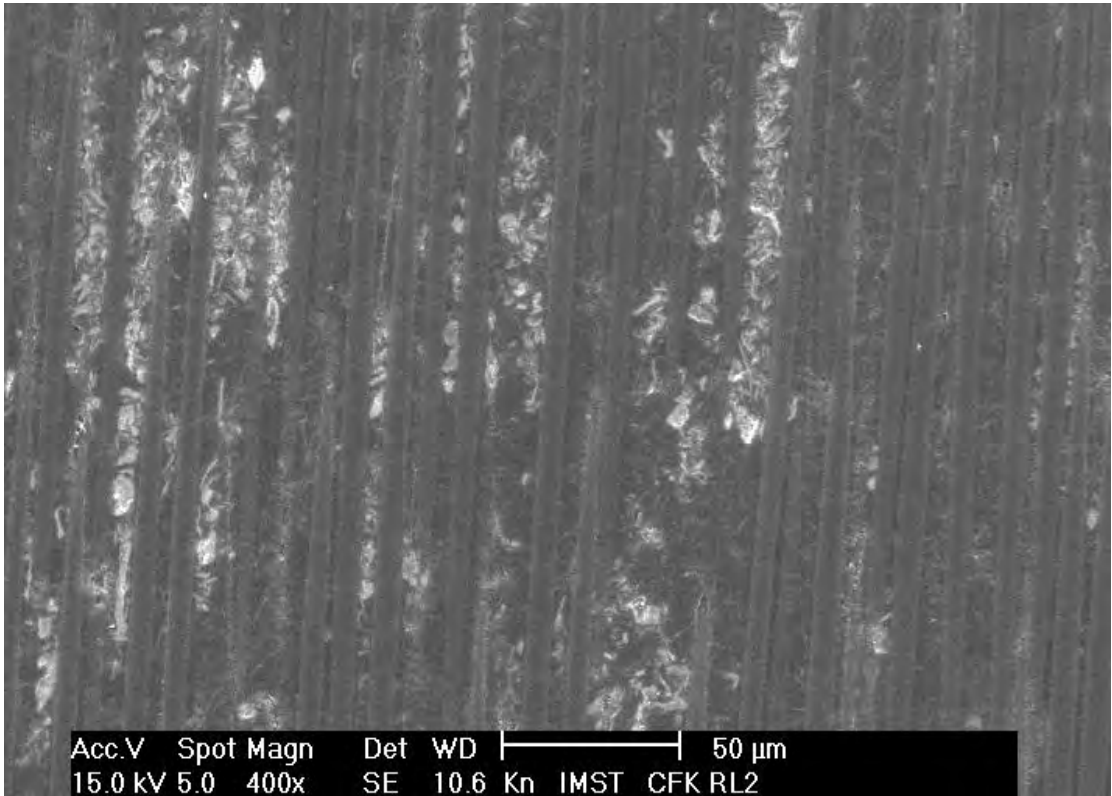
Fig. 85: Longitudinal section of a T/L20-T/HTSTS/UD65f pultruded tube. Filler particle agglomerations.
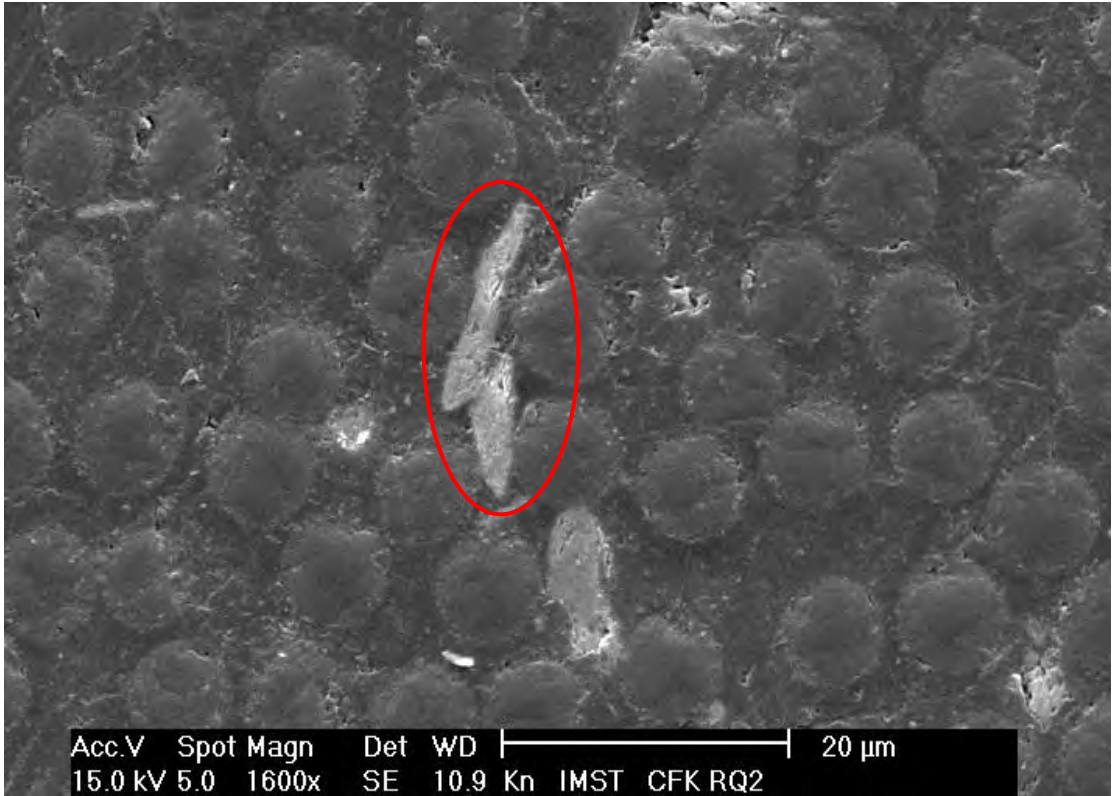
Fig. 86: Cross section of a T/L20-T/HTSTS/UD65f pultruded tube. Filler particles contain heavy elements and therefore exhibit a higher contrast. EDS was carried out for the marked particle (see Fig. 84).

5.1.2.2 *Pultruded profile R/L20-T/HTSTS/UD65f*

Light optical micrographs:
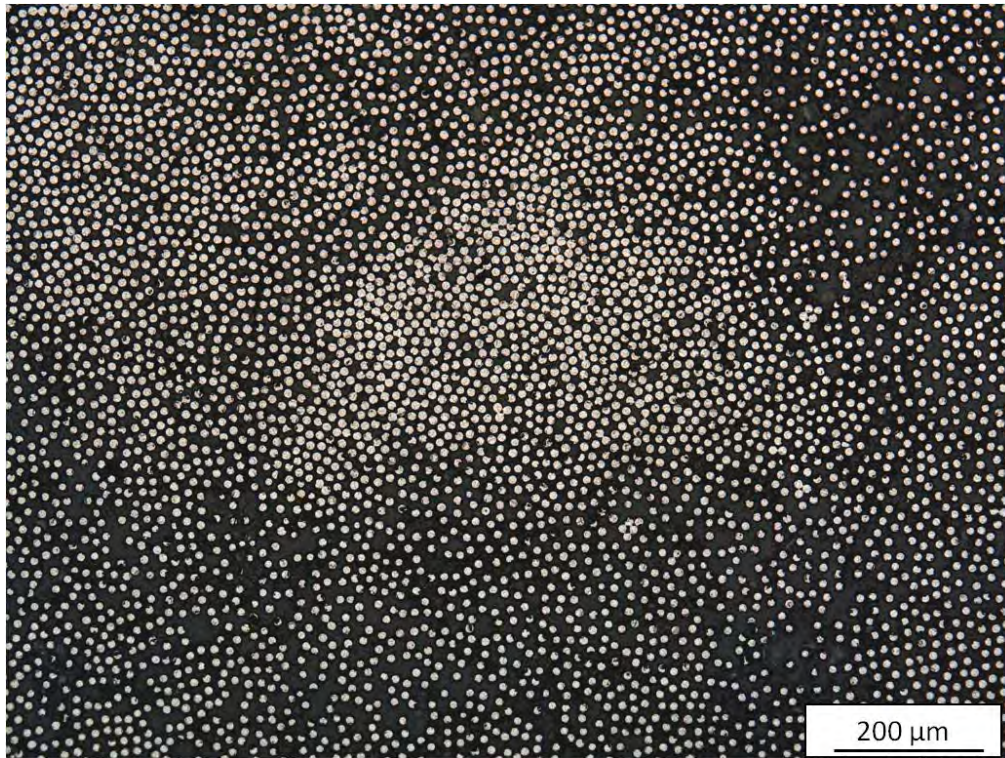
Fig. 87: Cross section of a R/L20-T/HTSTS/UD65f pultruded rod. Inhomogeneous fibre distribution. Clusters of up to five touching fibres can be observed.
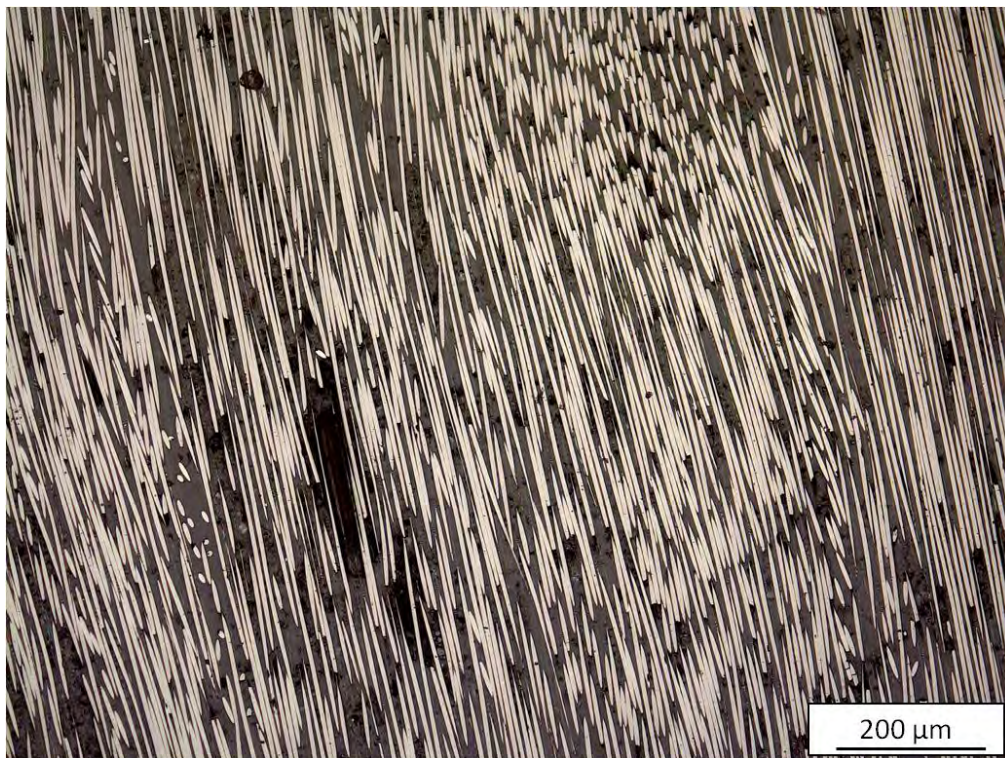
Fig. 88: Longitudinal section of a R/L20-T/HTSTS/UD65f pultruded rod. Fibre waviness and elongated porosity are observed. High resin content in areas with the highest fibre misorientation.

Secondary electron and back scatter electron scanning electron micrographs:
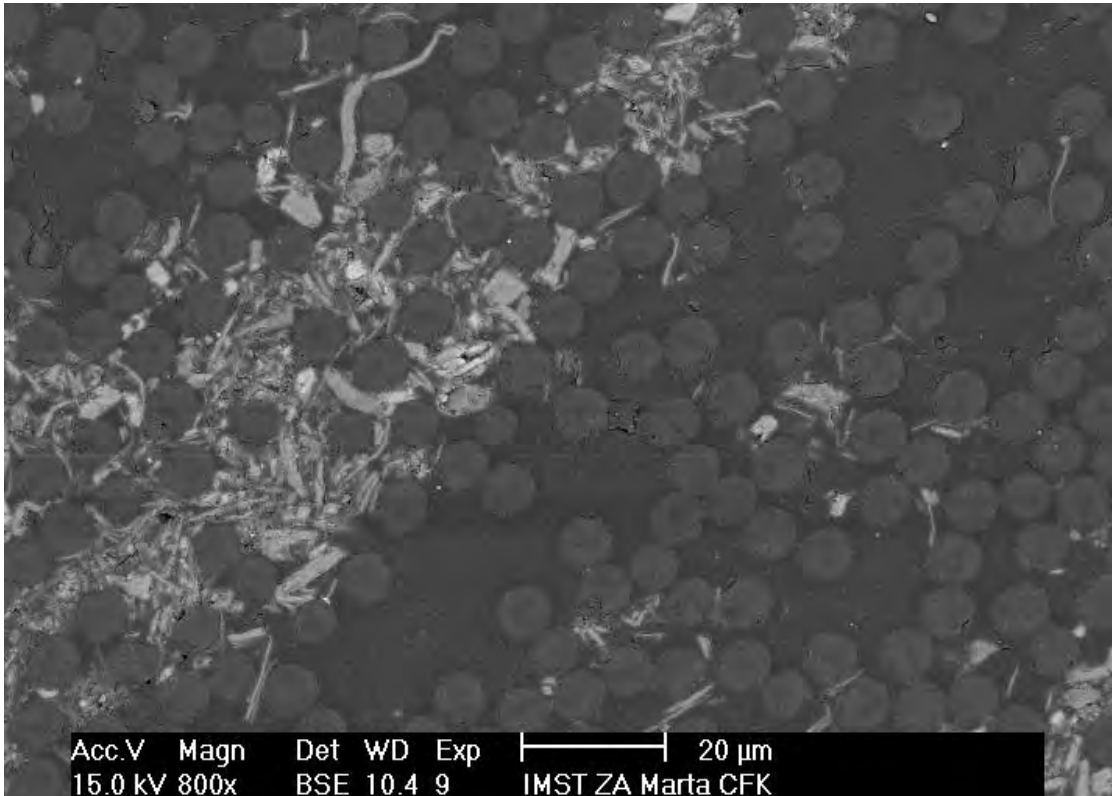
Fig. 89: Cross section of a R/L20-T/HTSTS/UD65f pultruded rod. Back scatter electron detector. Cracks within the matrix and microporosity as well as fibre contours are clearly recognizable.
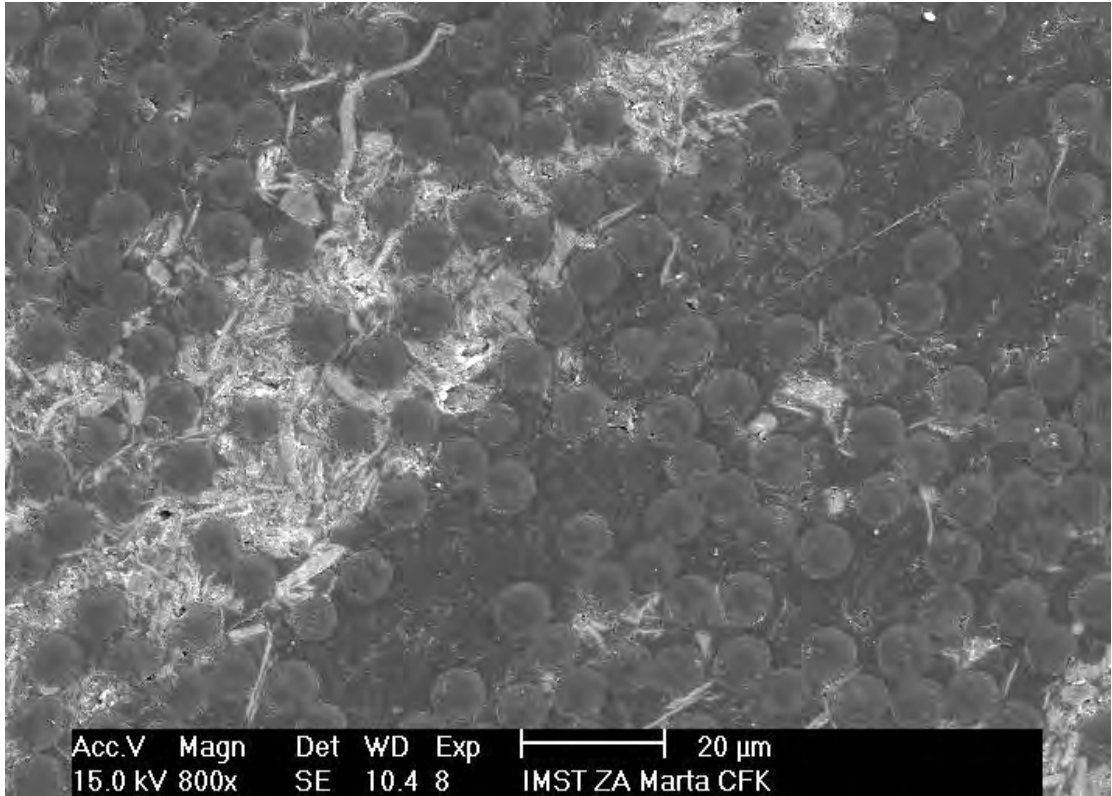
Fig. 90. Cross section of a R/L20-T/HTSTS/UD65f pultruded rod. Secondary electron detector. Higher contrast of the filler particles is achieved. Topographic features are better imaged with this detector.

78

5.1.2.3 *Pultruded profile R/Sika/Sigrafil-T700SC/UD65f*

<u>Light optical micrographs:</u>

Fig. 91: LOM Overall cross section panorama of a R/Sika/Sigrafil-T700SC/UD65f pultruded rod polished. Diameter 10 mm. Matrix rich regions, different fibre tows, two fibre types (sigrafil and T700SC) can be recognised.

These materials exhibit characteristic features of pultruded profiles, e.g. a very low porosity content. According to literature [15] [16], a high degree of reinforcement alignment should be expected due to pultrusion, instead a high degree or waviness and fibre misalignment was observed. Another unusual feature of these pultruded rods is the combination of fibre rovings with different cross section shape, namely circular and kidney-like fibres in the same profile.

On high magnification SEM pictures porosity can be observed. For the studied specimen a pore with a diameter of ~ 80 µm (Fig. 95) as well as some scattered pores with a very small diameter (Fig. 96) were observed. Fibre-matrix debondig and micro cracks are shown in Fig. 97. This could be a consequence of the materialographic preparation, but it has only been observed on these samples, so it could also be a defect already present in the profiles.
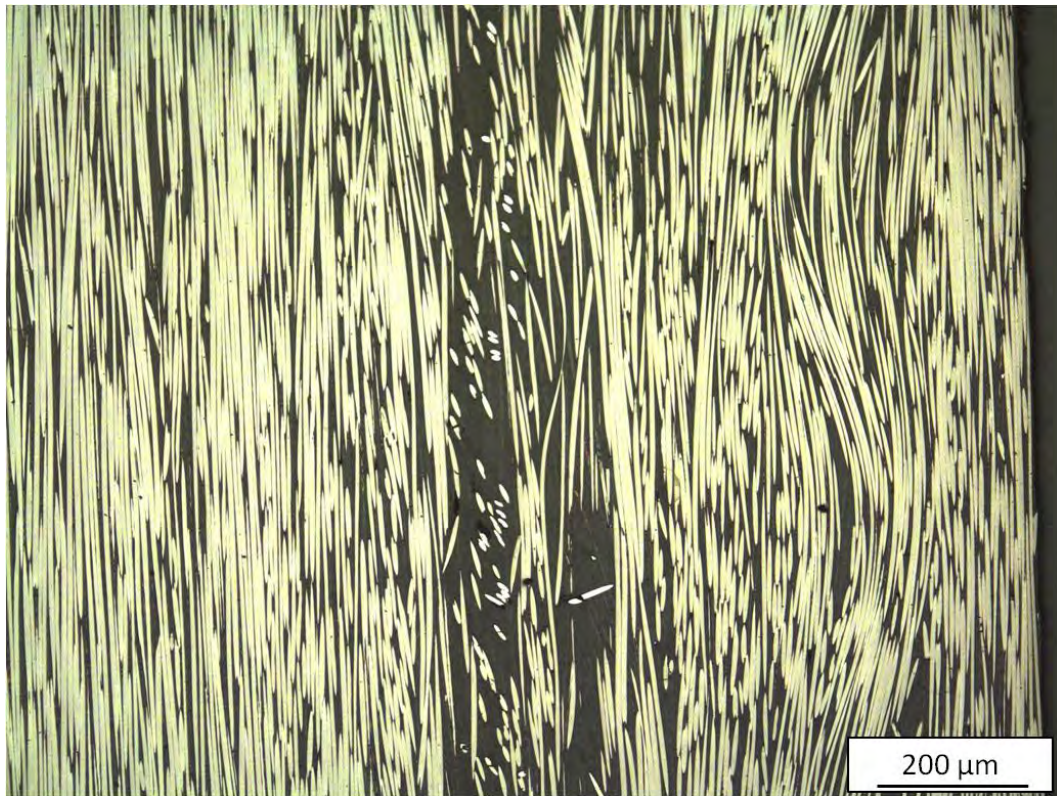
Fig. 92: Longitudinal section of a R/Sika/Sigrafil-T700SC/UD65f pultruded rod. High fibre misalignment degree near the surface of the rod is found, where most of the matrix-rich areas are observed.
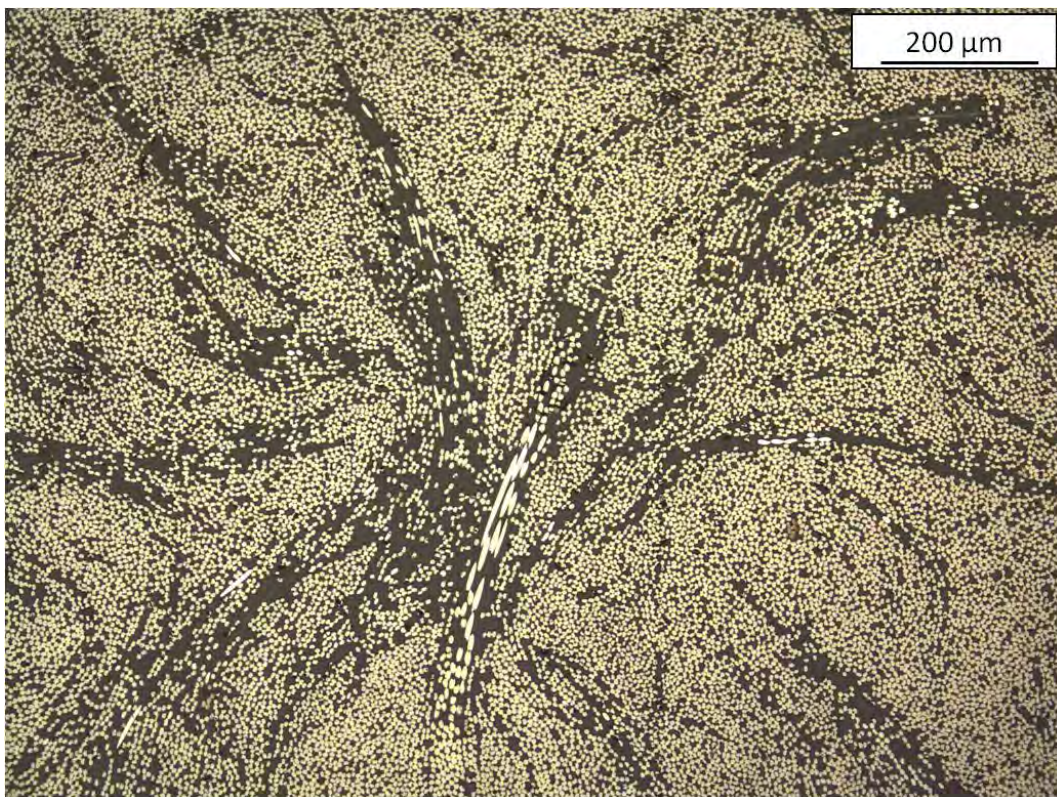
Fig. 93: Cross section of a R/Sika/Sigrafil-T700SC/UD65f pultruded rod. Misaligned fibres in matrix-rich regions. An inhomogeneous distribution of the reinforcement is observed, with the highest fibre volume fractions in the centre of the rods.

80
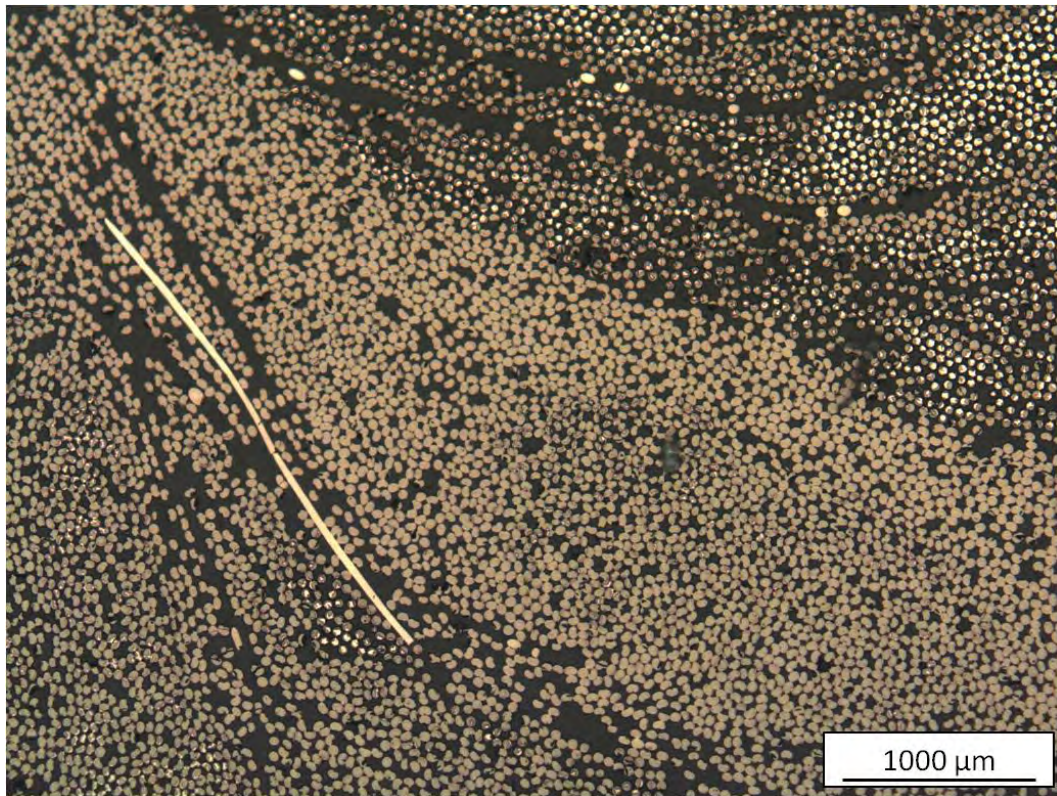
Fig. 94: Cross section of a R/Sika/Sigrafil-T700SC/UD65f pultruded rod showing two different fibre tows (circular and bean-shaped fibre cross sections). Misaligned fibres can be seen within matrix channels.

Secondary electron scanning electron micrographs:
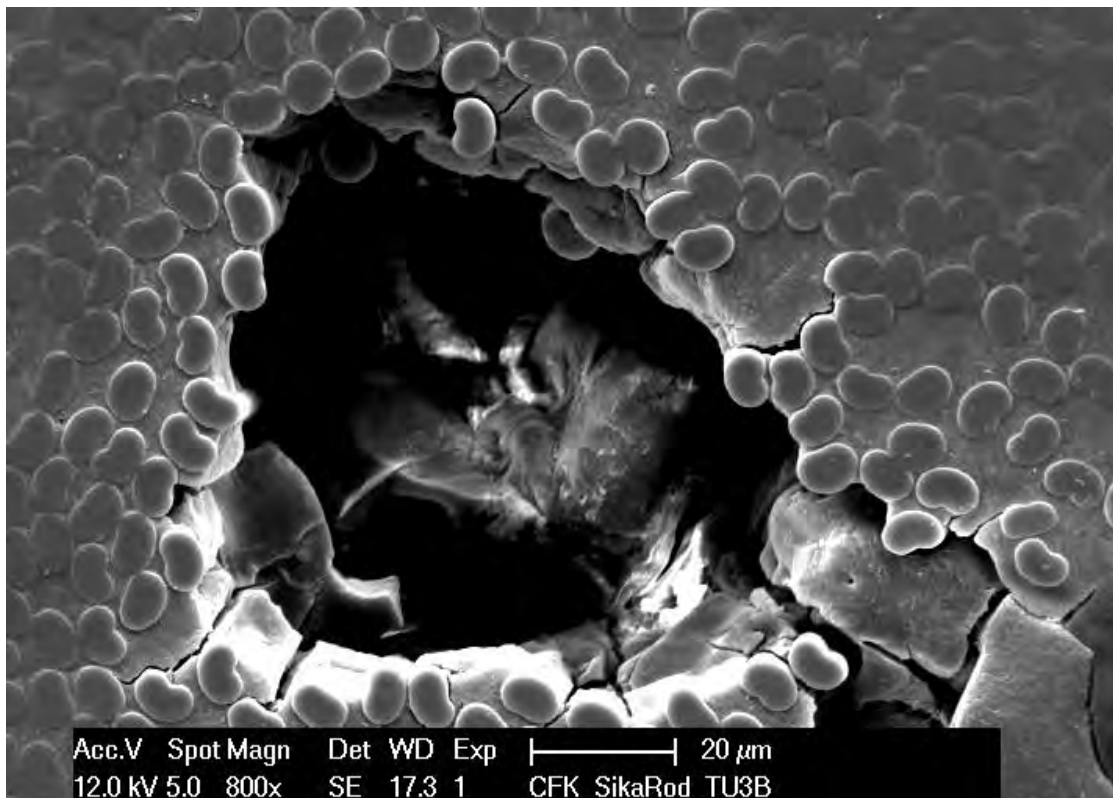
Fig. 95: Cross section of a R/Sika/Sigrafil-T700SC/UD65f pultruded rod polished and gold sputted sample. Zoom on a pore, perpendicular cracks and the inner surface of the matrix within the pore are observed.
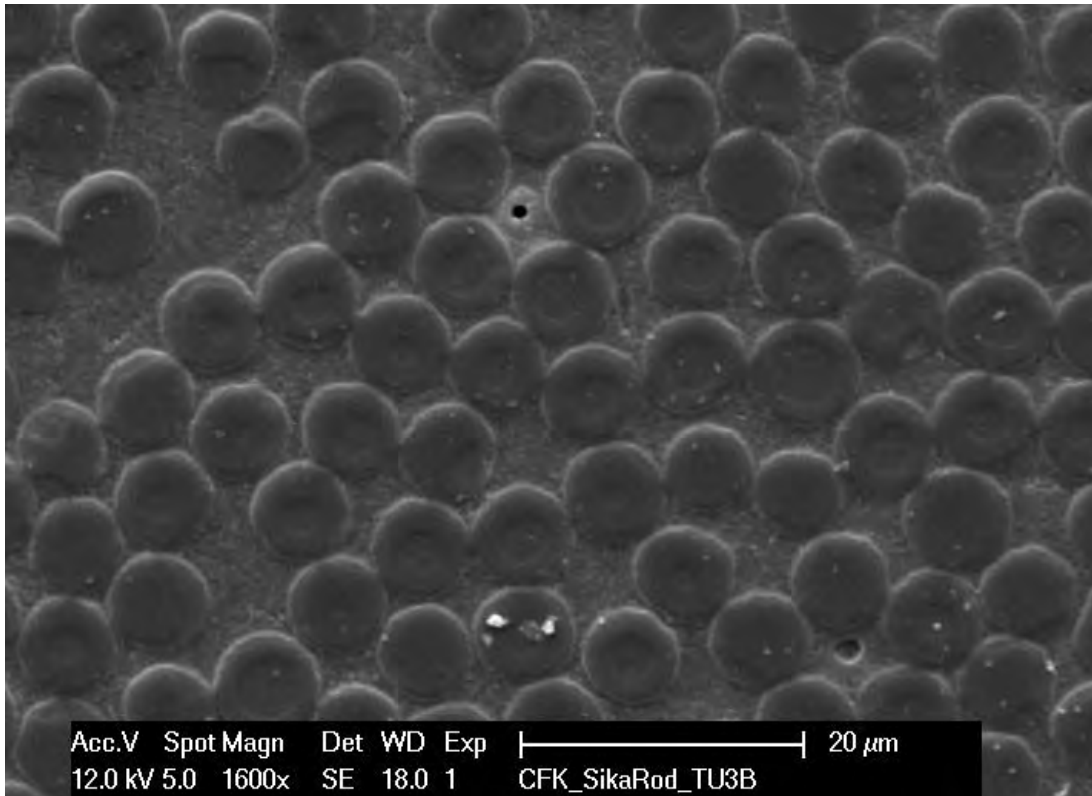
Fig. 96: Cross section of a R/Sika/Sigrafil-T700SC/UD65f pultruded rod polished and gold sputted sample. Very small pores with a diameter about 1µm can only be observed with SEM microscopy.
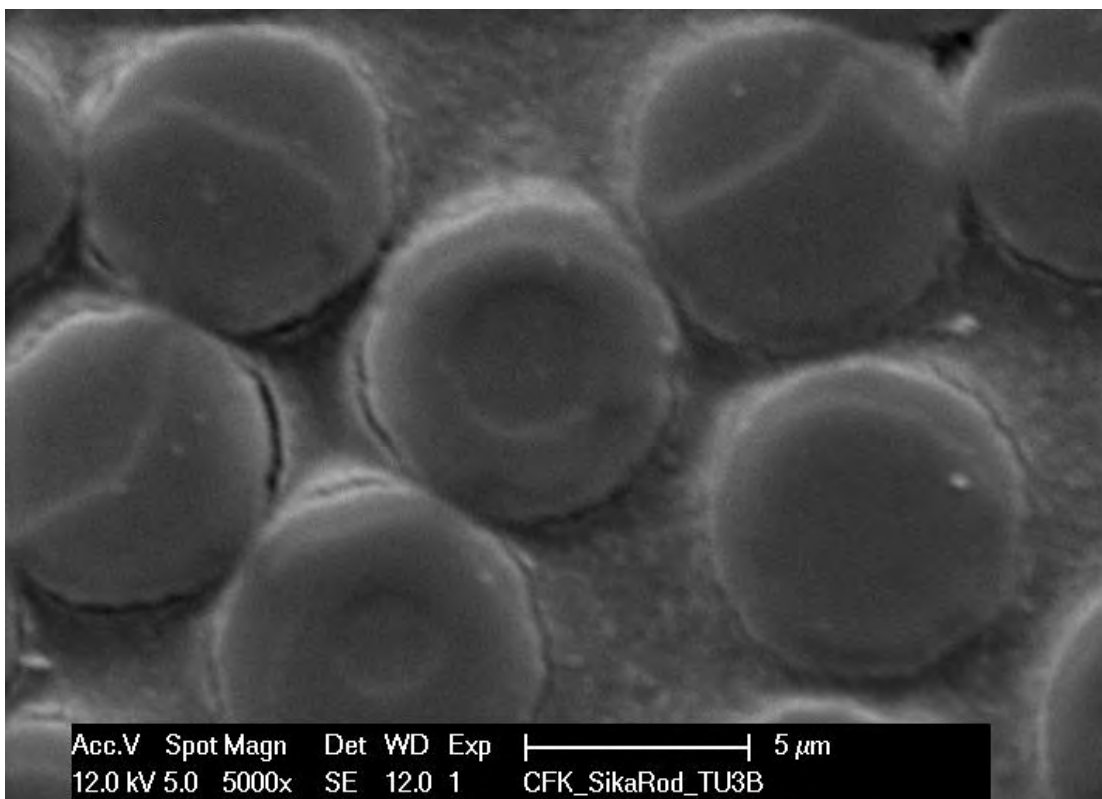
Fig. 97: Cross section of a R/Sika/Sigrafil-T700SC/UD65f pultruded rod polished and gold sputted sample. Fibre matrix debonding is observed at the interface between both components.

5.2 Materialography 3D

The following techniques were applied for 3D visualisation and characterisation:

- LOM cube: micrographs of all sides
- XCT: X-ray computed tomography
- SCT: high resolution synchrotron microtomography

5.2.1 Laminates

5.2.1.1 *Laminates HexPly8552/HSAS4/UD58f/0.2MPa/1*

Imaged in 3D by means of XCT:

Porosity segmentation by means of grey value thresholding up to a certain pore size limit (determined by the voxel size of the actual measurement) is possible due to the high contrast between air and the rest of the components present in the material. To distinguish between matrix and fibres is more complicated since both are C-based substances and have a very similar absorption coefficient (i.e. grey values).

Fig. 98 shows axial and transversal views of the laminates obtained from XCT scans; Fig. 99 shows segmented porosity in red, channel like pores along fibre direction and smaller spherical pores can be observed. The volume fraction of porosity found was 2.7 vol.%.
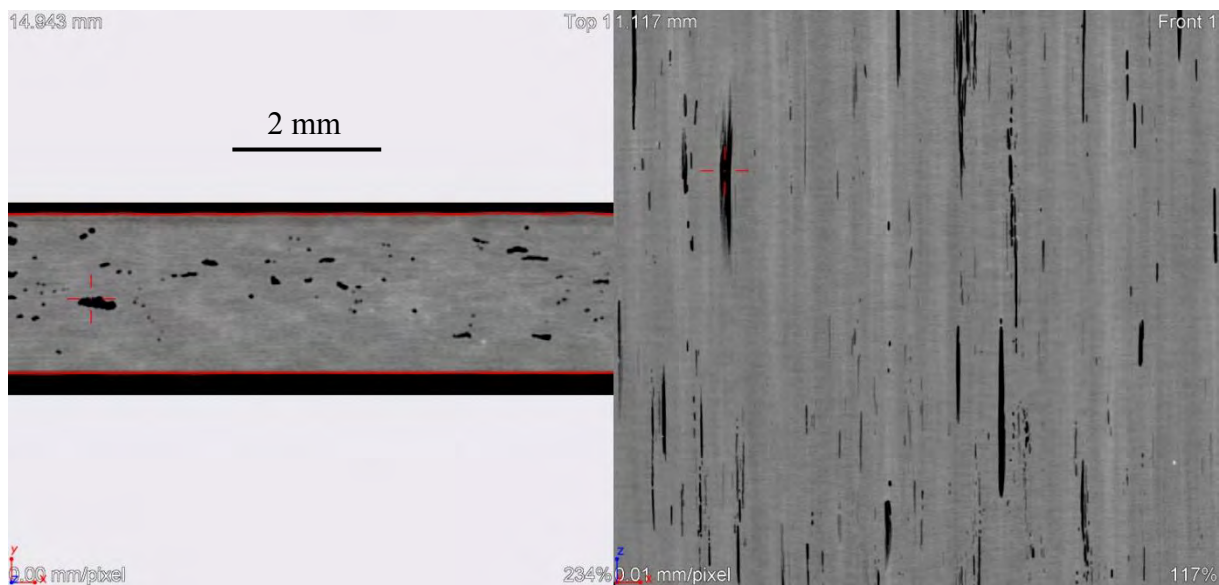
Fig. 98: Axial (left) and transversal (right) XCT slice images of a HexPly8552/HSAS4/UD58f/0.2MPa laminate. Pores are black, the grey areas correspond to matrix and fibre, which cannot be distinguished from each other. It is observed that most of the pores are elongated, particularly the large ones, whilst spherical smaller pores are formed rarely.
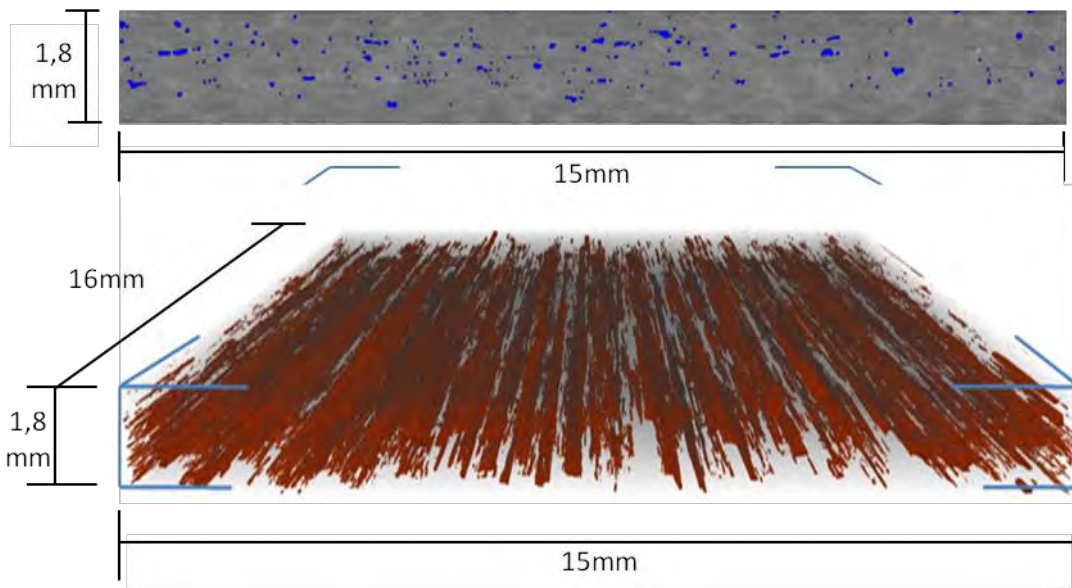
Fig. 99: Top: XCT axial slice of a HexPly8552/HSAS4/UD58f/0.2MPa/1 laminate showing segmented pores (blue). Bottom: 3D view of segmented porosity (red) within the whole scanned volume revealing channel like shape of the pores, going through the whole length of the studied specimen parallel to fibre direction. Voxel size of (11 μm)³.

5.2.1.2 *Laminates HexPly8552/HSAS4/UD58f/0.2MPa/2*

Imaged in 3D by means of XCT:

Fig. 110 shows segmented porosity in red, channel like pores along fibre direction and smaller spherical pores can be observed. The volume fraction of porosity found was 1.1 vol.%.
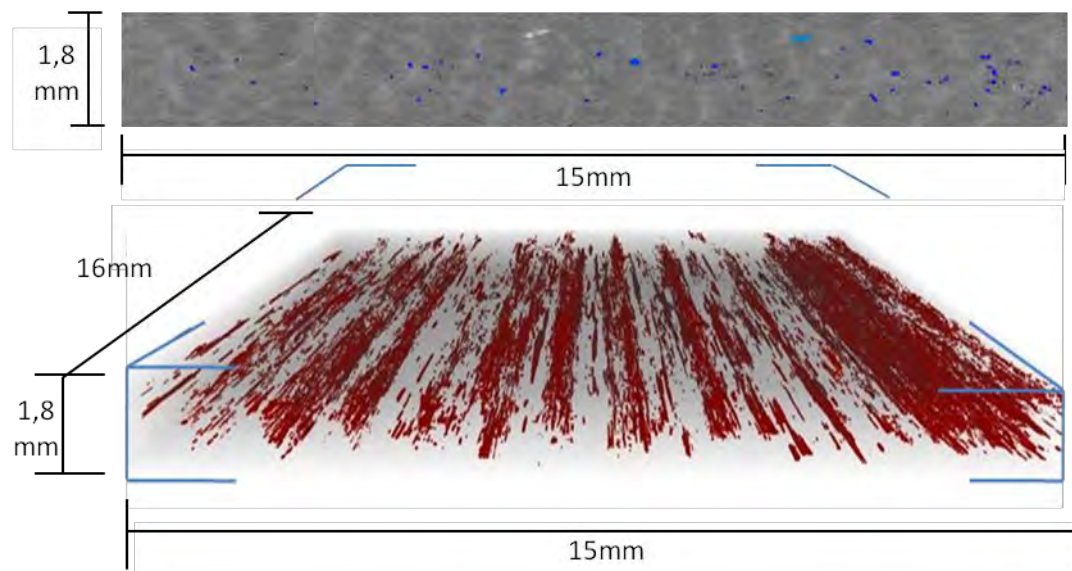
Fig. 100: Top: XCT axial slice of a HexPly8552/HSAS4/UD58f/0.2MPa/2 laminate showing segmented pores (blue). Bottom: 3D view of segmented porosity (red) within the whole scanned volume revealing channel like shape of the pores, going through the whole length of the studied specimen parallel to fibre direction. Voxel size of (11 μm)³.

5.2.1.3 *Laminates HexPly8552/HSAS4/± 45-58f/0.2MPa/2*

<u>Imaged by means of SCT:</u> Voxel size (1.4 µm)³. 2D slices (Fig. 101) and 3D view (Fig. 102).
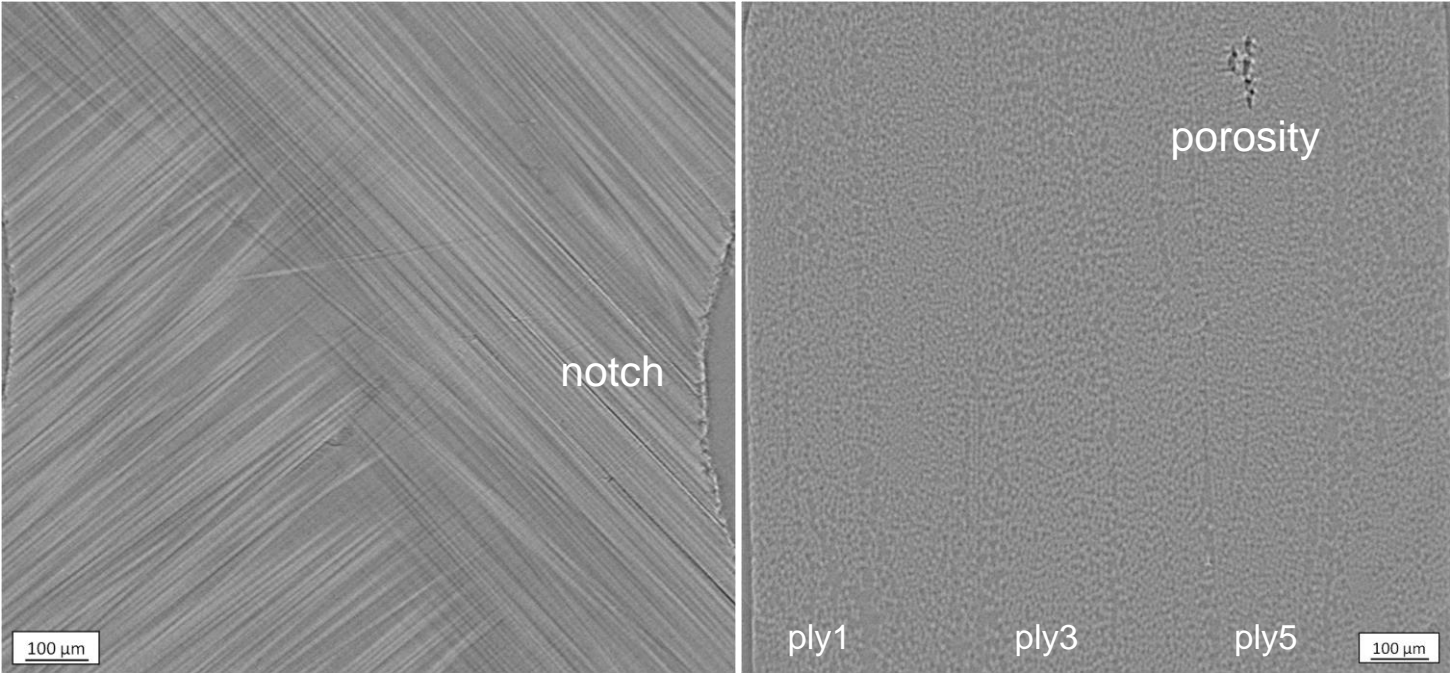
Fig. 101: SCT YZ and XY slices of the laminate. YZ slice at the interface between two plies with +45° and -45° fibre direction, fibre misalignment is observed. XY slice, all plies are visible, and porosity in ply 5.
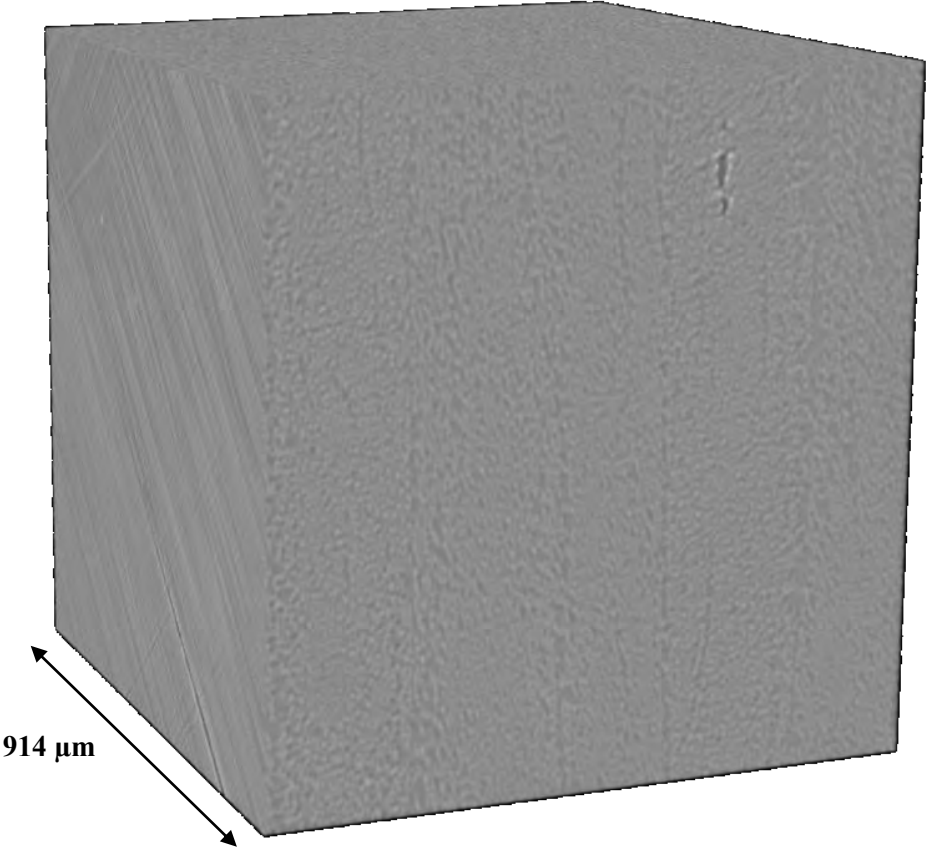
Fig. 102: 3D view. Volume size: (925x950x914) µm³. Voxel size of (1.4 µm)³.

5.2.1.4 *Laminates Sik/FT300B/0-90°/1bar/3*

In an attempt to obtain a 3D view of these materials, cubes were created using light optical micrographs of all 3 sides of the laminates:

1: Cross section perpendicular to fibre direction (in case of UD samples)

2: Longitudinal section in fibre direction

3: Perpendicular to textile surface
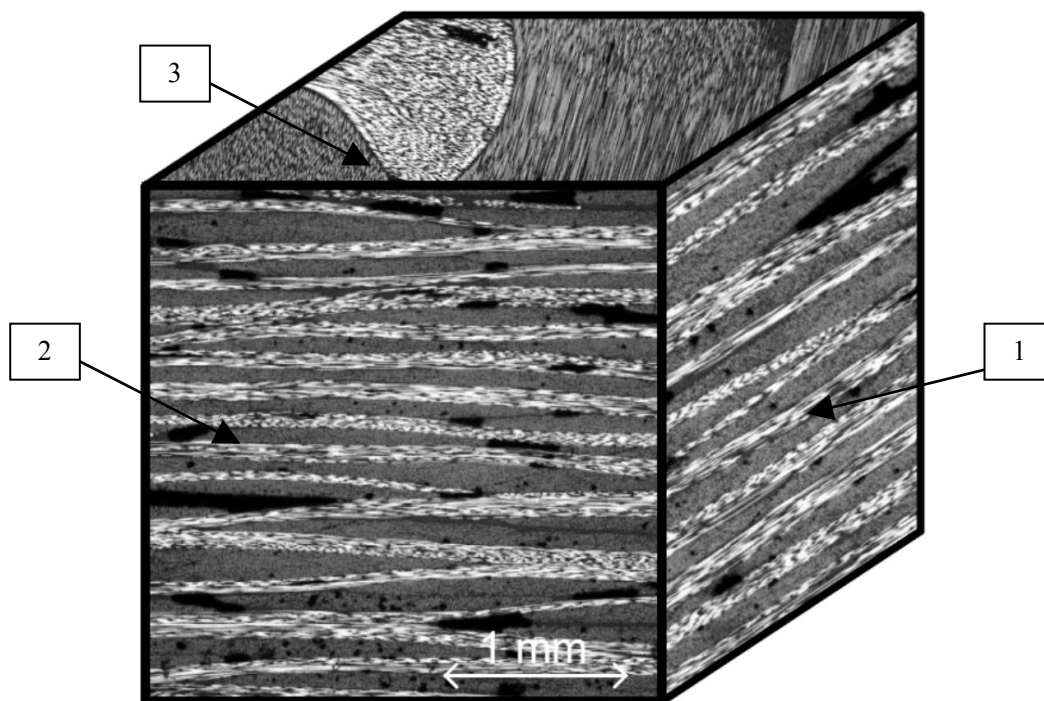
Fig. 103: Cube made with LOM micrographs showing all three sides of the Sik/FT300B/0-90°/1bar/3 laminate using the same magnification. The 0°/90° disposition of the fibres in the textile is clearly seen as alternated layers of longitudinal and cross sectional fibre views on both sides 1 and 2.

The same visualisation technique was applied on the other three UD laminates produced with the same epoxy matrix Sika CR133. The results are shown in the next sections 5.2.1.5 to 5.2.1.7. The side 1 of all UD materials exhibit matrix rich regions between stacked layers and different degrees of porosity. The side 2 contains elongated pores in all three materials. The side 3 looks different for each laminate, depending on the kind of textile used. The same UD-bands were used to manufacture Sik/HTS5631/UD/1bar/4 and Sik/HTS5631/UD/3bar/4, but since the pressure on the second one was higher, the packing of the plies is more compact.

5.2.1.5 *Laminates Sik/HTA40/UD/1bar/3*
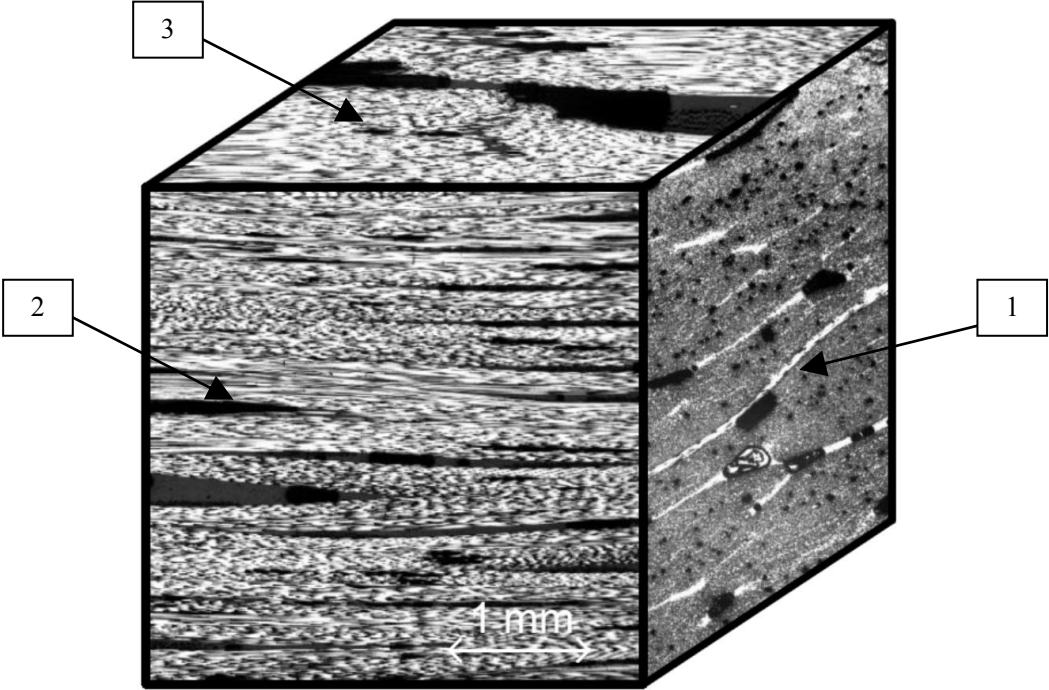
Fig. 104: Cube made with LOM micrographs showing all three sides of the laminate using the same magnification.

5.2.1.6 *Laminates Sik/HTS5631/UD/1bar/3*
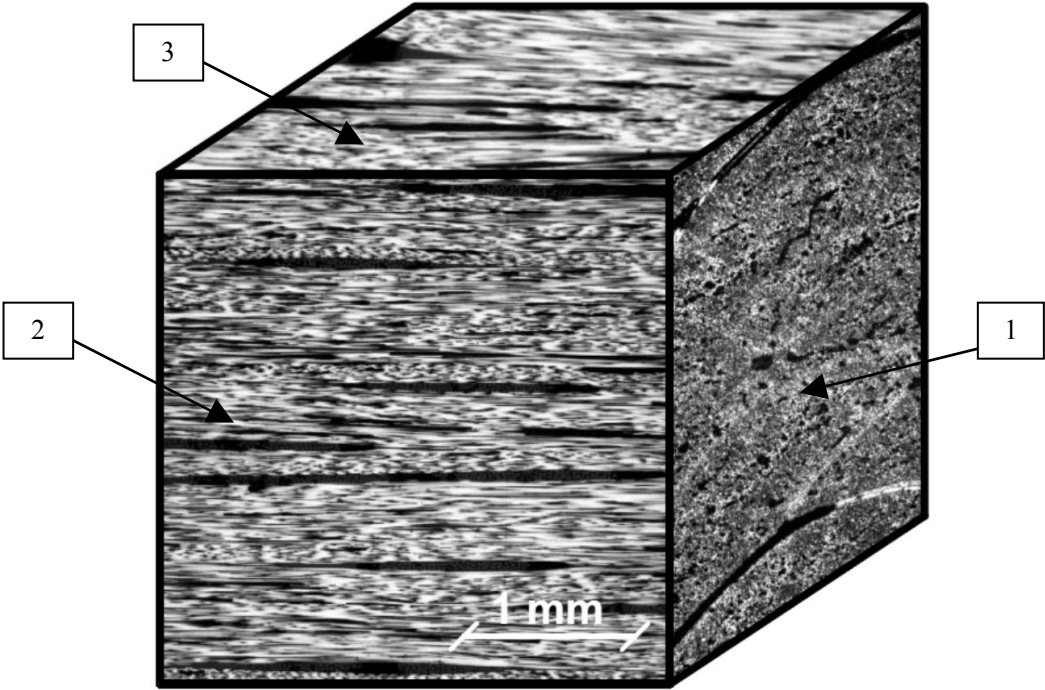
Fig. 105: Cube made with LOM micrographs showing all three sides of the laminate using the same magnification.

5.2.1.7 *Laminates Sik/HTS5631/UD/3bar/4*
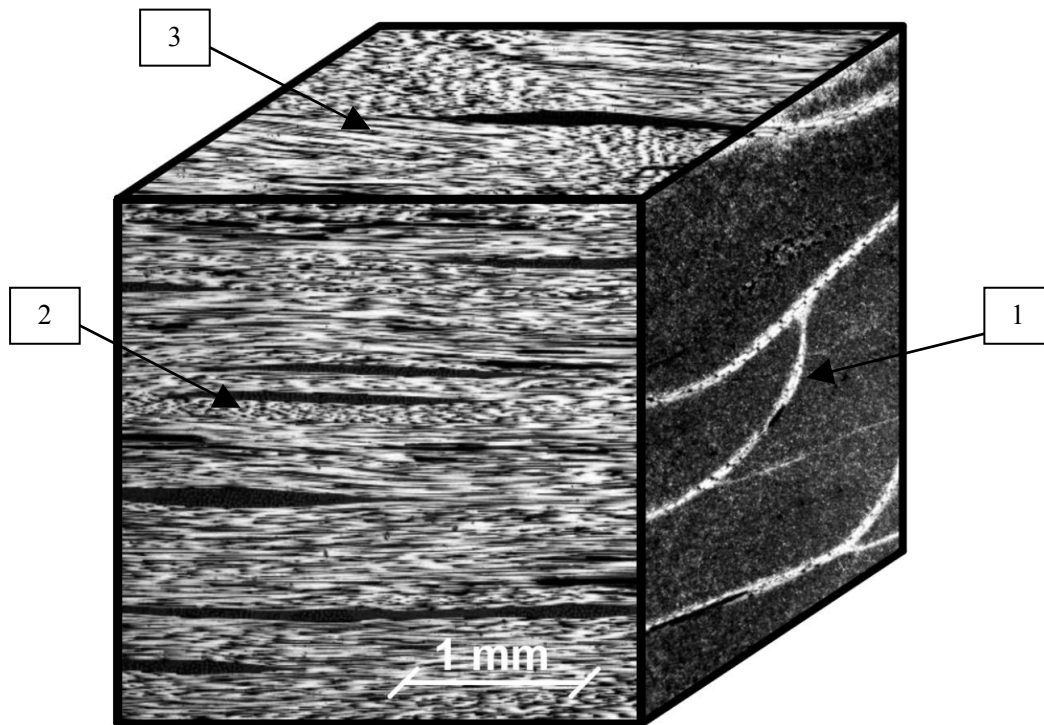
Fig. 106: Cube made with LOM micrographs showing all three sides of the laminate using the same magnification.

These laminates were also imaged in 3D by means of XCT. Segmentation of interesting features was applied to the scanned volumes yielding three dimensional views of porosity distribution as well as the waviness of the bundles structure. The results are shown in Fig. 107 and Fig. 108. The size of the visualized volume is indicated in the caption of each picture.
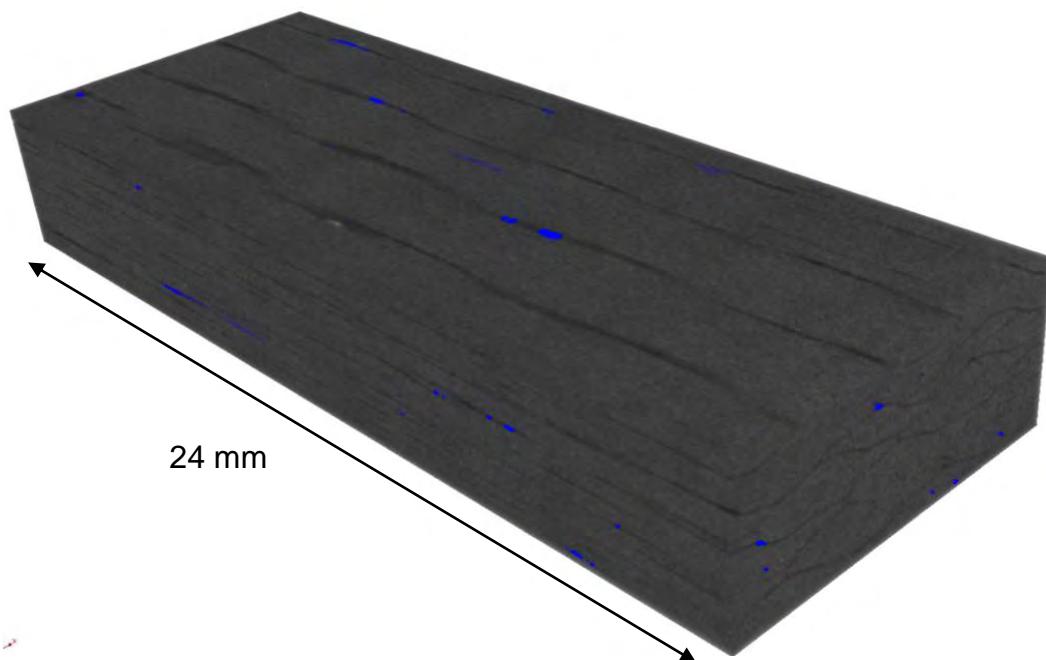
Fig. 107: XCT scanned volume of a laminate imaged in 3D. Grey values correspond to different densities. Porosity is highlighted in blue. Volume size is: 9mm×3.7mm×24mm. Voxel size of (16 µm)³.
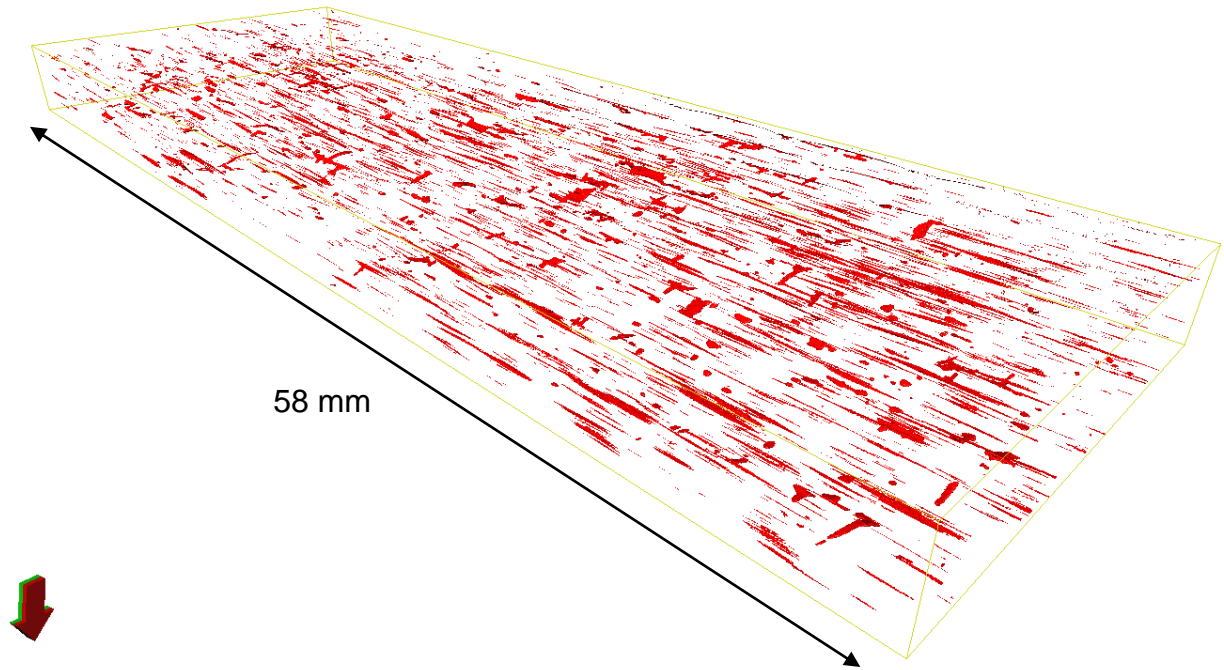
Fig. 108: XCT scanned volume of a laminate; segmented porosity is shown in red, matrix and fibres are transparent. Volume size: 20mm×4mm×58mm. Voxel size of (16 µm)³. Porosity fraction: 0.3 vol.%.

A small cut-out section of the laminate imaged using XCT in Fig. 107 and Fig. 108 was also imaged in 3D by means of LOT serial sectioning. Fibres and porosity were segmented (see Fig. 109). Fibre orientation analysis yielded a high degree of UD fibre alignment.
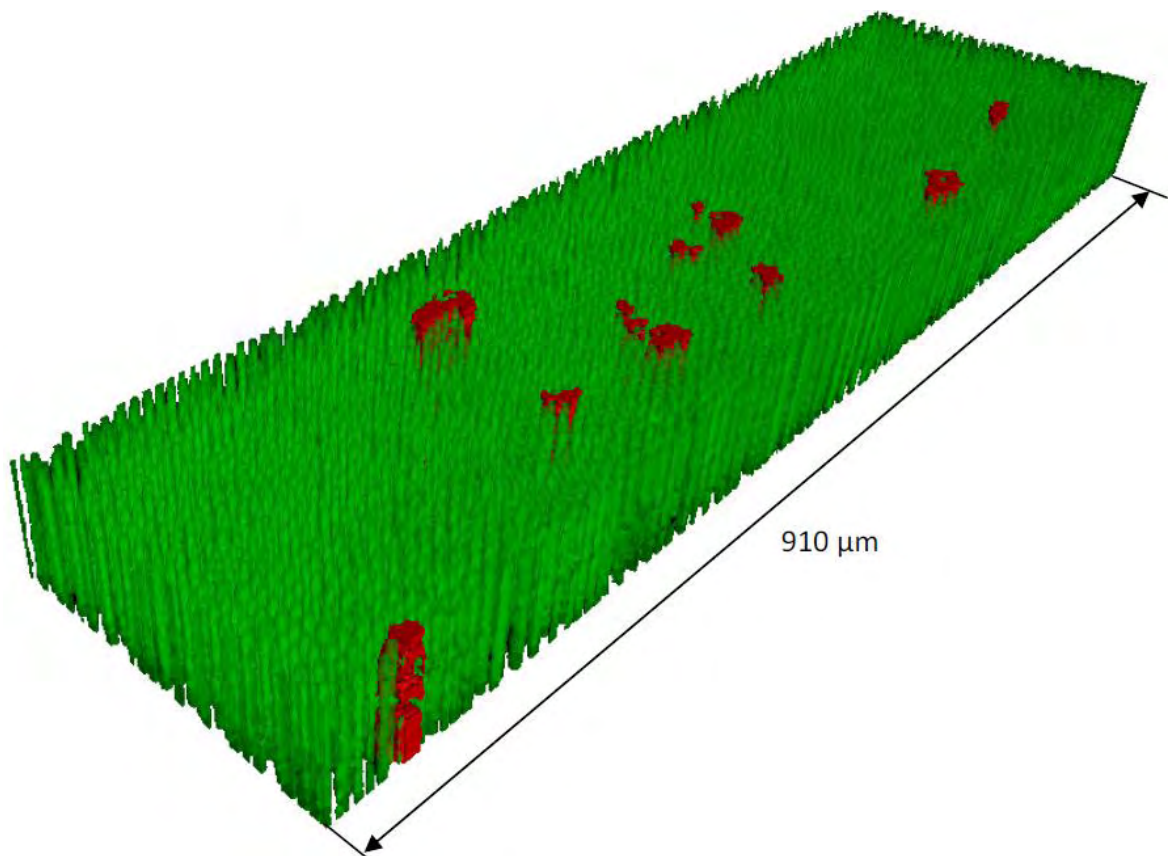
Fig. 109: Volume obtained with LOT. Segmented fibres are green, the porosity is shown in red and the matrix is transparent. Volume size: (910×187×80) µm³. Voxel size of (0.6×0.6×4 µm)³.

5.2.2 Pultruded profiles

5.2.2.1 *Pultruded profile T/L20-T/HTSTS/UD65f*

Slice images of a cut-out volume of approximately $(2.8 \times 1.1 \times 2.4)$ mm³ are shown in Fig. 110 and Fig. 111. Voxel size $(1.5 \, \mu m)^3$. Within this volume, the fraction of pores is 0.03 vol.% and the volume fraction of the filler is 2.2 vol.%. The greatest amounts of pores and filler agglomerations are found to be in fibre direction. It is also observed that pores are present in filler rich areas only. The biggest pores found in the studied region have a size of 11000 μm^3.
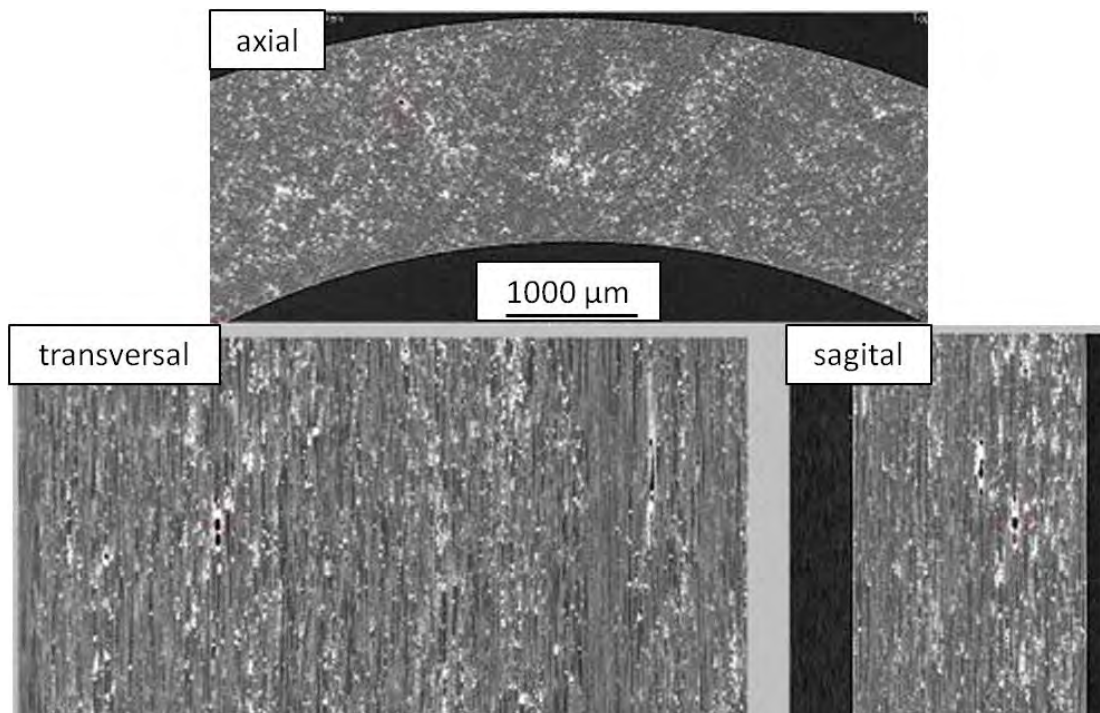
Fig. 110: CT slice images of a cut-out of a tube, tube thickness: 1.5 mm. The mineral filler (white contrast) is not homogeneously distributed within the specimen. Pores can be found in regions with higher filler particle agglomerations. Fibre misalignment can be observed. Voxel size of $(1.5 \, \mu m)^3$.
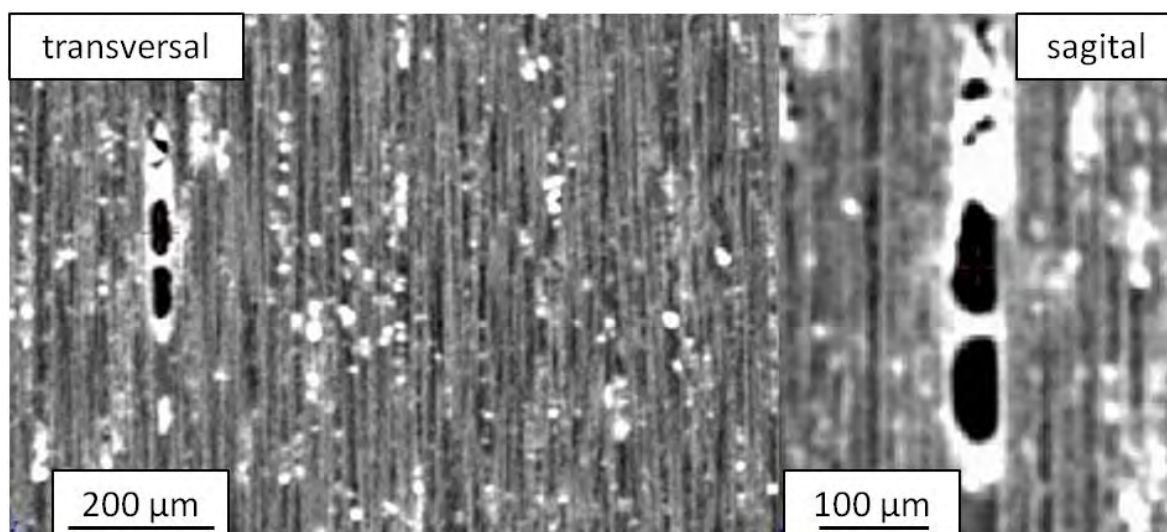
Fig. 111: Zoom showing filler particles (white) associated to pores (black). Since the resolution was increased to $(1.5 \, \mu m)^3$ per voxel, single fibres are detectable, although since matrix and fibres have very similar grey values, it is hard to distinguish them. Fibre misalignment can be observed as well.

5.2.2.2 *Pultruded profile R/L20-T/HTSTS/UD65f*
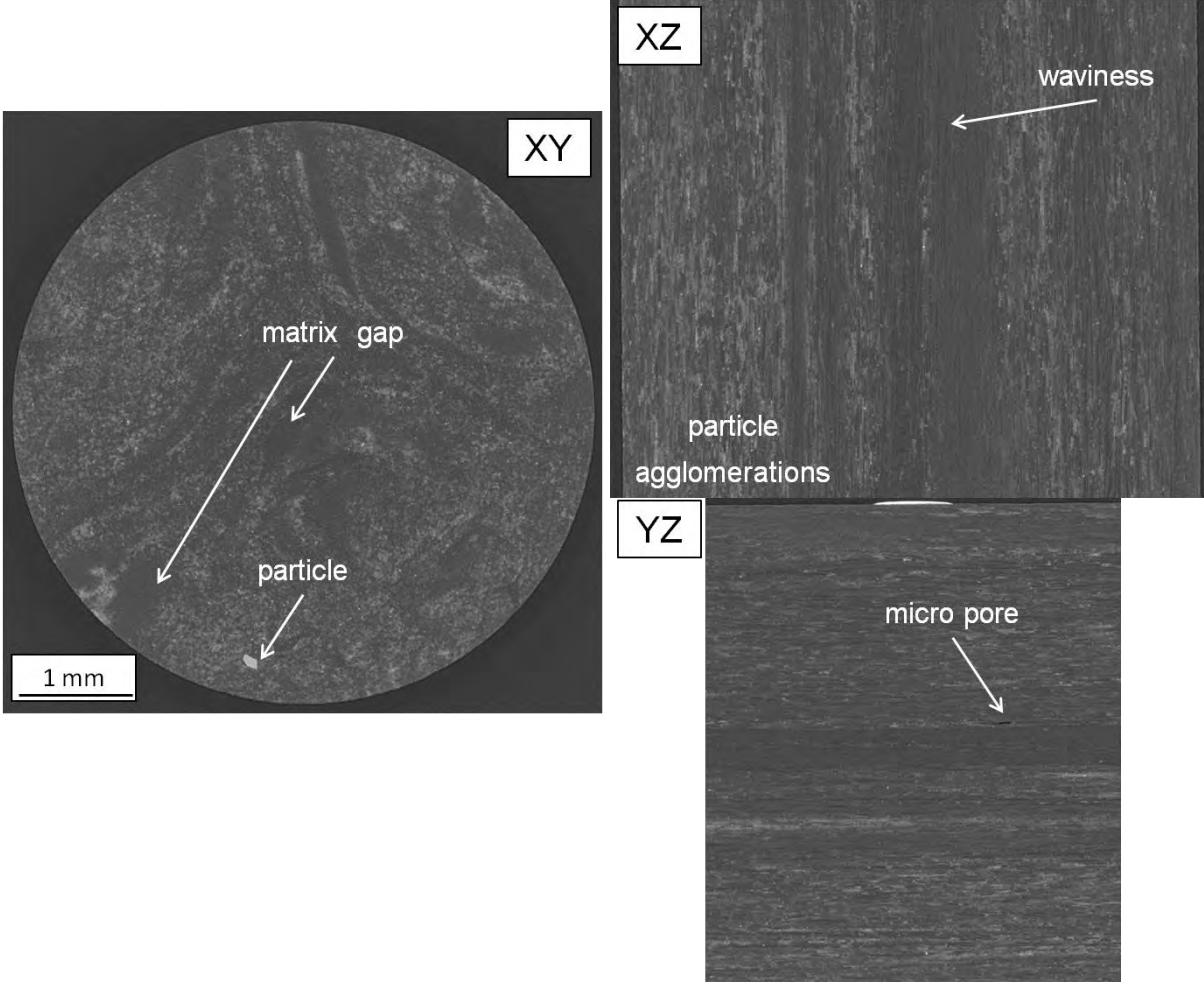
Fig. 112: XCT slices of rod (diameter 5 mm). Filler particles agglomerations, matrix-rich regions / matrix gaps (as a consequence of matrix flow between tows), small pores and waviness can be observed. Voxel size of (2.5μm)³, a 3D view of the studied volume is showed on the bottom.
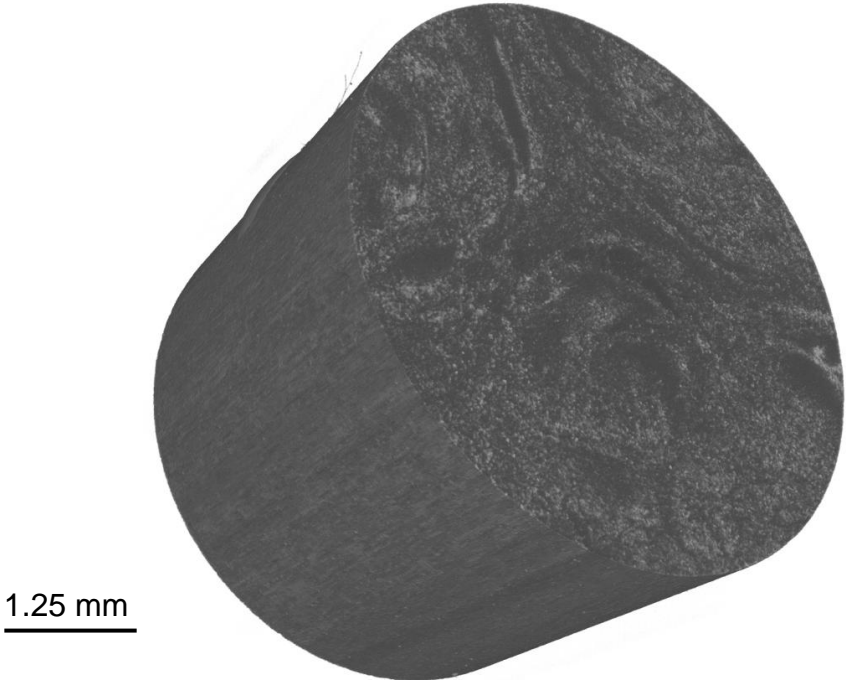
Slice images of a XCT scanned volume of approximately (5.1×5.1×4.2) mm³ and the 3D view of the same volume are shown in Fig. 112. In Fig. 113 a smallest cut-out of the same kind of pultruded rod material imaged by means of light optical tomography (LOT) is presented. In this volume fibres (blue) and filler (red) could be segmented. The size of this LOT volume is (170×175×50) μm³, with a voxel size of (0.6×0.6×5 μm)³.
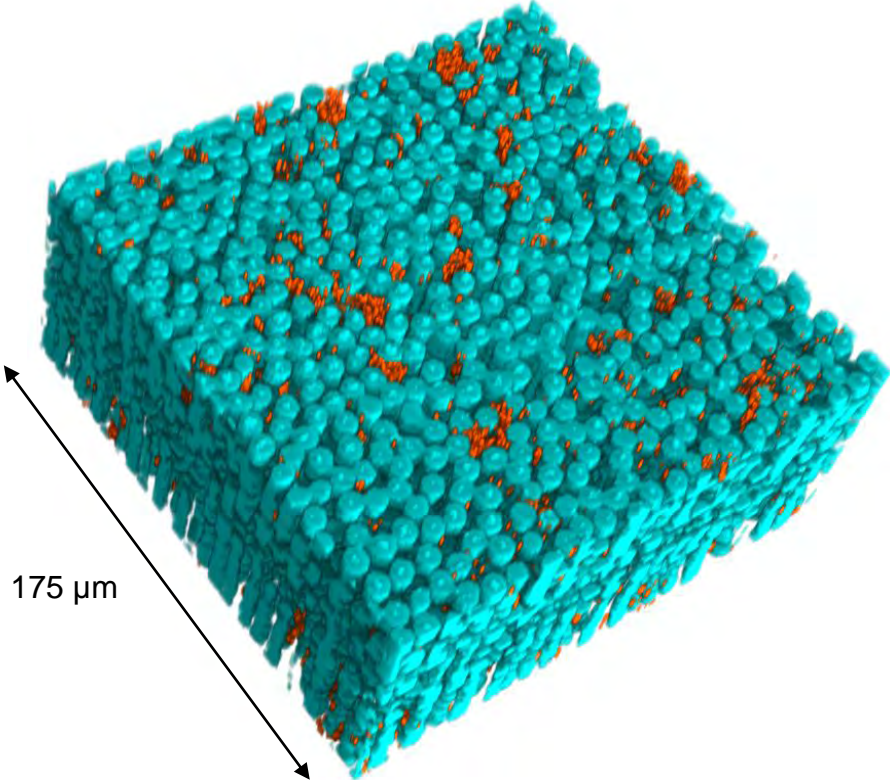
Fig. 113: Light optical tomography (serial sectioning). Segmented fibres (blue) and filler particles (red). Volume size: (170×175×50) μm³. Voxel size of (0.6×0.6×5 μm)³. Particles volume fraction: ~ 5 vol.%.

5.2.2.3 *Pultruded profile R/Sika/Sigrafil-T700SC/UD65f*
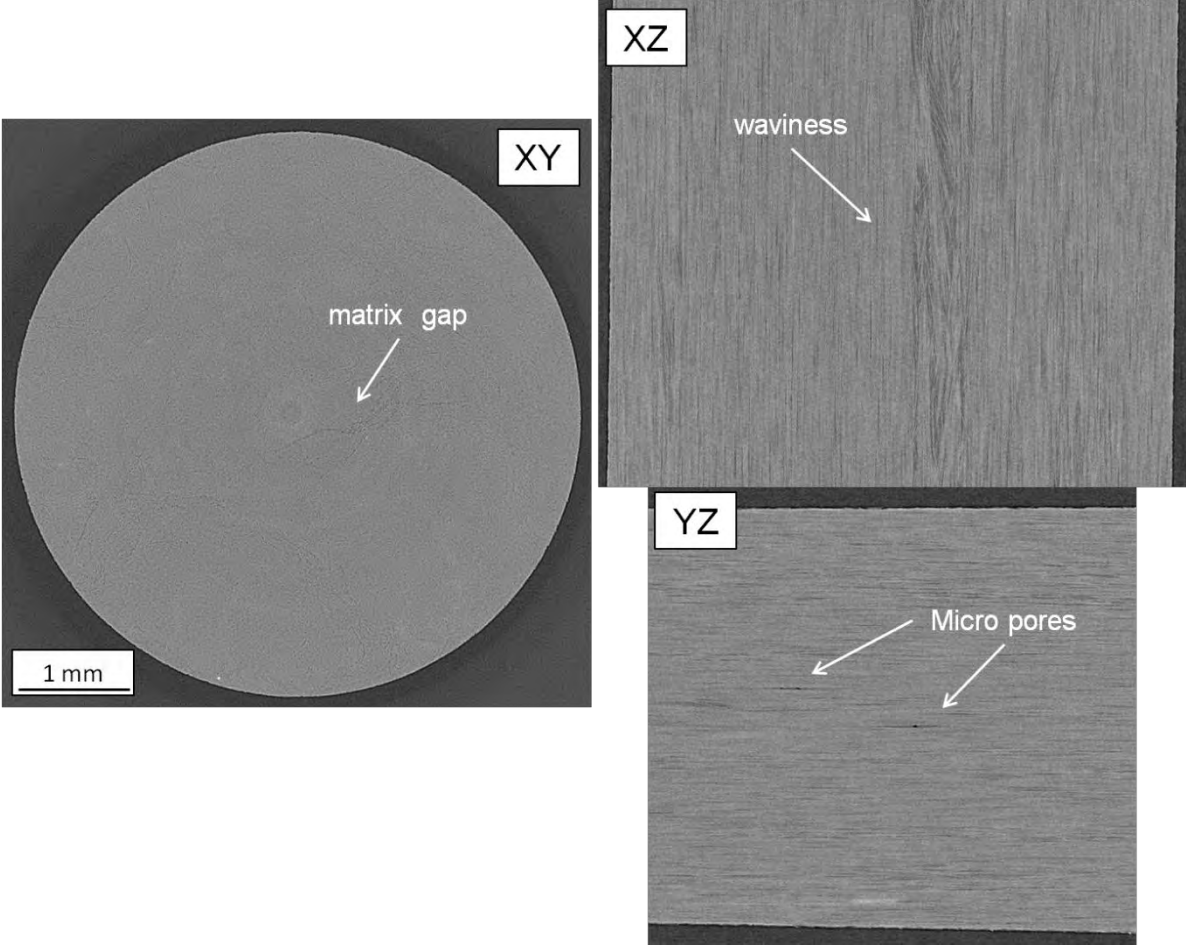
Fig. 114: XCT slices of rod (diameter 5 mm). Matrix gap is observed in the centre of the rod. Small pores and waviness can be observed on the XZ and YZ longitudinal sections. Voxel size of (2.5µm)^3. A 3D view of the same CT volume is showed on the bottom.
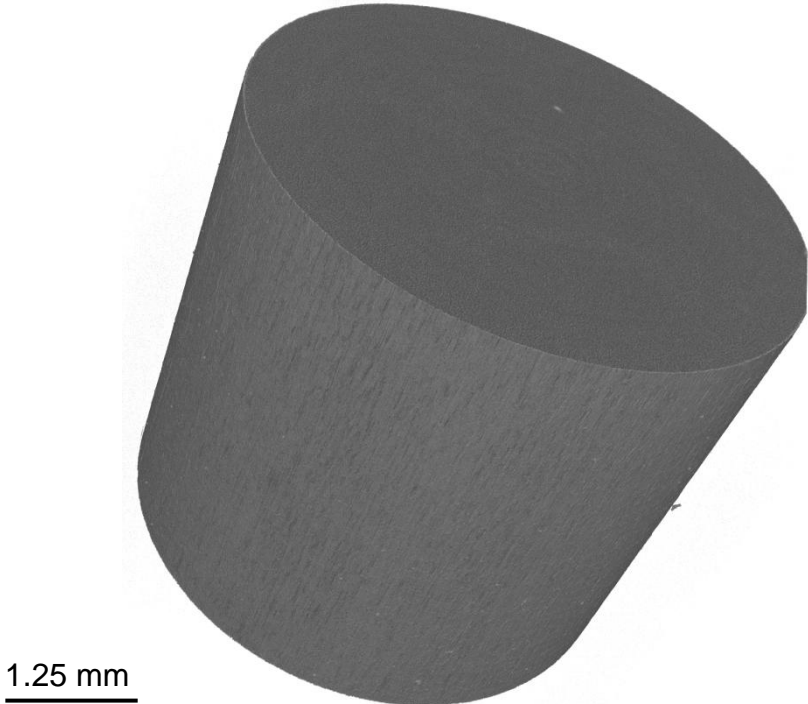
5.3 Thermal Analysis

5.3.1 Thermogravimetric Analysis (TGA)

In Tab. 21 the results obtained for all different studied CFRP samples are summarized. Some examples of curves obtained for each kind of material under the different conditions studied will be shown in the following subchapters.

Sample	W_f %	W_m % W_{part} %	V_f %	V_m %	$V_{porosity}$ %	V_{part} %
HexPly8552 Laminates						
HSAS4/UD58f/0.2MPa/1	65.5±0.4	34.3±0.4	57.9±0.4	41.7±0.5	0.4	-
HSAS4/±45-58f/0.2MPa/2	65.6	34.4	58.2	42.0	n.d.	-
Sika CR132 Laminates						
FT300B/0-90°/1bar/3	55.9	44.1	43.8	52.9	3.3	-
HTA40/UD/1bar/3	62.3	34.7	51.3	43.8	3.2	1.7
HTS5631/UD/1bar/3	68.8	31.2	57.2	40.2	2.6	-
HTS5631/UD/3bar/4	73.3	26.7	63.8	36.0	0.2	-
Hexion L418 Laminates						
FT300/0-90°/1bar/5	66.6	33.4	53.6	41.0	5.4	-
HTA40/UD/1bar/5	69.0	28.2	55.7	34.9	7.9	1.5
HTS5631/UD/1bar/5	77.6	22.4	62.7	27.9	9.5	-
HTS5631/UD/3bar/6	76.0	24.0	65.7	31.9	2.4	-
L20 pultruded tubes						
T/HTSTS/UD65f	62.3±1.6	33.6±2.0 4.7±0.1	53.8±2.8	45.0±1.8	n.d.	2.6±0.1
L20 pultruded rods						
R/HTSTS/UD65f exterior	60.2±0.3	32.1±0.4 7.6±0.6	53.2±0.2	43.6±0.6	n.d.	4.3±0.3
R/HTSTS/UD65f centre	58.4±0.5	34.1±0.6 7.3±0.5	51.6±0.5	46.4±0.7	n.d.	4.2±0.3
Sika CR 141 pultruded rods						
R/Sigrafil-T700SC/UD65f	69.7±0.4	30.2±0.4	62.8±0.4	40.2±0.6	n.d.	-

Tab. 21: TGA results for all studied CFRP samples. Weight fractions obtained directly from the measurements and corresponding calculated volume fractions.

Prepreg based, laminates produced with a cure pressure of 3 bars and pultruded profiles exhibit the highest fibre volume fractions. The error propagation for the calculation of V_m and V_f from the mass fraction determined by TGA yields and absolute error of ± 2 vol.% for each. Thus absolute values of porosities in vol.% are inaccurate for high quality composites with low porosity contents. Given V_p values are to be interpreted qualitatively not quantitatively. Porosity contents cannot be determined for samples with mineral filler particles [89].

5.3.1.1 *Laminates HexPly8552*

Some of the TGA curves obtained for the two HexPly 8552 based laminates, produced with the same prepreg using different plies-stacking and curing cycle are presented here.

The summarized results are presented in Tab. 21. Two exemplary curves are shown in Fig. 115 for the HexPly8552/HSAS4/UD58f/0.2MPa/1 material (UD, cycle 0) and Fig. 116 for the HexPly8552/HSAS4/±45-58f/0.2MPa/2 prepreg laminates (multidirectional, cycle 1).
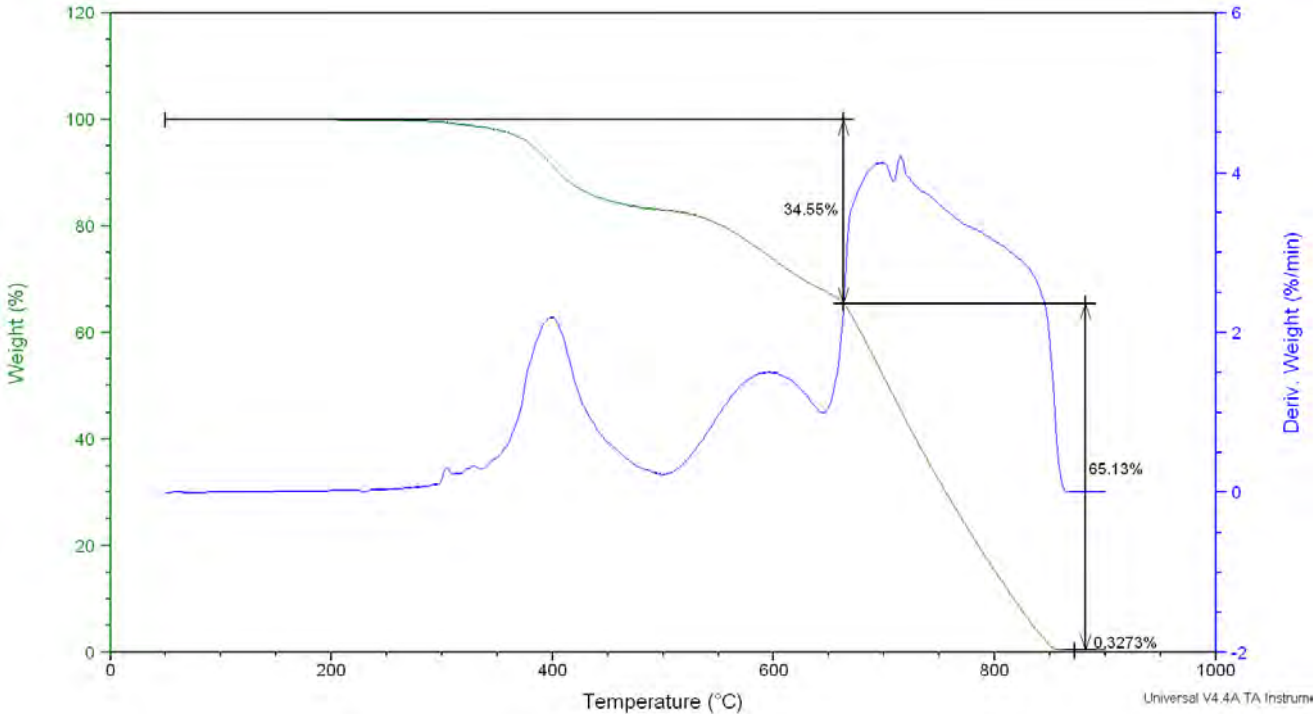
Fig. 115: TGA weight % vs. temperature (°C) curve obtained for a HexPly8552/HSAS4/UD58f/0.2MPa/1 sample using air atmosphere until 900°C with a constant heating rate of 10 K/min. This method was yielding the best results for this laminates.
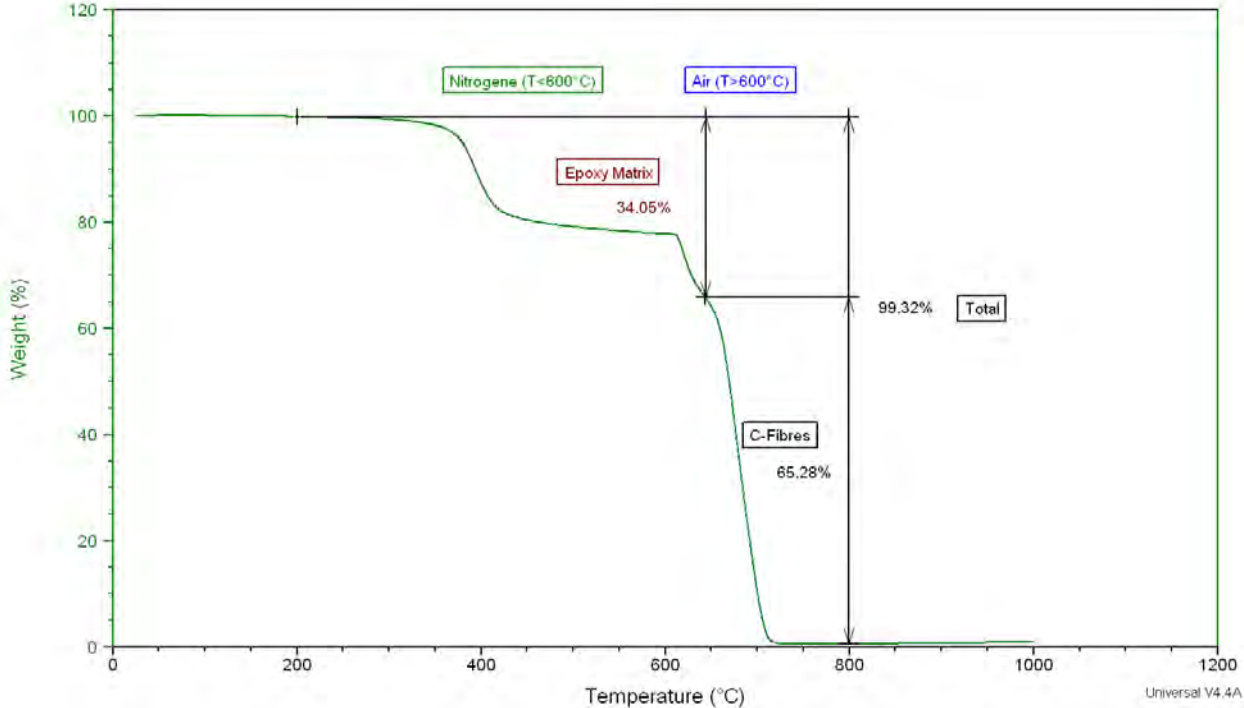
Fig. 116: TGA weight % vs. temperature (°C) curve obtained for a HexPly8552/HSAS4/±45-58f/0.2MPa/2 sample using N$_2$ atmosphere until 600°C changing then to air atmosphere until 1000°C with a constant heating rate of 10 K/min. Small sample (m = 21 mg).

5.3.1.2 Laminates Sika Biresin CR132 matrix
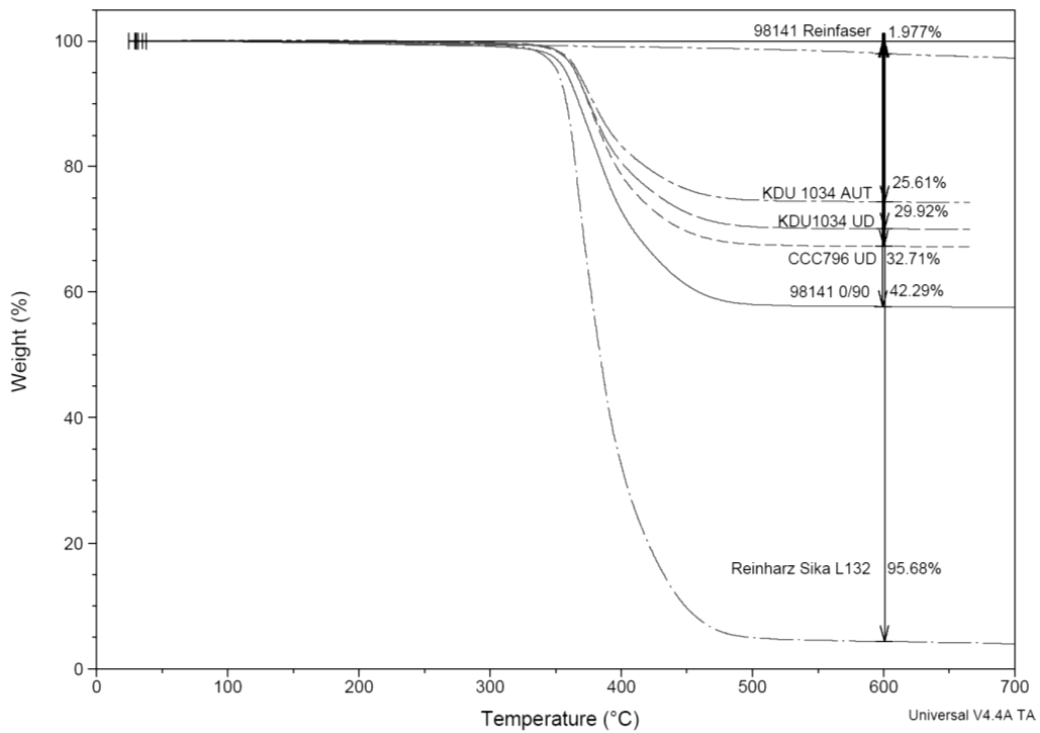
Fig. 117: TGA weight % vs. temperature (°C) curve obtained for all four different Sika CR132 laminates using N₂ atmosphere until 850°C with a constant heating rate of 10 K/min. Curves for pure epoxy and pure fibres are also shown. Recalculation of weight volumes was done taking them into account.

5.3.1.3 Laminates Hexion L418 matrix
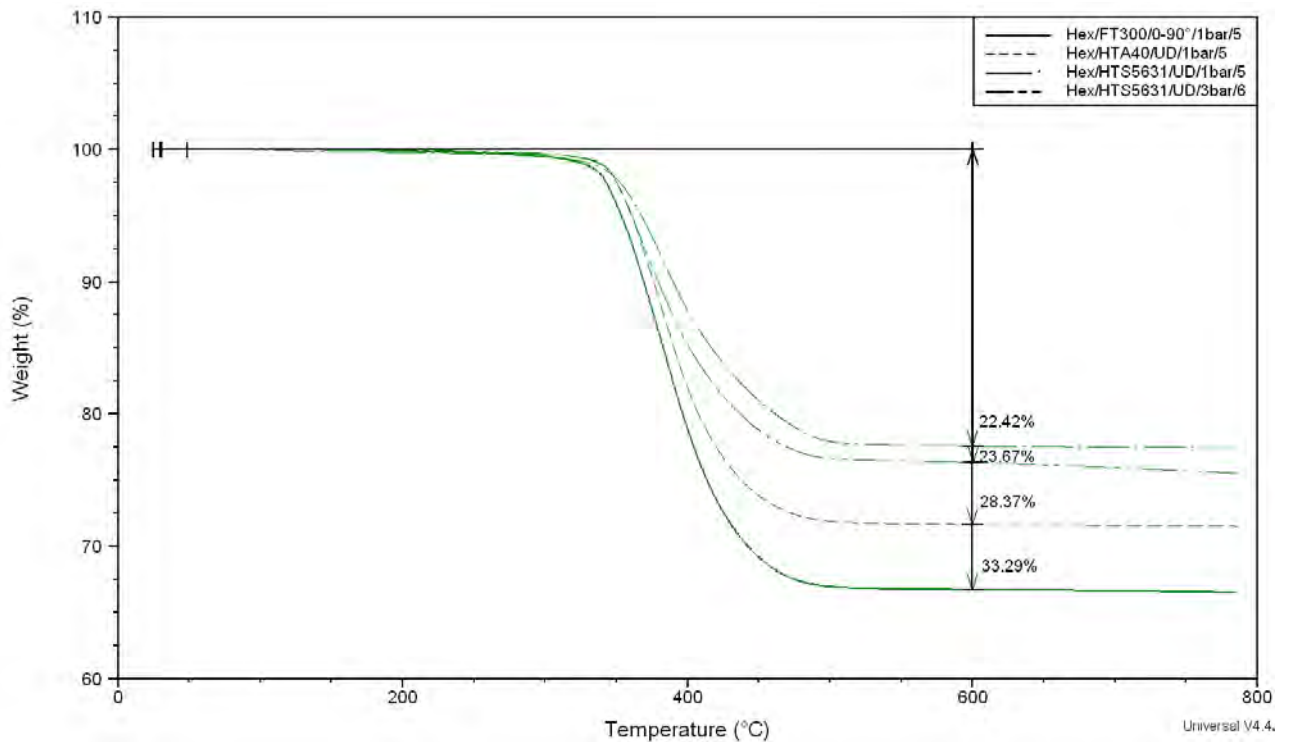
Fig. 118: TGA weight % vs. temperature (°C) curve obtained for all Hexion L418 based laminates using N₂ atmosphere until 850°C with a constant heating rate of 10 K/min. Equivalent results were obtained for measurements using air atmosphere.

5.3.1.4 *Pultruded profile T/L20-T/HTSTS/UD65f*

For these samples, heating under air atmosphere yielded the best results allowing calculating the volume fraction of the mineral filler particles embedded in the matrix. All samples were small, since they were cut-out slices of the tubes (m = 60-70 mg). An exemplary curve is shown in Fig. 119.
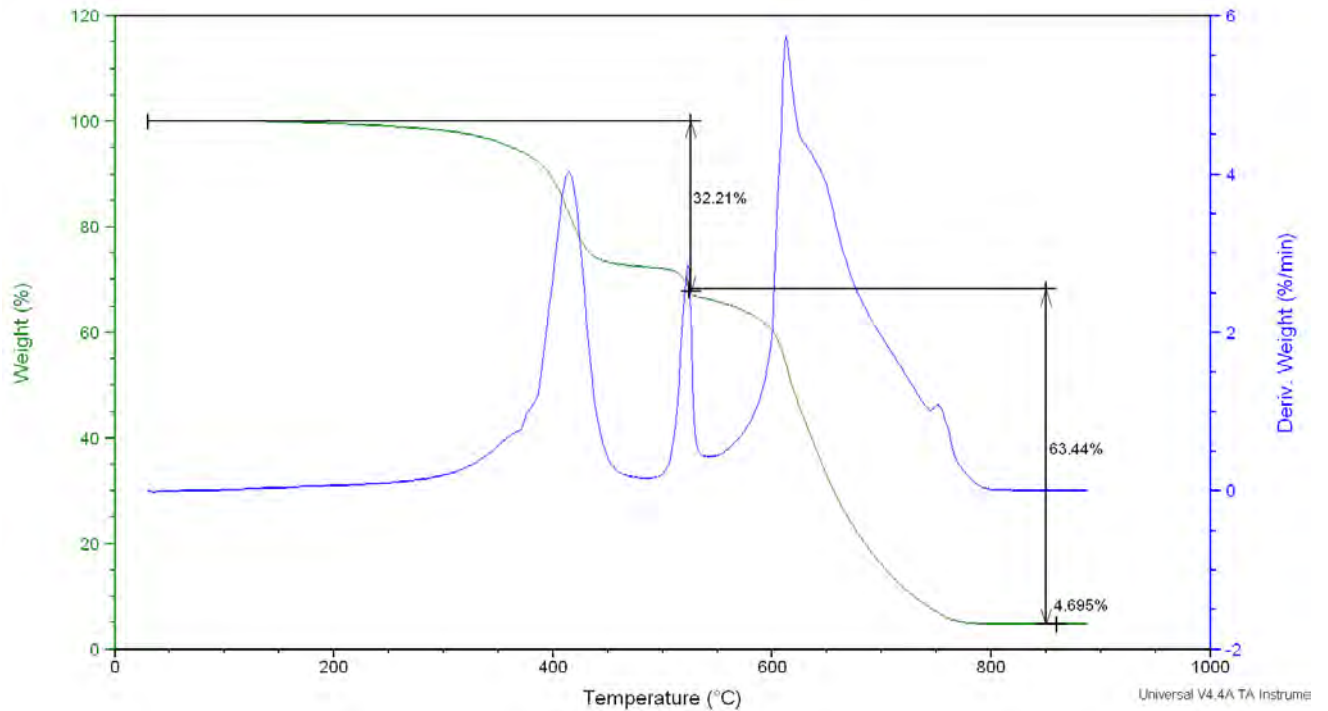
Fig. 119: TGA weight % vs. temperature (°C) curves obtained for a T/L20-T/HTSTS/UD65f sample using air atmosphere until 900°C with a constant heating rate of 10 K/min. After matrix and carbon fibre are consumed, the mineral particles remain and the weight fraction of all three components is obtained.

5.3.1.5 *Pultruded profile R/L20-T/HTSTS/UD65f*

Pure air atmosphere does not yield good results for these samples. A mixed atmosphere using first N_2 flow until 600°C, followed by an isothermal step 20 minutes in case of large samples, and air between 600°C and 1000°C, including an isothermal step at 900°C for large samples to assure full combustion, was found to be more suitable.

After matrix and carbon fibre are consumed the mineral particles remain, and the fraction of all three constituents is obtained. Porosity volume fraction cannot be resolved [89].

As explained in chapter 4.2.4.1, two kinds of samples were studied; samples from the centre of the rod (see Fig. 120) and samples taken from the border of the rods. It is observed that samples taken from the borders contain a higher fibre weight fraction (see Fig. 121).
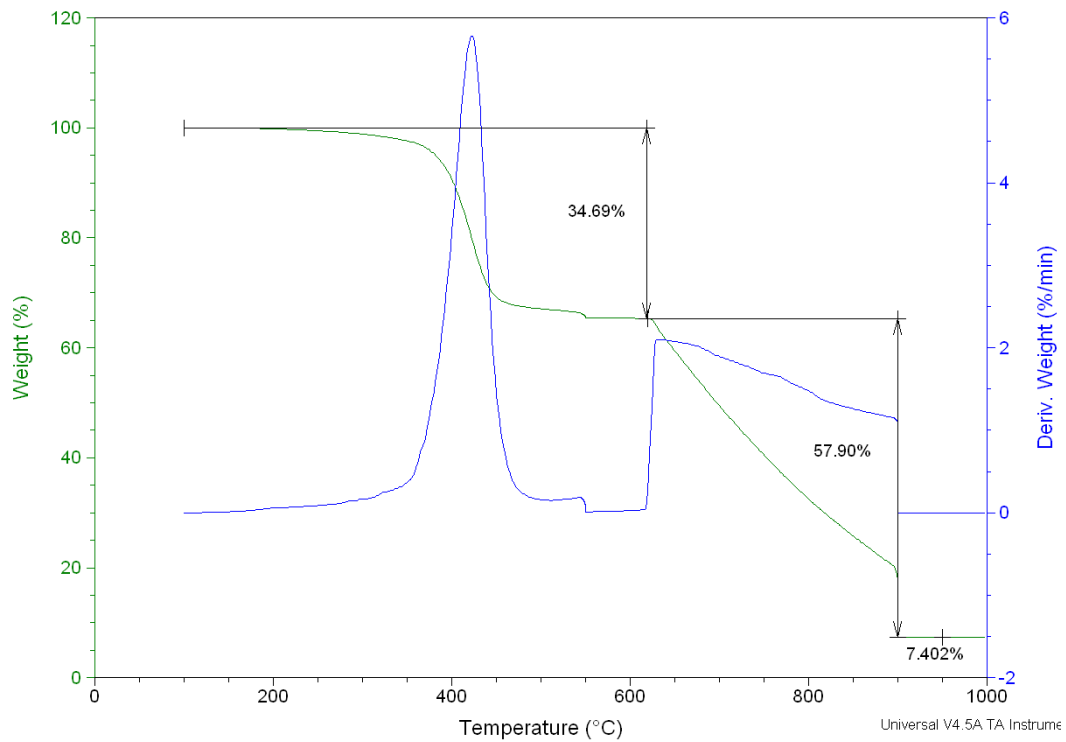
Fig. 120: TGA weight % vs. temperature (°C) curves obtained for R/L20-T/HTSTS/UD65f samples using a mixed atmosphere: N_2 until 600°C (isothermal step 20 minutes, for large samples) and air until 1000°C (isothermal step at 900°C for large samples to assure full combustion). Sample taken from the centre of the rod.
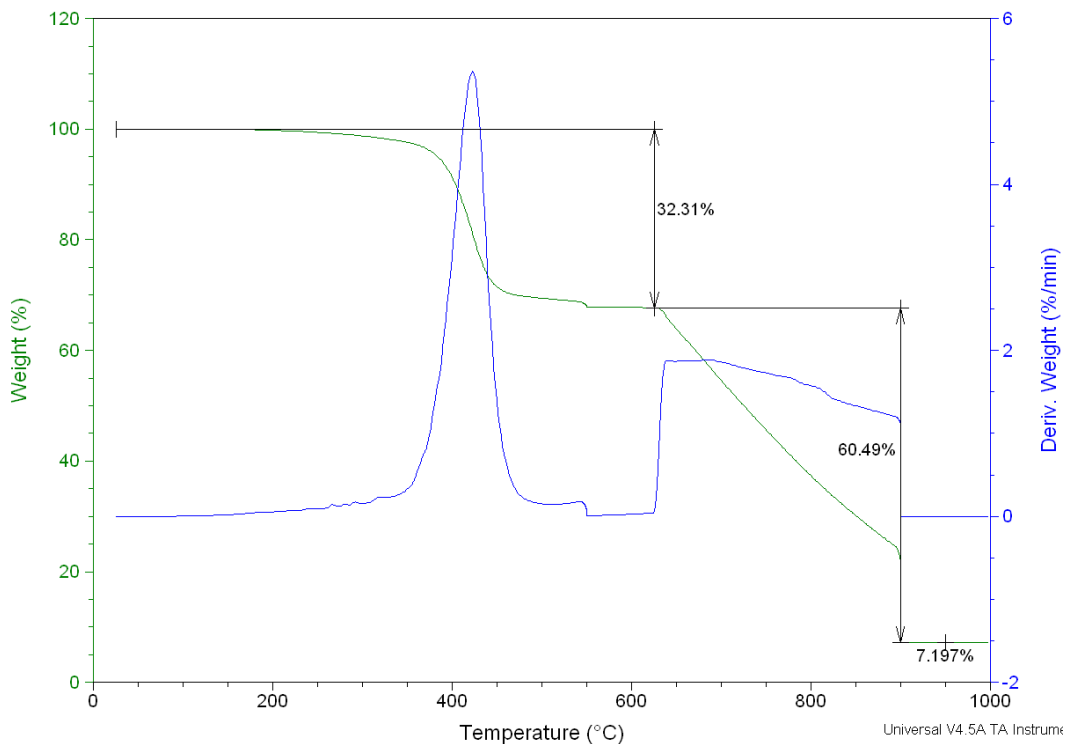
Fig. 121: TGA weight % vs. temperature (°C) curves obtained for R/L20-T/HTSTS/UD65f samples using the same mixed atmosphere as in the previous figure. After matrix and carbon fibre are consumed the mineral particles remain, and the fraction of all three constituents is obtained. Sample taken from the border of the rod.

5.3.1.6 *Pultruded profile R/Sika/Sigrafil-T700SC/UD65f*

No difference was observed between centre and border samples for these profiles. A comparison between air and N_2 atmosphere until 1000°C is shown in Fig. 122. The curve obtained using N_2 until 650°C then switching to air until 1000°C combined with constant temperature plateaus at 600°C and after 900°C is presented in Fig. 123. This method was used for samples with weight larger than 400 mg to assure full combustion of all constituents.
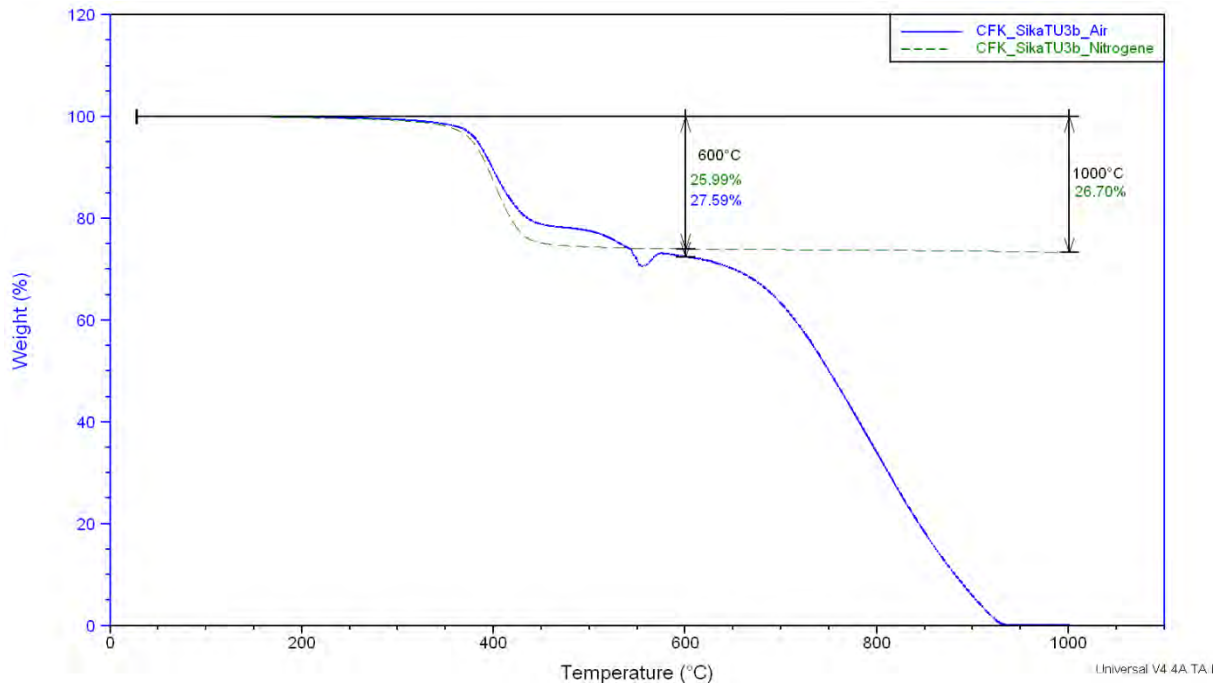
Fig. 122: TGA weight % vs. temperature (°C) curves obtained for two samples using two different atmospheres: N_2 atmosphere (green) and air atmosphere (blue), heating with 10 K/min until 1000°C.
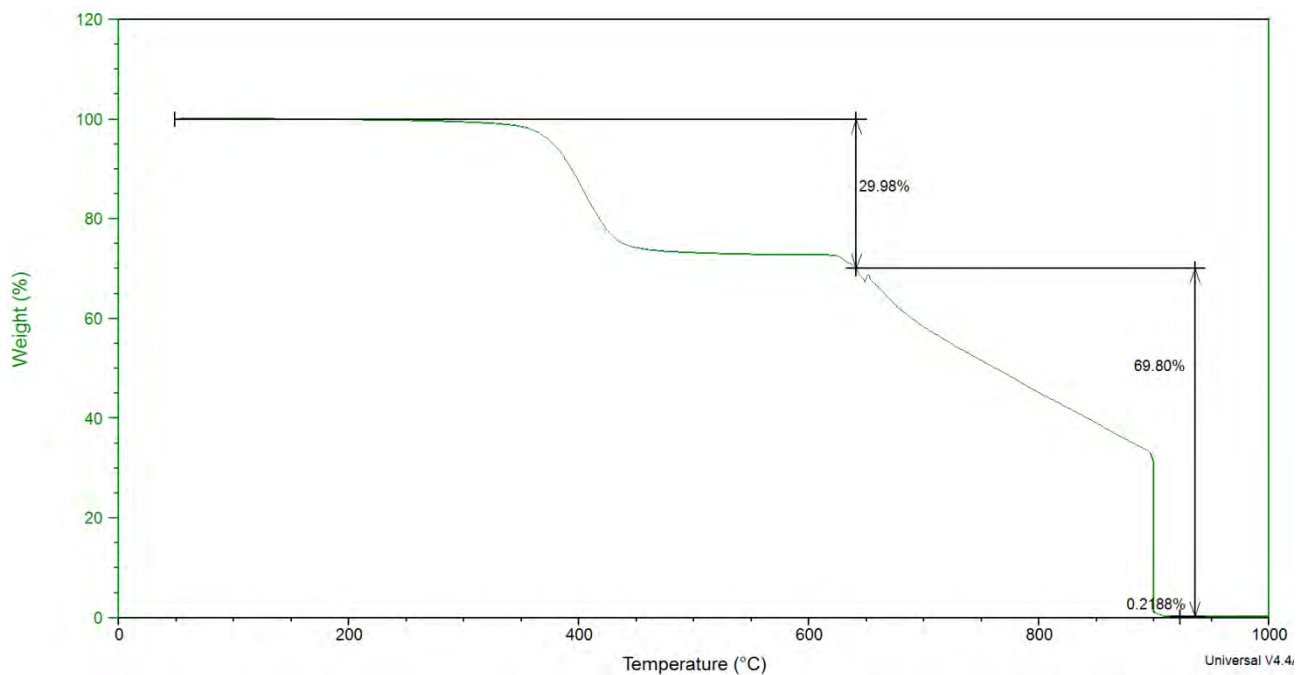
Fig. 123: TGA weight % vs. temperature (°C) curves obtained using N_2 atmosphere until 600°C, followed by air until 1000°C. Heating rate 10 K/min. For big samples this method yielded the best results.

5.3.2 Differential Scanning Calorimetry (DSC)

Results obtained for all different CFRP samples are shown in Tab. 22, containing average values for the glass transition temperature (Tg) measured using the same heating rate. Examples of curves obtained for each material under the different conditions studied will be shown individually in the following subchapters. Detailed results are listed in the annex B. Furthermore, on pultruded rod samples DSC analysis was performed after undergoing the heat treatments presented in chapter 4.2.3. The summarized results obtained for heat treated samples will be shown in the subchapter corresponding to these two materials.

Sample	Tg $_{Beginning}$ (°C)	Tg (°C)	Tg $_{End}$ (°C)
HexPly8552 Laminates			
HSAS4/UD58f/0.2MPa/1	202 ± 6	215 ± 2	221 ± 1
HSAS4/UD58f/0.2MPa/2	199 ± 3	212 ± 2	214 ± 4
<Tg (°C)>	**201 ± 2**	**214 ± 3**	**218 ± 6**
Sika CR132 Laminates			
FT300B/0-90°/1bar/3	117 ± 7	125 ± 4	133 ± 1
HTA40/UD/1bar/3	105 ± 2	117 ± 0	126 ± 1
HTS5631/UD/1bar/3	123 ± 1	129 ± 0	136 ± 0
HTS5631/UD/3bar/4	124 ± 1	129 ± 1	133 ± 1
<Tg (°C)>	**119 ± 8**	**127 ± 5**	**132 ± 3**
Hexion L418 Laminates			
FT300/0-90°/1bar/5	112 ± 2	119 ± 2	124 ± 2
HTA40/UD/1bar/5	108 ± 2	115 ± 1	121 ± 0
HTS5631/UD/1bar/5	98 ± 2	105 ± 3	110 ± 4
HTS5631/UD/3bar/6	100 ± 2	107 ± 2	113 ± 2
<Tg (°C)>	**105 ± 6**	**111 ± 5**	**117 ± 6**
L20 pultruded tubes			
T/L20-T/HTSTS/UD65f	73 ± 1	79 ± 2	90 ± 1
L20 pultruded rods			
R/HTSTS/UD65f – AR-1st	71 ± 3	76 ± 2	84 ± 5
R/HTSTS/UD65f – AR-2nd	101 ± 2	112 ± 3	122 ± 5
<Tg (°C)> 1st	**72 ± 1**	**77 ± 2**	**87 ± 3**
Sika CR 141 pultruded rods			
R/Sig-T700SC/UD65f – AR-1st	60 ± 2	63 ± 2	65 ± 2
R/Sig-T700SC/UD65f – AR-2nd	89 ± 2	100 ± 2	109 ± 2

Tab. 22: Average results for glass transition temperature interval obtained for all studied CFRPs in as received condition. Heating rates used for laminate samples was 3K/min, for pultruded samples 5K/min. Overall average values are also given when samples have the same kind of matrix.

The glass transition is observed as an endothermic step on the reversible heat flow curve. Because the glass transition involves a change in heat capacity, but does not involve a latent heat, it is called a second order transition; therefore no constant Tg value but a temperature interval should be given [5]. These results present begin, middle point and end of the transition. Highest values are observed for the HexPly8552 system (HT) and the lowest for the L20 epoxy (LT), which is a relatively old system with a lower temperature resistance.

5.3.2.1 *Laminates HexPly8552*

Fig. 124 shows the typical DSC results obtained for the laminates HexPly8552/HSAS4/UD58f/0.2MPa/1 cured with cycle 0 (see Fig. 22). Three curves are plotted; heat flow which is the sum of the reverse heat flow and non-reverse heat flow curves.
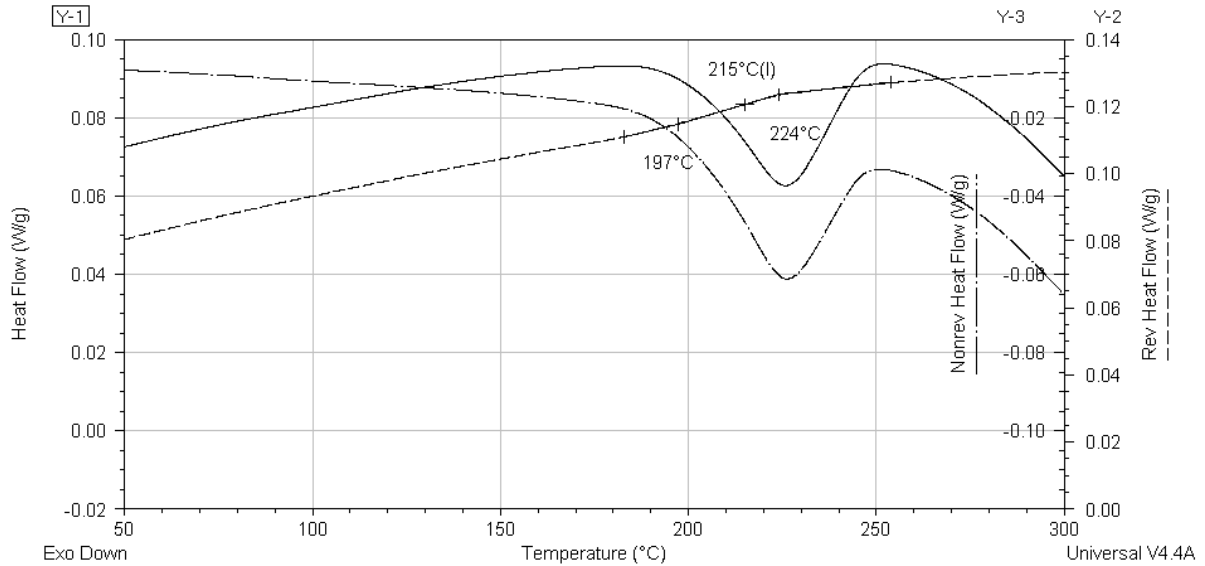
Fig. 124: Heat flow, reverse heat flow and non-reverse heat flow curves obtained for a HexPly8552/HSAS4/UD58f/0.2MPa/1 specimen. A post curing dwell is observed in the non-reversible curve at about 225°C. The glass transition step is observed in the reversible curve between 197°C and 224°C.

Fig. 125 shows the typical DSC results obtained for the laminates HexPly8552/HSAS4/UD58f/0.2MPa/2 cured with cycle 1 (see Fig. 22). Three curves are plotted; heat flow which is the sum of the reverse heat flow and non-reverse heat flow curves.
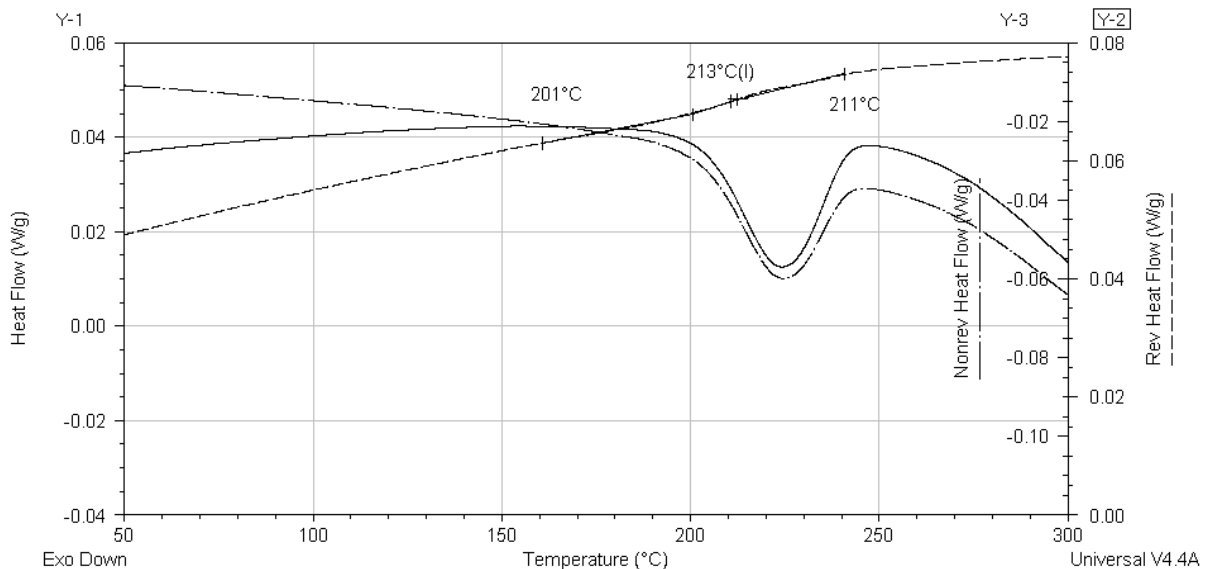
Fig. 125: Heat flow, reverse heat flow and non-reverse heat flow curves obtained for a HexPly8552/HSAS4/UD58f/0.2MPa/2 specimen. A post curing dwell is observed in the non-reversible curve. The glass transition step is observed in the reversible curve.

Fig. 126 and Fig. 127 show typical DSC results obtained for the laminates produced using Sika Biresin CR132 and Hexion L418 matrix respectively. No post-curing peak observed.

5.3.2.2 *Laminates Sika Birresin CR132 matrix*
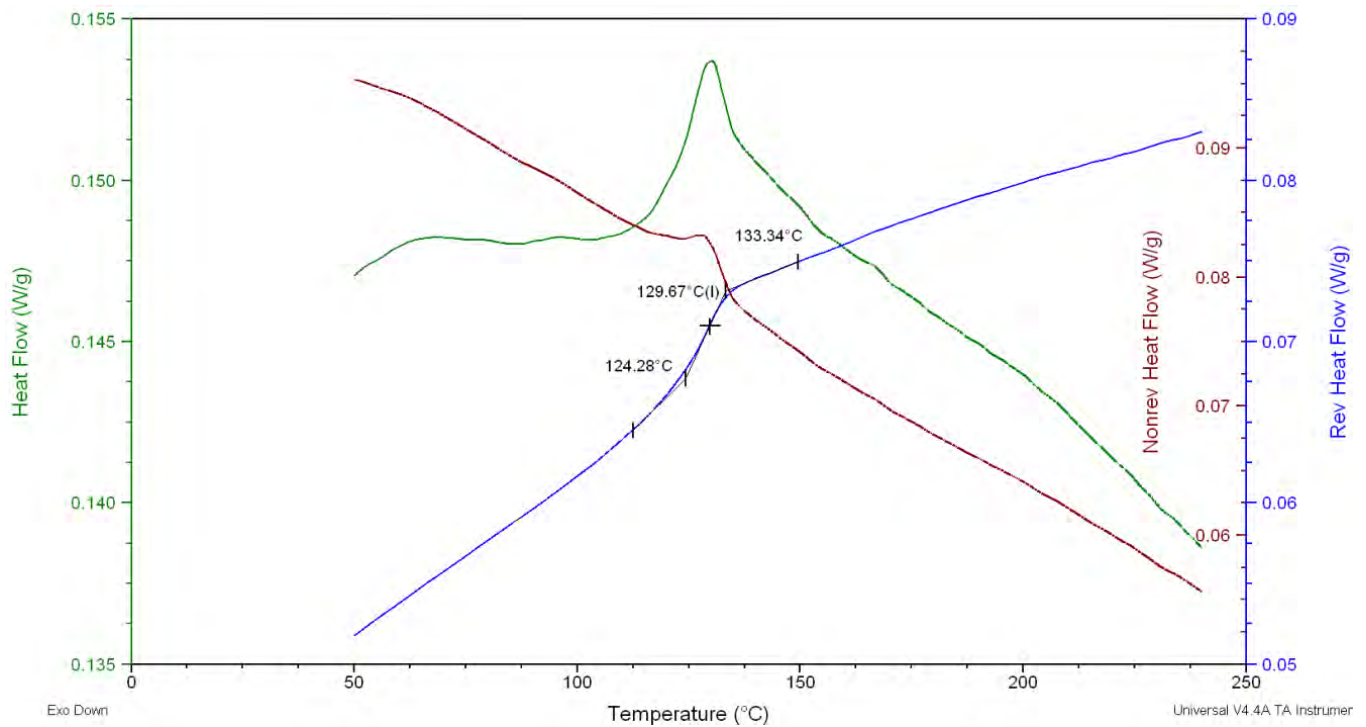
Fig. 126: Heat flow, reverse heat flow and non-reverse heat flow curves for a Sik/HTS5631/UD/3bar/4 specimen. The glass transition temperature step was observed in the reversible heat flow curve.

5.3.2.3 *Laminates Hexion L418 matrix*
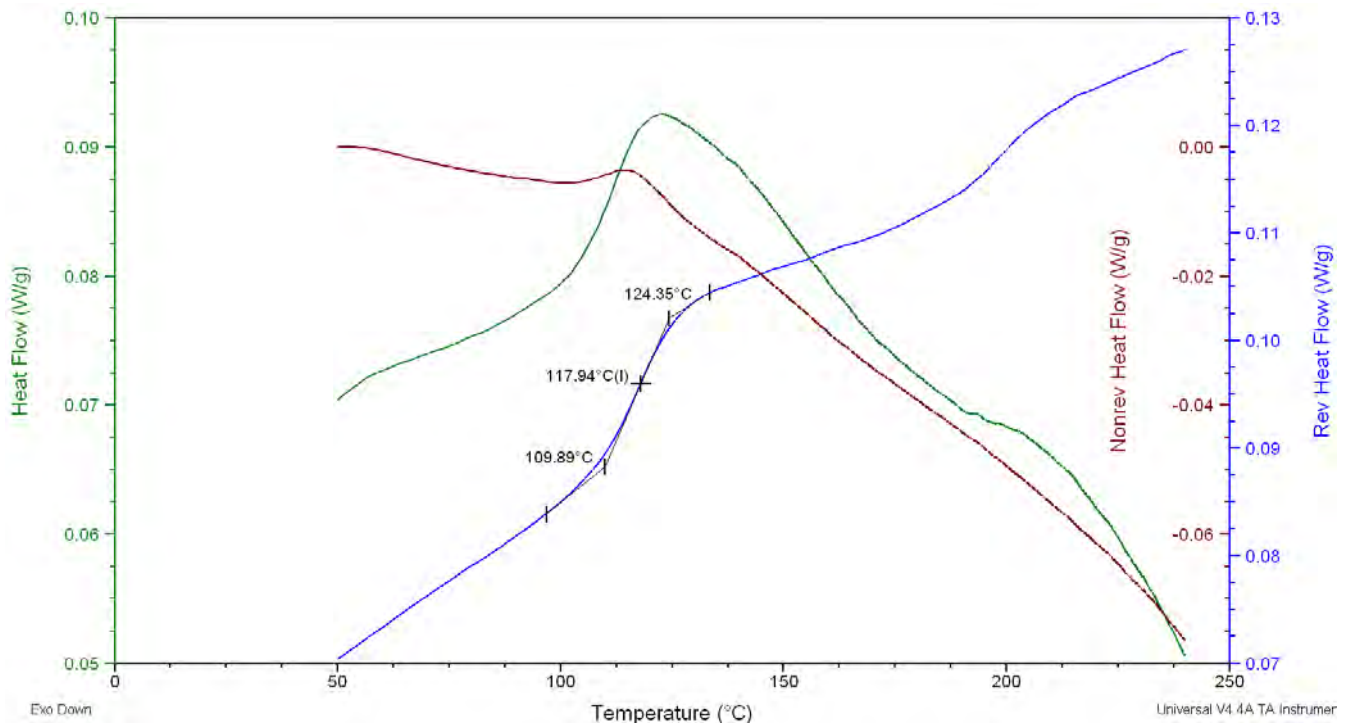
Fig. 127: Heat flow, reverse heat flow and non-reverse heat flow curves for a Hex/FT300/0-90°/1bar/5 specimen. The glass transition temperature step was taken from the reversible heat flow curve.

5.3.2.4 *Pultruded profile T/L20-T/HTSTS/UD65f*
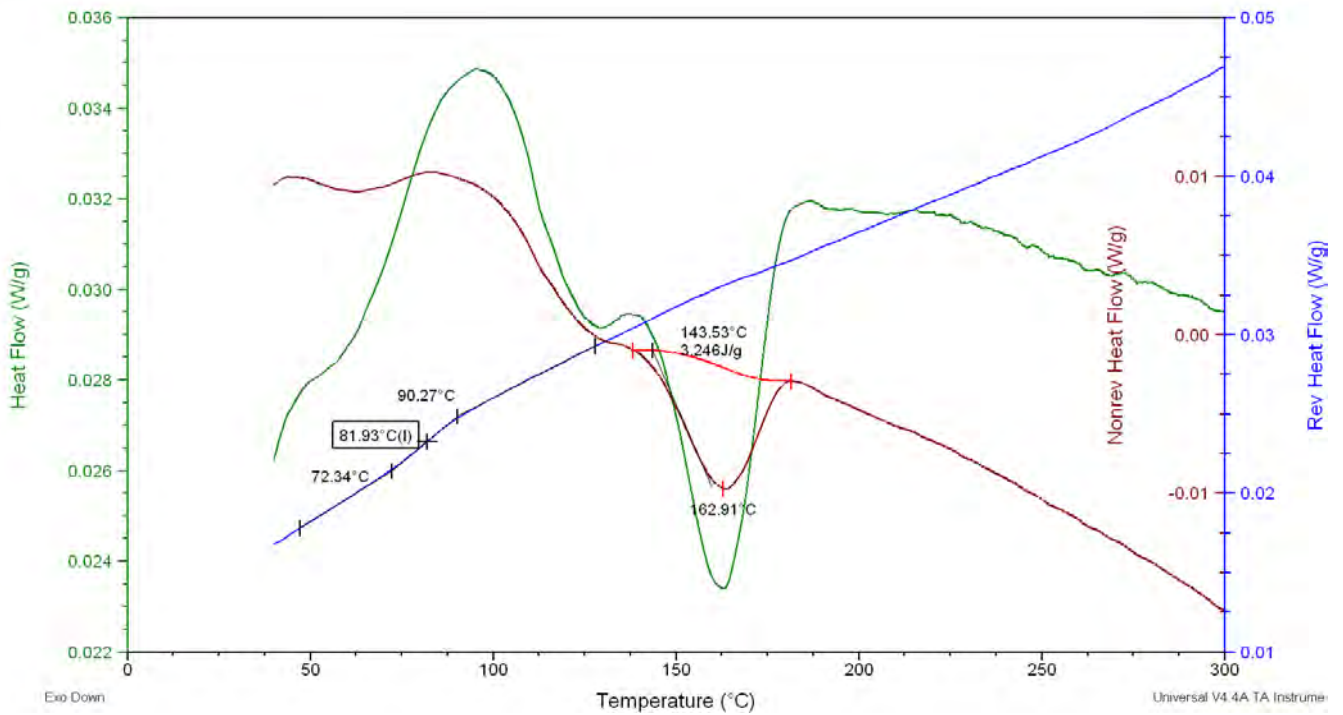
Fig. 128: Heat flow, reverse heat flow and non-reverse heat flow curves for a T/L20-T/HTSTS/UD65f pultruded specimen. The glass transition temperature step was observed in the reversible heat flow curve. A post curing peak is observed between 140°C and 180°C degrees in the non reversible heat flow curve.

5.3.2.5 *Pultruded profile R/L20-T/HTSTS/UD65f*
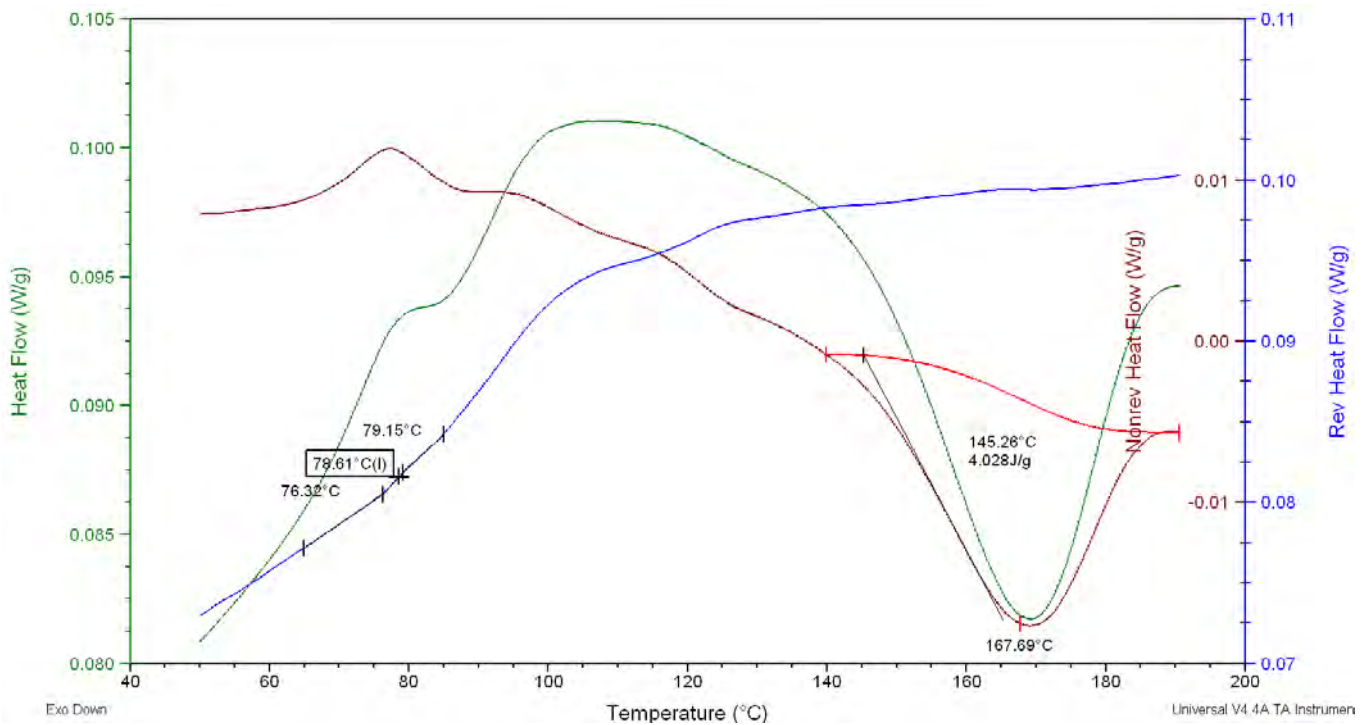
Fig. 129: Heat flow, reverse heat flow and non-reverse heat flow curves for a R/L20-T/HTSTS/UD65f pultruded specimen. The glass transition temperature step was observed in the reversible heat flow curve. A post curing peak is observed between 140°C and 180°C degrees in the non reversible heat flow curve.

103

Typical DSC results with post curing peak energy integrated are shown inFig. 128 and Fig. 129. Fig. 130 shows reverse heat flow curves for the same sample undergoing three consecutive heating-cooling cycles.
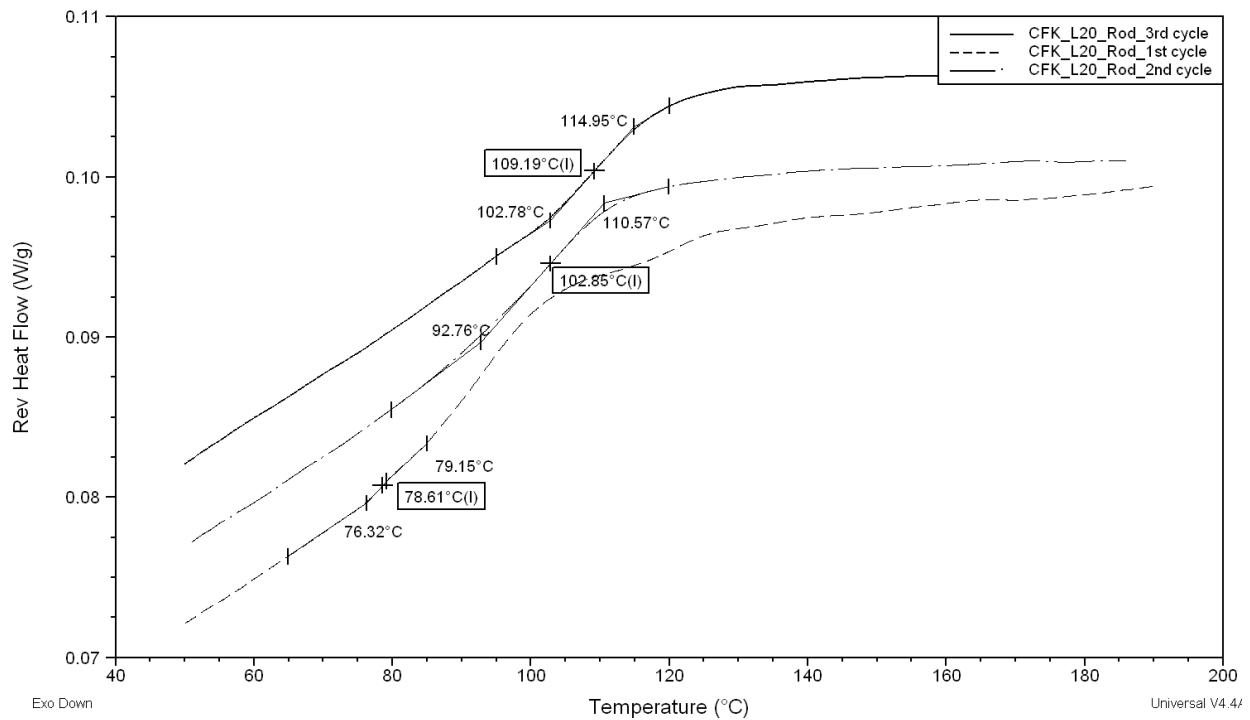
Fig. 130: Results obtained for one DSC sample tested using three consecutive heating-cooling cycles to study the evolution of the Tg values after each heating-cooling cycle. Higher values of Tg are observed after the sample was undergoing a heating-cooling cycle.

Results of DSC analysis after heat treatment:

The different heat treatments applied to these samples are summarized in chapter 4.2.3. The results obtained regarding glass transition temperature interval and post-curing peak (when observed) are shown in Tab. 23 and will be discussed in the section 6.3.

Sample code	DSC in-situ heat treatment. [10 K/min to T_{iso} (°C) - time (h)]	Glass transition temp. interval $Tg \pm 1$ [°C]	Heat peak [J/g] [Begin T peak(°C) Max T peak(°C)]
DSC-HT1	100°C – 2h	79 – **91** – 103	4.79 [144°C-168°C]
DSC-HT2	140°C – 2h	92 – **100** – 112	No peak
DSC-HT3	170°C – 1h	97 – **108** – 118	No peak

Tab. 23: Values for glass transition temperature interval and released energy (integral under exothermic peak) obtained after the different heat treatments for R/L20-T/HTSTS/UD65f pultruded samples studied.

5.3.2.6 *Pultruded profile R/Sika/Sigrafil-T700SC/UD65f*

A typical DSC result with post curing peak energy integrated is shown in Fig. 131. The three curves: heat flow (green), reverse heat flow (blue) and non-reverse heat flow (red) obtained with a heating rate of 5K/min. In measurements done with 10K/min heating rate it was observed that the glass transition temperature occurs earlier if the heating rate is higher, although the post-curing peak maximum shifts to higher temperature values.
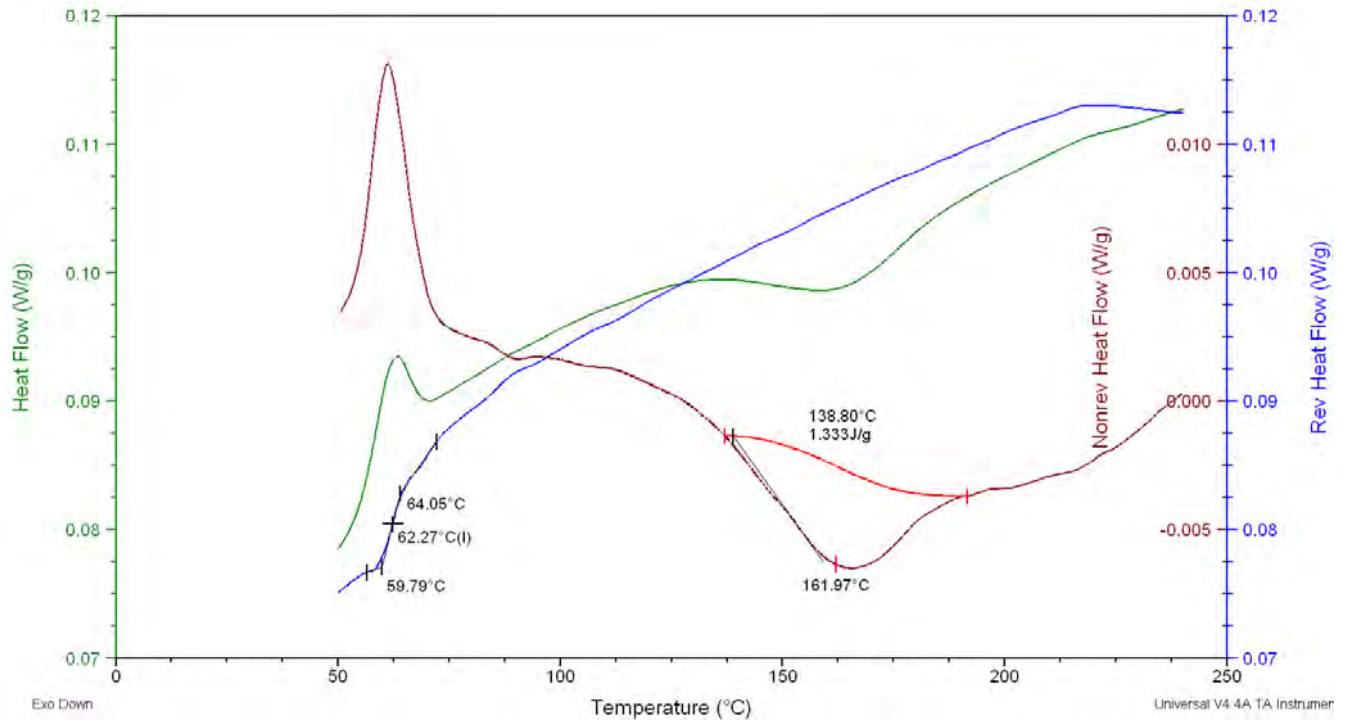
Fig. 131: Heat flow, reverse heat flow and non-reverse heat flow curves for a R/Sika/Sigrafil-T700SC/UD65f pultruded specimen. Measurement was carried out with 5 K/min heating rate. The glass transition temperature step was observed in the reversible heat flow curve. A post curing peak is observed between 135°C and 190°C degrees in the non reversible heat flow curve, with a maximum around 160°C.

Fig. 132 shows the reversible heat flow curves corresponding to consecutive thermal cycles on one sample using controlled heating rates. Tg increases after each heating cycle.
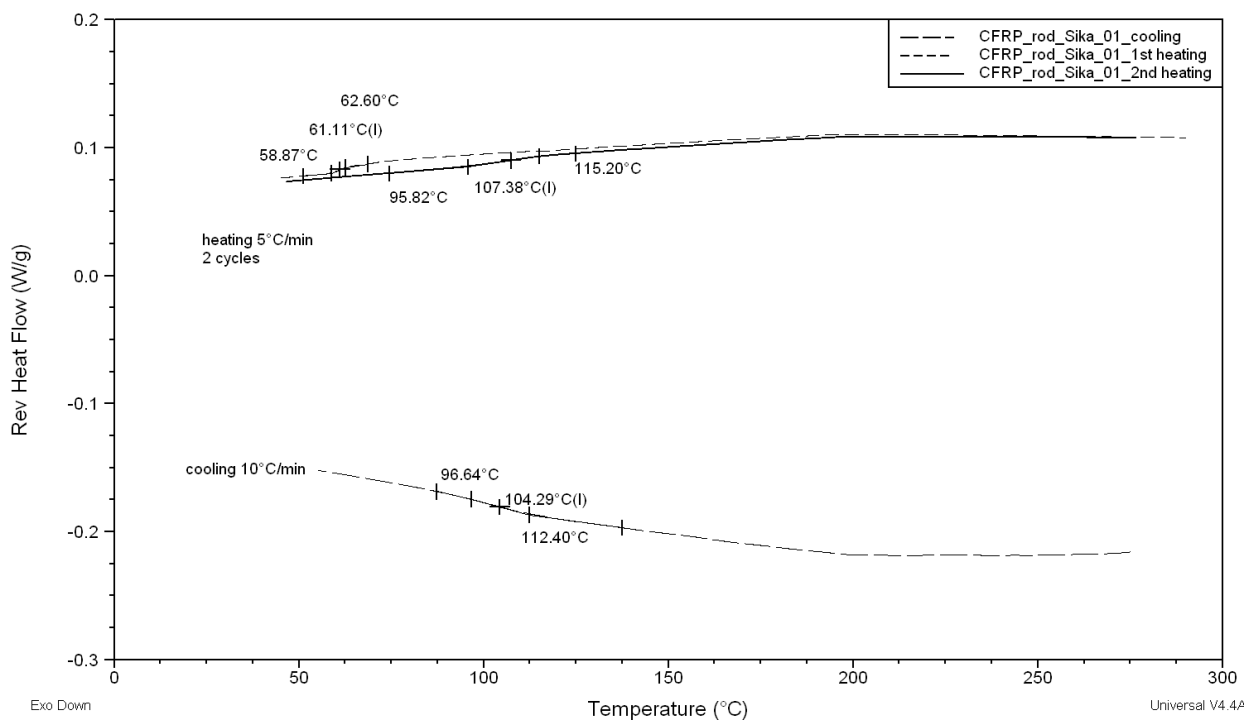
Fig. 132: Glass transition step observed in reverse heat flow curves for a specimen undergoing 3 cycles (heating 5°C/min – cooling 10 K /min– heating 5 K/min).

105

Results of DSC analysis after heat treatment:

The different heat treatments applied to these samples are summarized in chapter 4.2.3. The results obtained regarding glass transition temperature interval and post-curing peak (when observed) are shown in Tab. 24 and will be discussed in the section 6.2.

Sample code	Where	Heat treatment Temp (°C) – time (h)	Glass transition temp. interval Tg ± 2 [°C]	Heat peak [J/g] [Begin T peak(°C) Max T peak(°C)]
DSC-HT(70°-4h)	furnace	70° – 4h	58 – **62** – 80	0.98 [138°C-153°C]
DSC-HT(90°-4h)	furnace	90° – 4h	60 – **65** – 72	0.93 [138°C-159°C]
DSC-HT(120°-3h)	furnace	120° – 3 h	75 – **86** – 93	0.26 [138°C-153°C]
DSC-HT(120°-4h)	furnace	120° – 4 h	77 – **86** – 94	0.23 [138°C-150°C]
DSC-HT(120°-5h)	furnace	120° – 5h	76 – **83** – 93	0.23 [138°C-153°C]
DSC-HT(140°-3h)	in-situ	140° – 3h	85 – **94** – 103	No peak
DSC-HT(140°-4h)	in-situ	140° – 4h	85 – **96** – 105	No peak
DSC-HT(150°-3h)	in-situ	150° – 3h	86 – **96** – 104	No peak
DSC-HT(150°-3.5h)	in-situ	150° – 3.5h	86 – **97** – 106	No peak
DSC-HT(150°-4h)	in-situ	150° – 4h	88 – **97** – 107	No peak
DSC-HT(160°-2h)	in-situ	160° – 2h	87 – **97** – 105	No peak
DSC-HT(160°-2.5h)	in-situ	160° – 2.5 h	95 – **101** – 109	No peak
DSC-HT(160°-3h)	in-situ	160° – 3h	89 – **99** – 109	No peak
DSC-HT(160°-3.5h)	in-situ	160° – 3.5 h	91 – **102** – 111	No peak
DSC-HT(160°-4h)	in-situ	160° – 4h	92 – **102** – 111	No peak
DSC-HT(165°-1h)	in-situ	165° – 1h	82 – **93** – 103	No peak
DSC-HT(170°-1.5h)	in-situ	170° – 1.5h	85 – **96** – 104	No peak
DSC-HT(175°-2h)	in-situ	175° – 2h	89 – **97** – 108	No peak
DSC-HT(190°-10h)	furnace	190° – 10h (e1)	85 – **94** – 102	No peak
DSC-HT(190°-10h)	furnace	190° – 10h (e2)	89 – **98** – 105	No peak
DSC-HT(250°-1h)	in-situ	250° – 1h	99 – **111** – 118	No peak
DSC-HT(250°-2h)	in-situ	250° – 2h	99 – **111** – 118	No peak

Tab. 24: Values for glass transition temperature interval and released energy (integral under exothermic peak) obtained after the different heat treatments studied.

Calculating the degree of cure α_{DSC} was not possible, because the total reaction enthalpy of the studied epoxy systems was unknown. Though a quantitative study could not be carried out a qualitative comparison between as received and the different heat treated conditions will be presented in chapter 6.2.

5.3.3 Dynamic Mechanical Analysis (DMA)

DMA results obtained for all five different studied CFRPs classified in groups depending on their epoxy matrix are shown Tab. 25. Storage modulus at room temperature and glass transition interval values obtained from both the storage modulus step and the tan delta maximum (loss factor) are indicated. Examples of curves obtained for each material under the different conditions studied will be shown individually in the following subchapters. Detailed results are listed in the annex C.

Sample	E'_{RT} [GPa]	$T_B - T_g - T_E$ [°C] (Storage modulus)	T_g [°C] (Loss factor)
HexPly8552 Laminates			
HSAS4/UD58f/0.2MPa/1	117 ± 6	117 – 222 ± 3 – 225	225 ± 1
HSAS4/UD58f/0.2MPa/2	119 ± 7	119 – 217 ± 3 – 223	223 ± 4
<Tg (°C)>	**-**	**220 ± 4**	**224 ± 1**
Sika CR132 Laminates			
FT300B/0-90°/1bar/3	35 ± 8	102 – 119 ± 3 – 131	124 ± 3
HTA40/UD/1bar/3	91 ± 5	101 – 121 ± 1 – 231	124 ± 3
HTS5631/UD/1bar/3	101 ± 12	113 – 123 ± 1 – 132	126 ± 1
HTS5631/UD/3bar/4	106 ± 8	106 – 124 ± 2 – 134	127 ± 1
<Tg (°C)>	**-**	**121 ± 3**	**125 ± 2**
Hexion L418 Laminates			
FT300/0-90°/1bar/5	52 ± 10	116 – 124 ± 0 – 132	128 ± 0
HTA40/UD/1bar/5	88 ± 6	119 – 125 ± 0 – 133	129 ± 0
HTS5631/UD/1bar/5	113 ± 12	113 – 123 ± 1 – 130	127 ± 1
HTS5631/UD/3bar/6	117 ± 30	114 – 122 ± 0 – 129	126 ± 0
<Tg (°C)>	**-**	**123 ± 1**	**127 ± 1**
L20 pultruded rods			
R/HTSTS/UD65f – AR-1st	91 ± 6	84 – 95 ± 1.5 – 111	101 ± 1
R/HTSTS/UD65f – AR-2nd	93 ± 5	93 – 107 ± 0.8 – 126	116 ± 2
Sika CR 141 pultruded rods			
R/Sig-T700SC/UD65f – AR-1st	129 ± 6	91 – 117 ± 1 – 152	145 ± 1
R/Sig-T700SC/UD65f – AR-2nd	144 ± 8	123 – 141 ± 2 – 175	161 ± 2

Tab. 25: DMA results summary for all studied CFRP materials. Average glass transition temperature interval values obtained from storage modulus curve and from loss factor maximum. The storage modulus in GPa at room temperature.

Results obtained for the glass transition of the pultruded profiles are not in good agreement with those of the modulated DSC analysis (see Tab. 22). On one hand sample size is not comparable, DSC samples are much smaller and only a part of them undergoes glass transition (the fibres are inert in this case). On the other hand DMA is based on stiffness measurements and energy loss, whilst DSC bases on heat capacity measurements. In the case of DMA a known problem is the so called thermal lag, which bases upon the difference between the actual sample temperature and the temperature detected by the thermocouple, this ultimately leads to higher Tg values. Also it should be pointed out that the glass transition is a second order transition, both time and temperature dependent, which makes it very sensitive to the applied oscillation frequency [90].

5.3.3.1 Laminates HexPly8552

Exemplary DMA results for laminates produced from prepregs with epoxy HexPly 8552 are shown in this section. Storage modulus (green), loss modulus (blue) and tan delta (red) are plotted. Fig. 133 shows the results corresponding to laminates cured with cycle 0 (see Fig. 22) and Fig. 134 shows the corresponding curves for laminates cured with cycle 1 (see Fig. 22).
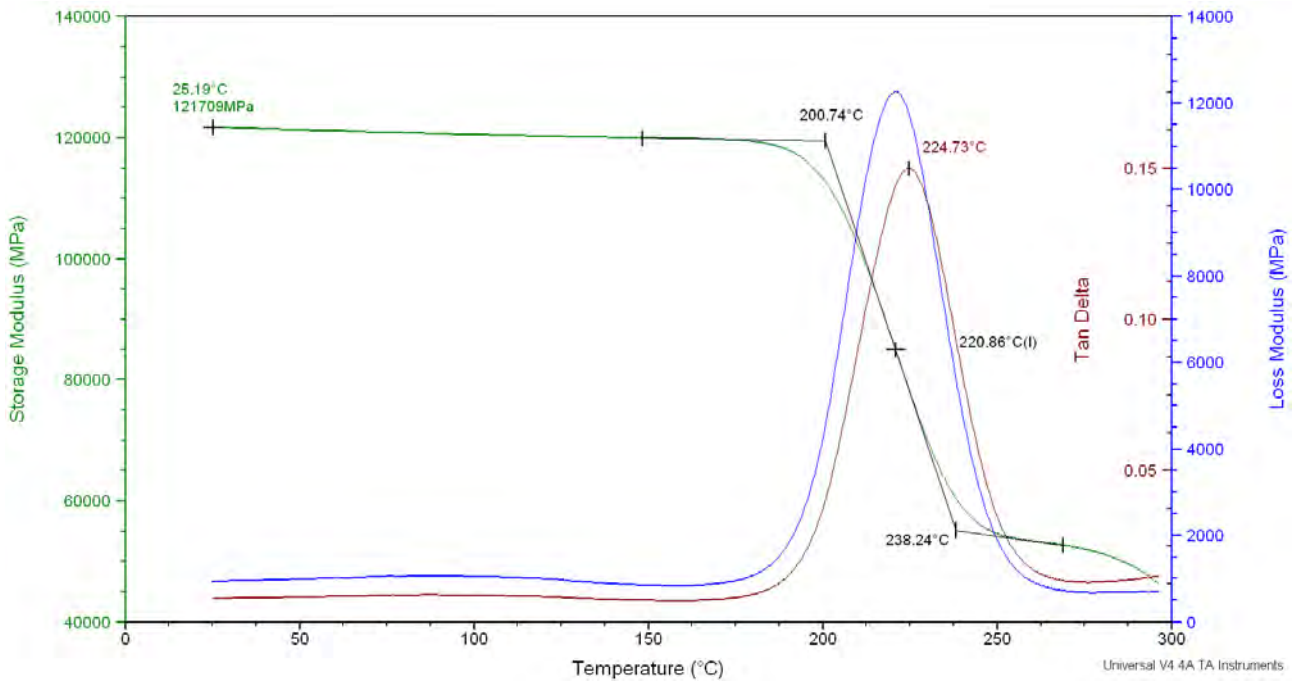
Fig. 133: Laminates HexPly8552/HSAS4/UD58f/0.2MPa/1. Storage and loss modulus curves obtained for DMA measurement. Sample tested in 3P-bending with 5 K/min to 300°C (Amplitude = 70 µm, Frequency = 1Hz).
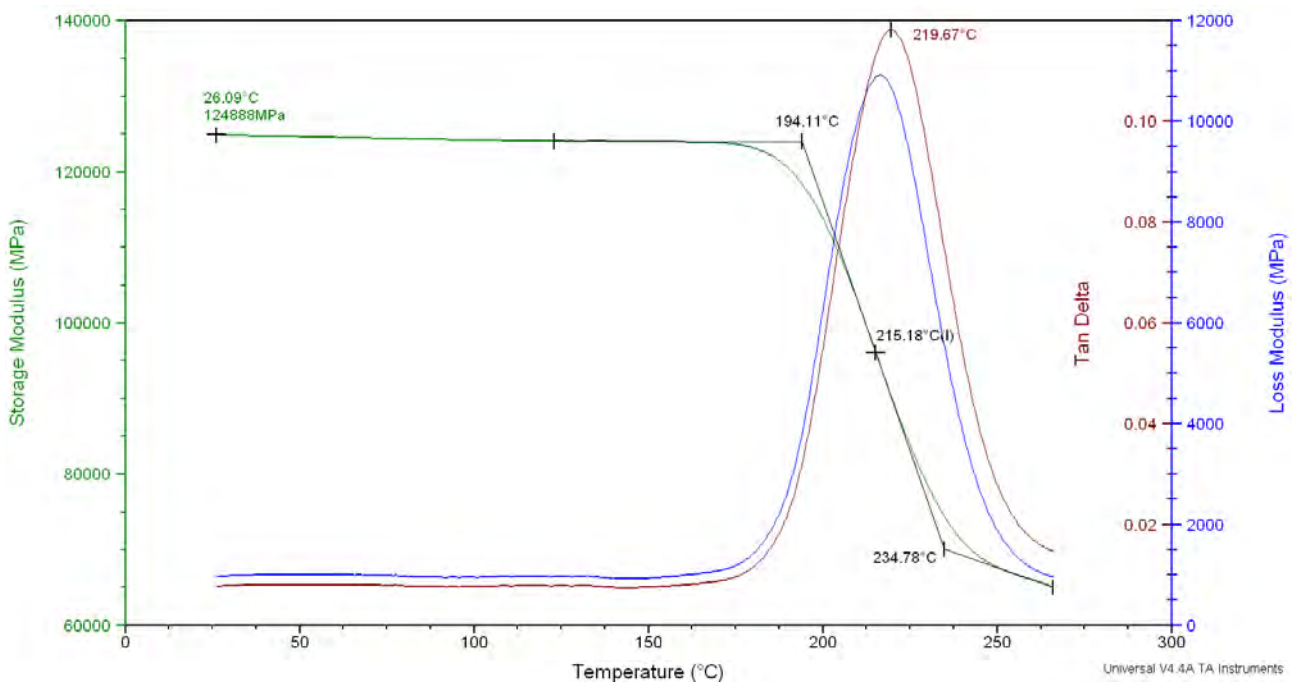
Fig. 134: Laminates HexPly8552/HSAS4/UD58f/0.2MPa/2. Storage and loss modulus curves obtained for DMA measurement. Tested in 3P-bending with 5 K/min to 270°C (Amplitude = 70 µm, Frequency = 1Hz).

5.3.3.2 *Laminates Sika Biresin CR132 matrix*

DMA results for laminates produced with epoxy Sika Biresin CR132 are shown in Fig. 135.
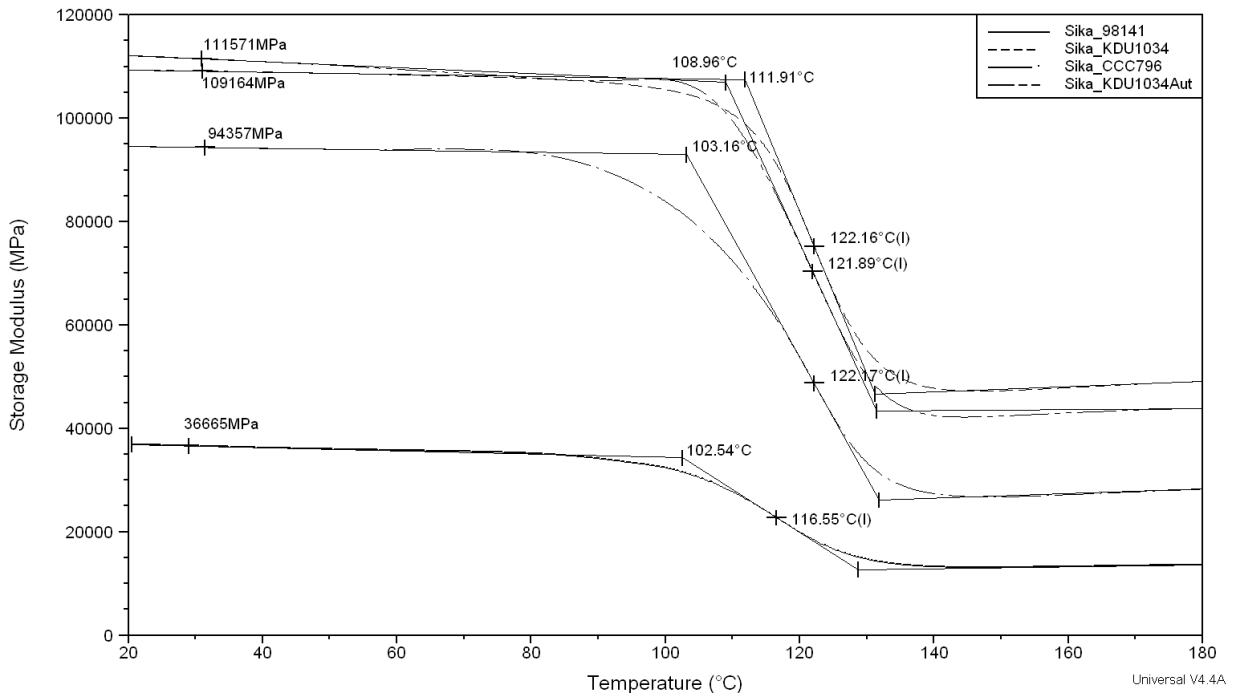
Fig. 135: Storage modulus curves for the four laminates produced with Sika CR132 epoxy matrix. Tested in 3P-bending tested with 3 K/min to 200°C (Amplitude = 70 μm, Frequency = 1Hz).

5.3.3.3 *Laminates Hexion L418 matrix*

DMA results for laminates produced with epoxy Hexion L418 are shown in Fig. 136.
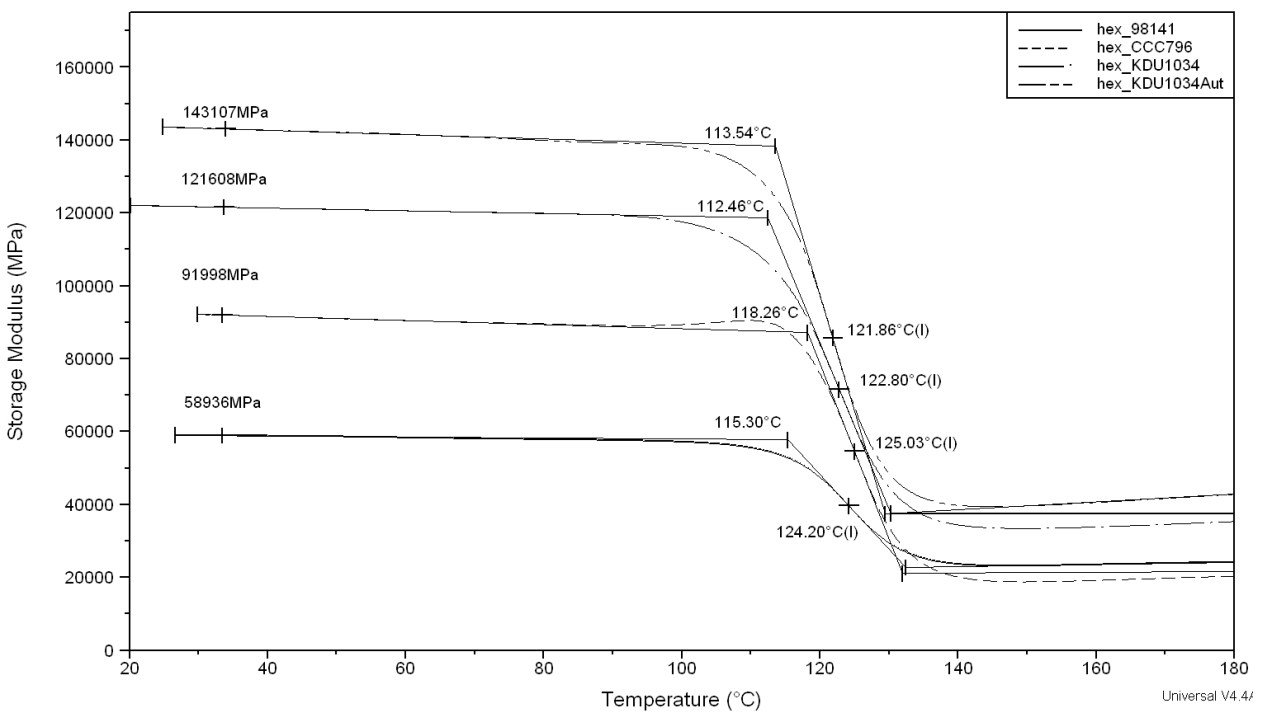
Fig. 136: Storage modulus curves for the four laminates produced with Hexion L418 epoxy matrix. Tested in 3P-bending with 3 K/min to 200°C (Amplitude = 70 μm, Frequency = 1Hz).

109

5.3.3.4 *Pultruded profile R/L20-T/HTSTS/UD65f*

DMA results for the pultruded rods with L20 matrix are shown in Fig. 137. Each sample was measured using two consecutive and identical heating cycles under the same conditions. The values obtained for the glass transition temperature from storage modulus (green) and tan delta (red) curves are indicated as well as the storage modulus at room temperature.
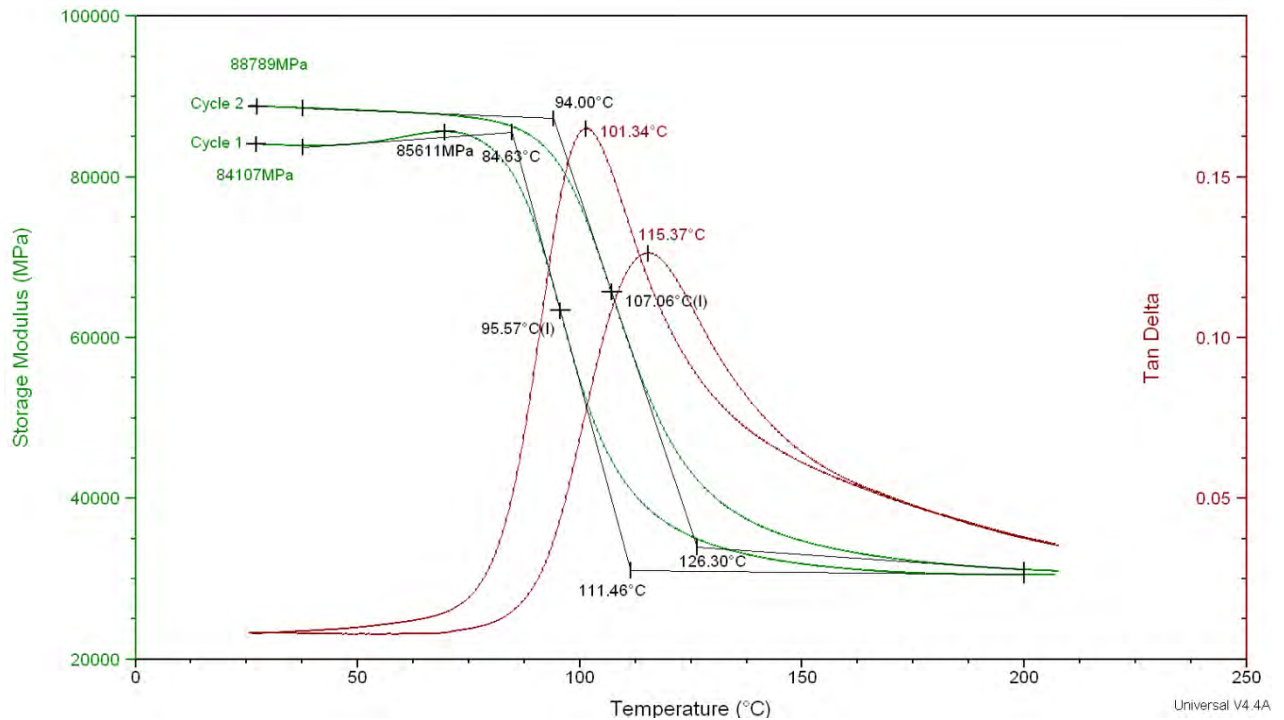
Fig. 137: DMA curves for a sample in as received condition tested using two consecutive heating cycles. Tested in 3P-bending tested with heating rate 3 K/min to 210°C. Amplitude = 70 μm, Frequency = 1Hz.

DMA was carried out not only on samples in as received condition but also on samples who had been submitted to the heat treatments mentioned in chapter 4.2.3. Average results for all studied conditions are shown in Tab. 26.

Sample code	Cycle	E'_{RT} [GPa]	T_g [°C] (Storage modulus)	T_g [°C] (Loss factor)
DMA-AR	1st	91 ± 6	84 – **95 ± 1.5** – 111	101 ± 1
	2nd	93 ± 5	93 – **107 ± 0.8** – 126	116 ± 2
DMA-HT(100-2h)	1st	90 ± 2	90 – **101 ± 0.6** – 117	107 ± 0
	2nd	92 ± 1	99 – **111 ± 0.6** – 131	118 ± 1
DMA-HT(140-2h)	1st	94 ± 3	96 – **107 ± 0.3** – 123	112 ± 2
	2nd	98 ± 1	105 – **116 ± 0.7** – 134	122 ± 3

Tab. 26: DMA results obtained for pultruded rods with L20 matrix in as received condition and after certain heat treatments. Storage modulus at room temperature and glass transition values obtained from the storage modulus step and from the tan delta maximum are shown for each one of the consecutive heating cycles.

5.3.3.5 *Pultruded profile R/Sika/Sigrafil-T700SC/UD65f*

DMA results for the pultruded rods with Sika matrix are shown in Fig. 138. Each sample was measured using two consecutive and identical heating cycles under the same conditions.
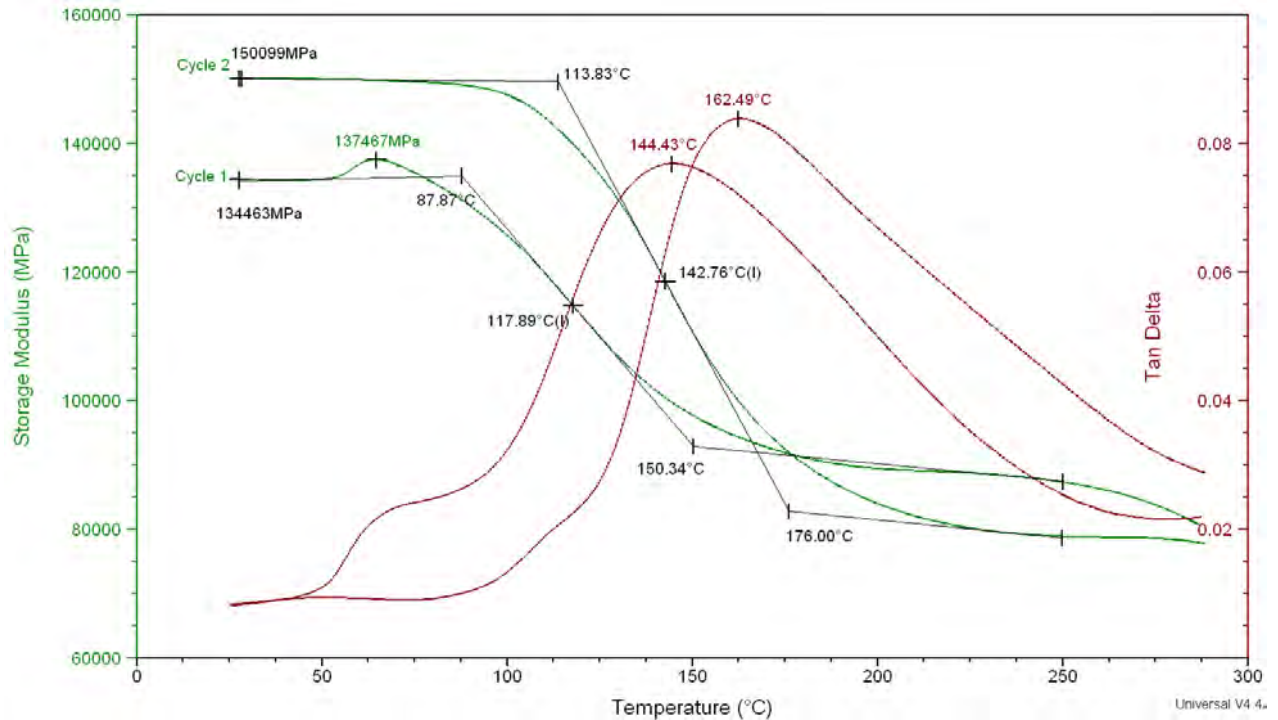
Fig. 138: DMA curves for a sample in as received condition tested using two consecutive heating cycles. Heating rate was 3 K/min to 290°C. Amplitude = 70 μm, Frequency = 1Hz. Post curing of the resin is observed as a maximum on the storage modulus curve during the first cycle with at about 65°C. The values obtained for the glass transition temperature from storage modulus (green) and tan delta (red) curves are indicated as well as the storage modulus at room temperature.

DMA was also carried out on samples after submitting them to the heat treatments mentioned in chapter 4.2.3. Results for as received and all heat treated conditions are shown in Tab. 27.

Sample code	Cycle	E'_{RT} [GPa]	T_g [°C] (Storage modulus)	T_g [°C] (Loss factor)
DMA-AR	1st	129 ± 6	91 – **117 ± 1** – 152	145 ± 1
	2nd	144 ± 8	123 – **141 ± 2** – 175	161 ± 2
DMA-HT(90-4h)	1st	139 ± 2	87 – **123 ± 2** – 163	152 ± 3
	2nd	145 ± 9	118 – **145 ± 2** – 178	165 ± 1
DMA-HT(120-3h)	1st	129 ± 13	106 – **125 ± 0** – 162	153 ± 1
	2nd	141 ± 11	119 – **148 ± 5** – 183	170 ± 6
DMA-HT(120-4h)	1st	128 ± 8	109 – **122 ± 3** – 158	151 ± 1
	2nd	143 ± 6	112 – **139 ± 3** – 174	162 ± 3
DMA-HT(120-5h)	1st	132 ± 14	108 – **123 ± 1** – 162	156 ± 2
	2nd	142 ± 9	114 – **143 ± 1** – 178	165 ± 0
DMA-HT(160-6h)	1st	123 ± 19	113 – **133 ± 1** – 168	154 ± 2
	2nd	136 ± 17	114 – **140 ± 1** – 174	160 ± 2
DMA-HT(190-10h)	1st	124 ± 3	115 – **134 ± 2** – 168	155 ± 6
	2nd	138 ± 3	111 – **139 ± 2** – 175	163 ± 4

Tab. 27: DMA results obtained for pultruded rods with Sika CR141 matrix in as received condition and after certain heat treatments. Storage modulus at room temperature and glass transition value obtained from the storage modulus step and from the tan delta maximum are shown for both heating cycles.

5.3.4 Thermomechanical Analysis (TMA)

Results obtained for all studied CFRPs are summarized in Tab. 28. Glass transition temperature (Tg) and coefficient of thermal expansion (CTE_1 and CTE_2) corresponding to the lineal regions before and after the glass transition are presented.

Each sample was tested using two consecutive heating-cooling cycles applying adequate temperature intervals for each matrix system as indicated in Tab. 18. Sika CR132 laminates are 100% cured in as received condition, therefore both cycles were evaluated to obtain values of Tg and CTE. The other studied CFRPs were delivered in a partially cured condition, since cross-linking effects hinder the evaluation of the first cycle only the second can be evaluated. Tg can be determined for both cycles whereas CTE values only for the second.

Sample	Direction	1st Cycle			2nd Cycle		
		Tg1 (°C)	CTE_1 (μm/m·°C)	CTE_2 (μm/m·°C)	Tg2 (°C)	CTE_1 (μm/m·°C)	CTE_2 (μm/m·°C)
HexPly8552 Laminates							
HSAS4/UD58f/0.2MPa/1	0°	-	-	-	-	0.0 ± 0.2	0.2 ± 0.2
	90°	191±3	-	-	203±3	26 ± 1	78 ± 1
HSAS4/UD58f/0.2MPa/2	0°	-	-	-	-	0.4 ± 0.2	0.5 ± 0.2
	90°	189±3-	-	-	200±3	26	76
Sika CR132 Laminates							
Pure Biresin CR132	isotropic	131	71	167	126	71	137
FT300B/0-90°/1bar/3	0°	-	3	2	-	5	2
	90° I	x	x	x	x	x	x
	90° II	117	80	254	119	78	255
HTA40/UD/1bar/3	0°	-	0	0	-	1	0
	90° I	122	39	67	112	37	68
	90° II	128	51	175	117	51	177
HTS5631/UD/1bar/3	0°	-	-1	1	-	0	1
	90° I	130	15	32	122	17	40
	90° II	134	39	103	122	44	114
HTS5631/UD/3bar/4	0°	-	0	0	-	0	1
	90° I	124	28	83	119	34	90
	90° II	131	34	91	117	40	105
L20 pultruded Tubes							
T/HTSTS/UD65f	0°	-	-	-	-	0.8 ± 0.3	0 ± 0.5
	90°	78±2	-	-	91 ±4	49 ± 3	146 ± 13

Tab. 28: Results obtained for TMA analysis in fibre direction and perpendicular to it, for all heating cycles and all studied composites. Values corresponding to the lineal regions before the glass transition CTE_1 and after CTE_2.

5.3.4.1 *Laminates HexPly8552*

Samples tested in fibre direction (°0) showed almost no dimensional change, for this reason no glass transition temperature values can be obtained. The obtained CTE values are close to cero and constant through the whole heating cycle. This was expected since C-fibre have a slightly negative CTE value that compensates the matrix positive one [2] [91] [92].

5.3.4.2 *Laminates Sika Biresin CR132 matrix*
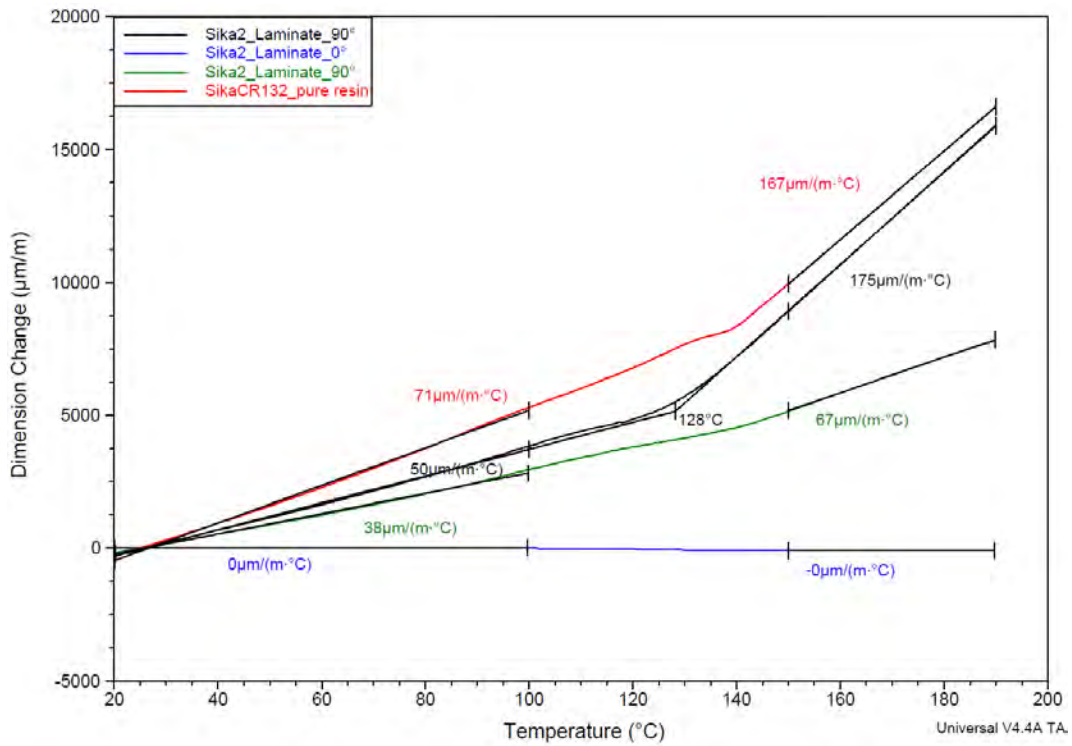
Fig. 139: Sik/HTA40/UD/1bar/3 laminates. One specimen, first cycle in all directions, perpendicular and in fibre direction twice. The red curve correspond to a pure epoxy sample, without reinforcement.

5.3.4.3 *Pultruded profile T/L20-T/HTSTS/UD65f*
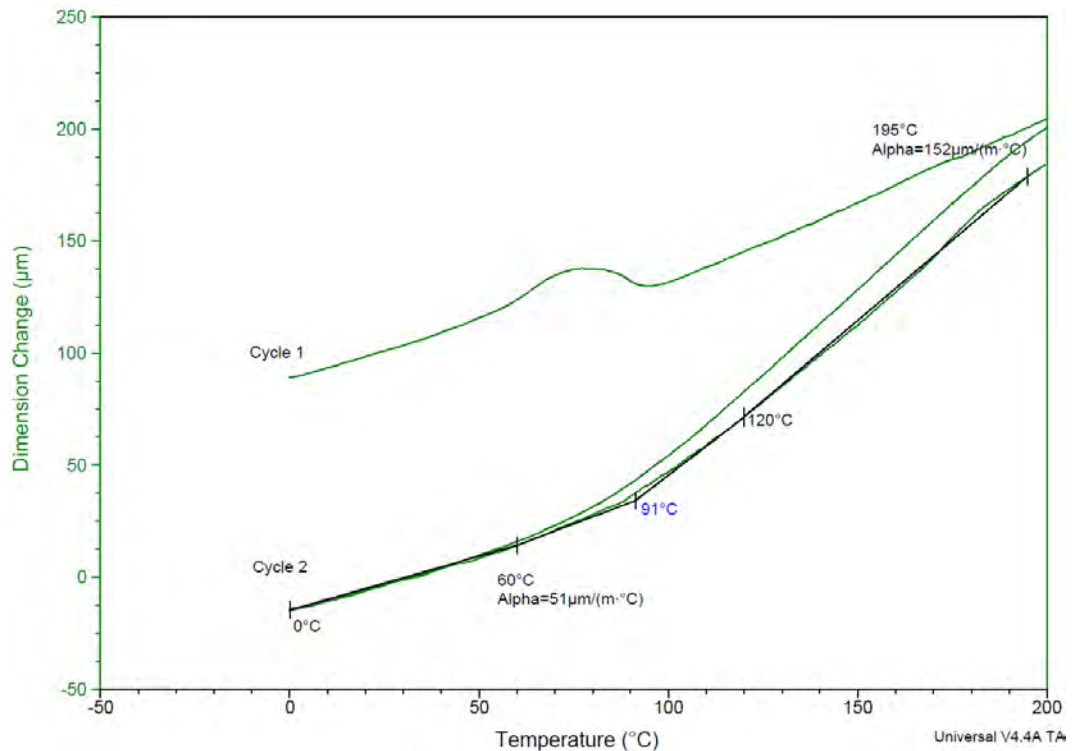
Fig. 140: Two cycles 90° to fibre. Linear CTE values before and after Tg, which occurs at about 91°C.

5.4 Mechanical Testing

5.4.1 Torsion tests

Torsion test was made on three different pultruded profiles with circular cross section; tubes with outer and inner diameter of 10 and 8 mm and rods with a diameter of 10 mm.

5.4.1.1 *Pultruded profile T/L20-T/HTSTS/UD65f*

Fig. 141 shows the stress-strain diagram of a sample tested until failure without hysteresis loops and figures Fig. 142 and Fig. 143 the stress-strain diagram of samples loaded with four and three hysteresis loops respectively. Tab. 29 contains the shear modulus, ultimate failure stress and maximum torque-angle values of all tested samples with and without hysteresis cycles. A decrease of the shear modulus after each loading-unloading cycle was observed for all samples tested with hysteresis cycles. During testing acoustic emission signals were recorded in-situ, AE results are shown in chapter 5.5.1. Samples were imaged by means of XCT before and after testing, the corresponding results are shown in section 5.5.3.
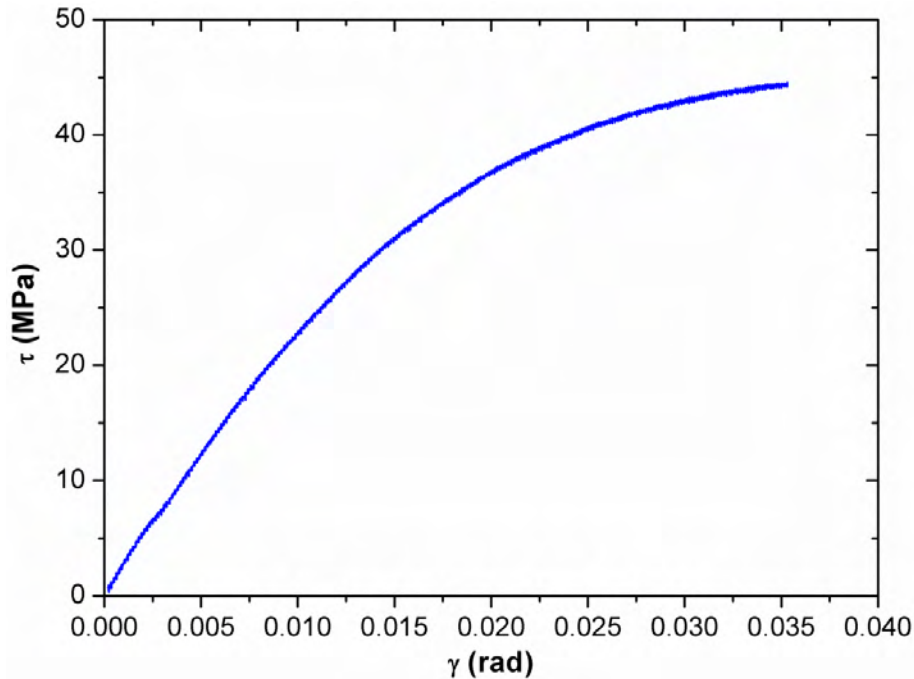
Fig. 141: Shear stress-shear strain diagram of sample $T_{10}\_L20\_01$ tested monotonically until failure.

Sample	$G_{tangent} \pm 0.1$(GPa)	$\tau_u \pm 0.1$(MPa)	$M_{T\,max} \pm 0.1$ (Nm)	$\theta_{max} \pm 0.001$(°)
$T_{10}\_L20\_01$	2.3	42.2	4.9	49.9°
$T_{10}\_L20\_02$	2.4	44.0	5.1	44.5°
Hysteresis	$G_{secant} \pm 0.1$(GPa)	$\tau_u \pm 0.1$(MPa)	$M_{T\,max} \pm 0.1$(Nm)	$\theta_{max} \pm 0.001$(°)
$T_{10}\_L20h1\text{-}3c$	G_1=3.3 G_2=3.1 G_3=2.9	interrupted	-	$\rightarrow$25°
$T_{10}\_L20h2\text{-}4c$	G_1=3.4 G_2=2.9 G_3=2.7 G_4=2.6	interrupted	-	$\rightarrow$35°
$T_{10}\_L20h3\text{-}3c$	G_1=3.1 G_2=2.7 G_3=2.4	38.8	4.5	39.3°
$T_{10}\_L20h4\text{-}3c$	G_1=2.8 G_2=2.5 G_3=2.2	37.9	4.4	53.5°

Tab. 29: Shear modulus (G), ultimate failure stress (τ_u) and maximal torque and angle values including the error of all samples tested. Samples tested with three or four hysteresis cycles h1-h4.
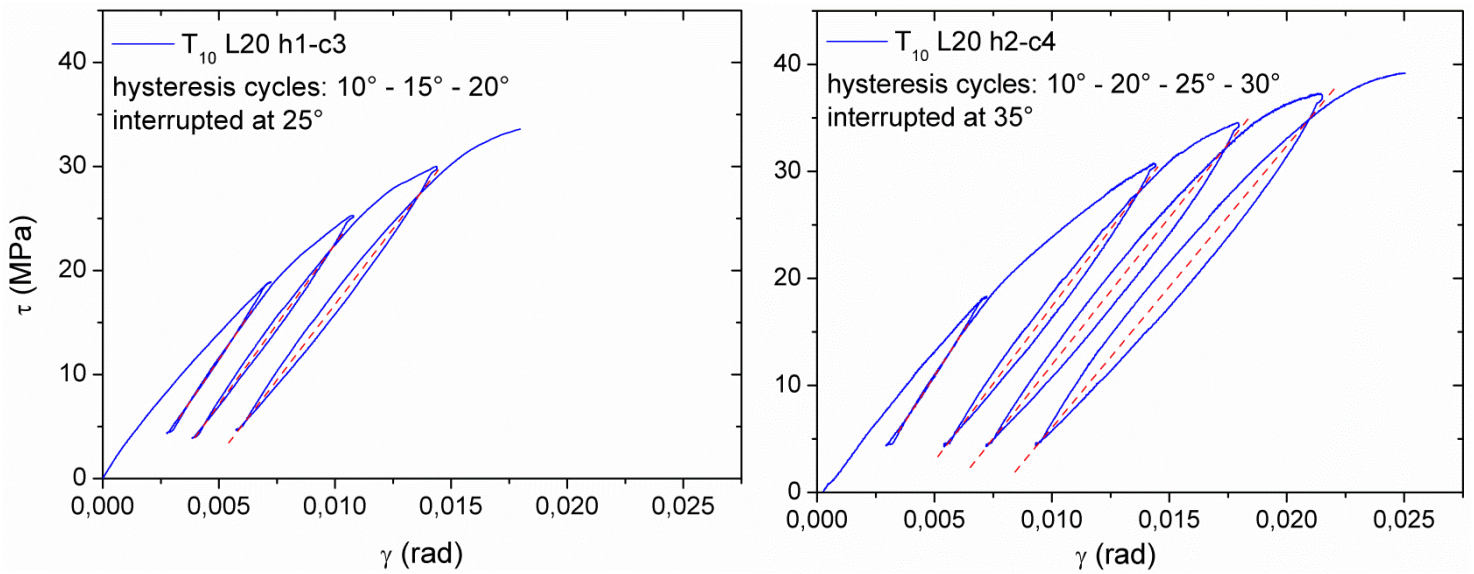
Fig. 142: Shear stress-shear strain diagram of samples T10_L20h1-3c and T10_L20h2-4c. Tested in torsion with three and four hysteresis cycles. Values of shear modulus for each hysteresis loop are summarized in Tab. 29. The tests were interrupted at 25° and 35° degrees twisting angle for further analysis with XCT (see section 5.5.3). In-situ acoustic emission measurements are shown in chapter 5.5.1.
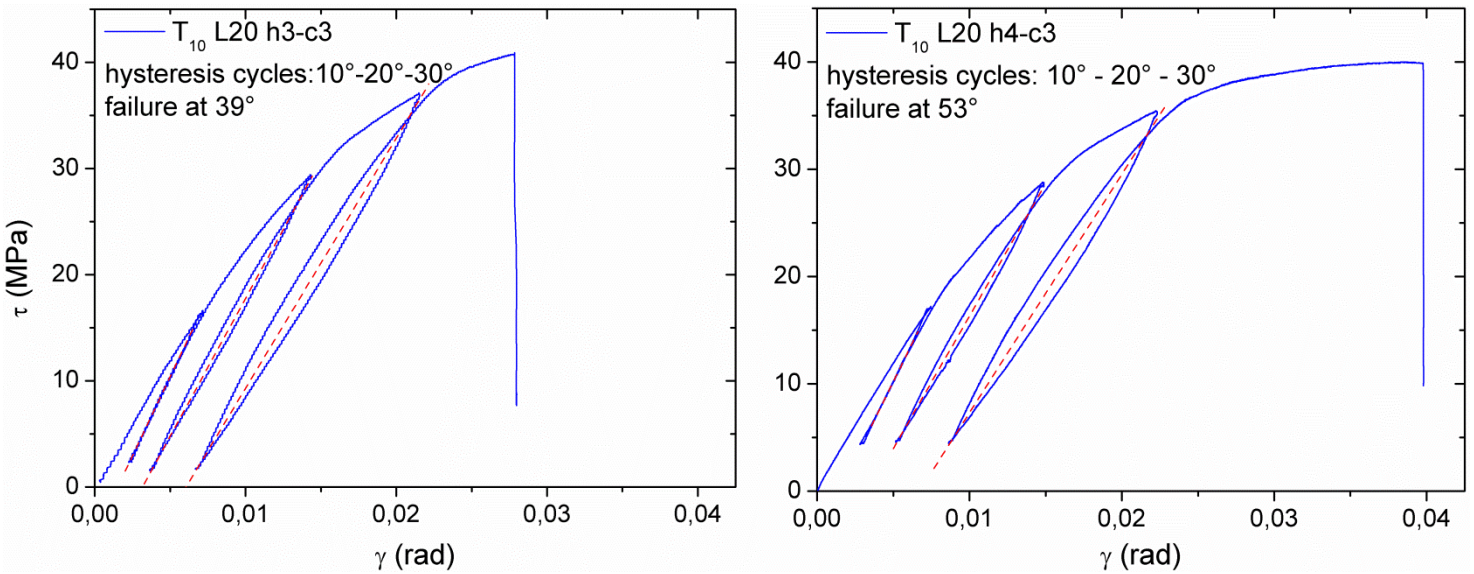
Fig. 143: Shear stress-shear strain diagram of samples T10_L20h3-3c and T10_L20h4-3c tested with hysteresis cycles until failure. Values of shear modulus for each hysteresis loop are summarized in Tab. 29. Acoustic emission signals were recorded in-situ, AE results are presented in chapter 5.5.1. Post mortem analysis with XCT is shown in section 5.5.3. Fractography of the samples is presented in chapter 5.5.4.

115

5.4.1.2 *Pultruded profile R/L20-T/HTSTS/UD65f*

Three kinds of measurements were done. Monotonic torsion test using different strain rates (1×10^{-3}, 3×10^{-3}, 5×10^{-3}, 7×10^{-3} and 10×10^{-3} rad/s). Modulated torsion test with amplitude 10^{-3} and a constant strain rate of 5×10^{-3} rad/s. Low cycle fatigue tests with loading-unloading cycles, to study damage evolution under torsion loading. Results are presented in Tab. 30.

Sample	Strain rate (rad/s)	$G_{tangent} \pm$ 0.1 (GPa)	$1^{st}\ M_{T\ max} \pm$ 0.1 (Nm)	$1^{st}\ \tau_u \pm$ 0.1 (MPa)	$2^{nd}\ M_{T\ max} \pm$ 0.1 (Nm)	$2^{nd}\ \tau_u \pm$ 0.1 (MPa)	$\Delta L \pm 0.01$ (mm)
R_{10}_L20_01	1×10^{-3}	1.4	1.4	55.4	-	-	n.a.
R_{10}_L20_02	1×10^{-3}	1.4	1.2	48.1	0.8	34.2	-0.06
R_{10}_L20_03	3×10^{-3}	1.5	1.1	44.8	1.2	49.7	-0.14
R_{10}_L20_04	3×10^{-3}	1.4	1.4	57.4	1.1	43.6	-0.15
R_{10}_L20_05	5×10^{-3}	1.5	1.4	58.7	1.5	62.7	-0.40
R_{10}_L20_06	5×10^{-3}	1.6	1.9	77.4	1.9	78.6	-0.45
R_{10}_L20_07	7×10^{-3}	1.5	1.2	47.7	1.3	55.0	-0.51
R_{10}_L20_08	0.01	1.4	1.4	55.4	1.3	53.8	-0.41
Modulated	Strain rate (rad/s)	$G_{tangent} \pm$ 0.1 (GPa)	$1^{st}\ M_{T\ max} \pm$ 0.1 (Nm)	$1^{st}\ \tau_u \pm$ 0.1 (MPa)	$2^{nd}\ M_{T\ max} \pm$ 0.1 (Nm)	$2^{nd}\ \tau_u \pm$ 0.1 (MPa)	$\Delta L \pm 0.01$ (mm)
R_{10}_L20_m1	5×10^{-3}	1.4	1.0	39.5	1.1-1.2	46.0-50.5	-0.47
Hysteresis	Strain rate (rad/s)	$G_{secant,\ cycle} \pm$ 0.1 (GPa)				ΔL (mm)	
R_{10}_L20_h1 - 23c	5×10^{-3}	G_1=1.5	G_2=1.3	G_3=0.6	G_4=0.4	-0.20	

Tab. 30: Results obtained for the L20 rods. Shear modulus, ultimate shear strength (maxima before first fibre failure and at the end) and change in elongation (ΔL) of the sample in z direction.
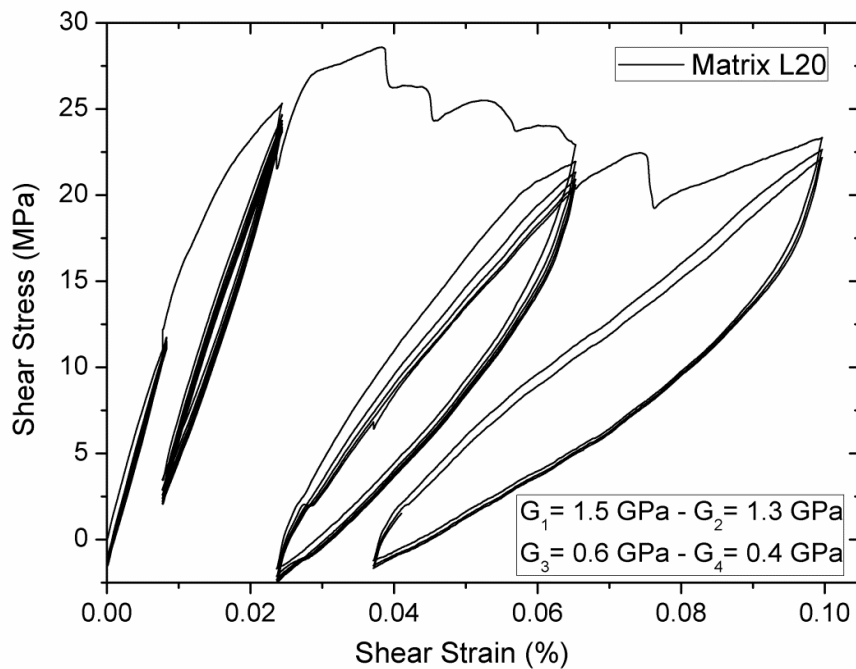
Fig. 144: Sample R_{10}_L20_ L20_h1 - 23c. Strain rate 5×10^{-3} rad/s. Four consecutive series of loading-unloading cycles with constant deformation values (9x0.2rad - 6x0.4rad - 5x1rad - 3x1.5rad) were applied. Shear modulus decreases with each loading-unloading cycle.
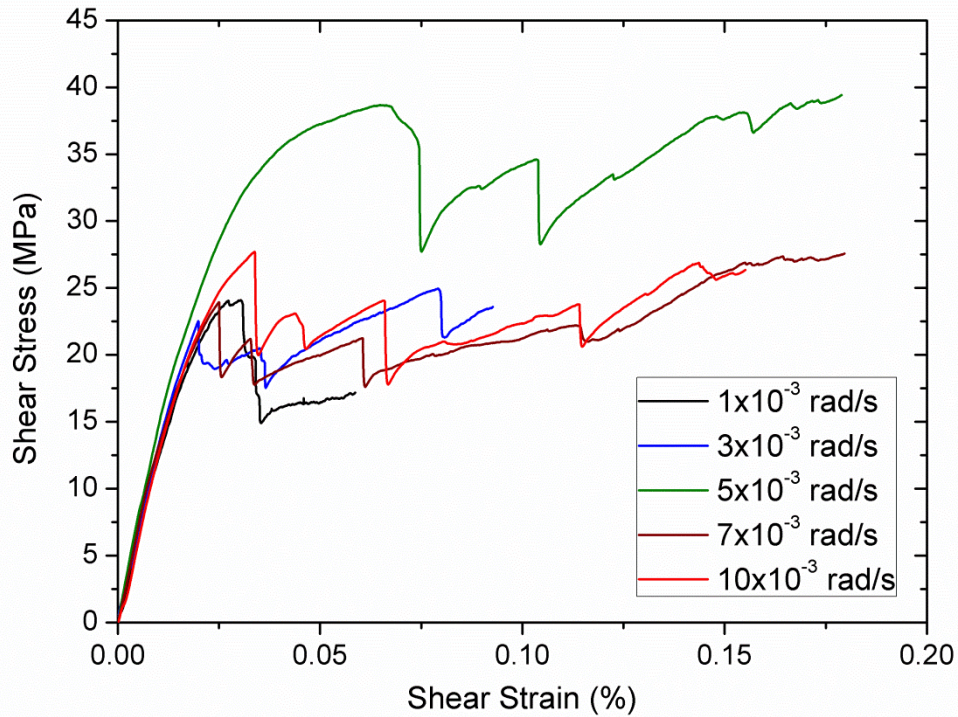
Fig. 145: Shear stress vs. shear strain curves obtained for the L20 rods at the different applied strain rates. Two or more maximal values of M_T are observed, this is related to stepwise fibre failure.

Exemplary curves for each tested strain rate are shown in Fig. 145, the curve corresponding to 5×10^{-3} rad/s is shown in Fig. 146, where also elongation change is plotted. It is observed that each sudden strength drop corresponds to a shortening of the specimens length. These steps correspond to fibre bundle failure.
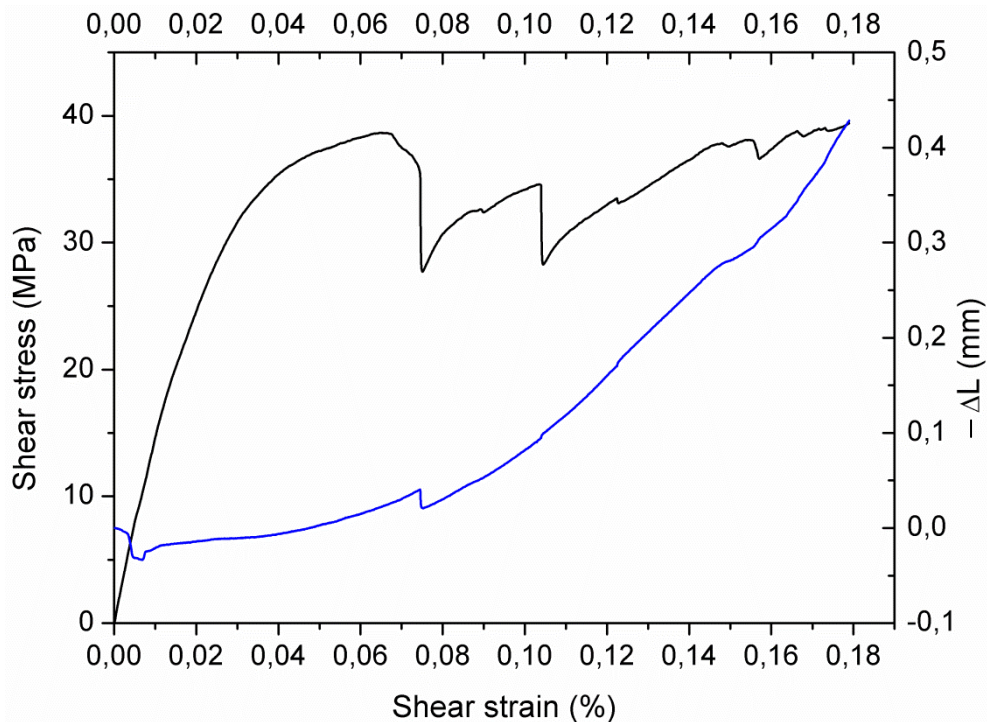
Fig. 146: Shear stress-strain curve for sample $R_{10}\_L20\_06$ tested with a strain rate of 5×10^{-3} rad/s. The blue curve corresponds to the elongation change of the sample recorded simultaneously during testing.

117

5.4.1.3 *Pultruded profile R/Sika/Sigrafil-T700SC/UD65f*

Three kinds of measurements were done. Monotonic torsion test using different strain rates (1×10^{-3}, 3×10^{-3}, 5×10^{-3}, 7×10^{-3} and 10×10^{-3}). Modulated torsion test with amplitudes 0.5×10^{-3} and 1×10^{-3} and a constant strain rate of 5×10^{-3} rad/s. Low cycle fatigue tests with loading-unloading cycles to study damage evolution under torsion loading. Results in Tab. 31.

Sample	Strain rate (rad/s)	$G_{tangent} \pm$ 0.1 (GPa)	$1^{st} M_{T\,max}$ $\pm$ 0.1 (Nm)	$1^{st} \tau_u \pm$ 0.1 (MPa)	$2^{nd} M_{T\,max}$ $\pm$ 0.1 (Nm)	$2^{nd} \tau_u \pm$ 0.1 (MPa)	ΔL (mm)
R_{10}_Sika_01	1×10^{-3}	2.1	1.5	59.5	1.5	59.5	n.a.
R_{10}_Sika_02	3×10^{-3}	2.2	1.7	68.9	2.1-1.9	85.6-79.0	-1.51
R_{10}_Sika_03	5×10^{-3}	2.0	1.8	74.1	2.4-2.2	99.0-88.4	-1.49
R_{10}_Sika_04	5×10^{-3}	1.9	1.4	57.0	1.8-1.8	74.6-73.7	-1.13
R_{10}_Sika_05	7×10^{-3}	2.1	1.6	63.6	2.0-2.8	83.5-116.1	-2.24
R_{10}_Sika_06	0.01	2.1	1.6	65.6	2.0-2.1	81.5-86.4	-2.25
Modulated	Strain rate (rad/s)	$G_{tangent} \pm$ 0.1 (GPa)	$1^{st} M_{T\,max}$ $\pm$ 0.1 (Nm)	$1^{st} \tau_u \pm$ 0.1 (MPa)	$2^{nd} M_{T\,max}$ $\pm$ 0.1 (Nm)	$2^{nd} \tau_u \pm$ 0.1 (MPa)	$\Delta L \pm 0.01$ (mm)
R_{10}_Sika_m1	5×10^{-3}	2.2	1.8	71.7	2.2	89.2	-0.74
R_{10}_Sika_m2	5×10^{-3}	2.1	1.7	70.9	1.9	79.0	-0.40
R_{10}_Sika_m3	5×10^{-3}	2.1	1.5	62.7	1.8	75.4	-0.40
Hysteresis	Strain rate (rad/s)	$G_{secant,\,cycle} \pm 0.1$ (GPa)				ΔL (mm)	
R_{10}_Sika_h1 - 27c	5×10^{-3}	G_1=2.0	G_2=1.7	G_3=1.4	G_4=1.0	-1.1	

Tab. 31: Results obtained for the Sika rods. Shear modulus, ultimate shear strength (maxima before first fibre failure and at the end) and change in elongation (ΔL) of the sample in z direction.
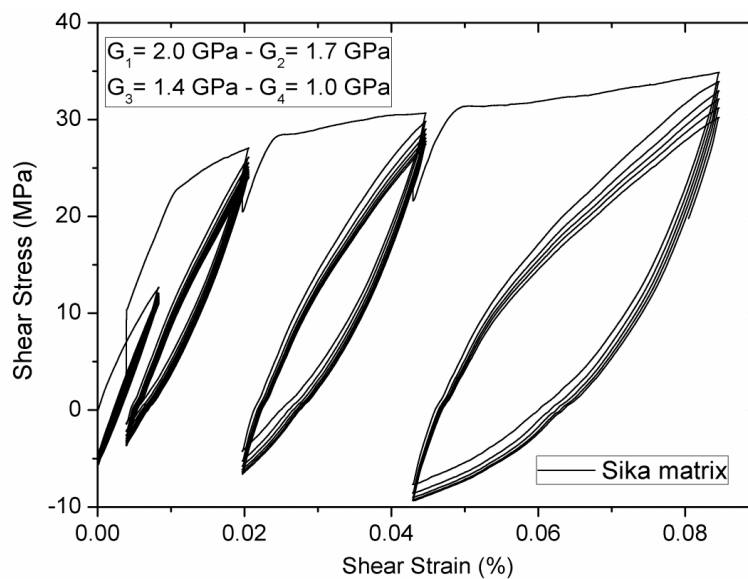
Fig. 147: Sample R_{10}_Sika_ h1 - 27c. Strain rate 5×10^{-3} rad/s. Four consecutive series of loading-unloading cycles with constant deformation values (8x0.2rad - 8x0.4rad - 6x0.6rad - 5x1rad) were applied.

118
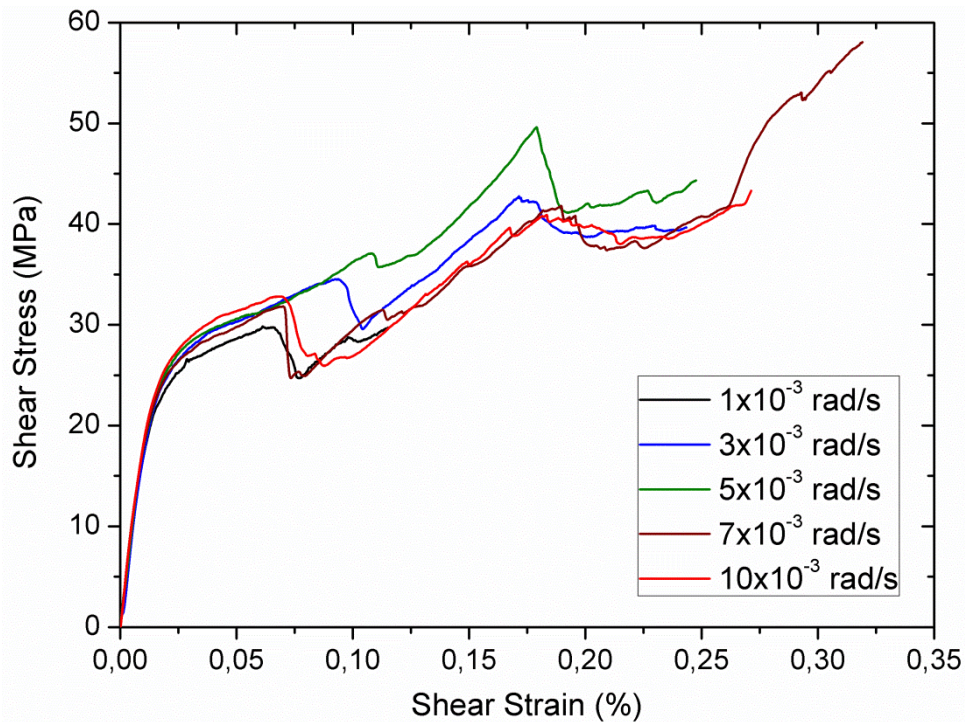
Fig. 148: Shear stress vs. shear strain curves obtained for the Sika rods at the different applied strain rates. Two or more maximal values of M_T are observed, this is related to stepwise fibre failure.

Exemplary curves for each tested strain rate are shown in Fig. 148, the curve corresponding to $5x10^{-3}$ rad/s is shown in Fig. 149, where also elongation change is plotted. It is observed that each sudden strength drop corresponds to a shortening of the specimens length. These steps correspond to fibre bundle failure.
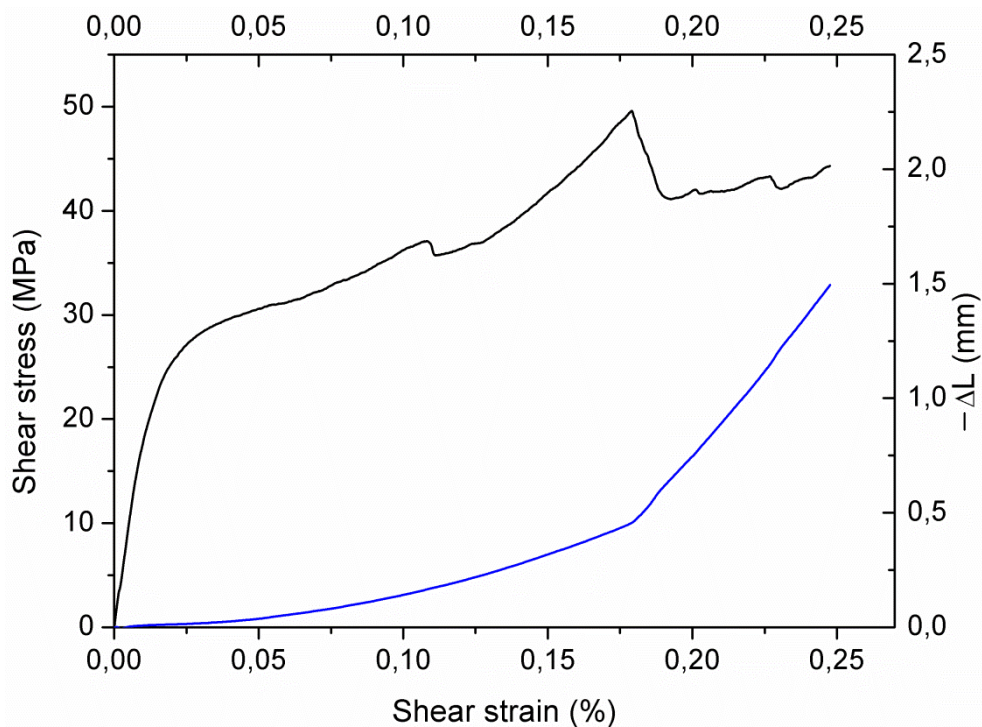
Fig. 149: Shear stress-strain curve for sample R_{10}_Sika_03 tested with a strain rate of $5x10^{-3}$ rad/s. The blue curve corresponds to the elongation change of the sample recorded simultaneously during testing.

Modulated measurements for both kinds of pultruded rods are shown in Fig. 150.
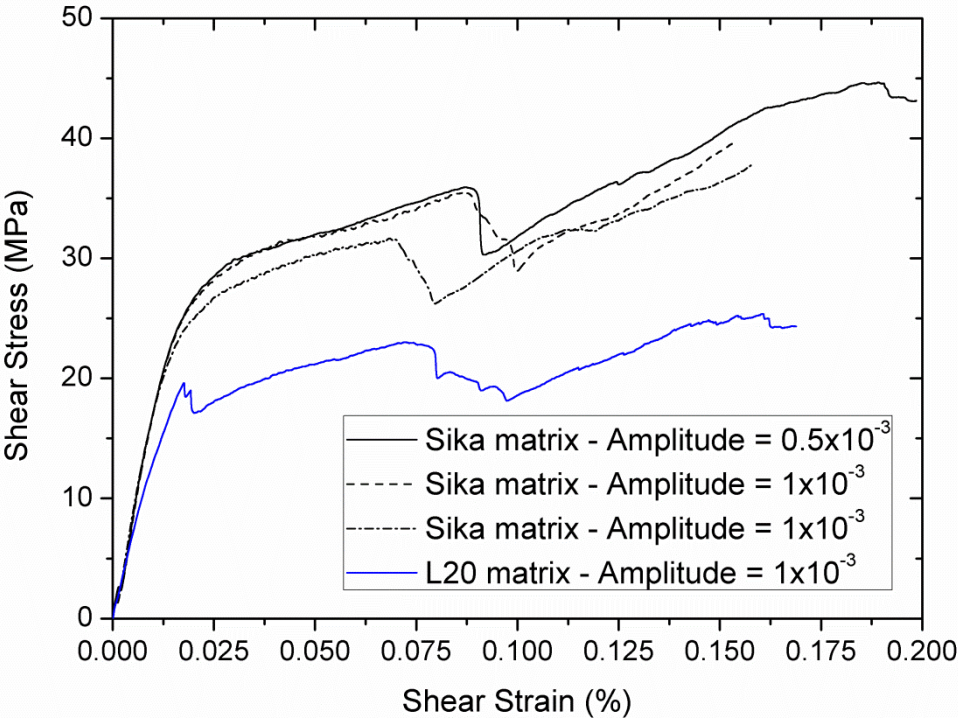
Fig. 150: Shear stress-strain curves for all samples tested with modulated strain rates.

Shear stress-strain curves for Sika CR 141 or L20 pultruded rods is presented in Fig. 151.
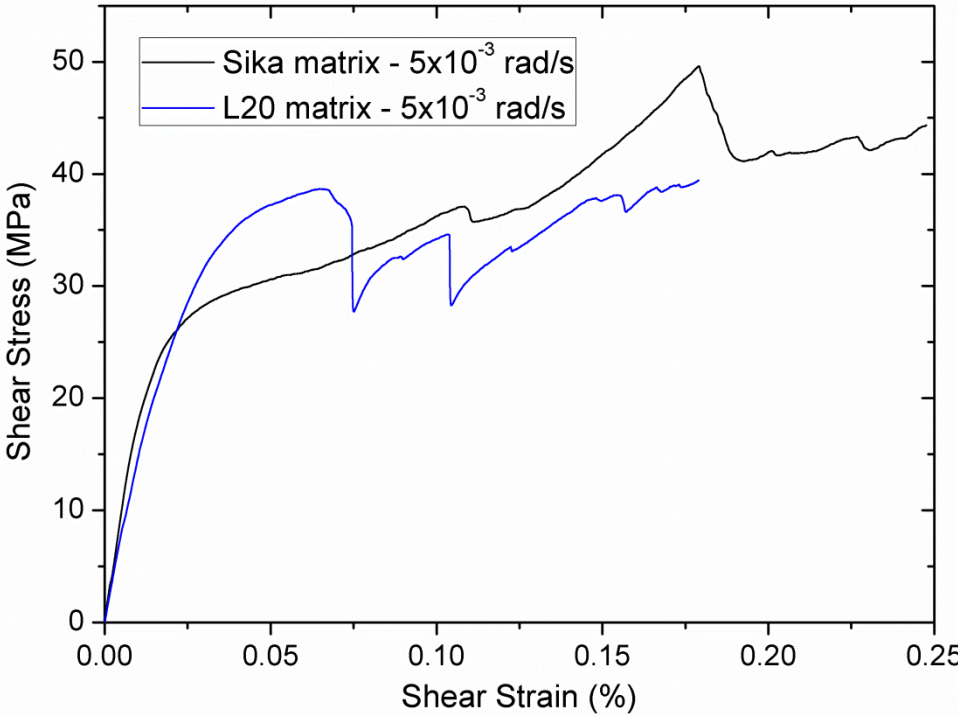
Fig. 151: Shear stress-strain curves at the same strain rate for pultruded specimens with the two different matrix systems. After first fibre breakage L20 rods show no higher strength values whereas Sika CR141 rods experience plastic deformation and reach strength values twice as high as in the elastic region.

5.4.2 Four-point bending test

Twelve different materials were studied, not only laminates but also pultruded rod profiles who were machined to flat specimens with the dimensions specified in Tab. 19. In Tab. 32, average results for as received and heat treated conditions are summarized. Detailed results can be found in annex E.

Sample	E_b (GPa)	σ_u (MPa)	ε_u (%)	ε_f (%)
HexPly8552 Laminates				
HSAS4/UD58f/0.2MPa/1	126 ± 5	1644 ± 79	1.5 ± 0.1	-
HSAS4/UD58f/0.2MPa/2	133 ± 4	1956 ± 186	1.7 ± 0.3	-
Sika CR132 Laminates				
Sik/FT300B/0-90°/P3-4P-0°	43 ± 3	544 ± 33	1.27 ± 0.10	-
Sik/HTA40/UD/P3-4P-0°	93 ± 3	794 ± 50	0.87 ± 0.03	-
Sik/HTS5631/UD/P3-4P-0°	103 ± 7	795 ± 39	0.79 ± 0.03	-
Sik/HTS5631/UD/P4-4P-0°	111 ± 8	918 ± 53	0.85 ± 0.03	-
Hexion L418 Laminates				
Hex/FT300/0-90°/P5-4P-0°	48 ± 1	611 ± 35	1.28 ± 0.11	-
Hex/HTA40/UD/P5-4P-0°	98 ± 4	741 ± 36	0.79 ± 0.04	-
Hex/HTS5631/UD/P5-4P-0°	116 ± 3	739 ± 24	0.66 ± 0.03	-
Hex/HTS5631/UD/P6-4P-0°	123 ± 3	973 ± 48	0.80 ± 0.03	-
L20 pultruded rods				
R/L20-T/HTSTS/UD-4P-0°-AR	85 ± 6	1026 ± 76	1.16 ± 0.06	1.32 ± 0.12
R/L20-T/HTSTS/UD-4P-0°-HT1	88 ± 4	994 ± 62	1.12 ± 0.07	1.42 ± 0.17
R/L20-T/HTSTS/UD-4P-0°-HT2	88 ± 7	1046 ± 82	1.16 ± 0.03	1.19 ± 0.03
R/L20-T/HTSTS/UD-4P-0°-HT3	92 ± 5	1070 ± 66	3.14 ± 0.27	1.27 ± 0.02
Sika CR 141 pultruded rods				
R/Sika/Sig-T700/UD-4P-0°-AR	126 ± 9	1256 ± 88	1.07 ± 0.15	2.45 ± 0.62
R/Sika/Sig-T700/UD-4P-0°-HT1	107 ± 14	1150 ± 137	1.11 ± 0.06	2.22 ± 0.48
R/Sika/Sig-T700/UD-4P-0°-HT2	105 ± 19	1142 ± 219	1.35 ± 0.28	1.99 ± 0.53
R/Sika/Sig-T700/UD-4P-0°-HT3	102 ± 6	1111 ± 16	1.10 ± 0.08	1.69 ± 0.34
R/Sika/Sig-T700/UD-4P-0°-HT4	104 ± 17	1135 ± 157	1.09 ± 0.05	1.89 ± 0.51
R/Sika/Sig-T700/UD-4P-0°-HT5	110 ± 6	1218 ± 104	1.21 ± 0.10	2.33 ± 0.31

Tab. 32: Bending properties of all studied samples.

For the pultruded samples two different strain values are indicated: ε_u (ultimate strain) the strain corresponding to the stress maximum, and ε_f (final strain), which is the final strain achieved immediately before sample failure. Between this two points the samples exhibit relatively high strength and the stepwise failure of single fibre tows can be seen as stress drop down steps.

5.4.2.1 *Laminates HexPly8552*

Results for the HexPly8552 prepreg based laminates, manufactured with P1 and P2 process, tested in fibre direction (°0) are shown in Tab. 32.

Fig. 152 shows exemplarily the stress-strain curves of a P1 and a P2 sample tested monotonic until failure. Curves corresponding to two P1 samples are shown in Fig. 153 left, one tested with three loading-unloading cycles (reversal points at 300, 600 and 850 N) and another tested with nine loading-unloading cycles (reversal points at 300, 600, 700, 750, 800, 850, 900, 950 and 1000 N). Fig. 153 right shows the results obtained for P2 specimens loaded with the same hysteresis cycles with three and nine loading-unloading cycles.

Coupled in-situ acoustic emission (AE) measurements were done during testing of some specimens with and without hysteresis cycles. Some test were interrupted for XCT analysis, results are shown in section 5.5.3.
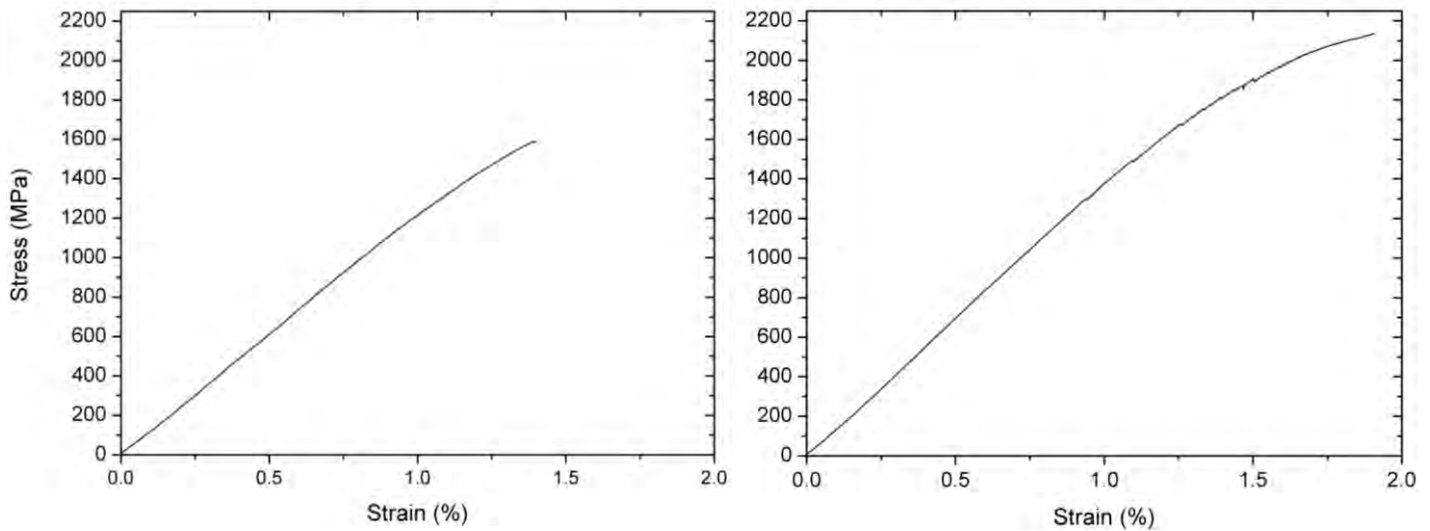
Fig. 152: Sample HexPly8552/P1-4P-0°-01 (left) and sample HexPly8552/P2-4P-0°-06 (right) tested in four point bending in fibre direction with a constant strain rate of 5 mm/min until failure.
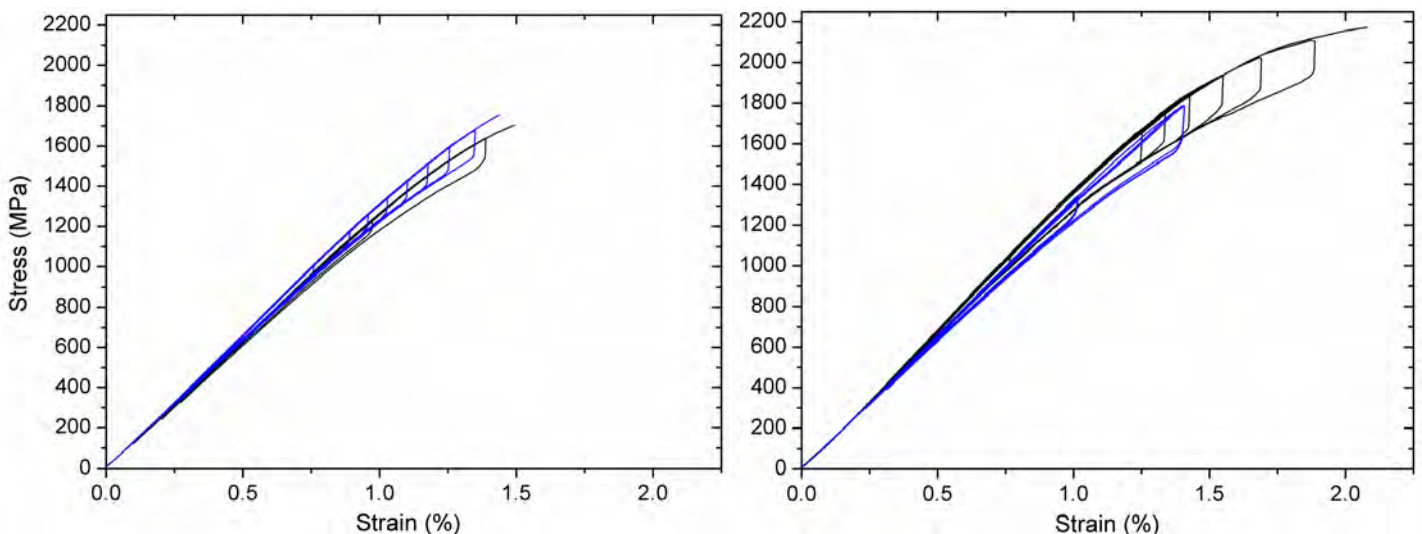
Fig. 153: Samples HexPly8552/P1-4P-0°-08 and 12 (left). Samples HexPly8552/P2-4P-0°-05 and 11 (right).

5.4.2.2 *Laminates Sika Biresin CR132 matrix*

The results for the four different Sika CR132 based laminates tested in fibre direction (°0) are shown in Tab. 32. Fig. 154 shows four exemplary stress-strain curves obtained for monotonic tests until failure.
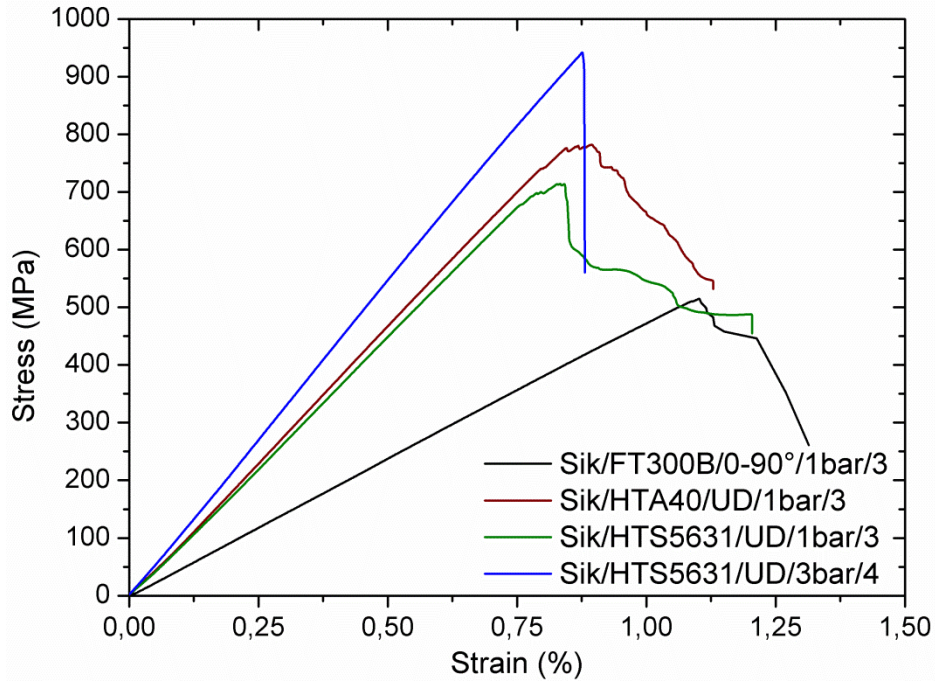
Fig. 154: Exemplary stress-strain curves for each of the four different laminates tested in four point bending in fibre direction with a constant strain rate of 5 mm/min until failure.

Fig. 155 and Fig. 156 show curves for samples tested with various loading-unloading cycles. Bending E-Modulus remains constant despite the cyclic load applied.
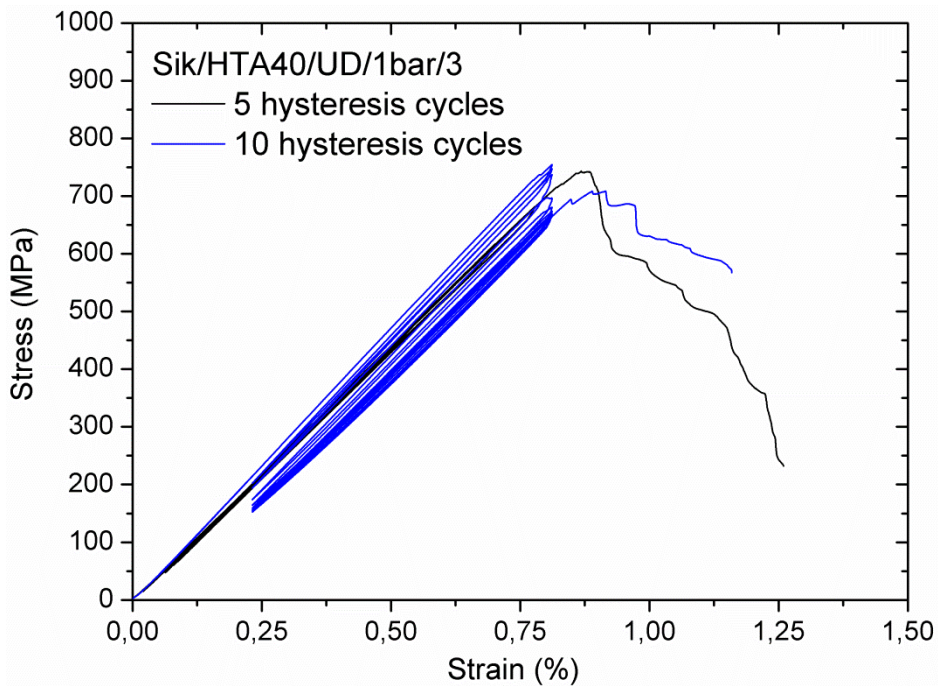
Fig. 155: Samples Sik/HTA40/UD/P3/h1-5c in black and Sik/HTA40/UD/P3/h2-10c in blue.
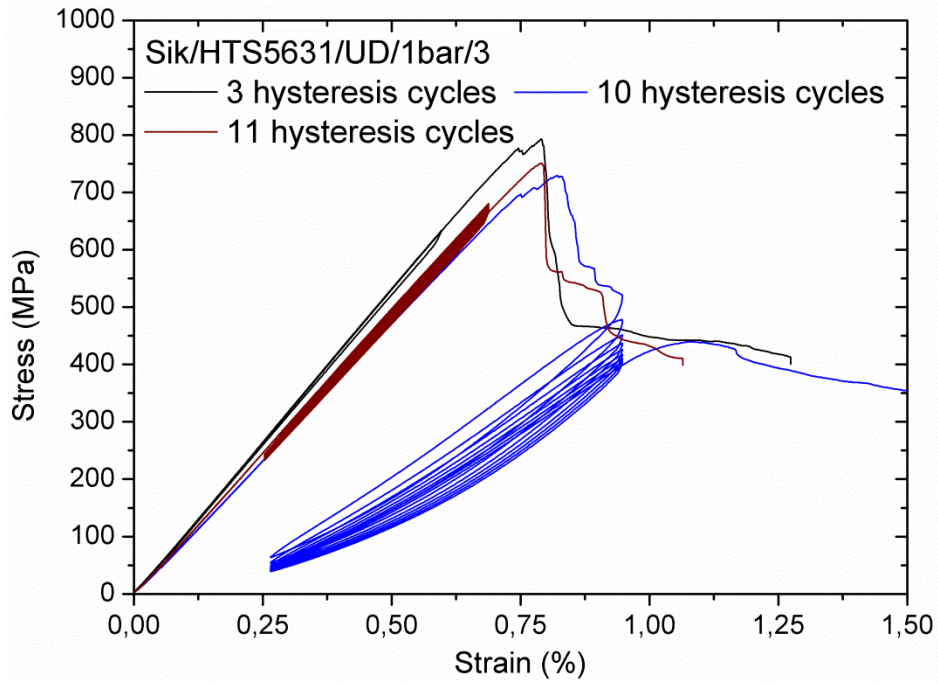
Fig. 156: Samples Sik/HTS5631/UD/P3/h1-3c in black, Sik/HTS5631/UD/P3/h2-10c in blue and Sik/HTS5631/UD/P3/h3-11c in red.

Fig. 157 presents a summary with all Sika CR132 four point bending curves in one diagram.
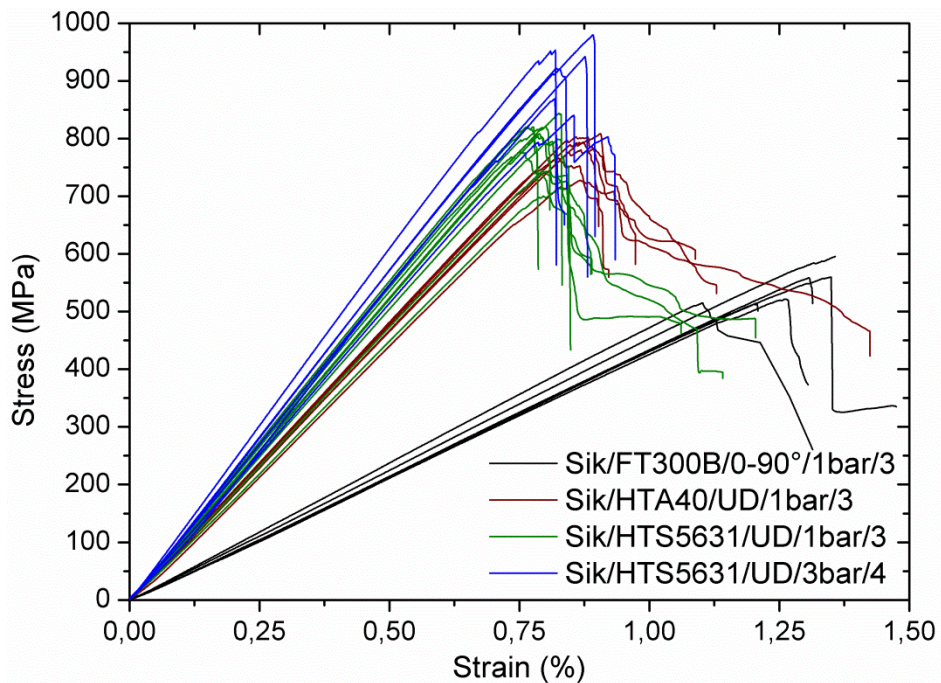
Fig. 157: Stress-strain curves for all different laminates produced using Sika CR132 epoxy matrix. Black curves are the 0°/90° laminates, coloured curves correspond to UD materials.

5.4.2.3 *Laminates Hexion L418 matrix*

The results for the four different Hexion L418 based laminates tested in fibre direction (°0) are shown in Tab. 32. Fig. 158 shows exemplarily stress-strain curves obtained for monotonic tests until failure for each kind of material.
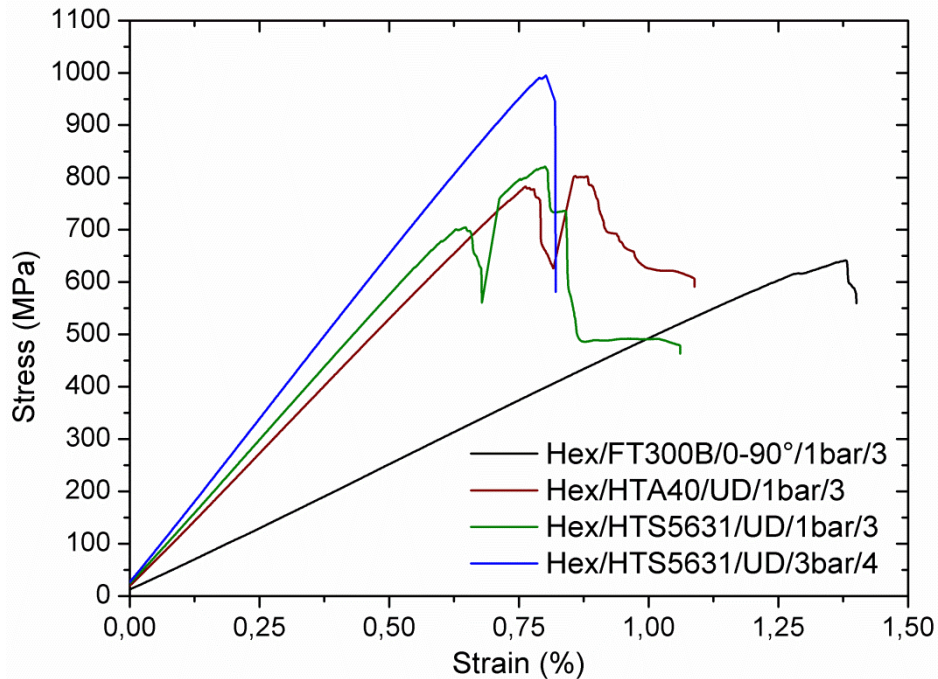
Fig. 158: Exemplary stress-strain curves for each of the four different laminates tested in four point bending in fibre direction with a constant strain rate of 5 mm/min until failure.

Fig. 159 presents a summary with all Hexion L418 four point bending curves in one diagram.
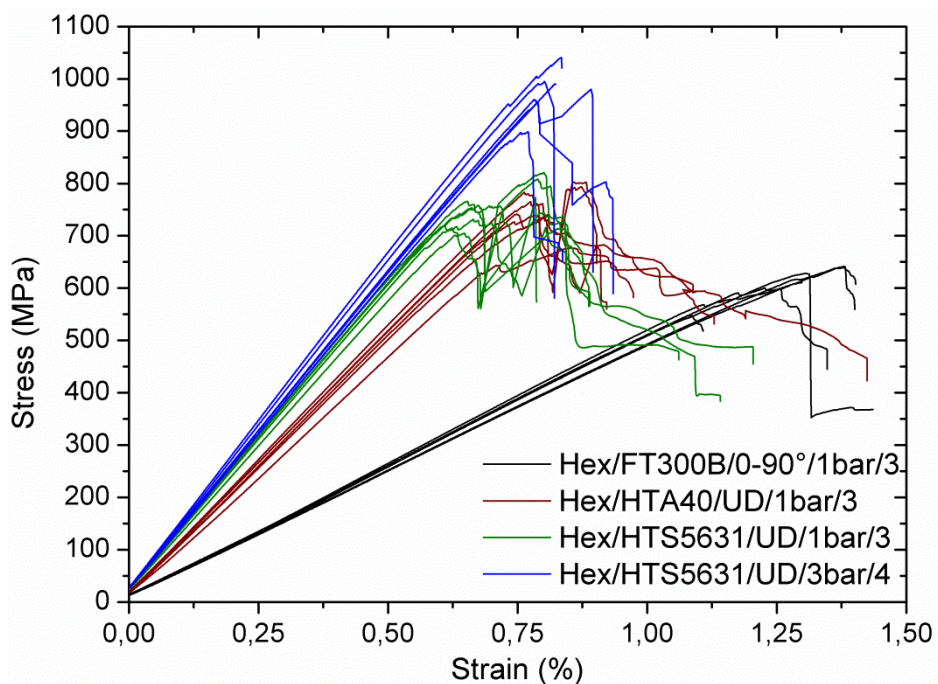
Fig. 159: Stress-strain curves for all different laminates produced using Hexion L418 epoxy matrix. Black curves are the 0°/90° laminates, coloured curves correspond to UD materials.

125

5.4.2.4   *Pultruded profile R/L20-T/HTSTS/UD65f*

The results for samples in as received (AR) condition and for the different heat treated samples tested in fibre direction (°0) are shown in Tab. 32. Fig. 160 shows a comparison between curves obtained for as received and the different heat treated samples.
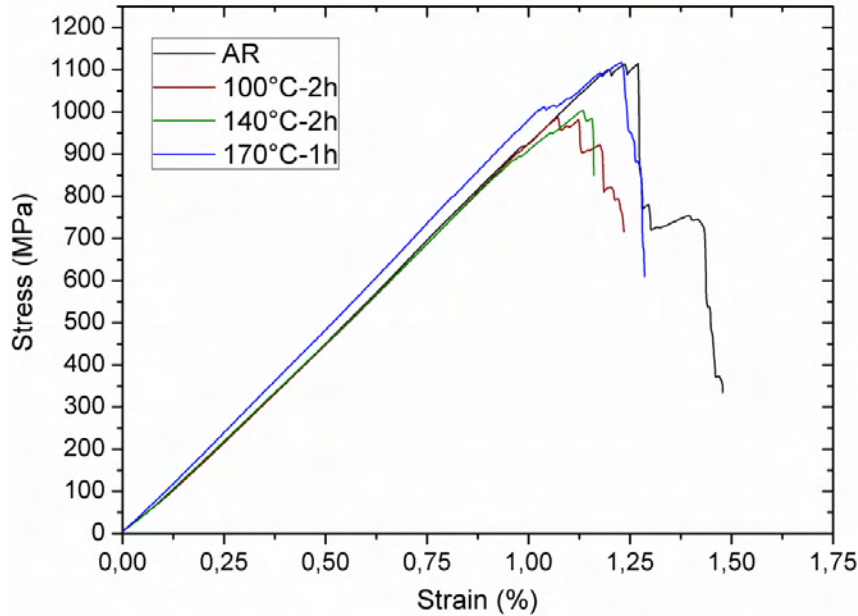
Fig. 160: Samples tested in four point bending in fibre direction with a constant strain rate of 5 mm/min until failure. Black curve correspond to as received condition, the coloured ones to heat treated specimens.

5.4.2.5   *Pultruded profile R/Sika/Sigrafil-T700SC/UD65f*

The results for samples in as received (AR) condition and for the different heat treated samples tested in fibre direction (°0) are shown in Tab. 32. Fig. 161 shows a comparison between curves obtained for as received and the different heat treated samples.
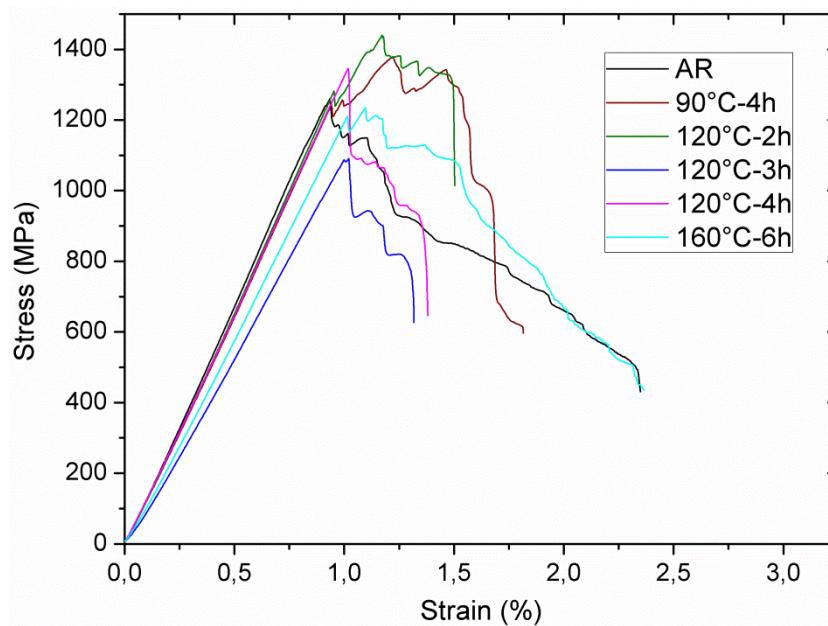
Fig. 161: Samples tested in four point bending in fibre direction with a constant strain rate of 5 mm/min until failure. Black curve correspond to as received condition, the coloured ones to heat treated specimens.

5.4.3 Interlaminar fracture toughness (Mode I&II)

Results obtained for the HexPly8552 laminates, manufactured with P1 and P2 process, tested in Modus I and II are shown in Tab. 33.

Sample	Modus I Interlaminar fracture toughness G_{Ic} (J/mm²)	Modus II Interlaminar fracture toughness G_{IIc} (J/mm²)
HexPly8552 Laminates		
HSAS4/UD58f/0.2MPa/P1-IFT	0.31 ± 0.03	0.67 ± 0.01
HSAS4/UD58f/0.2MPa/P2-IFT	0.34 ± 0.03	0.88 ± 0.06

Tab. 33: Interlaminar fracture toughness average results in modus I and modus II for the prepreg based laminates HexPly8552/P1 and HexPly8552/P2.

The interlaminar fracture toughness G_{Ic} of samples P1 is lower than that of samples P2, meaning that more energy is needed to propagate the crack in these materials. The scatter of the critical energy release rate of both sample types is in the same range and can be explained generally by the rather poor magnification of the magnifying glass and the subsequent systematic error in crack length determination.

The interlaminar fracture toughness G_{IIc} was about 30% higher in case of the P2 samples compared to the P1 samples. One of the P2 samples showed a decrease of the load at about 70N and a consequently minor gradient leading to a greater scatter of the values.

In the next two subchapters 5.4.3.1 and 5.4.3.2 exemplary curves for both modus I and II and both materials P1 and P2 are shown.

5.4.3.1 *Laminates HexPly8552 Modus I*

In Fig. 162 two load versus displacement curves for both types of laminates are shown. Crack was opened in four steps for each specimen. The interlaminar fracture toughness values calculated for each of the four successive crack opening lengths are shown in Fig. 163 for laminates produced with P1 and Fig. 164 for laminates produced with P2.
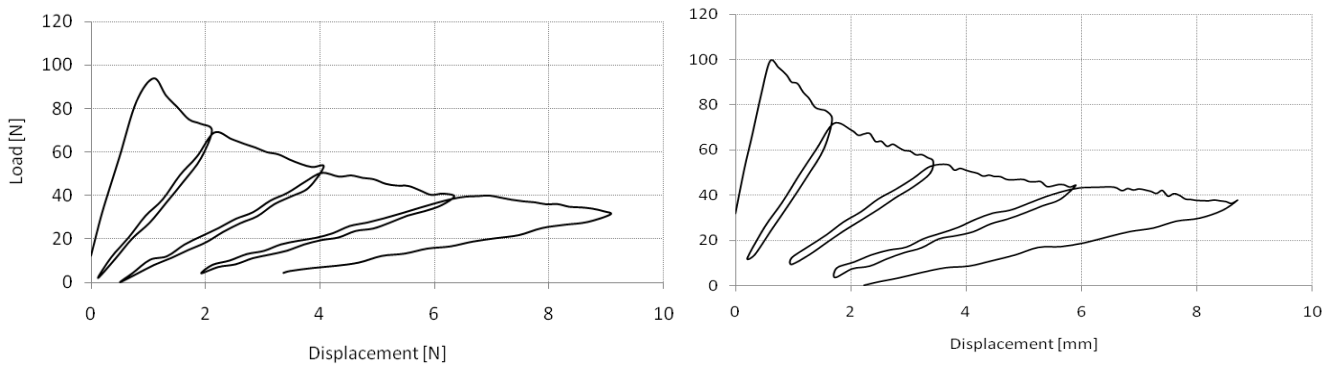
Fig. 162: Load versus displacement curves obtained for the laminates HexPly8552 P1 (left) and P2 (right).
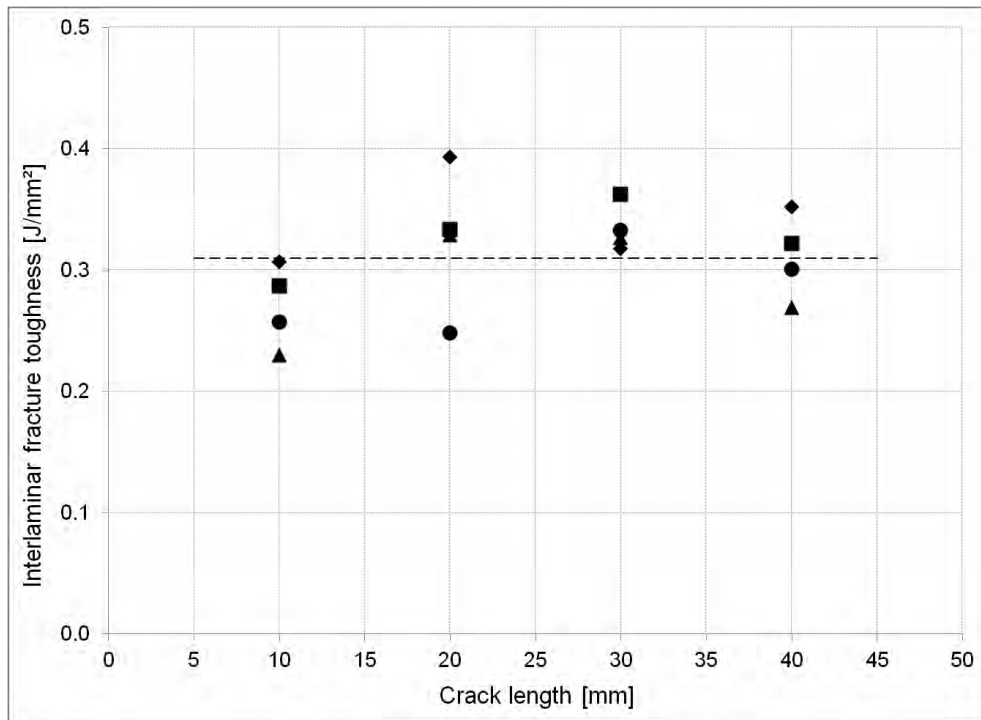
Fig. 163: Results for HexPly8552/P1 laminates tested in Modus I. Average G_{Ic} value shown as dashed line. Each different symbol corresponds to a specimen. Each sample has four successive crack opening lengths.
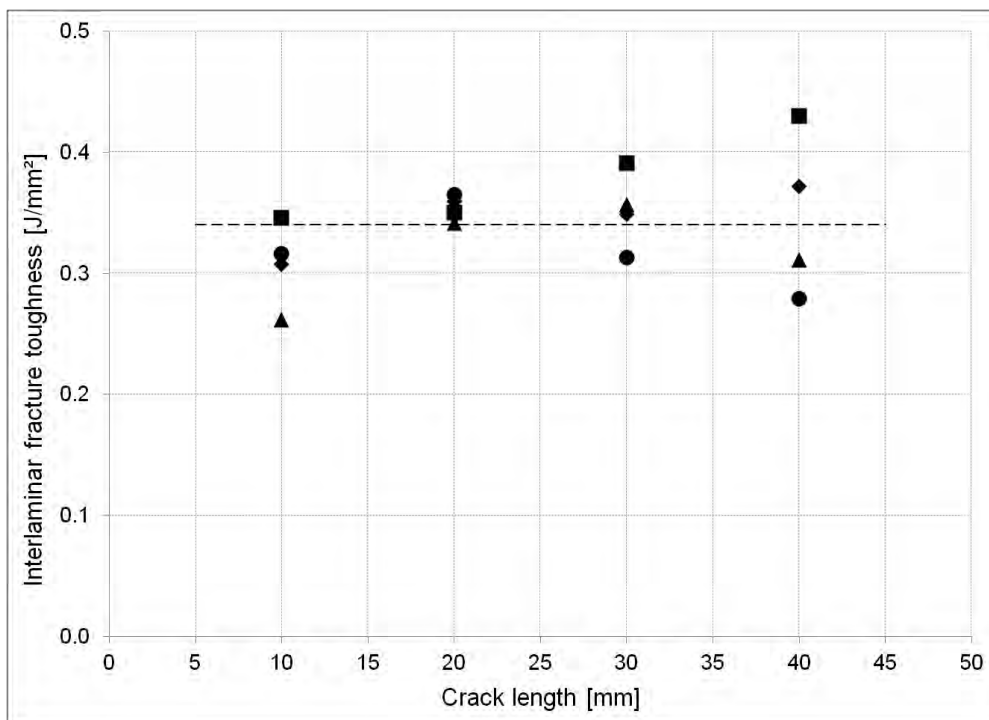
Fig. 164: Results for HexPly8552/P2 laminates tested in Modus I. Average GIc value shown as dashed line. Each different symbol corresponds to a specimen. Each sample has four successive crack opening lengths.

No fibre bridging was observed during mode I testing, therefore fracture toughness is independent of the crack length as depicted in Fig. 163 and Fig. 164.

5.4.3.2 *Laminates HexPly8552 Modus II*

Fig. 165 and Fig. 166 show load versus displacement curves for both types of laminates tested in modus II (three-point bending). Linear load increase is observed up to a certain deflection value where crack propagation leads to a sudden drop as a consequence of delamination.
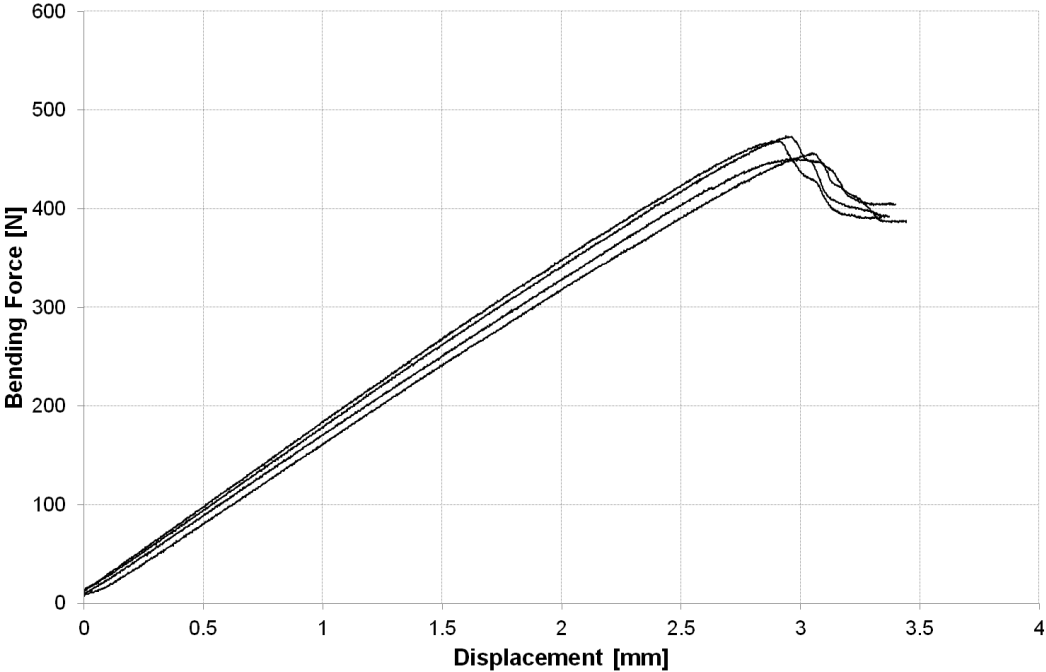
Fig. 165: Results modus II sample: HexPly8552/P1. Three-point bending.
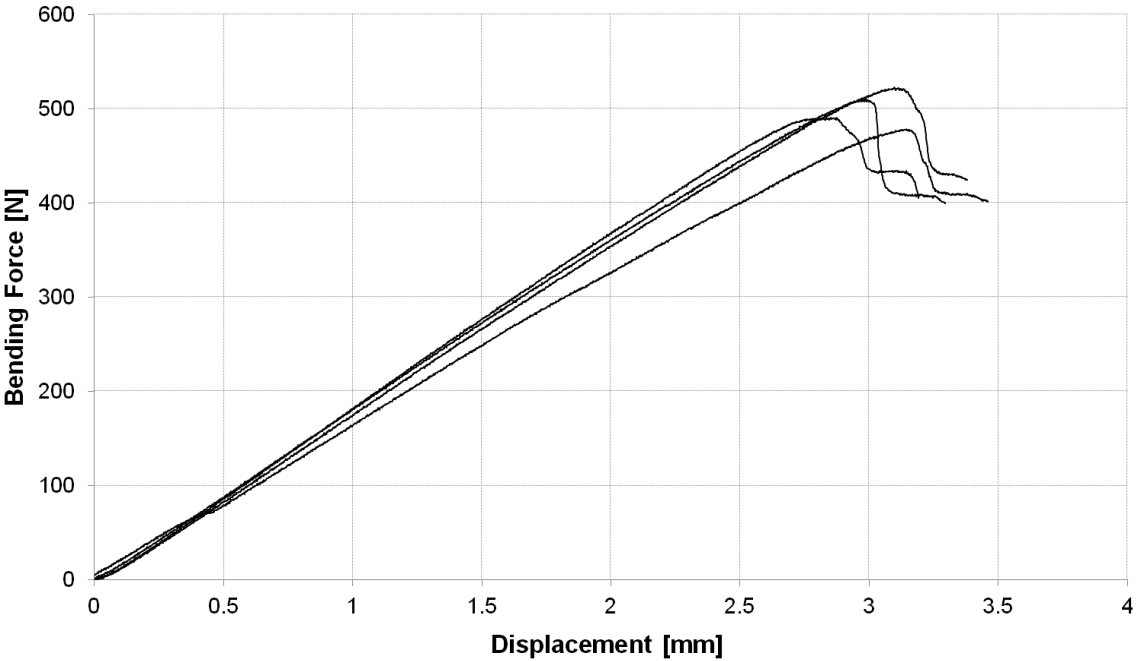
Fig. 166: Results modus II sample: HexPly8552/P2. Linear load increase is observed until crack propagation leads to a sudden drop at about 3mm deflection.

5.4.4 Short beam shear strength tests (SBS)

Results obtained for the different Sika CR132 and Hexion L418 based laminates tested with SBS are shown in Tab. 34, where average values for maximal force and apparent shear strength values calculated for all eight different laminates are presented.

Code	Sample	F_{max} (N)	F^{sbs} (MPa)
Sika CR132 Laminates			
Sika 1	Sik/FT300B/0-90°/P3-SBS	5044 ± 311	54.4 ± 3.3
Sika 2	Sik/HTA40/UD/P3-SBS	3625 ± 208	51.1 ± 1.4
Sika 3	Sik/HTS5631/UD/P3-SBS	3312 ± 181	53.1 ± 0.9
Sika 4	Sik/HTS5631/UD/P4-SBS	3118 ± 74	61.7 ± 1.3
Hexion L418 Laminates			
Hexion 1	Hex/FT300/0-90°/P5-SBS	4160 ± 153	53.0 ± 1.1
Hexion 2	Hex/HTA40/UD/P5-SBS	4102 ± 51	55.9 ± 1.1
Hexion 3	Hex/HTS5631/UD/P5-SBS	2360 ± 18	39.6 ± 0.5
Hexion 4	Hex/HTS5631/UD/P6-SBS	2616 ± 111	53.0 ± 2.2

Tab. 34: Average force and apparent shear strength results for all studied laminates tested in SBS.

A summary of results for all studied laminates is shown in Fig. 167. Since this property is an indicator of fibre-matrix interface quality, a change is observed when we compare laminates produced with the same fibre type and one or the other matrix system. In general Hexion L418 matrix yields lower values, which points out a weaker fibre-matrix bond. Regarding apparent shear strength of similar materials, the partially different results can be explained in terms of the porosity volume fractions. Further analysis is shown in section 6.4.
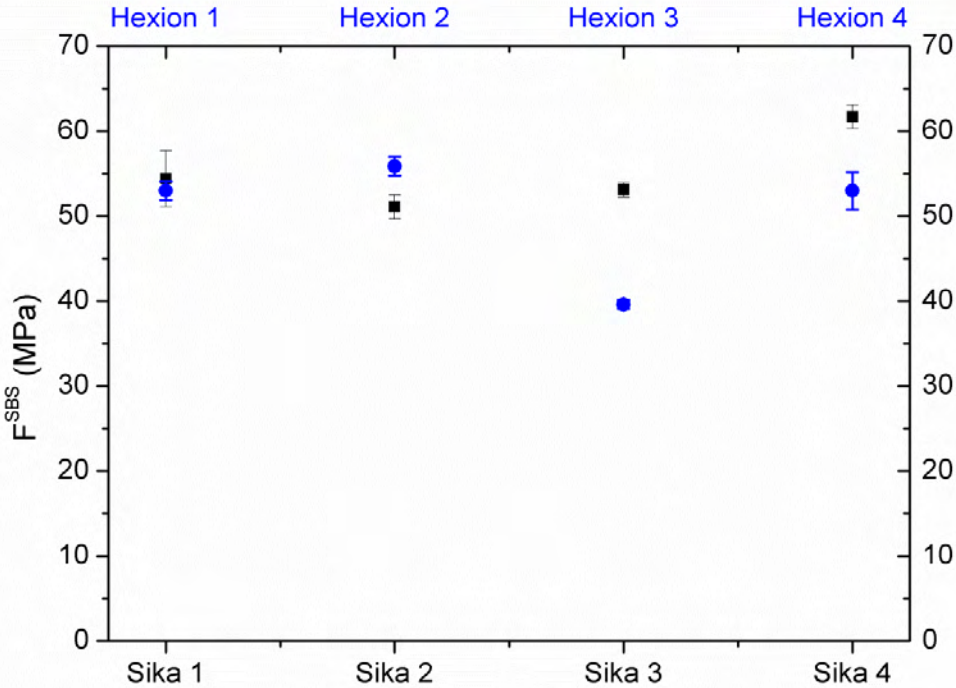
Fig. 167: Apparent shear strength values calculated for the four Sika CR132 and the four Hexion L418 based laminates.

5.4.4.1 *Laminates Sika Biresin CR132 matrix*

The force-displacement curves obtained for all tested specimens with Sika CR132 matrix are shown in Fig. 168.
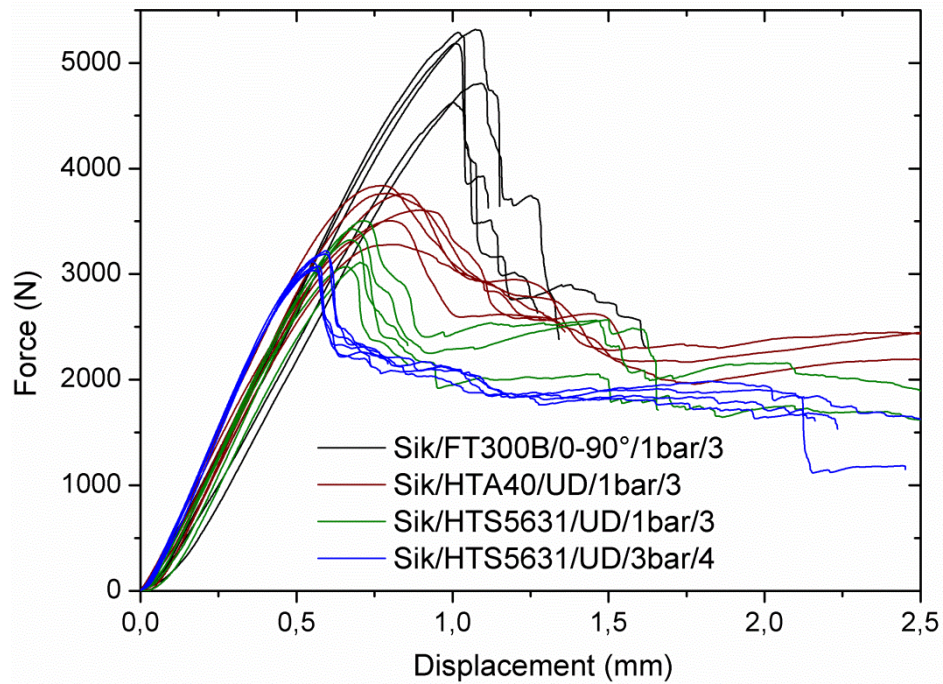
Fig. 168: Curves obtained for all four types of Sika CR132 based laminates.

5.4.4.2 *Laminates Hexion L418 matrix*

Force-displacement curves obtained for all tested specimens with Hexion L418 matrix are shown in Fig. 169.
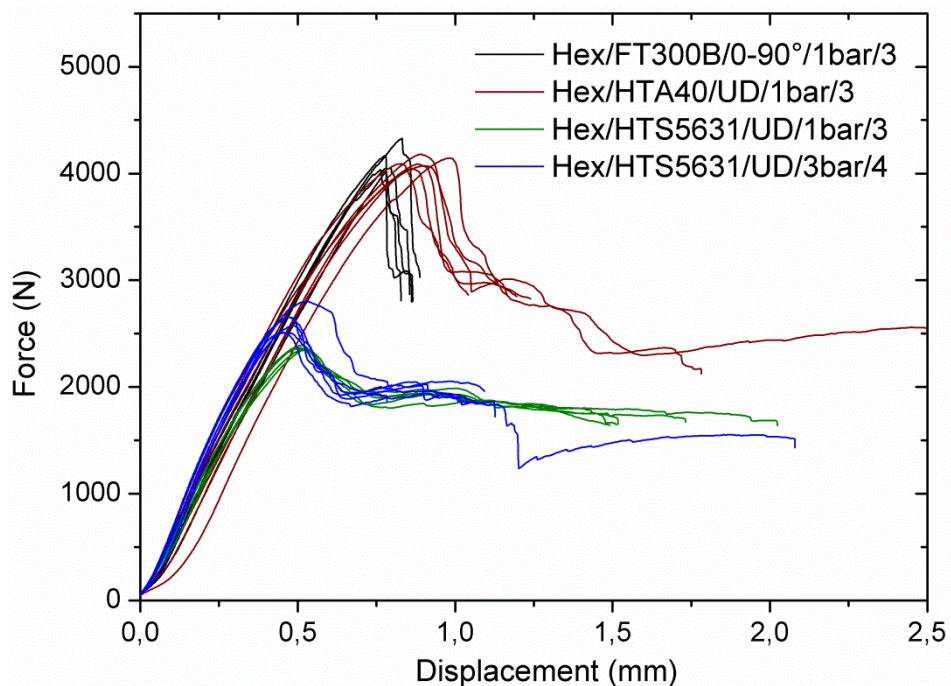
Fig. 169: Curves obtained for all four types of Hexion L418 based laminates.

5.5 Damage Analysis

5.5.1 In-situ acoustic emission during deformation

In-situ AE measurements on UD pultruded tubes during torsion test.

5.5.1.1 *Pultruded profile T/L20-T/HTSTS/UD65f*

A shear stress-shear strain curve and the corresponding AE count rate–time curves for a sample tested monotonically until failure are presented in Fig. 170. The shear stress-shear strain curve starts linearly and begins to bend above 2 Nm torque (20 MPa) towards decreasing tangent shear modulus. The in-situ AE count rate gives insight into the progress of the damage with increasing degree of deformation. The first AE signals appear at 0.7 Nm (4 MPa). A relatively low AE intensity persists until a few moments before failure, between 37 and 40 MPa consecutive strong AE signals are recorded.
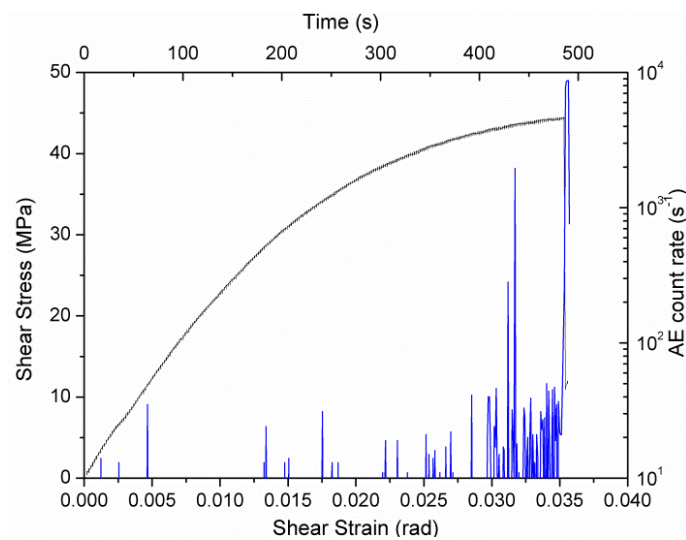
Fig. 170: Shear stress vs. shear strain and the corresponding AE count rate vs. time curves for sample T$_{10}$_L20_01 tested in torsion monotonically until failure.

In-situ AE measurements for samples tested with loading-unloading hysteresis cycles are shown in Fig. 171 for interrupted tests and Fig. 172 for samples tested until failure.
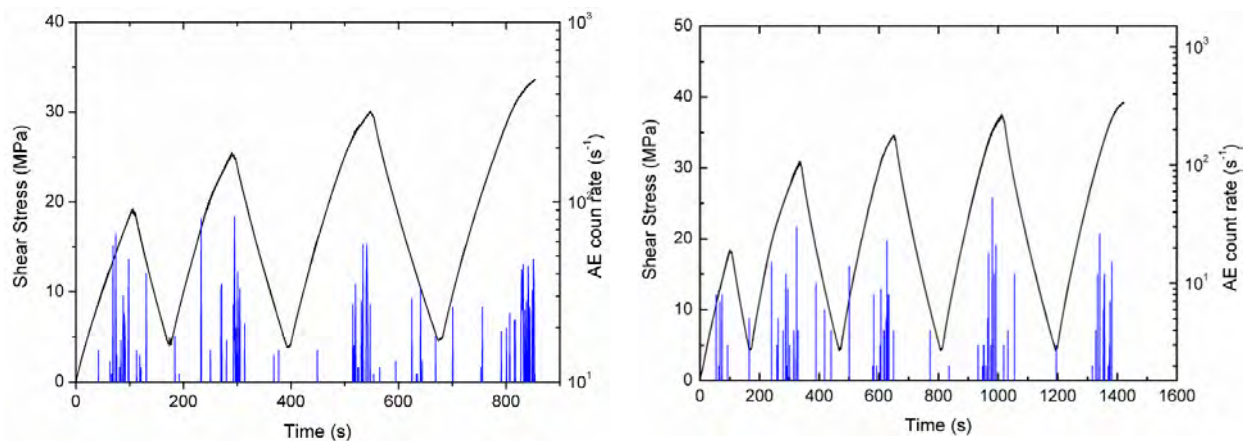
Fig. 171: Shear stress and AE count rate vs. time curves for samples T$_{10}$_L20h1-3c and T$_{10}$_L20h2-4c tested in torsion with three and four loading-unloading cycles. Test were interrupted before failure.

132

For samples tested using hysteresis cycles the AE activity starts also at about 0.7 Nm (4 MPa) and persists during the loading half-cycles as soon as the torque angle supersedes the maximum of the former cycle. The same behaviour has been observed on other materials and is called "Kaiser effect" [93]. Some higher intensity peaks are observed at torques of 3.3 Nm (30 MPa-19°) and 3.8 Nm (35 MPa-25°). These events are due to fibre-matrix debonding which is favoured by the cyclical nature of the test, while loading the sample deforms and the reinforcement is exposed to higher tensile load, then during unloading anticlockwise the specimen experiences relaxation and the interface between matrix and fibres is more lose.

Some AE signals were detected as well during the end of the unloading phase. This might be matrix cracking during specimens relaxation or unavoidable noises produced by the universal testing machine while changing from loading to unloading.
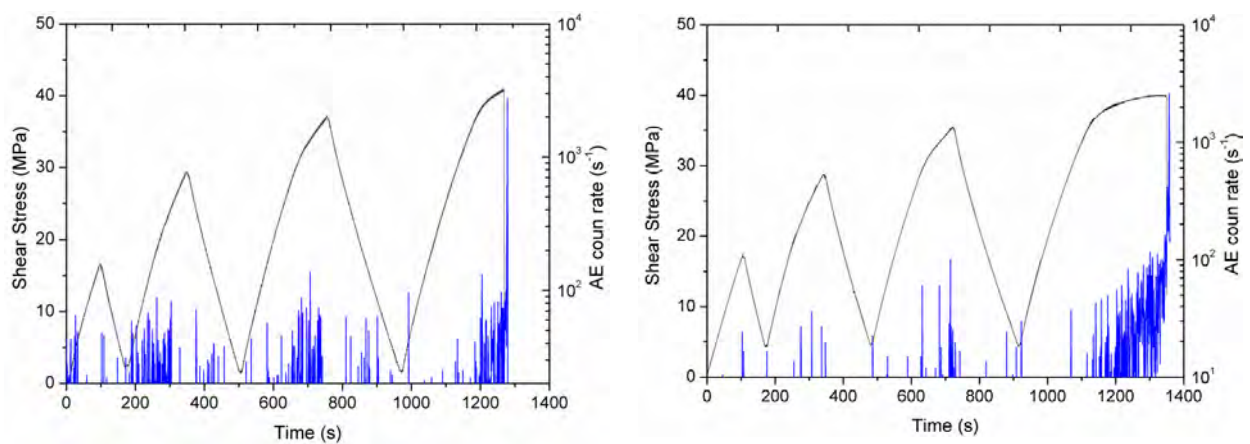
Fig. 172: Shear stress and AE count rate vs. time curves for samples T_{10}_L20h3-3c and T_{10}_L20h4-3c tested in torsion with loading-unloading cycles until failure. Fig. 143 shows the corresponding flow curves.

On samples tested until failure, fibre breakage can be clearly identified occurring instants before specimen failure, as a sudden increase of AE signals intensity, which corresponds with the drop in the shear stress-strain curve. The sound of fibres breaking can be also heard during the experiments, as a sizzling noise seconds before the explosive specimen failure.

For all studied UD-CFRP pultruded tubes tested in torsion with loading-unloading cycles, an increase of the AE activity was observed to be coupled with a decrease of the shear modulus revealed by a decrease of the slope of the dashed lines in the stress-strain diagram (see Fig. 141, Fig. 142 and Fig. 143). Similar results have been reported in [94] [95] [96].

5.5.2 In-situ synchrotron tomography during deformation

5.5.2.1 *Laminates HexPly8552/HSAS4/± 45-58f/0.2MPa/2*

In-situ tensile tests were carried out at the synchrotron facilities of the ESRF (Grenoble). The ten tensile steps at which tomography scans were taken are shown in Fig. 173. Volumes size after registration: 925x947x915 µm³. Voxel size: (1.4 µm)³. Only one manufacturing pore was found within one of the six plies, its size being:$0.4 \cdot 10^6$ µm³, that is 0.05%vol.
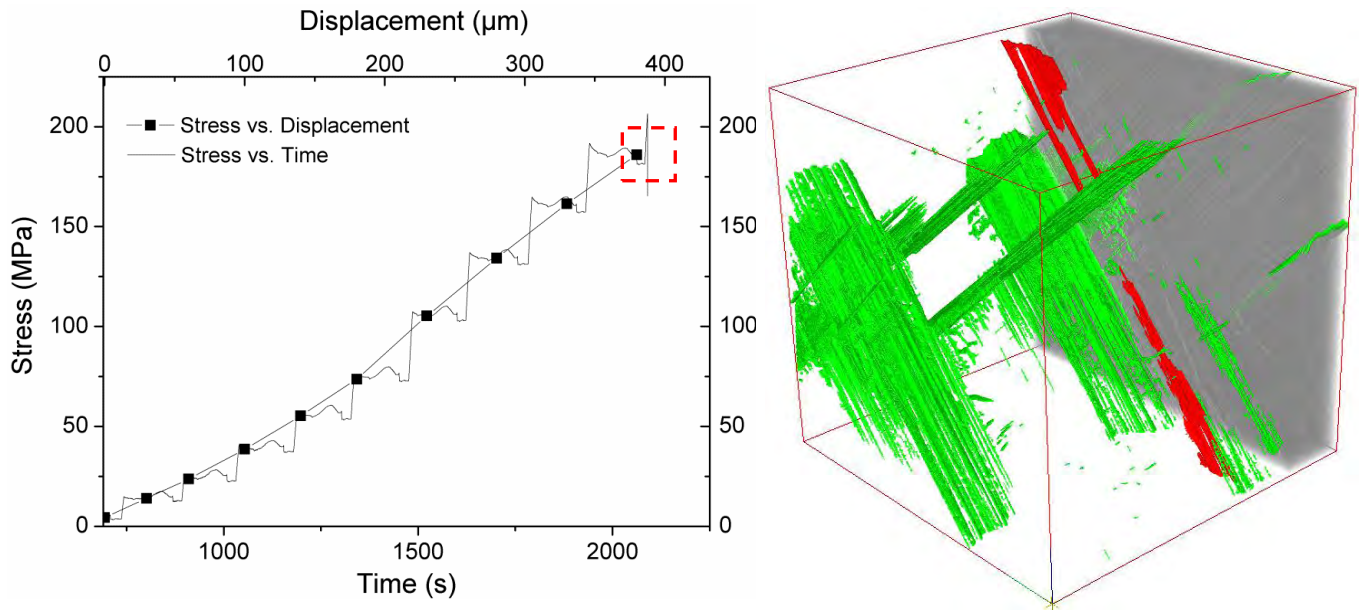
Fig. 173: Stress versus displacement and over the time during the tensile test. SCT scans (duration about 2 min) were made at the black square points. Sample failure occurred immediately after the tenth scan, highlighted in red. The 3D image corresponds to that last scan, the cracks and the interply delamination are segmented in green, manufacturing porosity in red. The outermost ply is shown in grey.

Fig. 174 shows a 2D slice of the first scanned volume, showing manufacturing porosity within the penultimate ply and machining cracks, who were induced during machining of the miniature notched tensile specimen shown in Fig. 44. The same features can as well be visualized in 3D, where porosity is segmented in red.
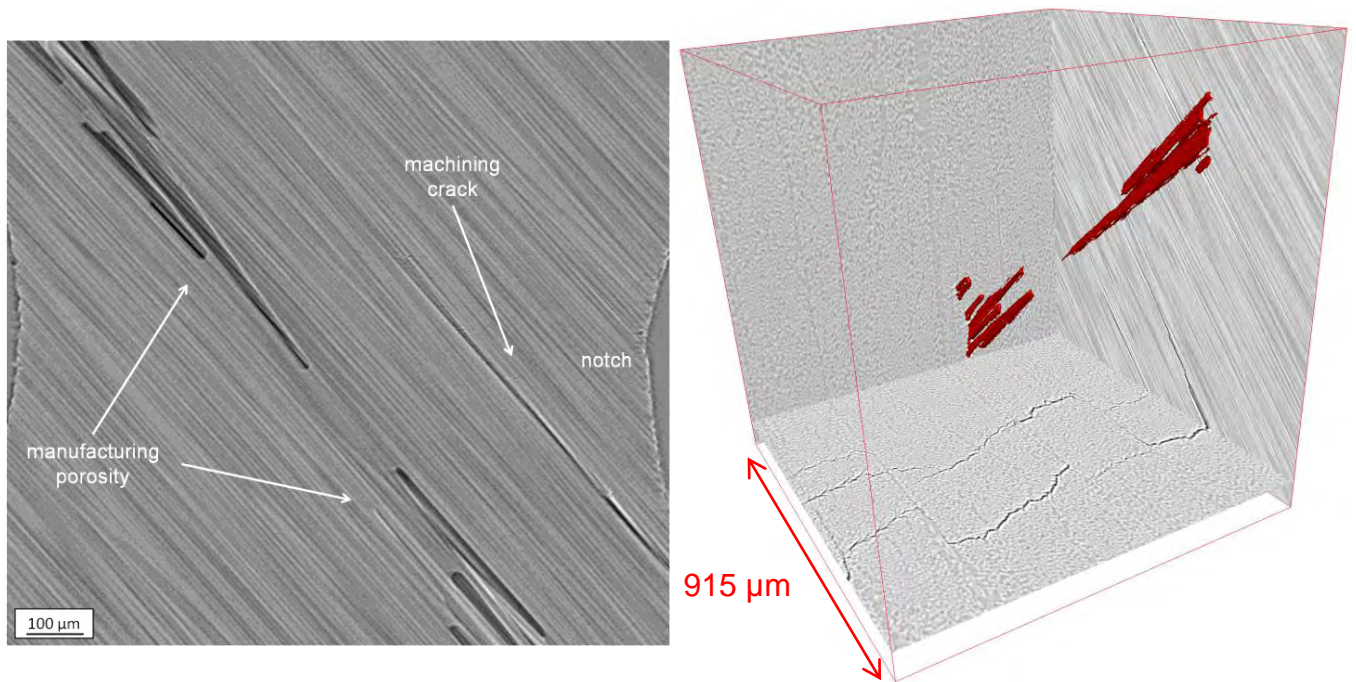
Fig. 174: Left: 2D slice of ply 5 showing porosity and cracks close to the notched region of the specimen, Right: Segmented pore in 3D is shown in red. It was formed during manufacturing of the laminate within the penultimate ply. Voxel size $(1.4 \ \mu m)^3$. Volume size: $(925 \times 947 \times 915 \ \mu m)^3 = 1.183 \ mm^3$.

134

Segmentation was made in order to assess the growth of existing cracks, the formation of new ones and the progress of delamination between plies. Fig. 175 shows the evolution of crack growth within the studied volume at different loading steps of the tensile test. Connected cracks have the same colour. Initial cracks induced during sample machining showed a stronger influence on damage progression and final failure than manufacturing porosity.
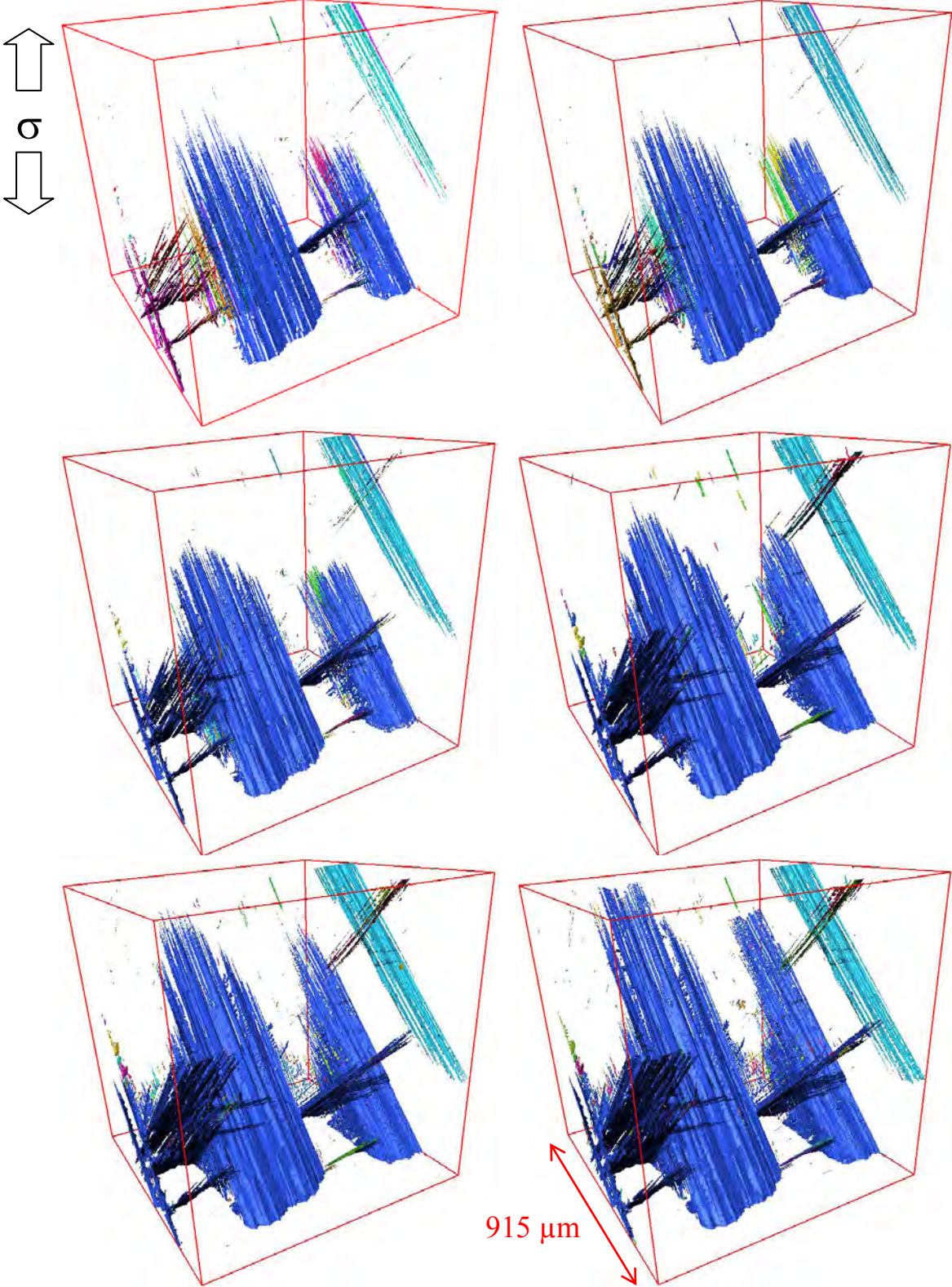
Fig. 175: Crack growth evolution from preload (up left) to the load prior to failure (bottom right).

The volume and area fractions of cracks exhibits a continuous increase above a threshold stress of 25 MPa (see Fig. 176). Total cracks volume at preload: $2.3 \cdot 10^6$ μm^3 (0.29%vol).
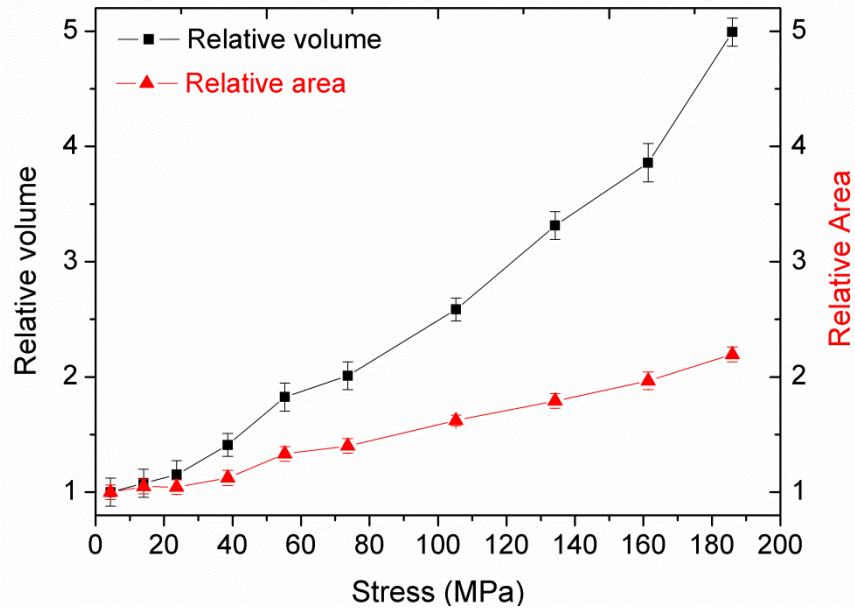
Fig. 176: Relative crack volume and area of the segmented cracks at the different loading steps of the tensile test. After the fifth step (~60MPa) the evolution of damage increases rapidly.

Orientation Analysis:

The reorientation of the fibres during loading was analysed individually for each ply using an algorithm based on the evaluation of the local structure tensor within the reconstructed 2D slices. The maxima of the distribution of the fibre orientations shift to values closer to the orientation of the loading axis. Furthermore, the histograms become broader indicating a more inhomogeneous fibre orientation distribution due to tensile deformation, see Fig. 177.
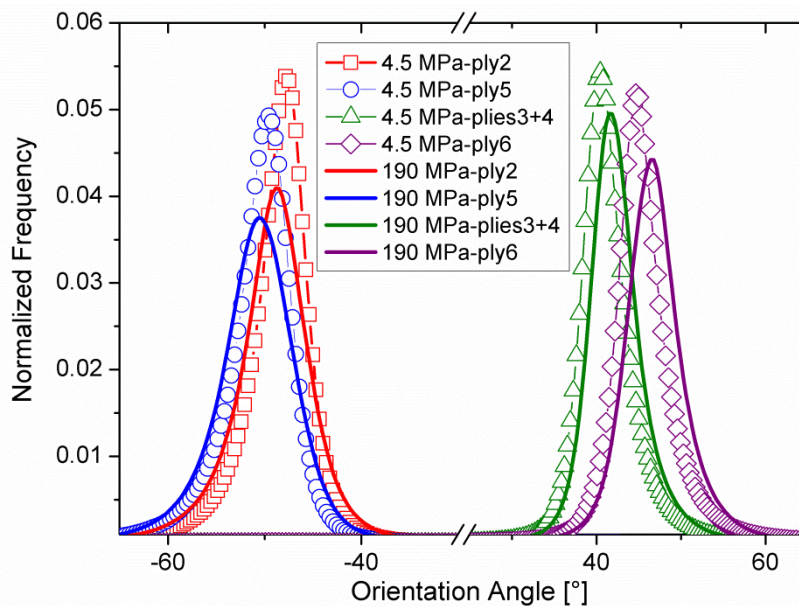
Fig. 177: Orientation angle for each ply at preload (4.5 MPa) and right before failure (190 MPa). The maxima of fibre orientation distribution shifts about 2 degrees.

5.5.3 X-ray tomography after deformation

5.5.3.1 *Laminates HexPly8552/HSAS4/UD58f/0.2MPa/2*

Fig. 178 shows top, side and bottom macroscopic views of a four point bending sample loaded until failure and Fig. 179 the CT axial slice of the sample. Main damage occurred on the tension side due to breaking of the fibres and delamination due to shear stresses. Two cracks parallel to the fibre orientation (marked as A and B) are visible on the CT slice but only crack B can be clearly identified at macroscopic scale. A possible reason for crack "A" initiation is an approximately 2 mm long pore found associated to this crack. The crack switches from one side of the pore to the other (slice 2) and at the end of the pore it switches back again to the original side (slice 3).
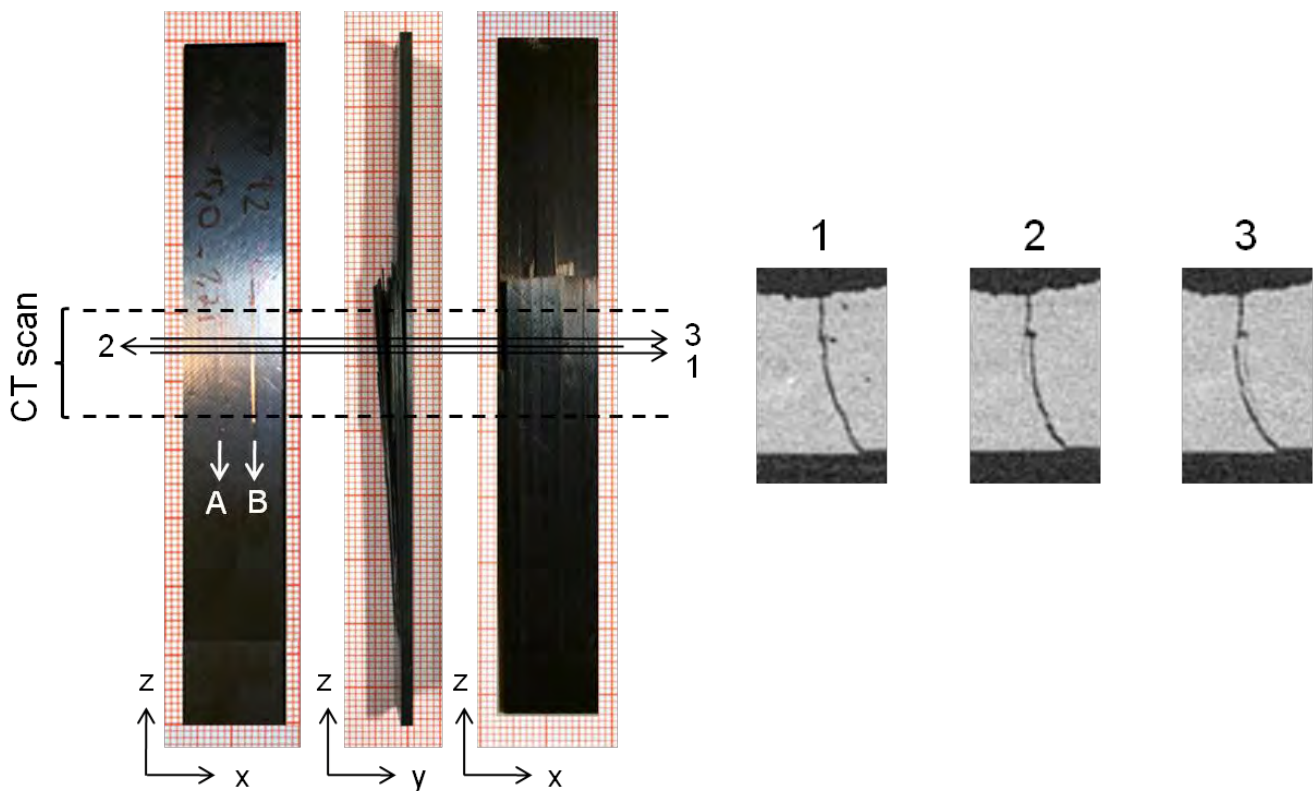
Fig. 178: Macroscopic view of a sample after four point bending showing the rupture of the fibres on the tension side and a small fracture on the compression side (crack B). Numbers "1", "2" and "3" mark the position of the CT slices on the right side.
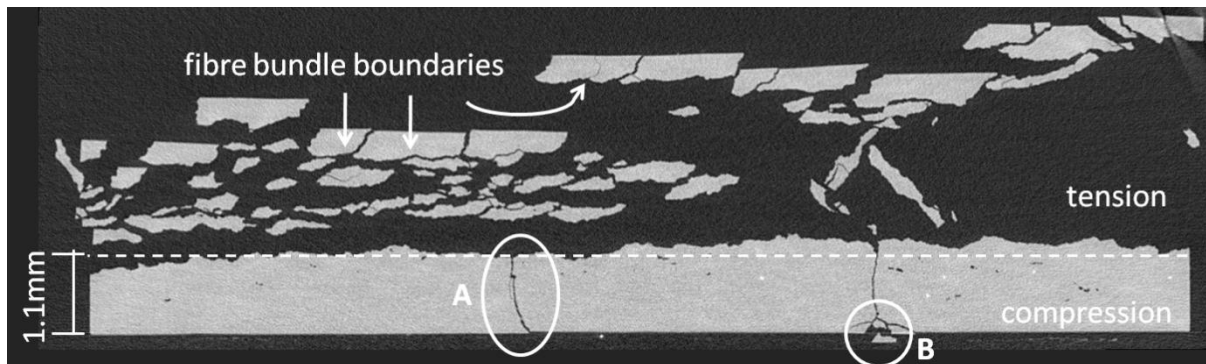
Fig. 179: CT axial slice of bending sample tested until failure. Voxel size: (11μm)³.

5.5.3.2 *Laminates Sik/HTS5631/UD/3bar/4*

Impregnated textile laminates after bending test. Fig. 180 shows 2D axial slices obtained from CT measurement. Fig. 181 shows the 3D view of the segmented delamination and the cracks.
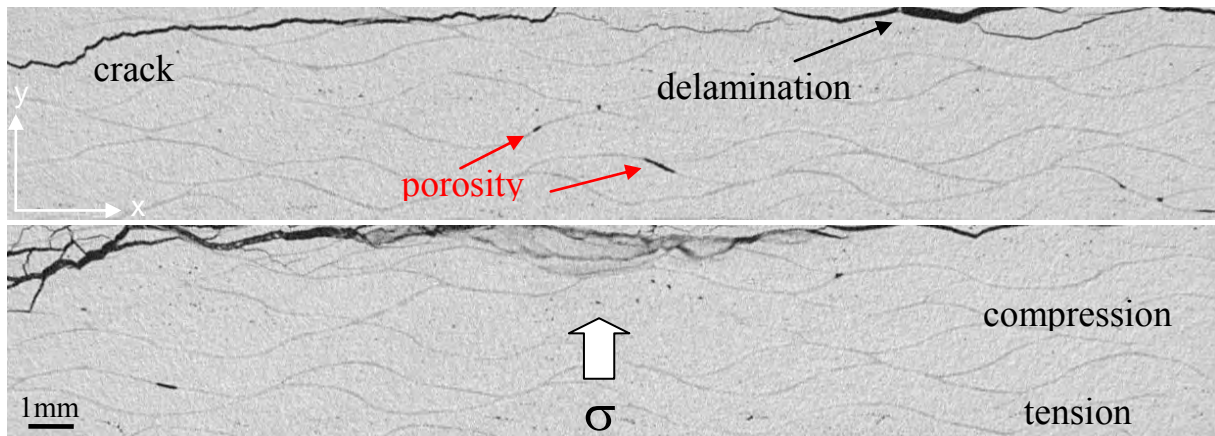
Fig. 180: Crack path and delamination as observed on XCT slices. Area observed: 19.8mm×4mm.
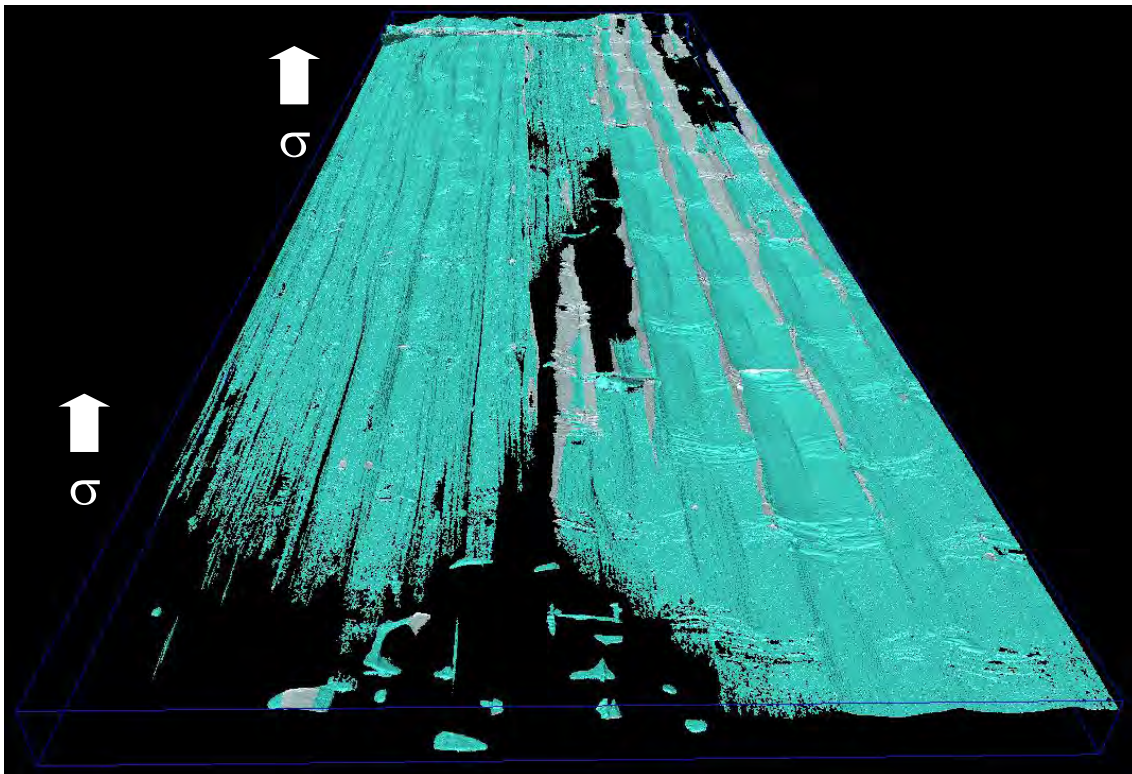
Fig. 181: Segmented cracks. Waviness is visible, as imprints on the matrix delaminated surface. The PES support fibres, running perpendicular to the carbon bundles are visible as well as imprints. Volume size: 19.8mm×0.5mm×59.3mm. Voxel size: $(16\mu m)^3$.

5.5.3.3 *Pultruded profile T/L20-T/HTSTS/UD65f*

Axial XCT slices are shown in Fig. 182 corresponding to a sample imaged before and after interrupted torsion test, no damage detected at the used resolution. Fig. 183 shows X-ray sum projections before and after for a sample tested until failure. A longitudinal crack was observed growing parallel to fibre direction in areas with higher amount of particle agglomerations, in 3D view (see Fig. 185) crack path is clearly visible.

138
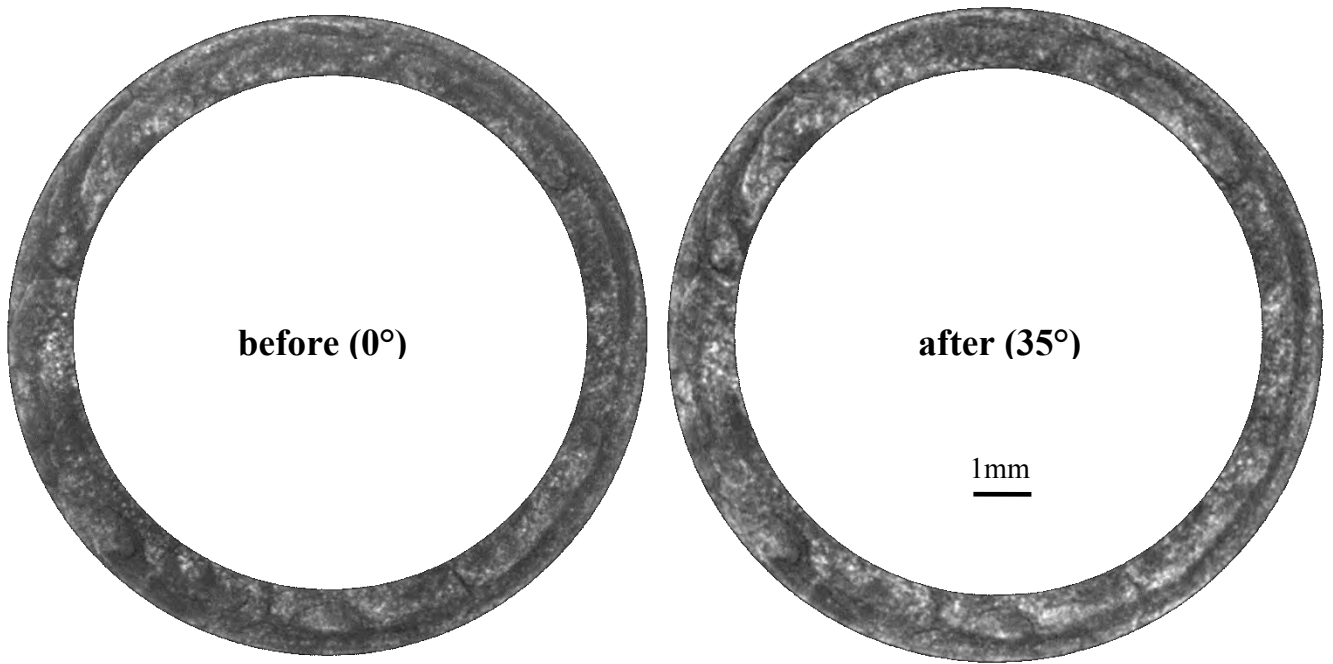
Fig. 182: Sample T_{10}_ L20h2-4c before (0°) and after interrupted test (35°). No damage observed at this magnification. Porosity cannot be resolved, particles volume fraction remains constant. A slight variation of wall thickness can be determined between 0.92 and 0.98 mm. Filler particles have a white contrast.
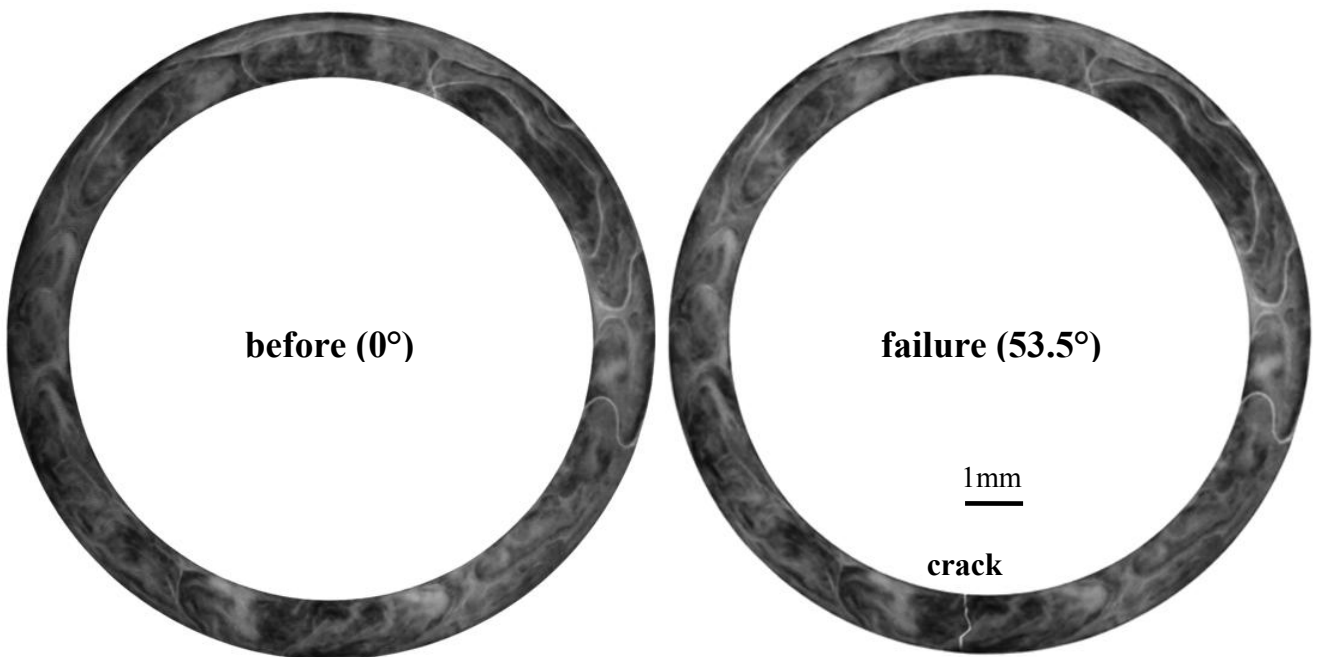
Fig. 183: X-ray sum projection view of 50 slices along the tube axis obtained from XCT. Bright regions correspond to low density matrix rich areas and darker regions to filler particles. This image reveals the structure of fibre bundles (contours are visible) as well the distribution of filler agglomeration. Sample T_{10}_ L20h4-3c before (0°) and after failure at 53.5° twisting angle, showing crack path in white.

139

Details of damaged zone before and after failure are shown in Fig. 184. It can be seen that the crack did not grow directly from one resin rich area to the next, but along the filler agglomerations, as it can be seen in Fig. 185 in a three-dimensional perspective.
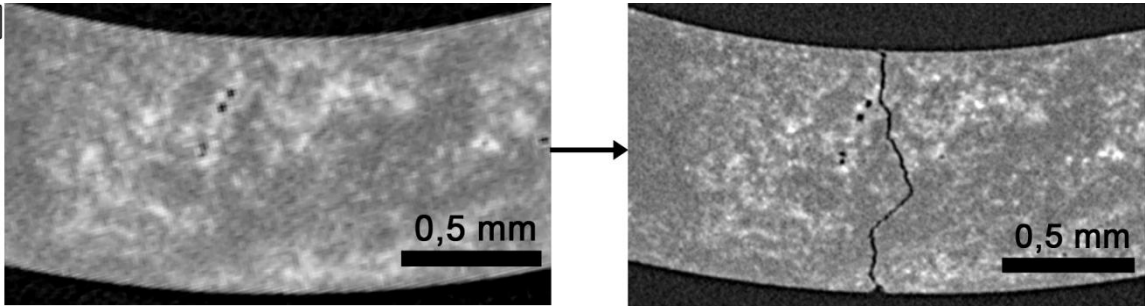
Fig. 184: XCT slices of the same sample before (left) and after (right) torsion tests. Detail of the area where damage occurred showing crack path. It is observed that porosity remains constant. Crack growth runs parallel to fibre direction along the length of the tube, preferentially near particle agglomerations.
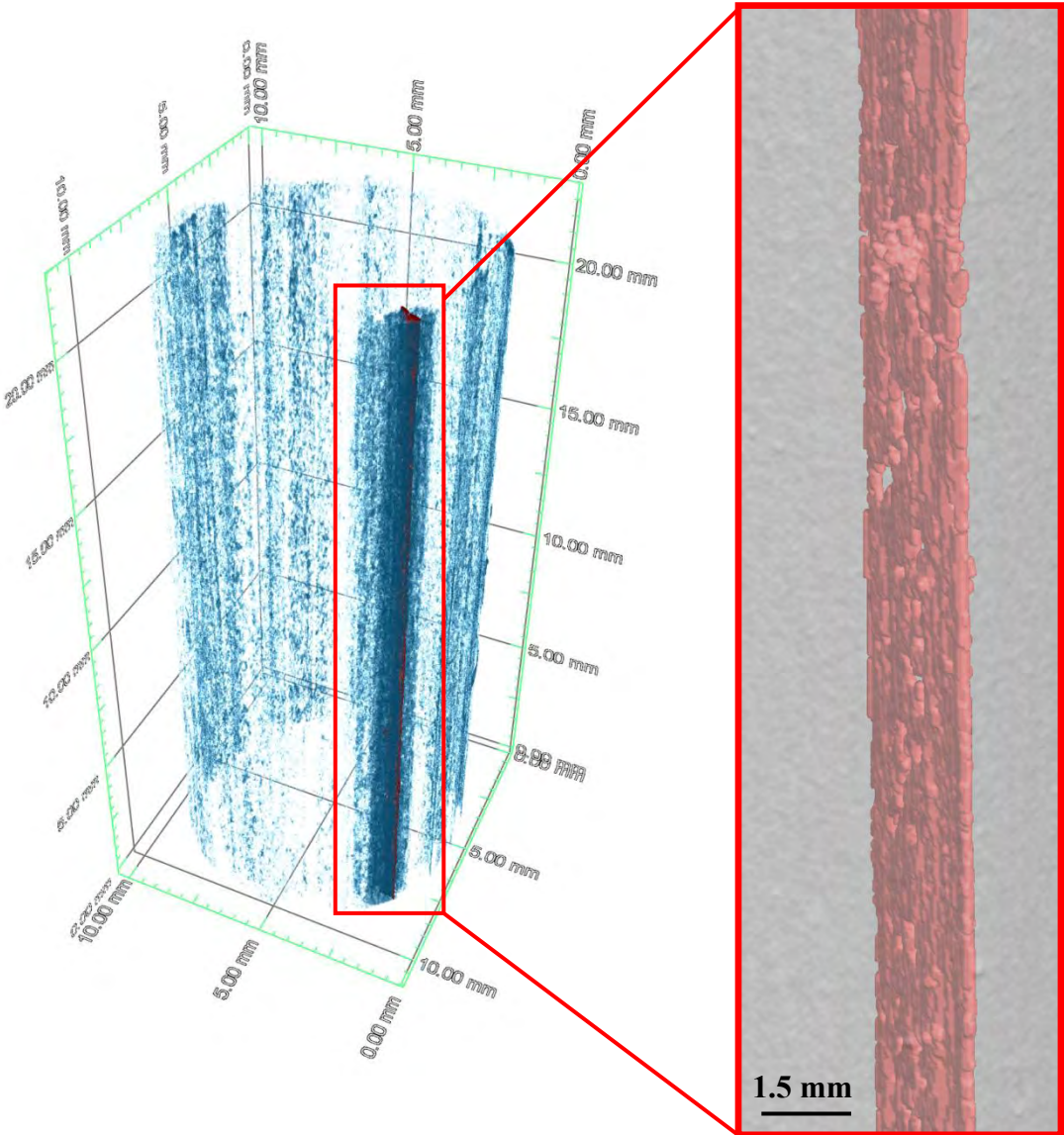
Fig. 185: Segmented features obtained from a XCT measurement: talc particle agglomerations are segmented in blue, the crack formed during torsion test is segmented in red (a zoom is also highlighted). Voxel size: (11µm)³.

5.5.3.4 *Pultruded profile R/L20-T/HTSTS/UD65f*

XCT slices of sample $R_{10}\_L20\_h1$-23c after torsion test with hysteresis cycles (see flow curve Fig. 144) are shown in Fig. 186, cracks are in matrix or filler particle rich regions.
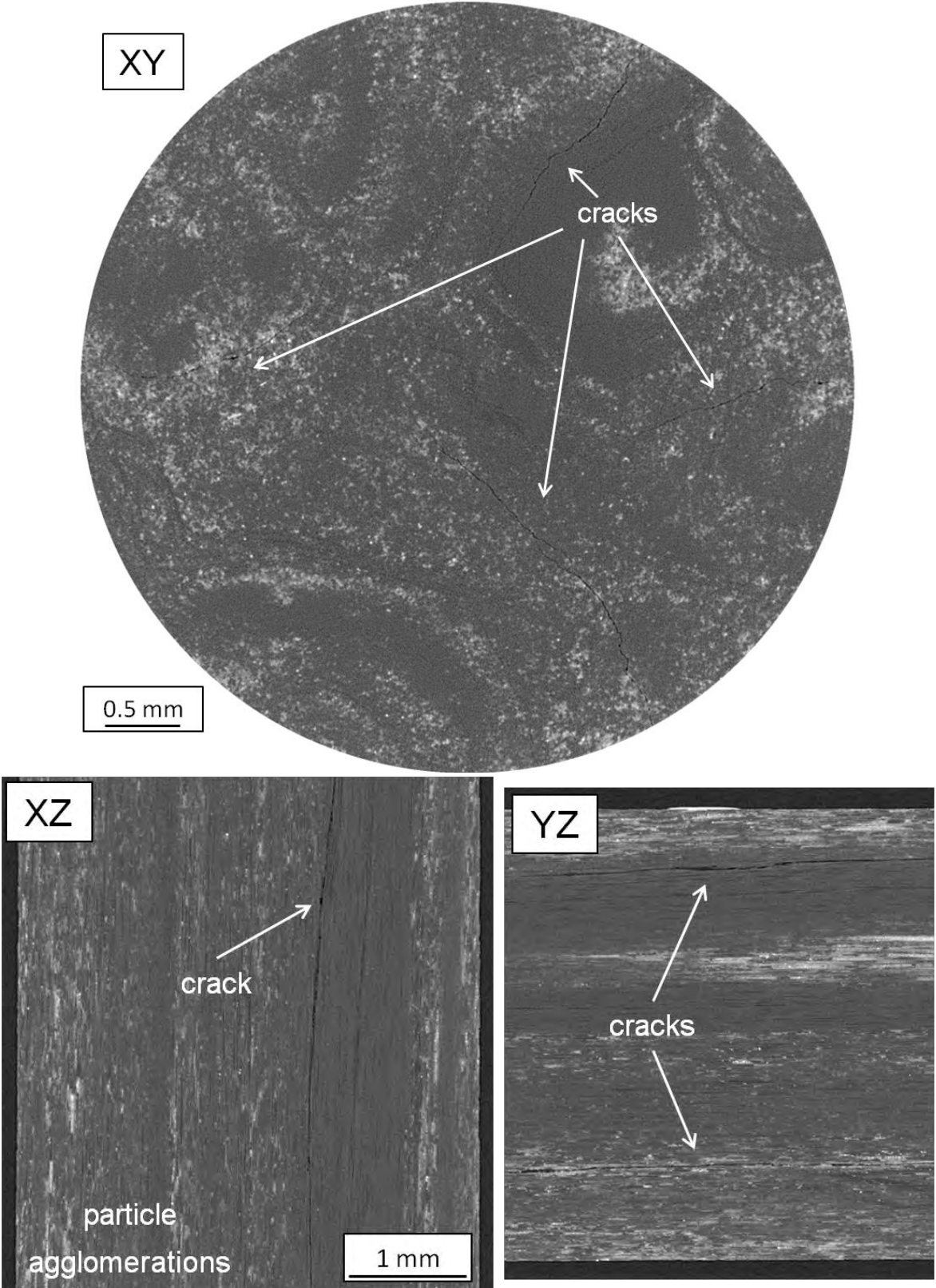
Fig. 186: XCT slices of a L20 pultruded rod tested in torsion with hysteresis cycles. Cracks grow in matrix-rich regions with high waviness degree or associated to mineral filler agglomerations (white).

5.5.3.5 *Pultruded profile R/Sika/Sigrafil-T700SC/UD65f*

Fig. 187 shows XCT slices of sample R_{10}_Sika_04 after failure. Specimen was tested monotonically until failure at a constant strain rate of $5x10^{-3}$ rad/s. Multiple radial cracks grow parallel to fibre direction (Z). Steps in shear stress-strain curve indicate fibre failure.
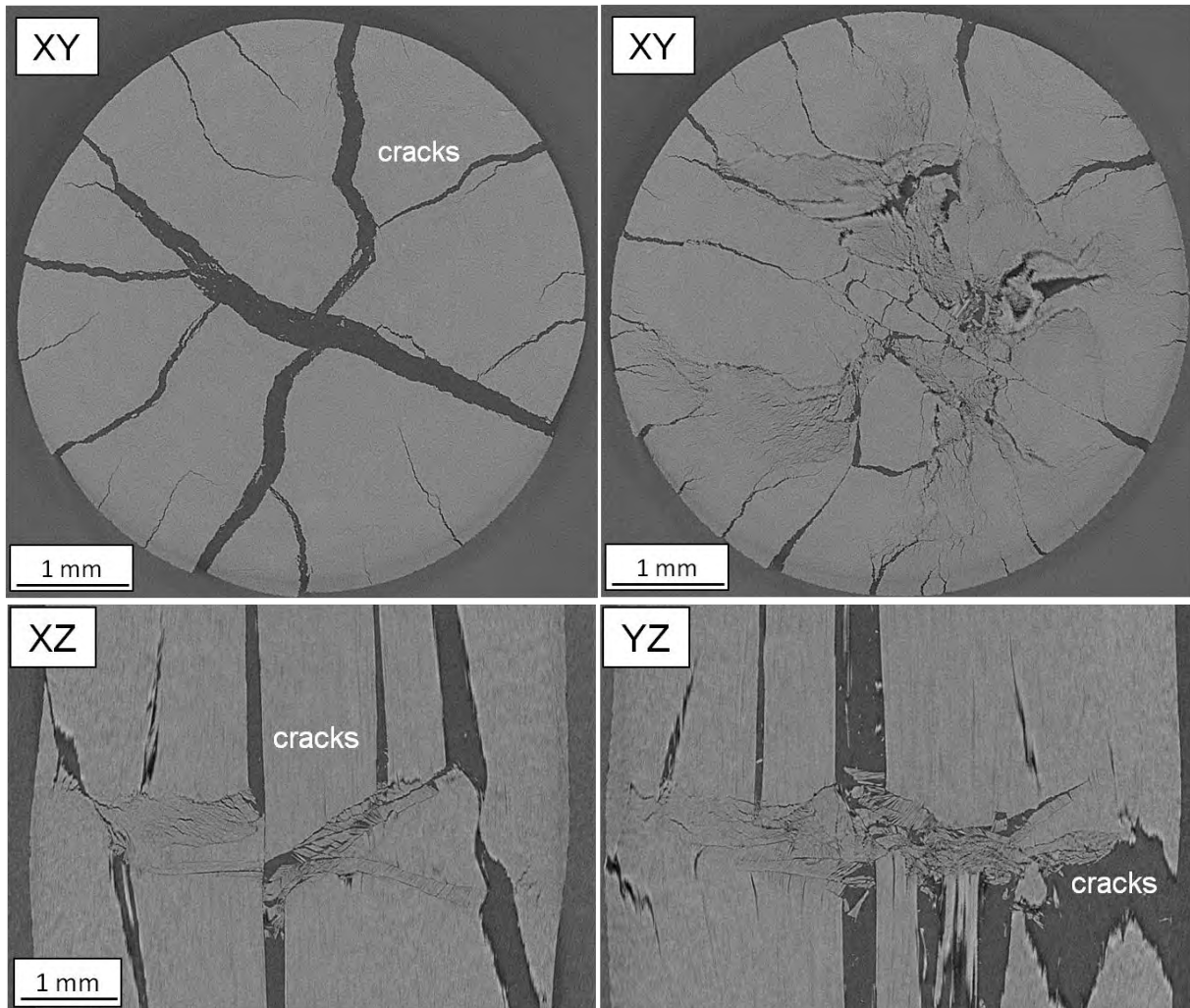
Fig. 187: XCT slices of a pultruded rod tested in torsion monotonically until failure. Cracks grow in matrix rich regions with high waviness degree. Failure in compression of fibre bundles and broken disconnected bundles are observed on transversal and sagittal slices. Voxel size: $(2.5\mu m)^3$.
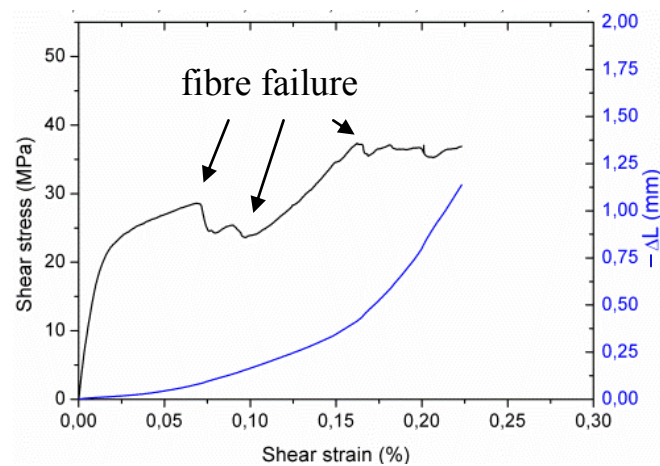
5.5.4 Fractography

5.5.4.1 *After 4-point bending test (laminates and rods)*

Scanning electron microscopy (SEM) fractographies were made on selected specimens after failure in four point bending test. The compression and tension sides perpendicular to fibre direction as well as the delaminated surfaces parallel to fibre direction were inspected. Detailed results for each CFRP material are shown in the following subchapters [64] [65].

5.5.4.1.1 *Laminates HexPly8552*

Micrographs obtained for both types of prepreg based laminates are shown in Fig. 188 to Fig. 190. The different observed fractographic features are indicated in the figure captions.
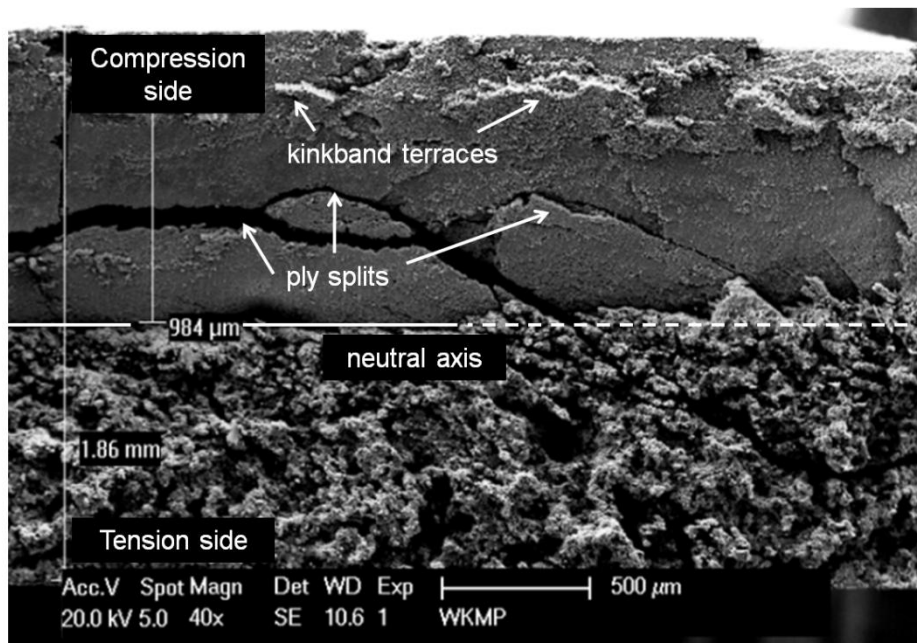
Fig. 188: Fibrous tension and flat compression side of a tested sample showing ply splitting and kinkband formations on the compression side and fibre pull-out on the tension side.
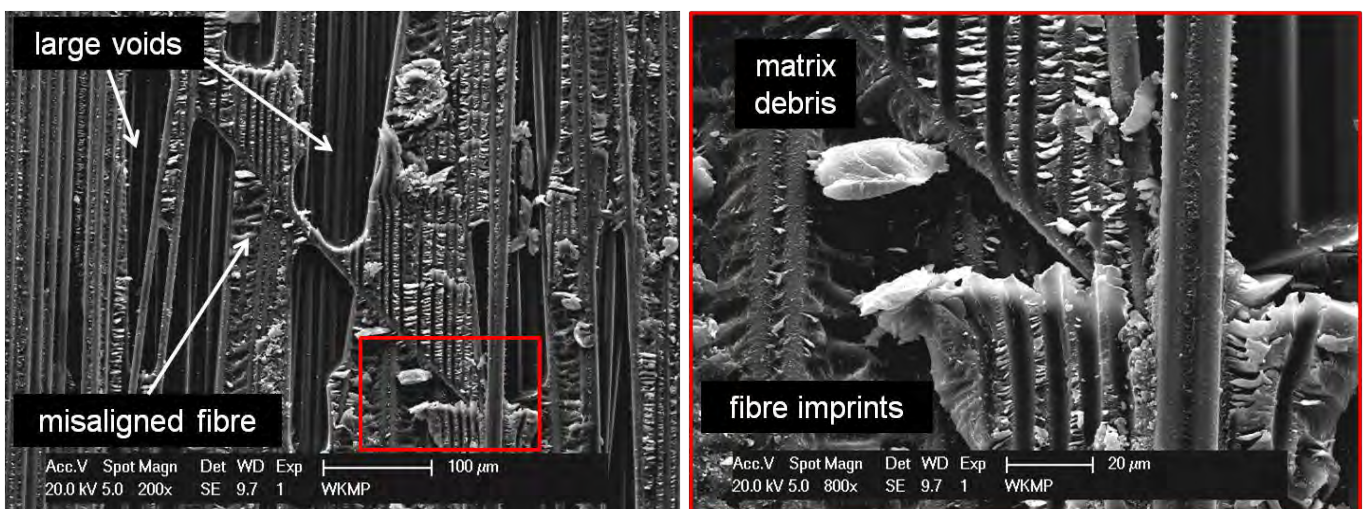
Fig. 189: Fracture surface of a HexPly8552 P1 laminate showing porosity imprints on matrix and misaligned fibre originating matrix debris (zoomed area).
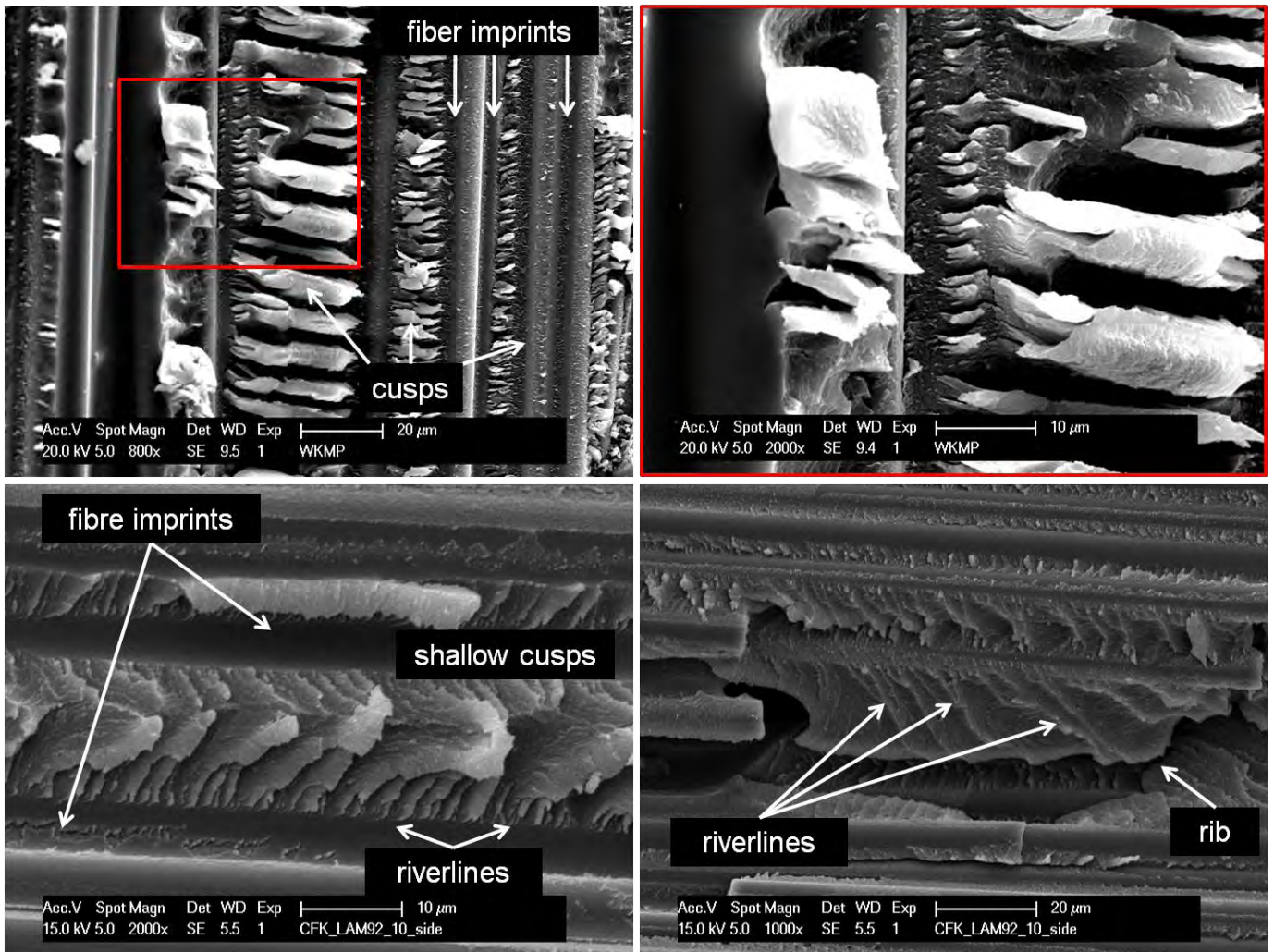
Fig. 190: Top: HexPly8552 P1 laminate fracture surface showing fibre imprints and cusps, whose size varies depending on the distance between neighbour fibres, and cusps detail showing cracks in the matrix perpendicular to fracture surface. Bottom: HexPly8552 P2 fracture surface showing fibre imprints and shallow cusps (indicators of a strong fibre-matrix adhesion). Riverlines and ribs are also observed.

5.5.4.1.2 Laminates Sika CR132

Micrographs of Sika CR132 laminates after four-point bending test are shown in Fig. 191 to Fig. 193. Different observed fractographic features are indicated in the figure captions.
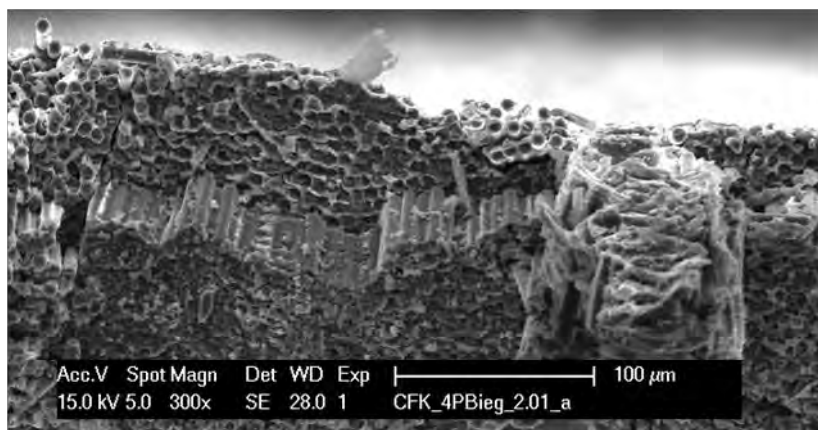
Fig. 191: Fracture surface of UD laminate. Matrix debris and a kinkband are observed.
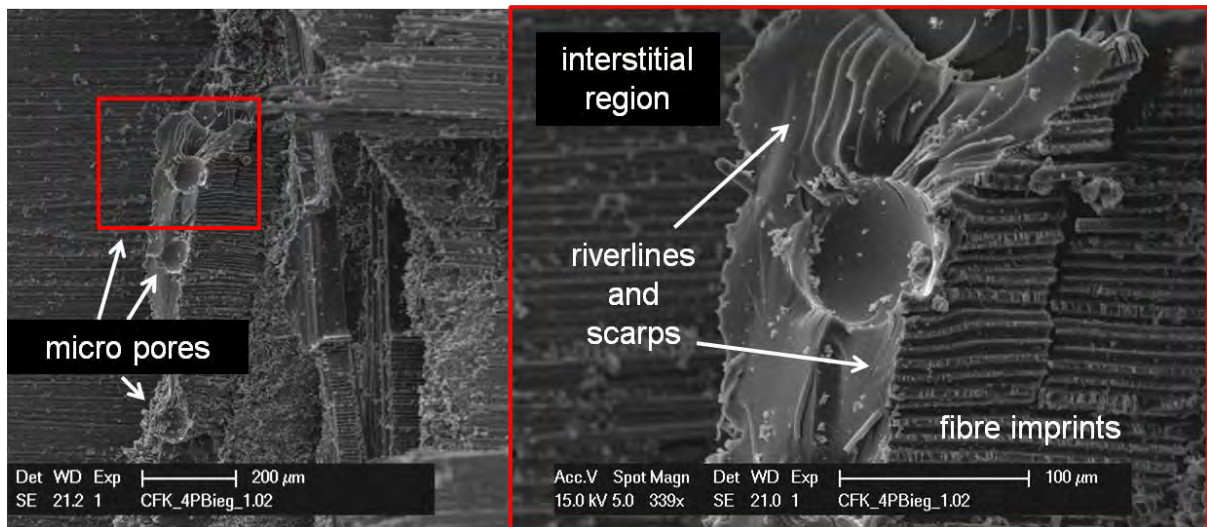
Fig. 192: Delaminated surface of a Sika CR132 0°/90° woven laminate. Interstitial region exhibits convergent riverlines and scarps around a gas micro pore; fibre imprints and a perpendicular crack.
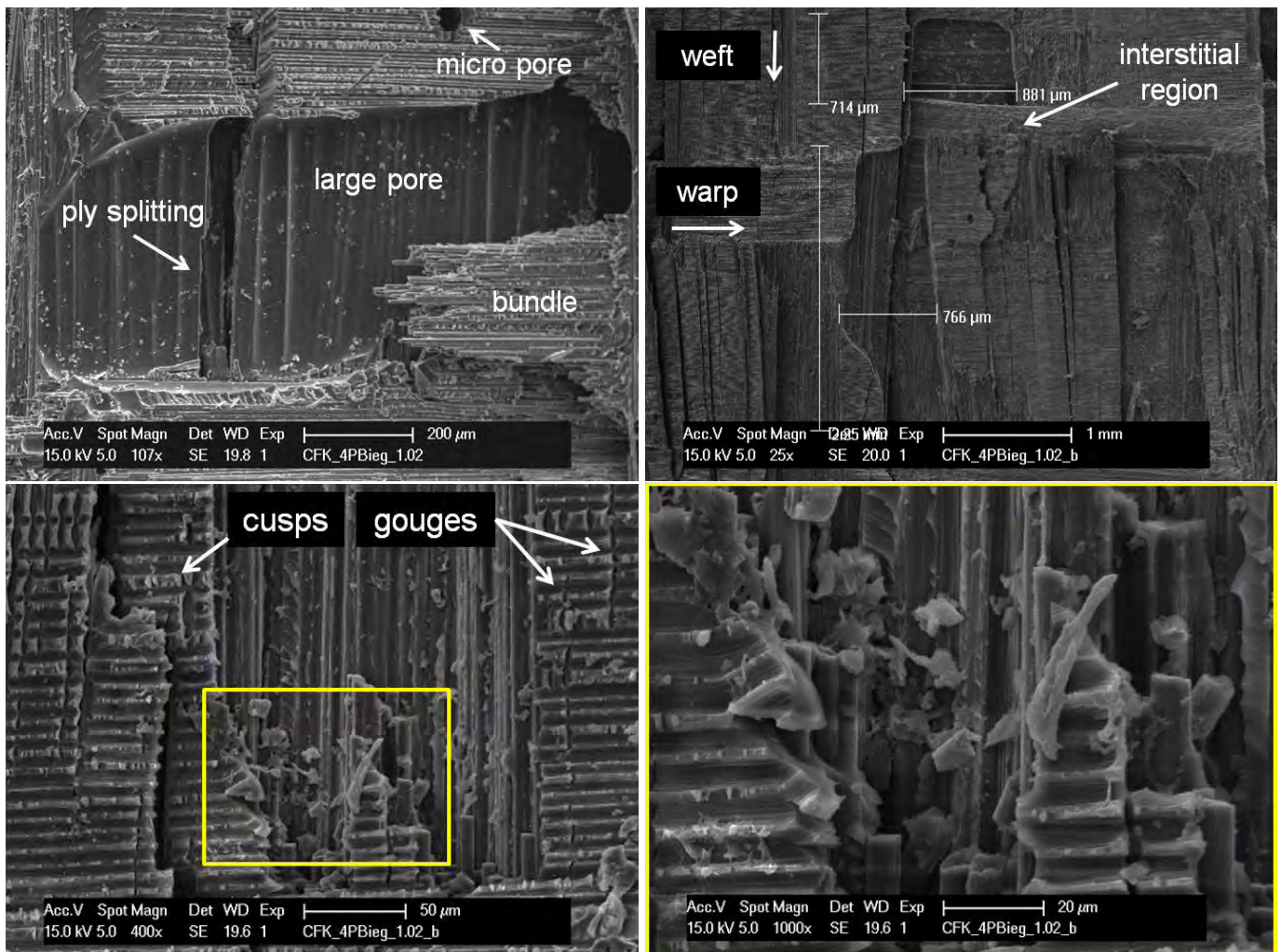
Fig. 193: Fracture surface of a Sika CR132 0°/90° woven laminate. Top left: large pore associated to a perpendicular crack, fractured bundle. Top right: Overview of interstitial region with large pore associated to a crack in weft direction. Porosity observed where 0° and 90° bundles cross impregnation is more difficult. Bottom left and right offer a closer view of this region. Features such as cusps and gouges are observed. Bottom right: matrix debris.

145

Fractography micrographs of pultruded rods after failure in four-point bending test are shown in Fig. 194 to Fig. 196.
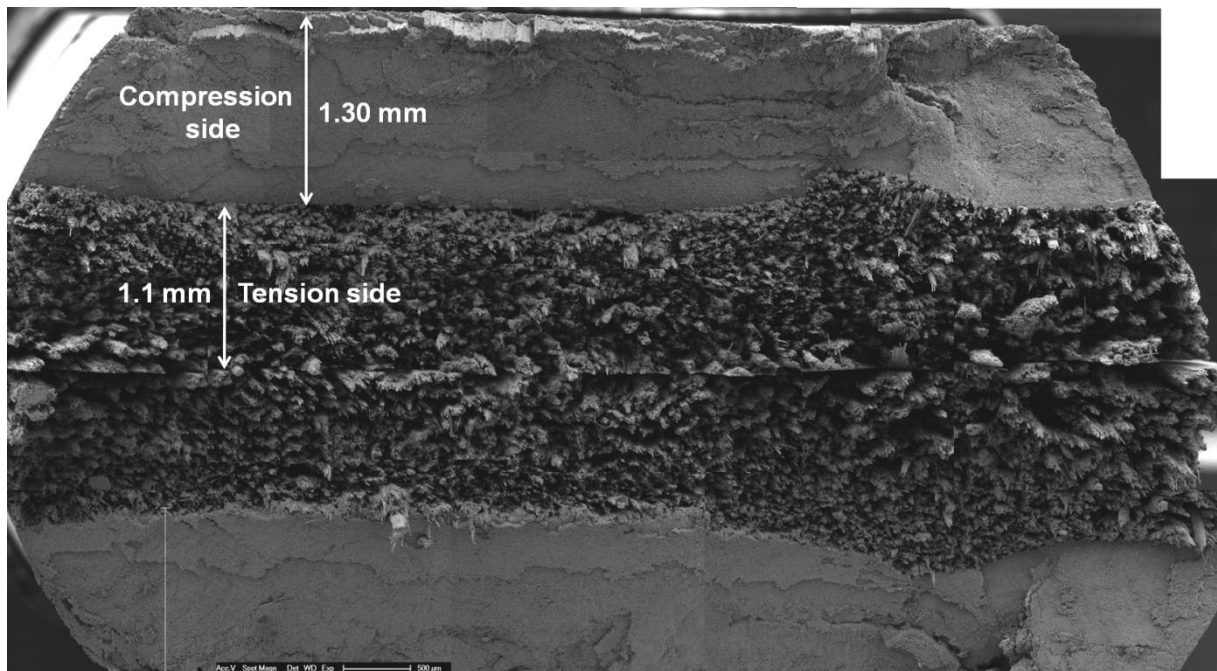
Fig. 194: Panorama overview of the cross section of the two parts a specimen broke into after failure in four-point bending. Each of the two parts present a compression and a tension side which are complementary with the ones on the other part. Along the cross section of the specimen, the area failing in compression is larger than the one failing in tension.
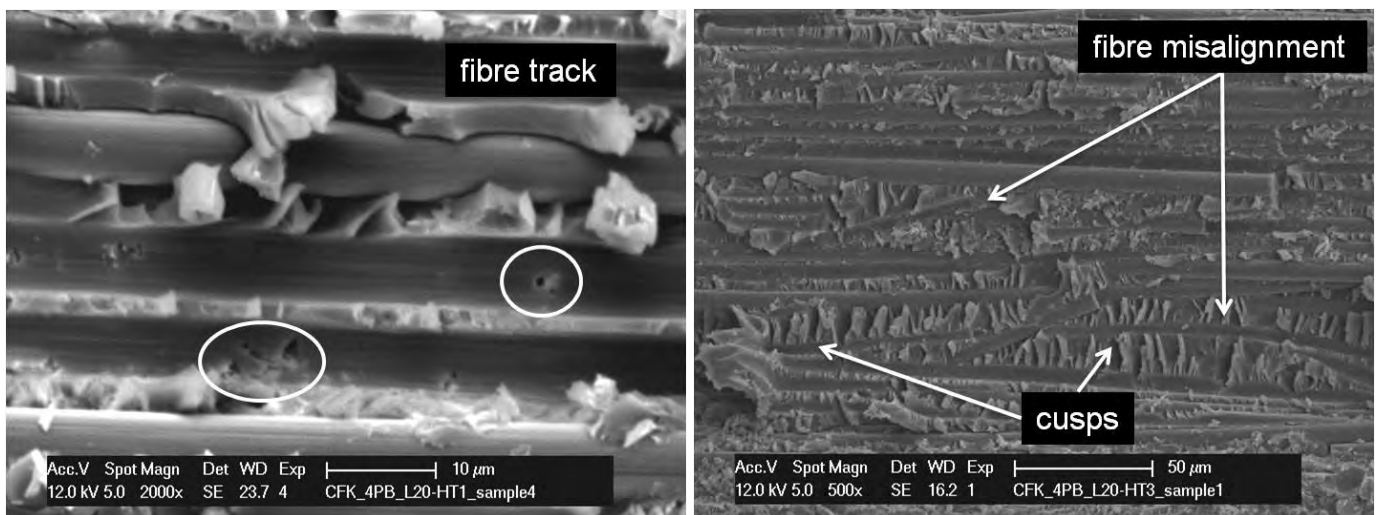
Fig. 195: Delaminated surface of a pultruded rod sample after four point bending test. The fibre misalignment observed in materialography micrographs is also visible on the fibre imprints that remain after delamination. Very small pores are observed on the resin around fibres, possibly originated by the presence of filler particles, which deteriorated the fibre-matrix adhesion.
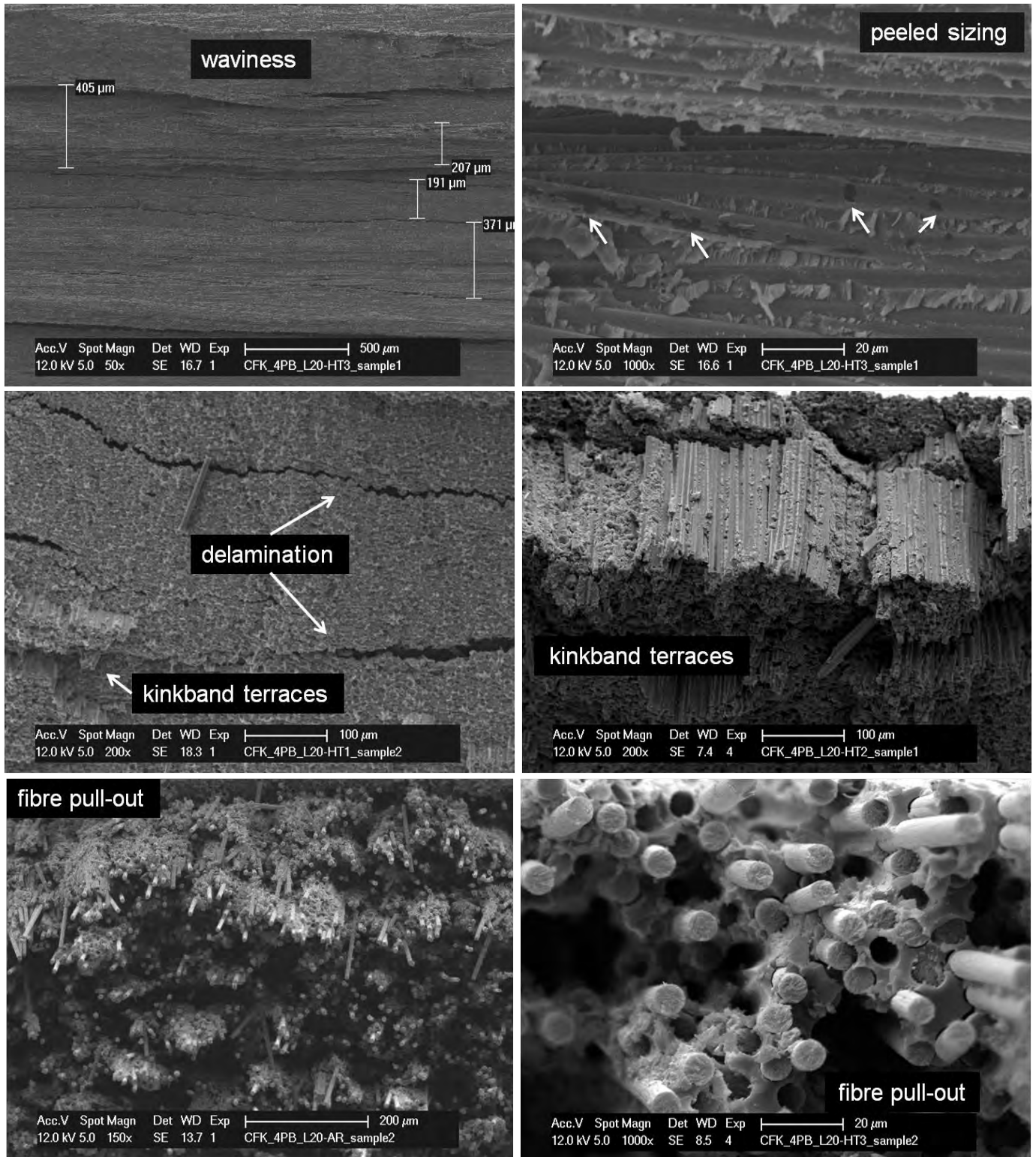
Fig. 196: Top: Delaminated surface. Crack paths and delamination occur parallel to the surface of the tows. Waviness of fibre tows. A smooth fibre surface is observed and the dark spots are areas where fibre has lost the sizing layer, a sign of poor matrix-fibre adhesion. Middle: Compression side of two samples thermally treated prior to testing. Kinkband terraces have a constant length through the whole fracture surface of about 200 µm for HT2 and 50 µm for HT1. Bottom: Tension side of a specimen in as received (AR) condition compared to a thermally treated specimen (170°C 1h). As a result of the different epoxy cure condition different pull out lengths can observed.

5.5.4.1.4   Pultruded profile R/Sika/Sigrafil-T700SC/UD65f
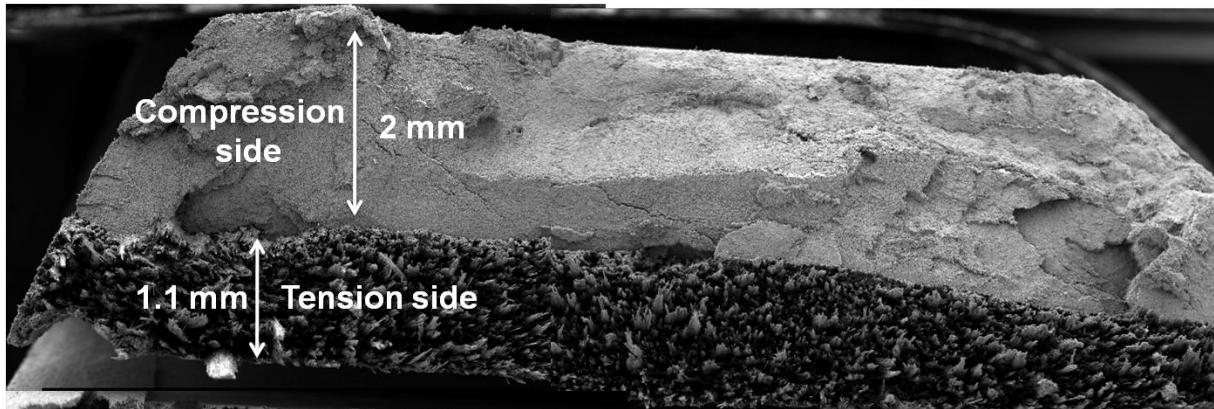
Fig. 197: Cross section panorama overview of one of the two parts a specimen broke into after failure in four-point bending. Compression and a tension side are indicated. Along the cross section of the specimen, the area failing in compression is larger than the one failing in tension.
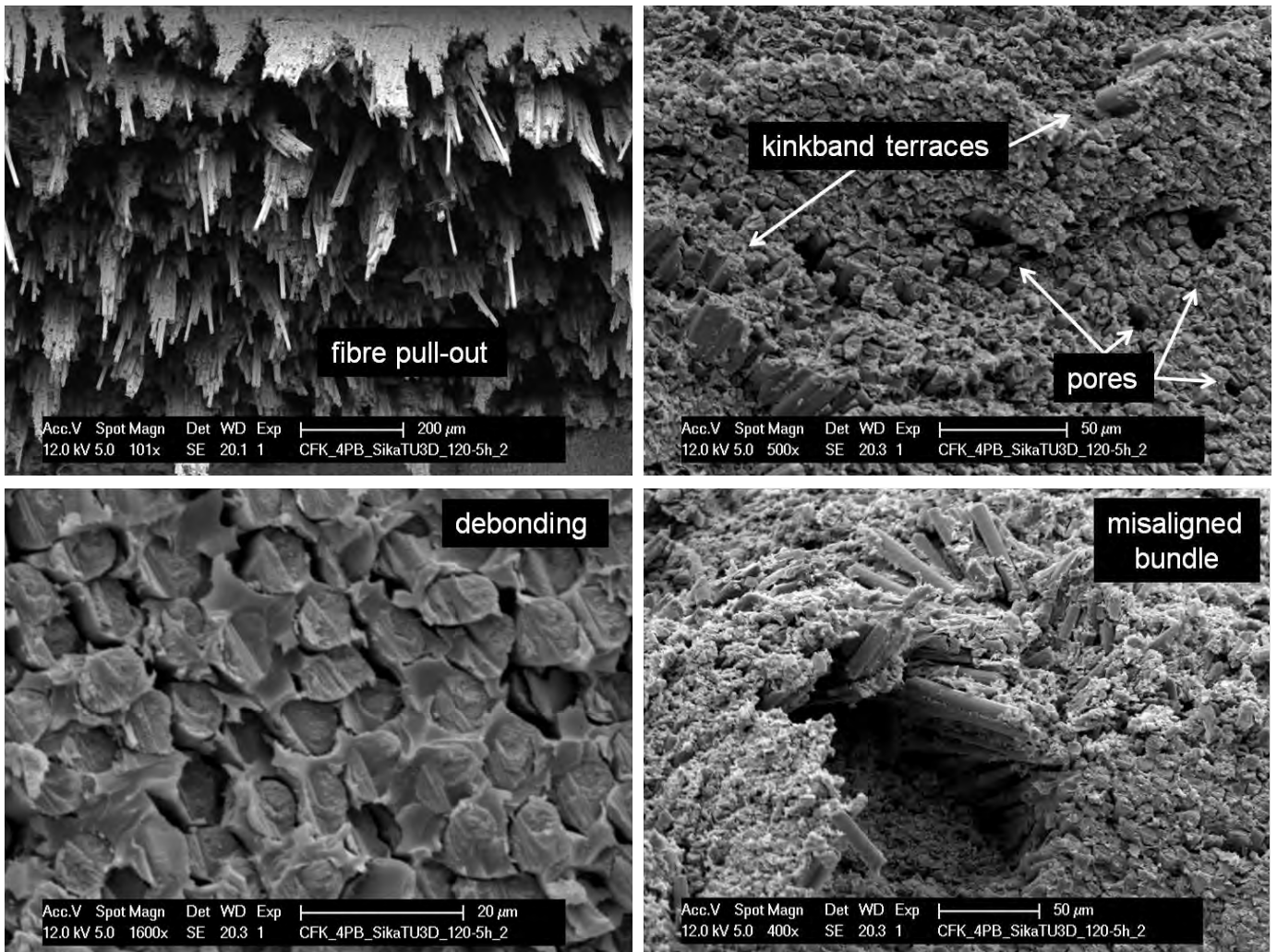
Fig. 198: Tension (top left) and compression sides of a thermally treated specimen (120°C-5h). Fibre pull-out is observed on the tensile side. On the compression side kinkband terraces associated to micro porosity, debonding and the fracture surface of microbuckled fibres can be seen. The effect of a misaligned bundle on fibre fracture modus is presented on the last micrograph.

5.5.4.2 *After torsion test*

5.5.4.2.1 *Pultruded profile T/L20-T/HTSTS/UD65f*

Fractographies of pultruded tubes after failure in torsion are shown in Fig. 199 and Fig. 200. Fibre fracture and fibre pull-out are observed, as well as matrix crack paths correlated to filler agglomerations and micro pores. Fibre bundles can be recognized after failure. Coarse resin fragments with sizes up to 150 μm can be found all over the studied surface indicating brittleness of the epoxy resin. The pulled out fibres lengths ($50 < L < 70$ μm) indicate poor bonding. The smooth surface of the fibres with just a few matrix debris attached are evidence of the weak bonding. This is confirmed by the presence of nearly bare fibres (an example is shown in Fig. 200).
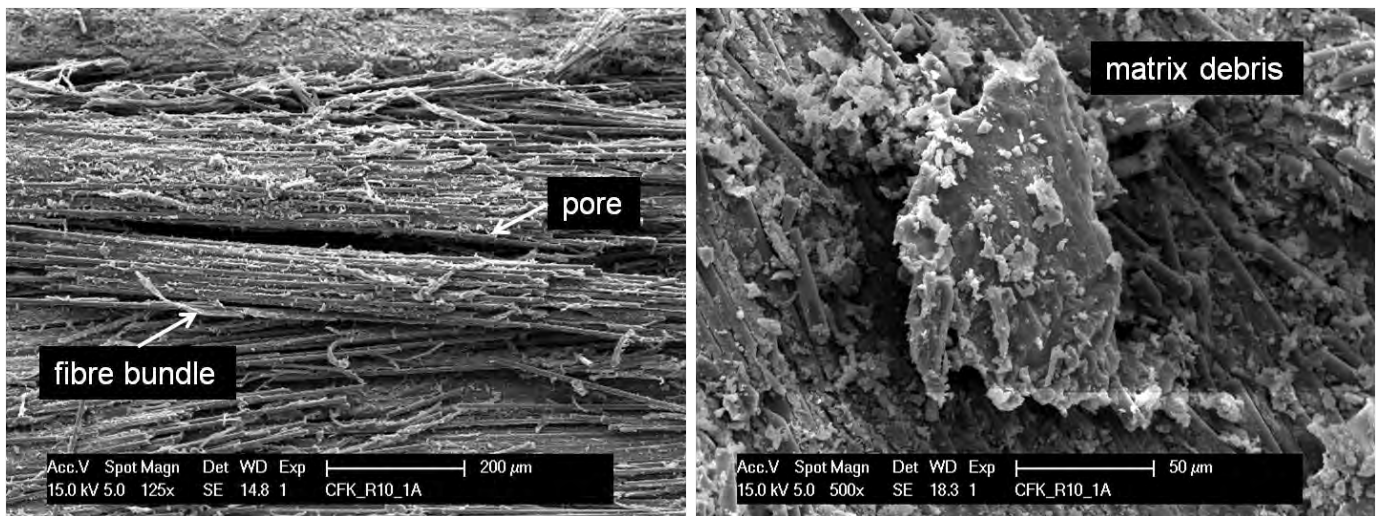
Fig. 199: Fracture surface of a pultruded tube after torsion test. Left: fibre bundle, longitudinal pore. Right: matrix debris and mineral particles.
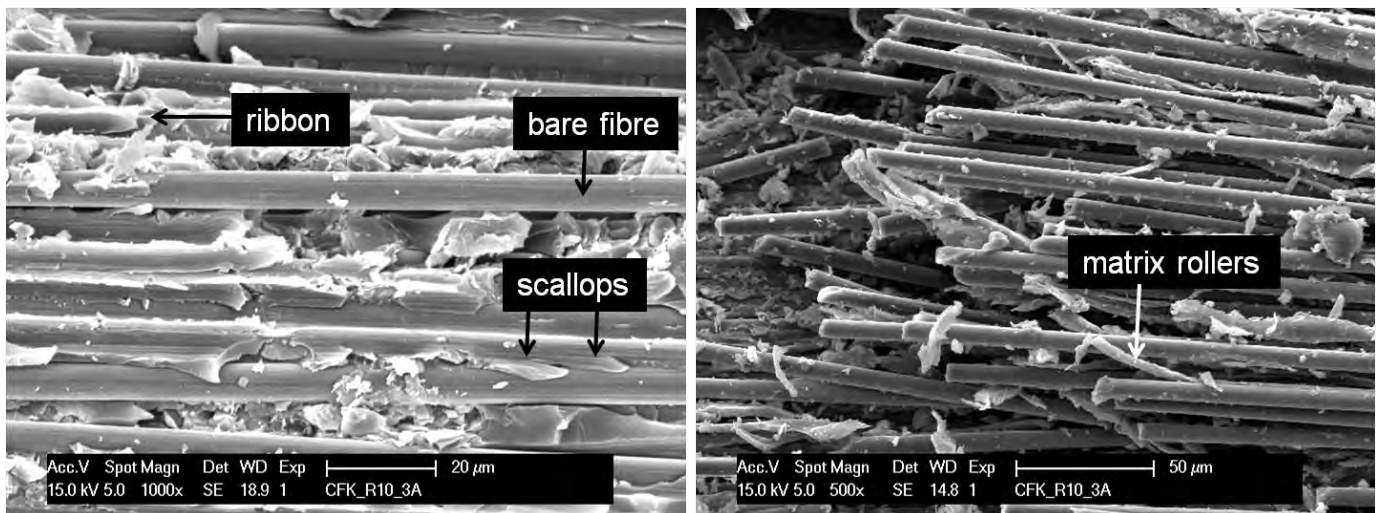
Fig. 200: Fractographies of the inner side of the crack formed along the specimen during torsion test until failure. Left: scallops, a matrix ribbon and a bare fibre. Right: matrix rollers and long pull-out fibres are a sign of weak bonding between fibre and matrix.

5.5.4.3   *After tensile test*

5.5.4.3.1   *HexPly8552/HSAS4/± 45-58f/0.2MPa/2*

Damage in carbon fibre reinforced polymer matrix composite laminates subjected to tensile stress is characterised by intra-laminar cracks (Fig. 202), delamination between plies, fibre pull-out (Fig. 201) and fibre fracture (Fig. 202).
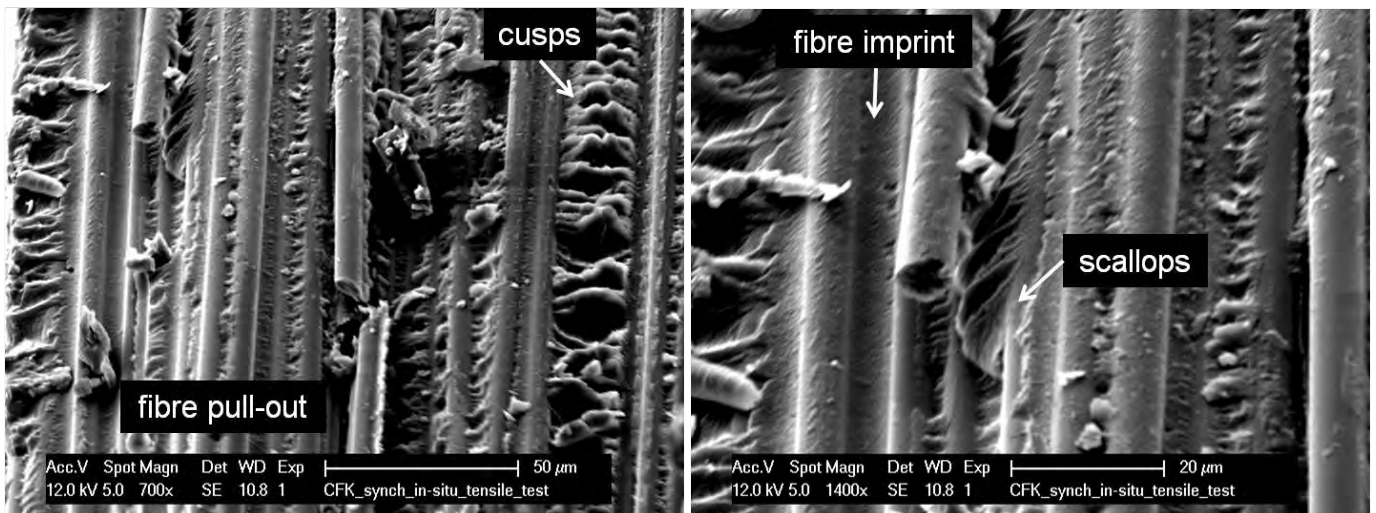
Fig. 201: Fracture surface of the ± 45° cross-ply laminate after tensile test. Fibre pull-out and cusps in the matrix rich areas between fibres are observed, same as for the unidirectional HexPly8552 laminates.
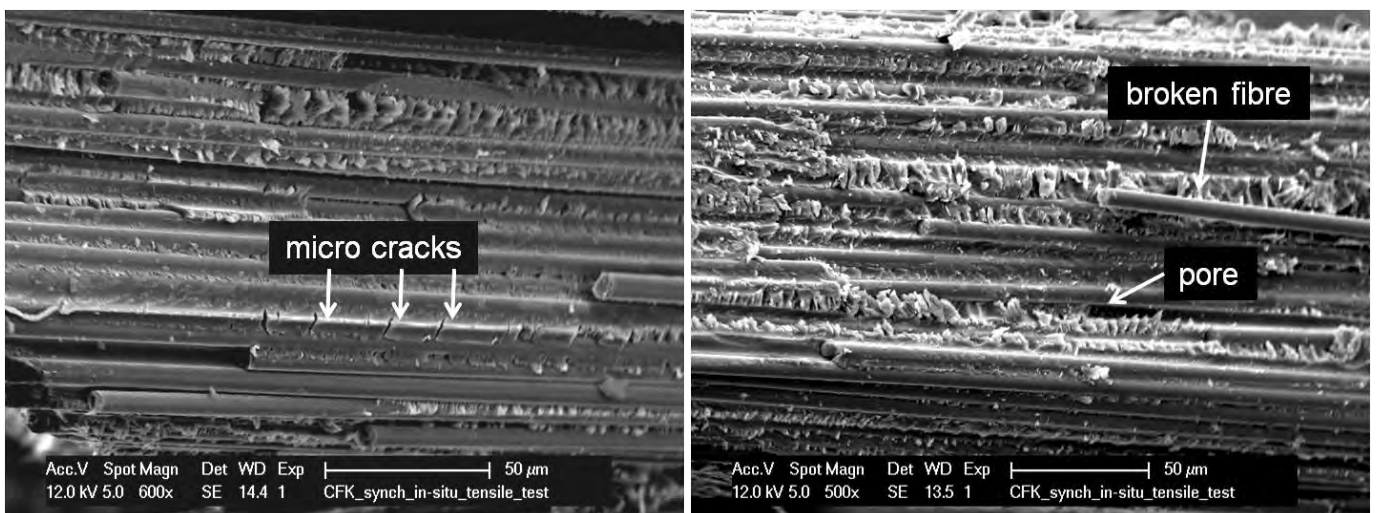
Fig. 202: Fracture surface of the ± 45° specimen after tensile test. Micro cracks, who were not resolved in microtomography slices, can be visualized. Similarly, very small pores can only be imaged by scanning electron microscopy. Broken fibres are found all over the fracture surface as a consequence of the fibre pull-out.

In section 6.6. these results are correlated to those obtained in-situ by means of high resolution synchrotron microtomography (SCT) during sequential tensile test.

6. Discussion

6.1 Assessment of different applied methods

In order to asses a particular property the most appropriate detection method has to be found, in some cases a combination of different complementary methods is appropriate.

A combination of methods is usually the best way to gather information from different points of view. For example, in materialography, different magnifications reveal different features while adding 3D imaging gives a better overall impression of the microstructure. The visualization software allows the quantification and segmentation of interesting features. The knowledge gained by means of tomography is enhanced when combined with classical materialography techniques, such as LOM or SEM, that offer detailed visualization of the smallest features. This is demonstrated in the study of the Sika CR132 based laminates Sik/HTS5631/UD/3bar/4 imaged in 3D by LOM-cubes, XCT and LOT for structural and defect characterisation (see section 5.2.1.7). Another example is the use of tomography (post mortem XCT or in-situ SCT) combined with SEM fractography after mechanical testing in order to explain damage initiation. For instance, a tomographic scan after mechanical testing can be used to localize the internal damage. Once the damaged region is detected, light optical microscopy or fractography provide a higher resolution to assess in greater detail features under the detection limit of the voxel size of the tomographic measurement. Gathering information from all methods ultimately gives insight into the damage mechanisms occurring during deformation (see section 5.5.4.3).

Considering porosity content; the trend of the results from LOM and XCT is the same, but XCT results seem to underestimate the porosity as shown in Fig. 203. Porosity is never uniformly distributed within the samples. XCT covers the biggest volume and enables the visualization of the distributions, spatial position, shape and size only of pores bigger than 3 voxels. LOM yields local porosity values of small areas with high resolution.
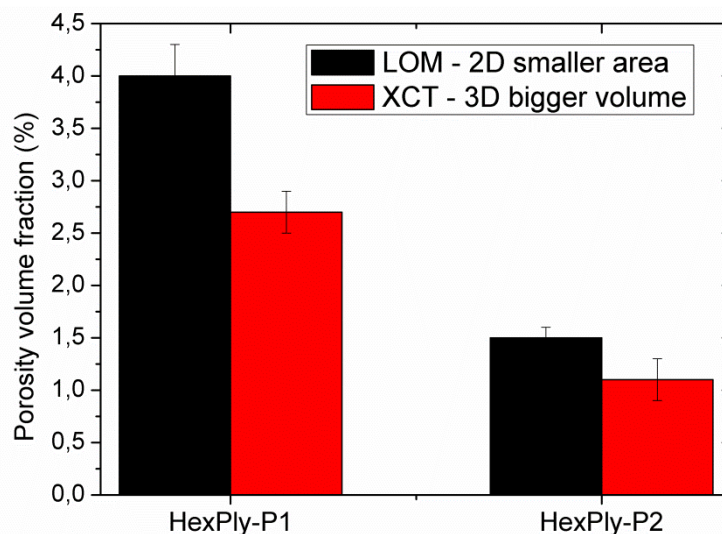
Fig. 203: Volume fraction of porosity obtained for prepreg laminates by LOM and XCT.

Glass transition temperature (Tg) results obtained from DSC, DMA (tan δ) and TMA for the same material exhibited good correlation (see Fig. 204). An example showing curves obtained from DMA and TMA measurements of the same kind of CFRP laminate is shown in Fig. 205, the three curves lead to the same Tg value, ratifying the obtained value.
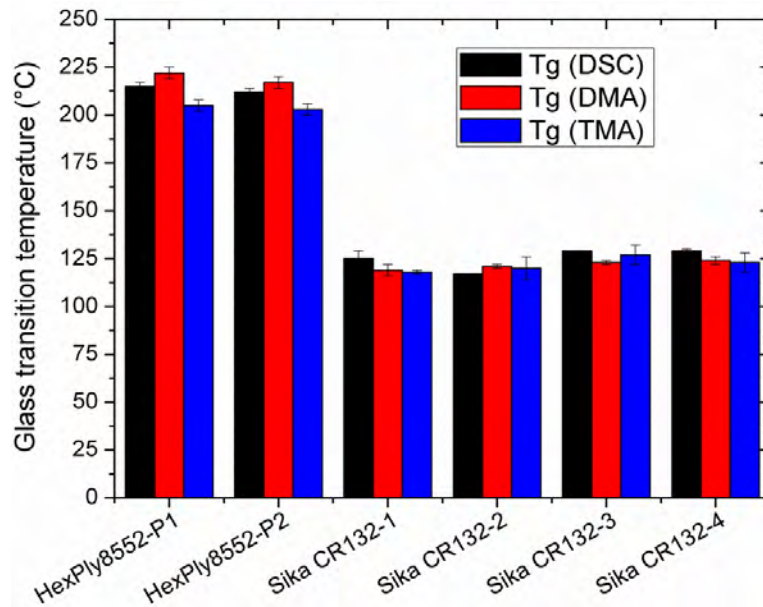
Fig. 204: Tg values obtained by means of DSC, DMA (tan δ) and TMA during first heating cycle.
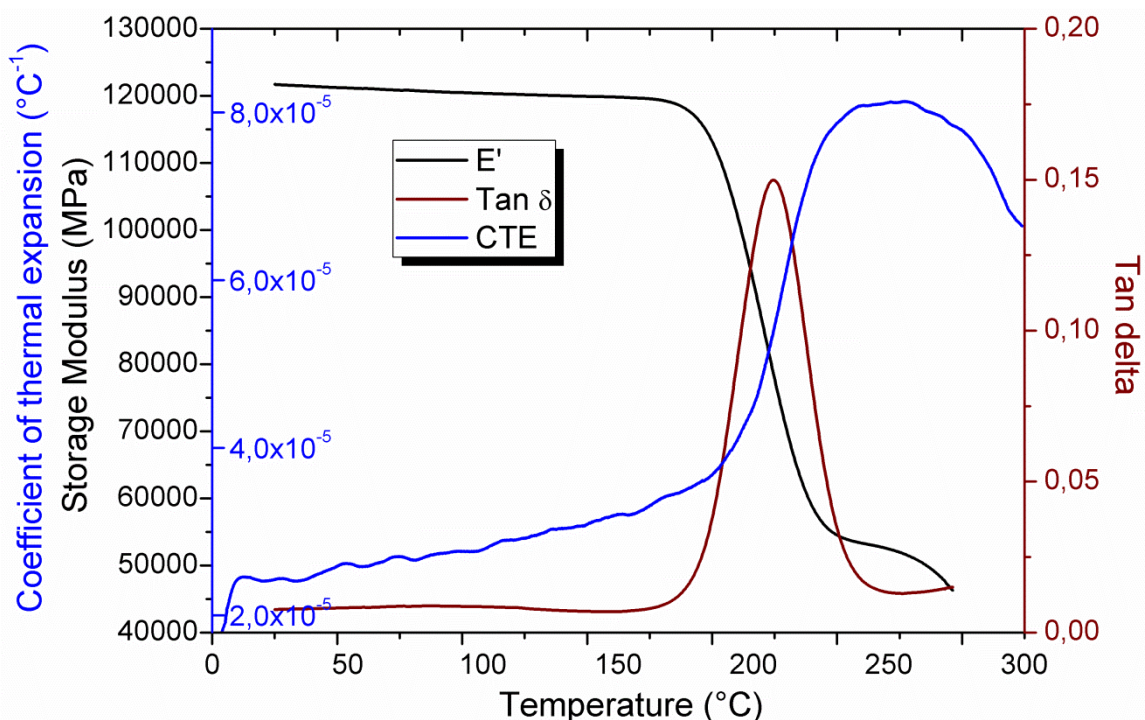
Fig. 205: HSAS4/UD58f/0.2MPa/1 laminates. CTE perpendicular to fibre direction, E' and Tan delta plotted together. Glass transition temperature transition occurs in all cases around 200°C.

Fig. 206 shows values for stiffness in fibre direction, in terms of storage modulus (E') and bending modulus (E_b) obtained for all CFRP materials in as received condition. It is observed that the E' values are slightly different from E_b, this may be explained by the three-point

bending configuration of the DMA set up. In a four-point-bending test the bending moment between the pressure rams remains constant along the specimen, allowing an estimation of E-modulus from a bigger test volume. Three-point bending tests only the surface region at the centre of the sample. Nevertheless in general good correlation is observed for stiffness values.
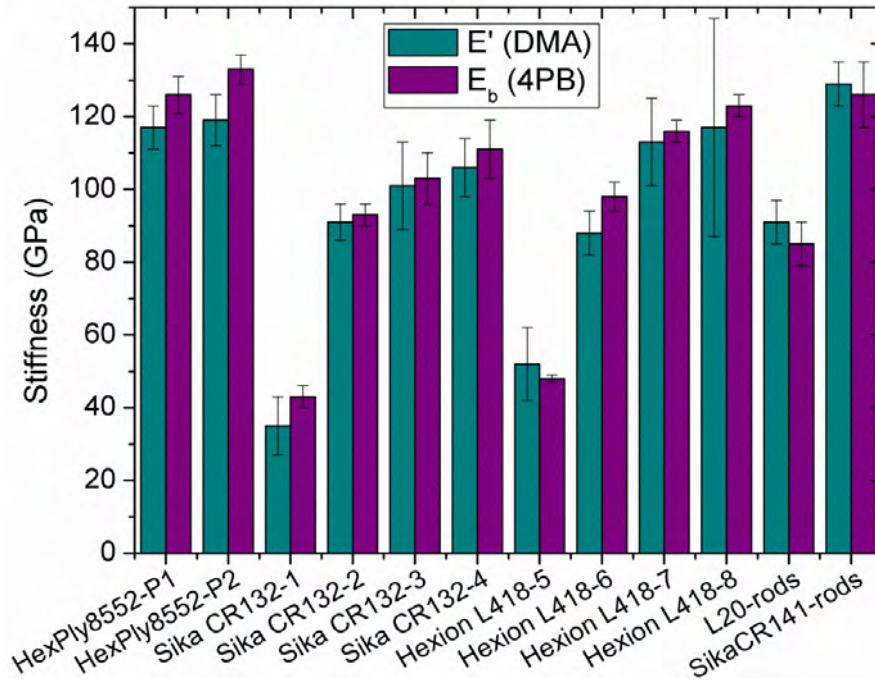
Fig. 206: Storage modulus (E') and bending modulus (E_b) values for all CFRPs tested with 4-point-bending test and DMA in as received condition.

6.2 Influence of production process on porosity content

A detailed analysis of the production processes, their parameters and their contribution to particular manufacturing defects is not the main objective of this work. As far as it was possible, the knowledge gained regarding the origin of manufacturing porosity will be briefly presented in this section.

The manufacturing processes used in the production of the investigated composites are very different and a direct comparison between them would thus not be adequate. All eleven laminates were produced at "laboratory" scale, by means of hand lay-up of prepregs or impregnated textile layers followed by moulding. Whereas the three pultruded profiles were produced in an automated way. In comparing these two manufacturing extremes, it can be said that less critical defects are observed in samples produced by pultrusion, than in the laminates. A reason for that may be that pultrusion allows a more precise control of the production parameters that are relevant for the formation of defects, whilst hand lay-up is more susceptible to defect formation.

UD pultruded rods produced with L20 matrix and filler particles present a significant scatter in the volume fraction distribution of the components observed in LOM (Fig. 31), confirmed by TGA; whilst Sika CR141 rods without particles have a more homogeneous distribution of fibres and matrix, however this material contains a mixture of two different C-fibre types.

6.2.1 Curing cycle

Two different laminates produced using the same prepregs and layer configuration (UD), as well as the same production process (compression moulding) were studied, however applying different curing cycles P1 and P2, which differ only on a temperature plateau as explained in section 4.1.1.1. The volume fraction of fibres, matrix and porosity was determined by means of XCT, TGA and LOM micrograph analysis. The volume fraction of fibres is the same for both types of laminates but the volume fraction of porosity is significantly influenced by the curing cycle. The laminates cured with cycle P1 had 2.7 vol.% of porosity, the ones cured with P2 only 1.1 vol.%. (see Fig. 207). Higher curing temperatures lead to a higher porosity content. One of the reasons may be the formation of gases during the polymerization reaction, the diffusion of which is hindered by the increased viscosity of the curing epoxy resin.
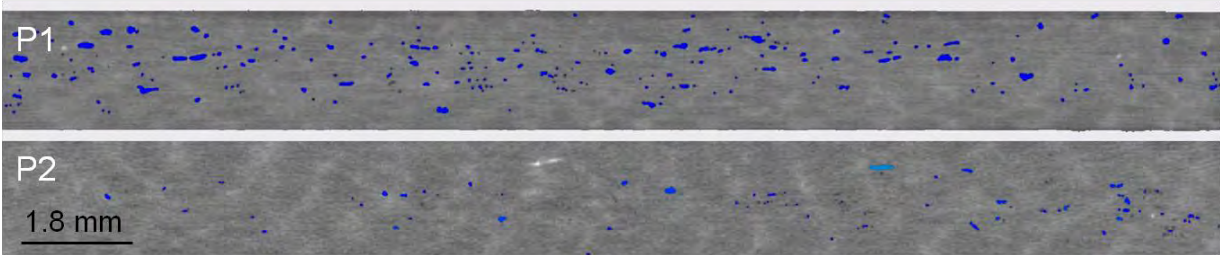
Fig. 207: XCT axial slices showing segmented porosity in blue. Voxel size: (11 µm)³.

6.2.2 Pressure

Two families of laminates produced by hand lay-up of impregnated textiles cured at room temperature under different curing pressures were studied. In Fig. 208 materials 1, 2, 3 from the Sika CR132 family and materials 5, 6, 7 from the Hexion L418 family were cured at 0.1MPa, whilst the other two materials were cured at 0.3MPa. The porosity content of material 4 and 8 is 0.2 vol.% and 2.4 vol.% respectively, much lower compared to laminates cured under 0.1MPa, underlining the influence of manufacturing pressure on porosity content.
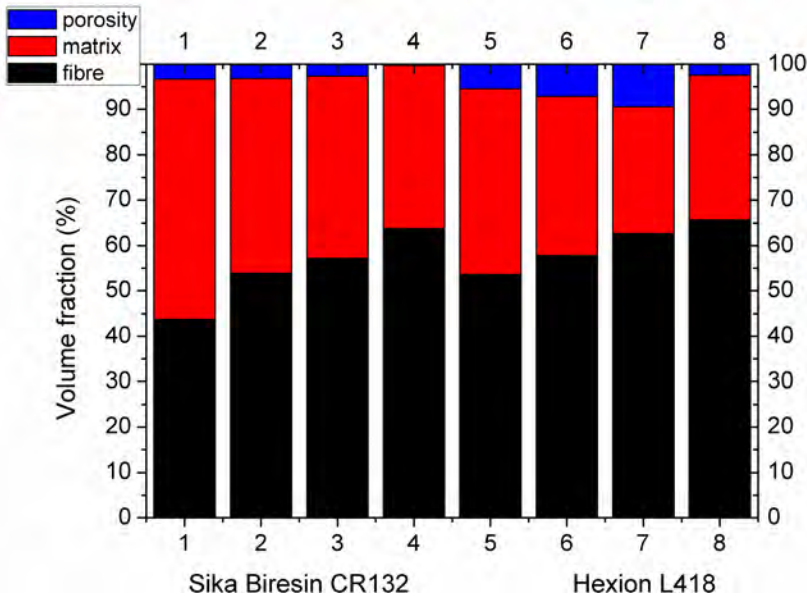
Fig. 208: Volume fraction of constituents obtained for all Sika CR132 and Hexion L418 impregnated textile laminates obtained from TGA measurements.

6.3 Effect of thermal treatments

6.3.1 Effect of thermal treatment on curing degree and glass transition temperature (Tg)

For the R/Sigrafil-T700SC/UD65f rods an investigation of the curing condition within the matrix after different heat treatments was made by means of modulated DSC analysis. For heat treatments at temperatures above 120°C or for holding times above 4h no post-curing peak is observed indicating a fully cured condition of the epoxy matrix (see Fig. 209).
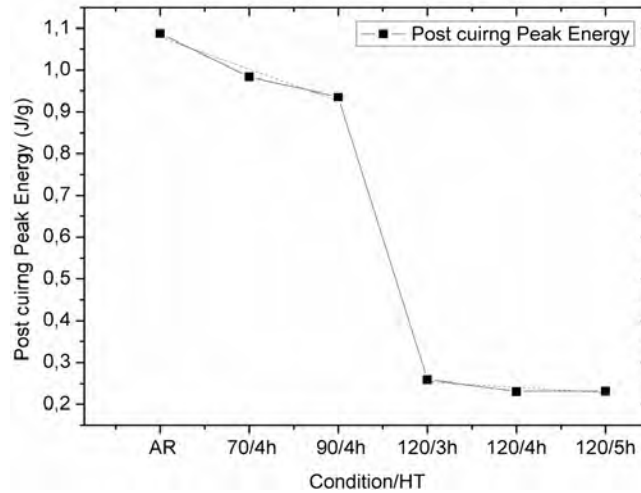
Fig. 209: R/Sigrafil-T700SC/UD65f pultruded rods. Post-curing energy released during MDSC analysis by as received samples (AR) and after different heat treatments. Post curing peak in Fig. 131.

The degree of cure of the resin controls primarily its viscosity. The rate of change of the degree of cure depends on the individual resin and its temperature history. The resin's heat of reaction is used as a measure of the degree of cure. The rate of change of the degree of cure is often not linear and makes it difficult to estimate the response of a resin to a new temperature profile. In thick structures, the heat of reaction may contribute significantly to the temperature exposure of the resin, affecting the degree of cure, and thus the viscosity.

Fig. 210 presents Tg results obtained from modulated DSC for pultruded rods after various thermal treatments. Long holding times do not increase Tg as much as high temperatures.
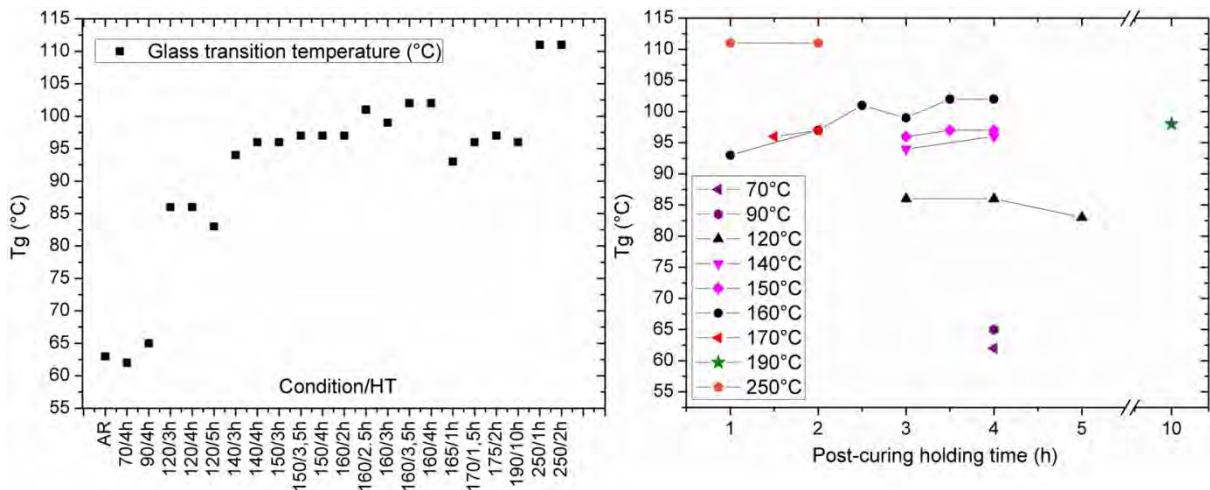
Fig. 210: Tg evolution for R/Sigrafil-T700SC/UD65f pultruded rods after different thermal treatments.

155

After the resin has gelled, the glass transition temperature is often used as an indicator of degree of cure. Fig. 211 presents Tg values obtained by means of DMA for all pultruded rod materials in as received (AR) condition and after different thermal treatment. In section 4.2.3.1, Tab. 14 presents a summary of all applied thermal treatments.
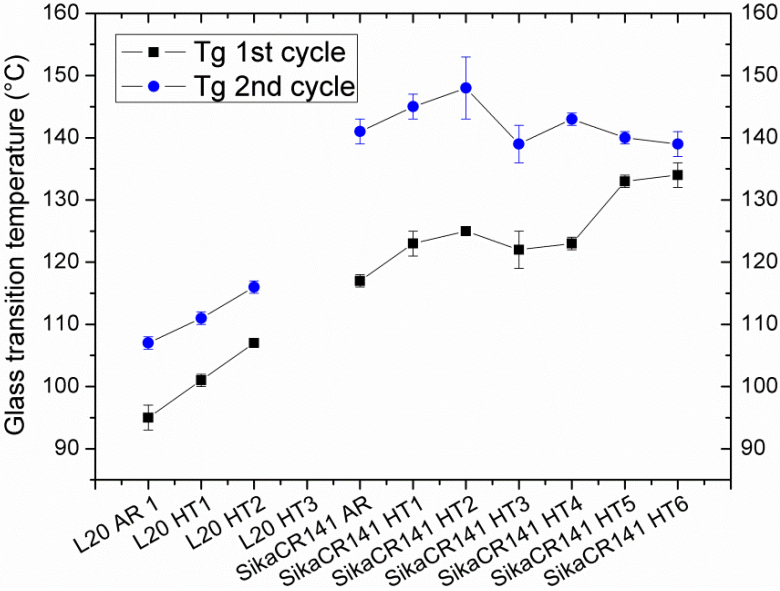
Fig. 211: Glass transition temperature from DMA for all pultruded rod materials after thermal treatment.

6.3.2 Effect of thermal treatment on storage and flexural E-modulus

In Fig. 212 stiffness values for all studied pultruded rods from four-point bending are compared with the storage moduli obtained from DMA using two consecutive heating cycles for all studied conditions (i. e. as received and after thermal treatment). All values are of the same order of magnitude and show the same tendency independently of the test method used. Thermal treatments details are explained in section 4.2.3.1, in Tab. 14.
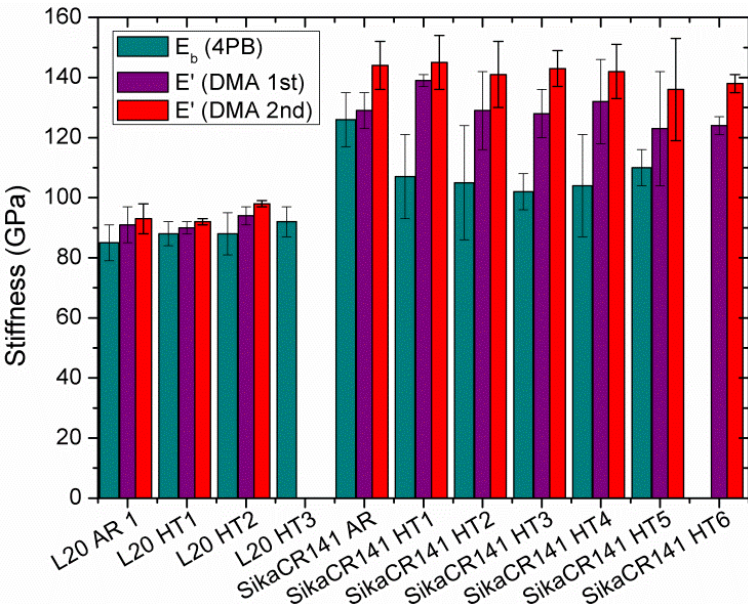
Fig. 212: Flexural modulus from four-point bending and storage modulus from DMA (applying 2 heating cycles) obtained for all pultruded rods in as received condition and after thermal treatment.

156

Pultruded rods produced with L20 matrix show no significant variation of the stiffness after thermal treatment, but a small increase is observed after the first DMA heating cycle. Sika CR 141 rods however exhibit a drop in the bending modulus after heat treatments, whereas the loss modulus increases slightly after the first heating in DMA (i.e. correspondingly, the loss modulus is somewhat higher in the second cycle). Fig. 213 presents the storage moduli corresponding to the T_g results presented in Fig. 211. Both T_g and E' grow with increasing temperature as a consequence of further crosslinking within the epoxy matrix.
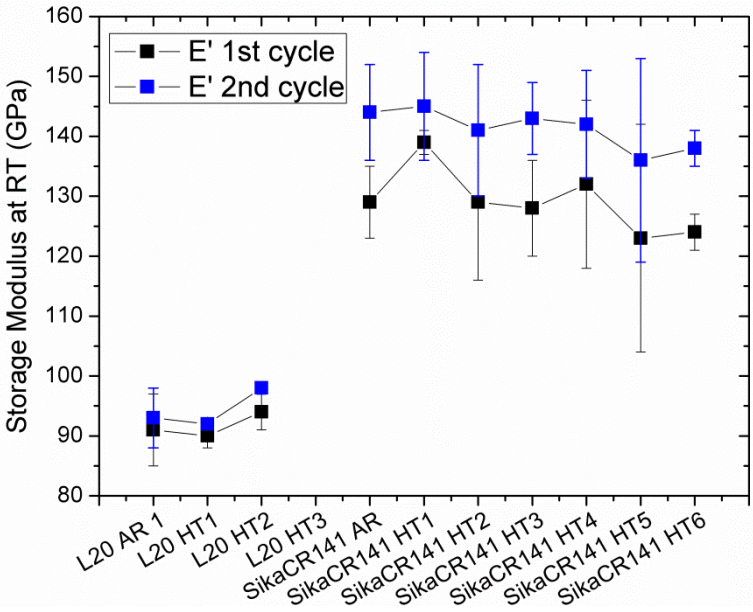
Fig. 213: Evolution of storage modulus (E') after different heat treatments for all pultruded rods obtained from DMA using two consecutive heating cycles.

6.3.3 Effect of thermal treatment on flexural properties

If we consider the obtained bending properties for samples tested after thermal treatment in comparison with values obtained for the as received condition (Fig. 214), we see no significant changes for the rods produced with L20 matrix. There is a slight decay of mechanical properties for the Sika CR41 rods, if the material is post cured at temperatures below 160°C, where the crosslinking reaction has its maximum (as observed in DSC curves, for instance in Fig. 131).
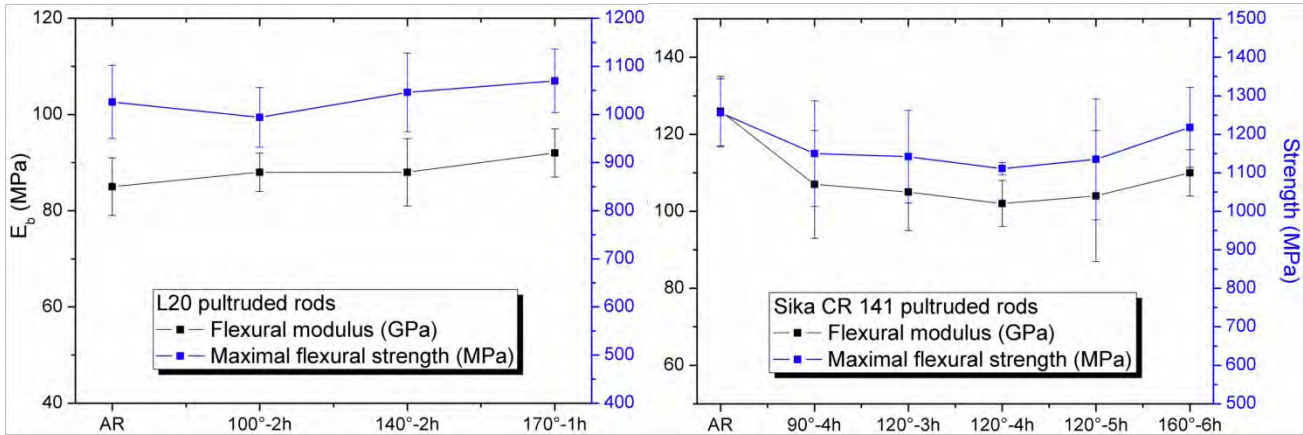
Fig. 214: Bending modulus (black) and ultimate bending strength (blue) obtained for pultruded rods.

6.4 Effect of porosity and fibre volume fraction on stiffness and strength

The mechanical properties of the composites are mainly determined by the mechanical properties of the constituents and their volume fraction. Applying the rule of mixtures (ROM) provides theoretical values that can be compared with experimental results (Tab. 35) [23]. But as mentioned in chapter 2 and 3, real composite materials contain always defects, inhomogeneous distribution of the constituents, porosity, waviness, etc. Their influence on the mechanical performance will be analyzed here.

Sample	Longitudinal Stiffness (GPa)			Long. Strength (MPa)	
	E (ROM)	E_b (4PB)	E' (DMA)	σ (ROM)	σ_u (4PB)
HexPly8552 Laminates					
HSAS4/UD58f/0.2MPa/1	136	126 ± 5	117 ± 6	2603	1644 ± 79
HSAS4/UD58f/0.2MPa/2		133 ± 4	119 ± 7		1956 ± 186
Sika CR132 Laminates					
HTA40/UD/1bar/3	131	93 ± 3	91 ± 5	1484	794 ± 50
HTS5631/UD/1bar/3	140	103 ± 7	101 ± 12	2713	795 ± 39
HTS5631/UD/3bar/4	156	111 ± 8	106 ± 8	3034	918 ± 53
Hexion L418 Laminates					
HTA40/UD/1bar/5	138	98 ± 4	88 ± 6	1562	741 ± 36
HTS5631/UD/1bar/5	149	116 ± 3	113 ± 12	2016	739 ± 24
HTS5631/UD/3bar/6	159	123 ± 3	117 ± 30	2147	973 ± 48
Pultruded Rods					
R/HTSTS/UD65f	124	85 ± 6	91 ± 6	2073	1026 ± 76
R/Sigrafil-T700SC/UD65f	142	126 ± 9	129 ± 6	2941	1256 ± 88

Tab. 35: Experimental longitudinal stiffness values of UD CFRP compared with results of the Rule of mixtures (ROM).

Experimental values of stiffness are in good agreement with ROM estimations, however for the strength, we observe a rather significant mismatch, this is due to premature fibre failure owing to stress localisations caused by defects like fibre-matrix debonding, touching fibres, fibre misalignment, inclusions and the statistical nature of fibre strength [92] [91] disturbing the global load transfer between the fibres. In order to be able to make statements about the influence of defects on a property, we have to keep the other factors as constant as possible, so we can for instance compare only variations of a mechanical property between two materials produced in a similar way and with either the same kind of matrix or the same fibre type.

Regarding strength in fibre direction, prepreg based laminates yield much higher values than the other textile laminates or the pultruded profiles. The strength of 0°/90° laminates is not much lower than that of the UD samples. The decrease in stiffness of the 0°/90° samples is much more pronounced. Prepreg based laminates P1 and P2 have almost the same volume fraction of fibres but differ in their porosity (as shown in section 6.1.2.1). The values of stiffness of the laminates with the lowest fraction of porosity is slightly higher and the strength obviously the highest. For the impregnated textile laminates produced with Sika CR 132 and Hexion L418 matrix, the dependence of the bending strength on of the bending modulus on fibre volume fraction are shown in Fig. 215 and Fig. 216. Materials 1 and 5 in these diagrams are 0°-90° laminates and therefore their stiffness values are much lower.
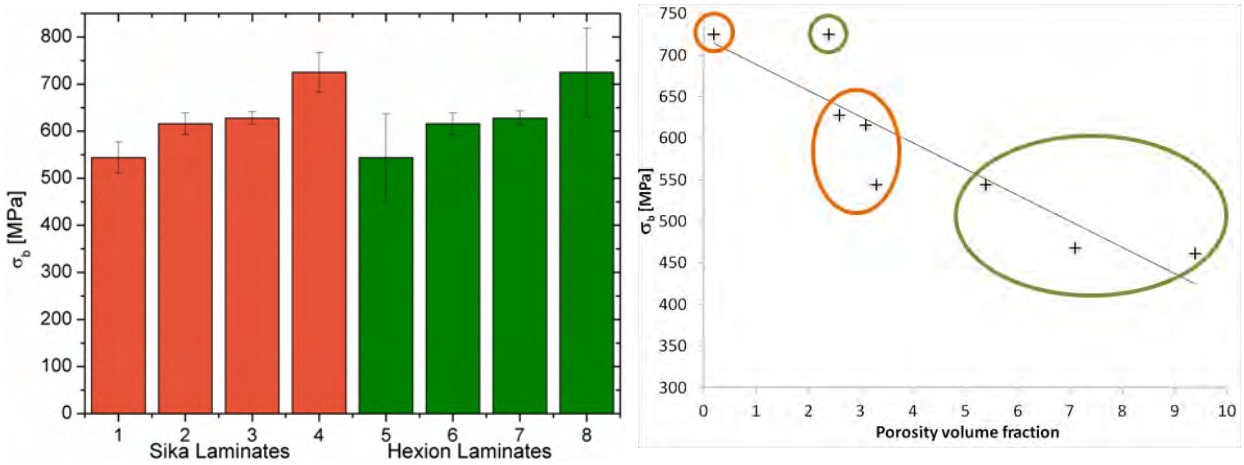
Fig. 215: Maximal 4-point bending shear strength for all laminates and dependence with porosity(vol.%).
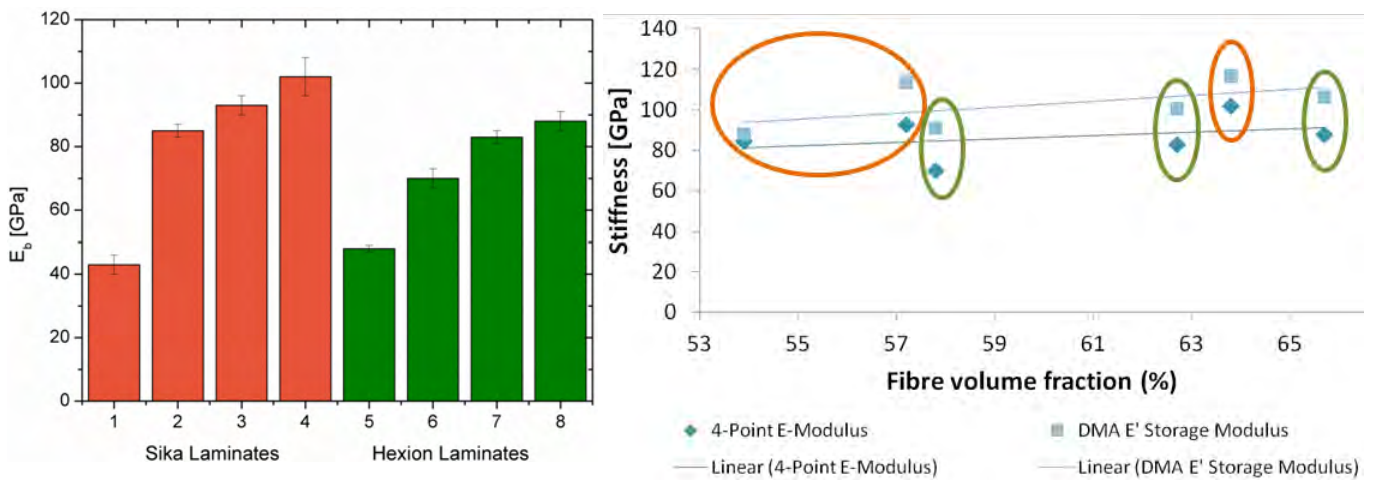
Fig. 216: Stiffness: E_b (4-point bending) and E' (DMA) related to fibre vol% for the six unidirectionally reinforced laminates. 1 and 5 are 0°/90° woven laminates.

6.4.1 Influence of fibre-matrix interface

The fibre-matrix interface is closely linked to the mechanical and thermal properties of CFRP materials. The quality of the interface is critical for load transmission. It also influences damage propagation within the composite during mechanical testing.
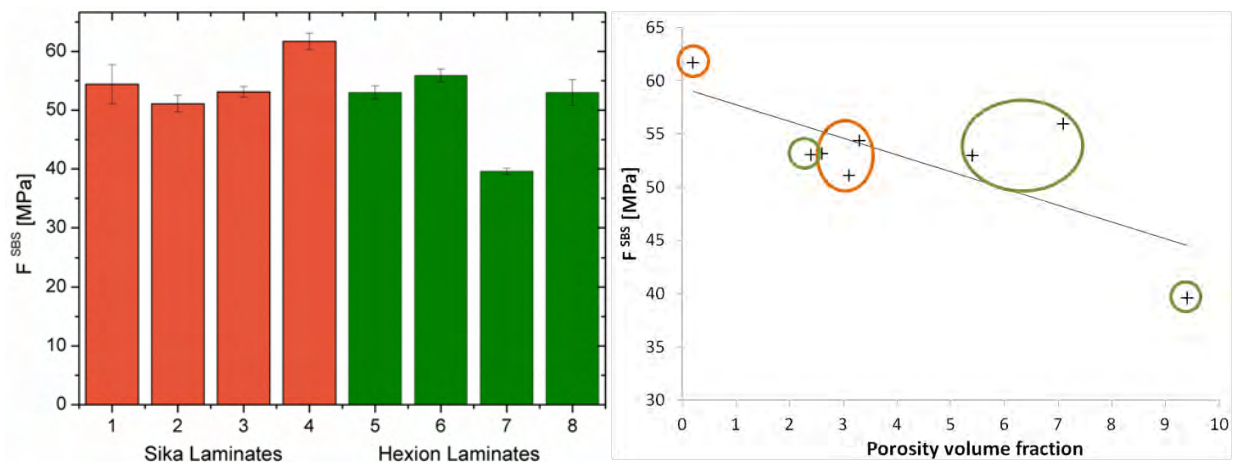
Fig. 217: Interlaminar shear strength results for all eight impregnated textile laminates and dependency with porosity volume fraction (vol.%).
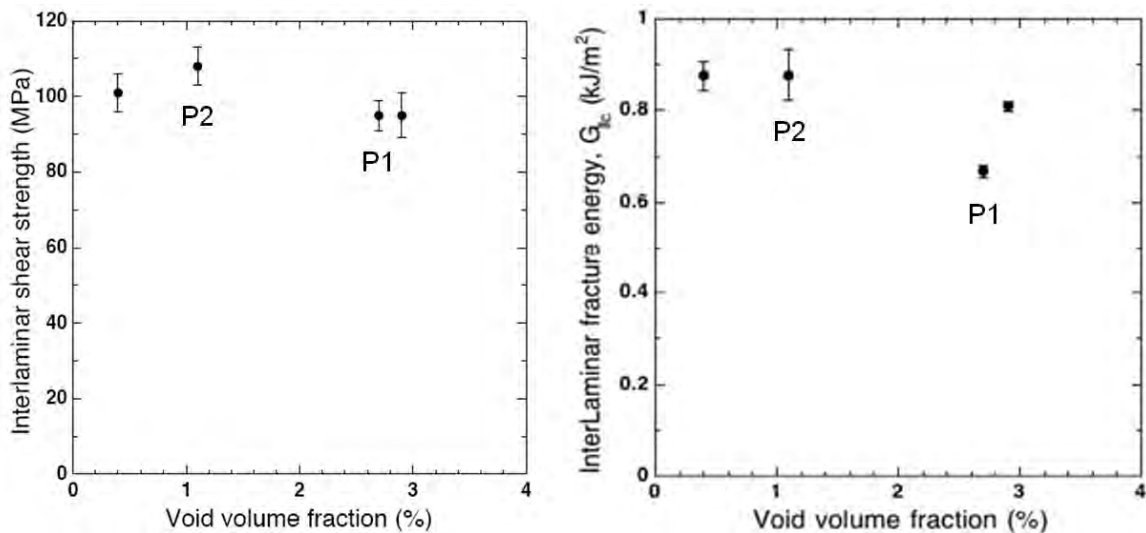
Fig. 218: Interlaminar shear strength and fracture toughness results for the two different prepreg based laminates and their dependence on porosity volume fraction. Threshold value porosity>1% vol. This results were provided by project partner Silvia Hernández and are published in [43].

The methods applied to investigate fibre-matrix interface were short beam shear (SBS) test and interlaminar fracture toughness. Results for the textile laminates are shown in Fig. 217. For these laminates the interlaminar shear strength is controlled by the volume fraction of porosity. Hexion materials with porosity >5 vol.% have the weakest interface. For prepreg based laminates (see Fig. 218) the interlaminar shear strength is controlled by the volume fraction of porosity above 1% vol. For smaller volume fractions the decrease in ILSS cannot be explained in terms of porosity, other factors cause it. Comparing the two studied laminates, it can be said that P2 materials have a stronger interface and a tougher matrix, this is also confirmed observing fractography micrographs, see Fig. 190 where the cusps formed on P2 laminates are different than the cusps in P1 laminates.

Another method yielding information about fibre-matrix bonding quality is dynamic mechanical analysis (DMA). Higher storage modulus means better interfacial adhesion. Tan δ peak can be related to interfacial adhesion strength, being an indicator of molecular motion. The higher the molecular motion, the greater is the area under the peak and the weaker the adhesion. The drop of storage modulus shows the transition between rigid and viscous regions given by the glass transition temperature, indicating an increase of molecular chain mobility and stress relaxation. A strong fibre-matrix interface allows less energy dissipation and the chain movement is restricted, that provides a more effective load transfer.

Fig. 219 shows DMA curves for the pultruded rods. Each specimen was tested using two consecutive heating cycles. Sika CR141 rods have a higher storage modulus which increases after the first heating, because the resin cured during the first heating (indicated by a small maximum at 64°C in the green curve). But these rods also have a broad tan δ peak, which indicates high molecular movement within the polymeric matrix. The different viscoelastic behaviour of the epoxy matrices is reflected by the shape of the tan δ maxima. L20 rods do not show any post-curing and maintain their properties after the first heating cycle. The tan δ peak is narrow, indicating high rigidity within the polymer. The fibre-matrix interface also

160

affects the thermal properties, since reinforcements with higher contact areas with the matrix promote the thermal stability, consequently interfacial defects reduce these properties [97].
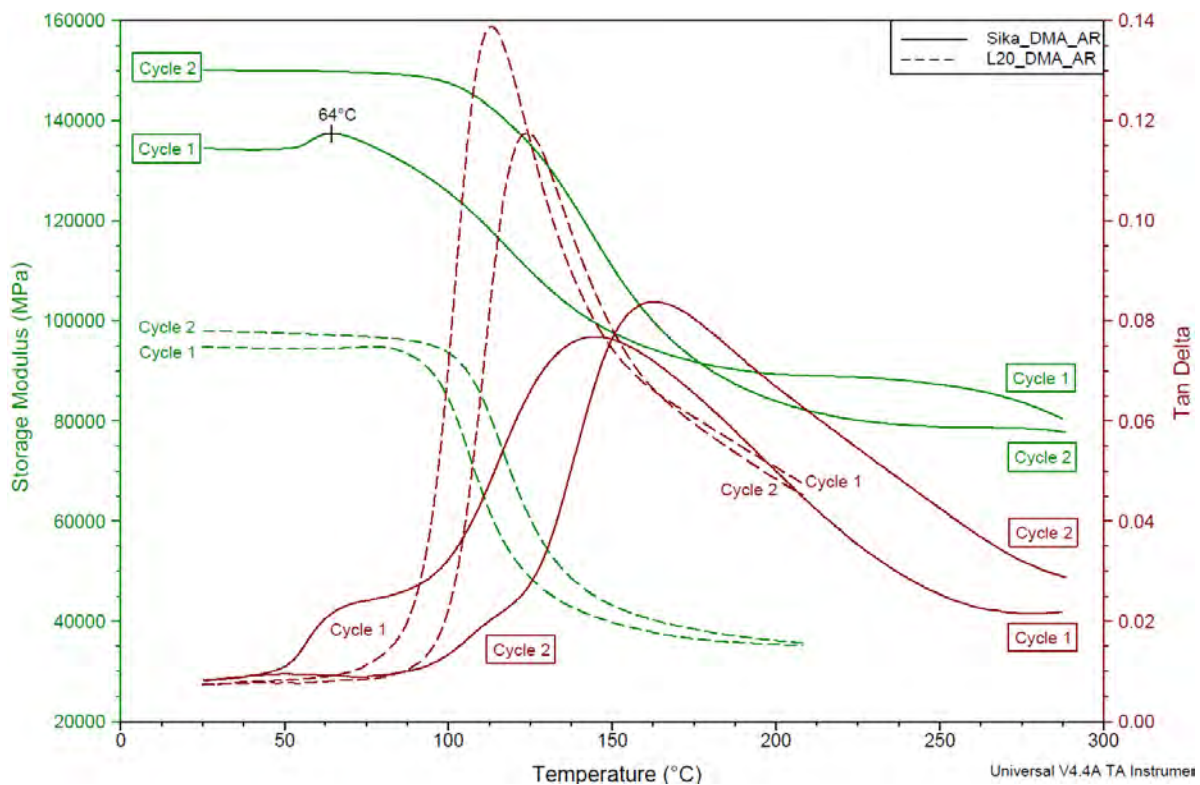
Fig. 219: Storage modulus (green) and tan delta (red) curves for the two consecutive heating cycles in 3-point-bending DMA tests applied to pultruded rods.

6.5 Effect of mineral filler particles

In the studied pultruded tubes, damage nucleates preferentially at regions with filler agglomerations, as shown in Fig. 185. This occurs by superimposing segmentation of the crack with that of filler particles while the rest of the composite is transparent. It demonstrates that the crack grew parallel to the fibre direction in the weakest zone, where high filler agglomerations are present. The intentional mixing of filler particles into the matrix produced degrading particle agglomerations, which generate large longitudinal pores causing weak areas by lack of reinforcement and of fibre-matrix bonding. Cracks initiate at those pores propagating until the final failure of torsion specimens.

6.6 Damage Analysis

Failure mechanisms observed in four point bending tests are as expected and reported by the standards [78]. Specimens failed either leaving three fragments cracked underneath each pressure ram or only two fragments starting from a crack underneath one of the load application lines. The latter occurred when the pressure rams did not simultaneously touch the sample and therefore shear forces cause deflections underneath the pressure rams. Then the flexural moment is not symmetrical any longer. Local fibre bundle failure also arose without cracks propagating through the whole thickness of the specimen also arose (see section 5.5.3). Generally, the same failure modes were observed in the different laminates tested by four-point bending.

161

Tubes tested in torsion always failed in the same manner, with a crack propagating along the length of the tested sample and across the wall thickness. Rod samples showed different mechanisms. Rods without filler particles exhibited higher plastic deformations and multiple crack growth originating from the centre of the rod.

There is a clear correlation between the shear stress-strain curves and the intensity of acoustic emission (AE) signals. An intermittent character of the AE signals indicates the degradation processes in the material. The first recorded AE signals can be ascribed to matrix crack growth and delamination between fibre bundles, which is the initial degradation process in carbon fibre composites. Subsequently, a slow increase in AE activity with respect to the strain is due to local fibre-matrix debonding induced by shear stresses. As the deformation proceeds, strong AE activity appears within a short period before the sample failure, which is attributed to fibre splitting, fibre fracture and pull-out accompanied by massive matrix cracking development.

The greatest number of AE signals recorded during the cyclic testing occur within the loading half-cycles. They increase progressively as the torque supersedes the previously achieved torque values. Such a AE behaviour is usually observed in crystalline materials and is called the Kaiser effect, where no AE signals at a fixed sensitivity level are detected, until previously applied stress levels are exceeded [93]. The AE signals during unloading represent a violation of the Kaiser effect. The unloading of the specimen might have induced noise from delaminated specimen regions sliding back by the elastic stress relaxation of the system. Similar AE results were obtained for all studied samples, tested in monotonic or cyclic mode.

AE count rates seem to be a suitable indicator to detect the degradation processes qualitatively, but it is not appropriate to identify them. It is not possible to distinguish the attributed mechanisms from each other by means of AE, since the AE signals of different events occur almost simultaneously. This method cannot tell where damage occurs, it is not localized and pseudo destructive, since the sample were tested to failure to record all signals. A decrease of the shear modulus after each loading-unloading cycle was observed for all samples tested with hysteresis cycles (Fig. 220).
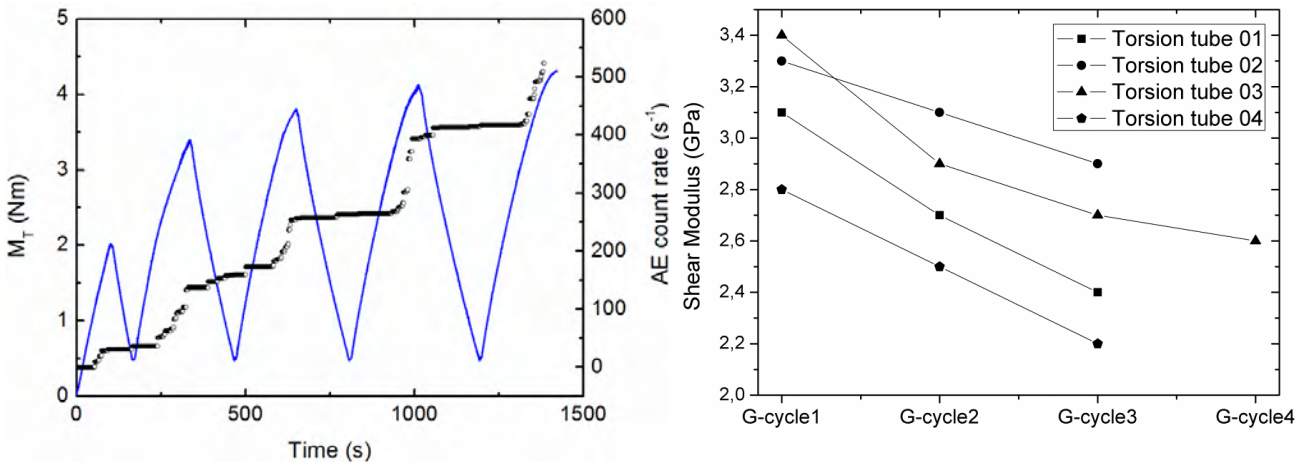
Fig. 220: Left: Accumulated AE count rates during a cycling torsion tests with loading-unloading cycles. Right: Shear modulus (G) evolution for tubes tested in torsion with three or four hysteresis cycles.

The bending properties of both pultruded rods are very similar (see Fig. 221), the maximal strength is of the same order of magnitude. The bending modulus of the Sika CR141 rods is higher than of the L20 samples. Both show a linear behaviour until first fibre breakage occurs. The failure of L20 rods occurs soon after that point, whilst Sika CR141 rods undergo further plastic deformation with a slow decay of strength during a progressing specimen failure.
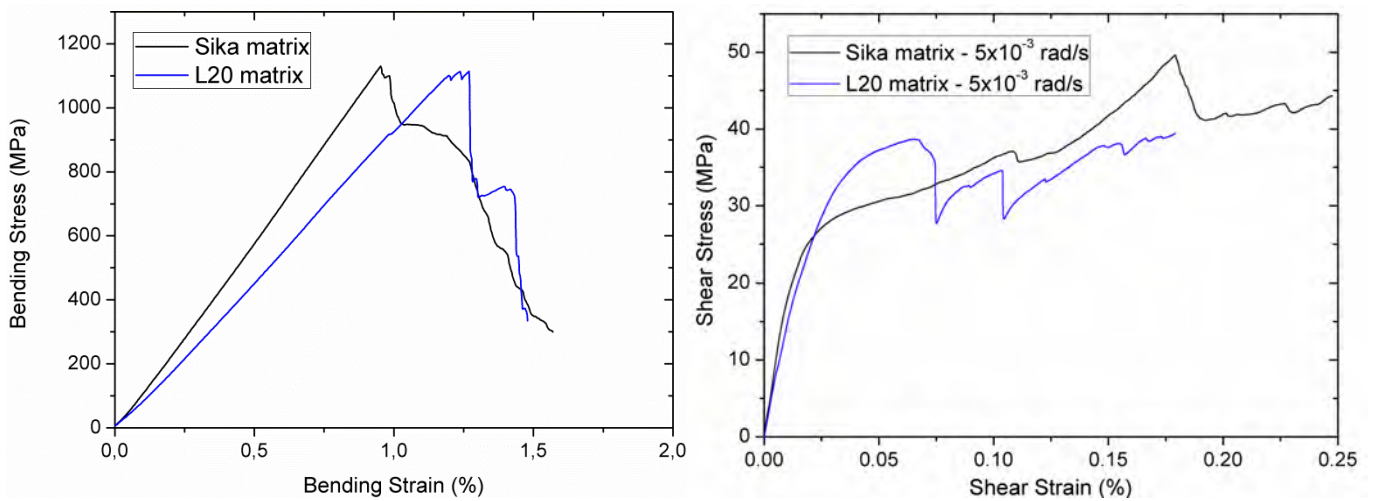
Fig. 221:Four point bending test results and shear stress vs. shear strain curves for two different UD CFRP rods studied.
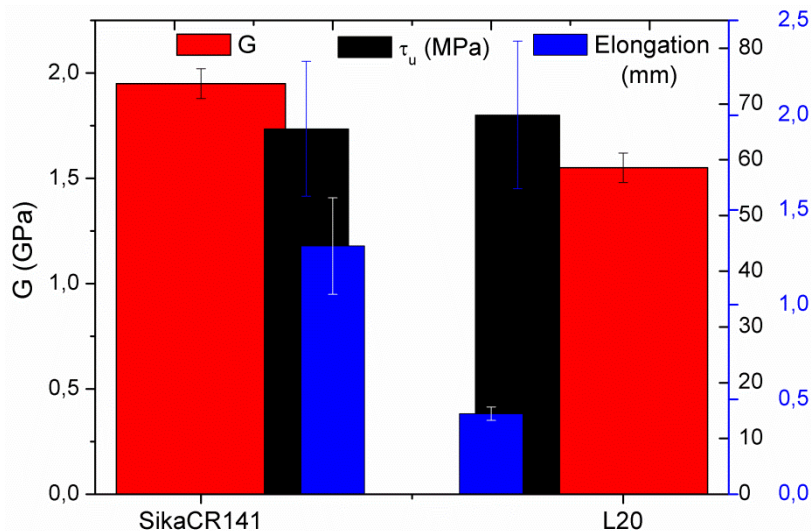
Fig. 222: Torsion properties of the two types of studied pultruded UD rods.

The behaviour of Sika CR141 based pultruded UD rods tested under torsion is very different from the one observed for L20 rods. The elongation values show a high degree of plasticity in the case of Sika Cr141 rods (Fig. 222). Strains higher than 0.05% cause the breakage of single fibre tows, which can be observed as steps within the flow curve for both rod types. The Sika CR141 specimen recovers after each step and shows strengthening, doubling the stress from the first fibre failure until fracture. The shear properties are highly influenced by the presence of mineral particles embedded in the matrix, which cause the sudden failure observed on L20 pultruded rods.

CFRP materials display complex failure modes, typically involving multiple interacting damage processes occurring at various length scales. These include fibre fracture, fibre kinking, fibre pull-out, fibre scissoring, fibre splitting, matrix cracking, fibre-matrix debonding and delamination. Fibre fracture takes place in the micrometer range, whereas delaminations may occur over distances ranging from millimetres to the whole dimension of the component. The interaction between all these damage mechanisms is an important factor and the dominant mechanism defines the load-bearing capacity of a composite component. Damage propagation was studied in ±45º cross-ply laminates subjected to in-situ tensile tests. The inner plies developed a higher crack concentration than the outer plies. Delamination started in the outermost ply interface. Fig. 223 shows slices at different deformation stages. Crack opening and cusps growth are observed. The same features as observed in Fig. 201 by SEM fractography.
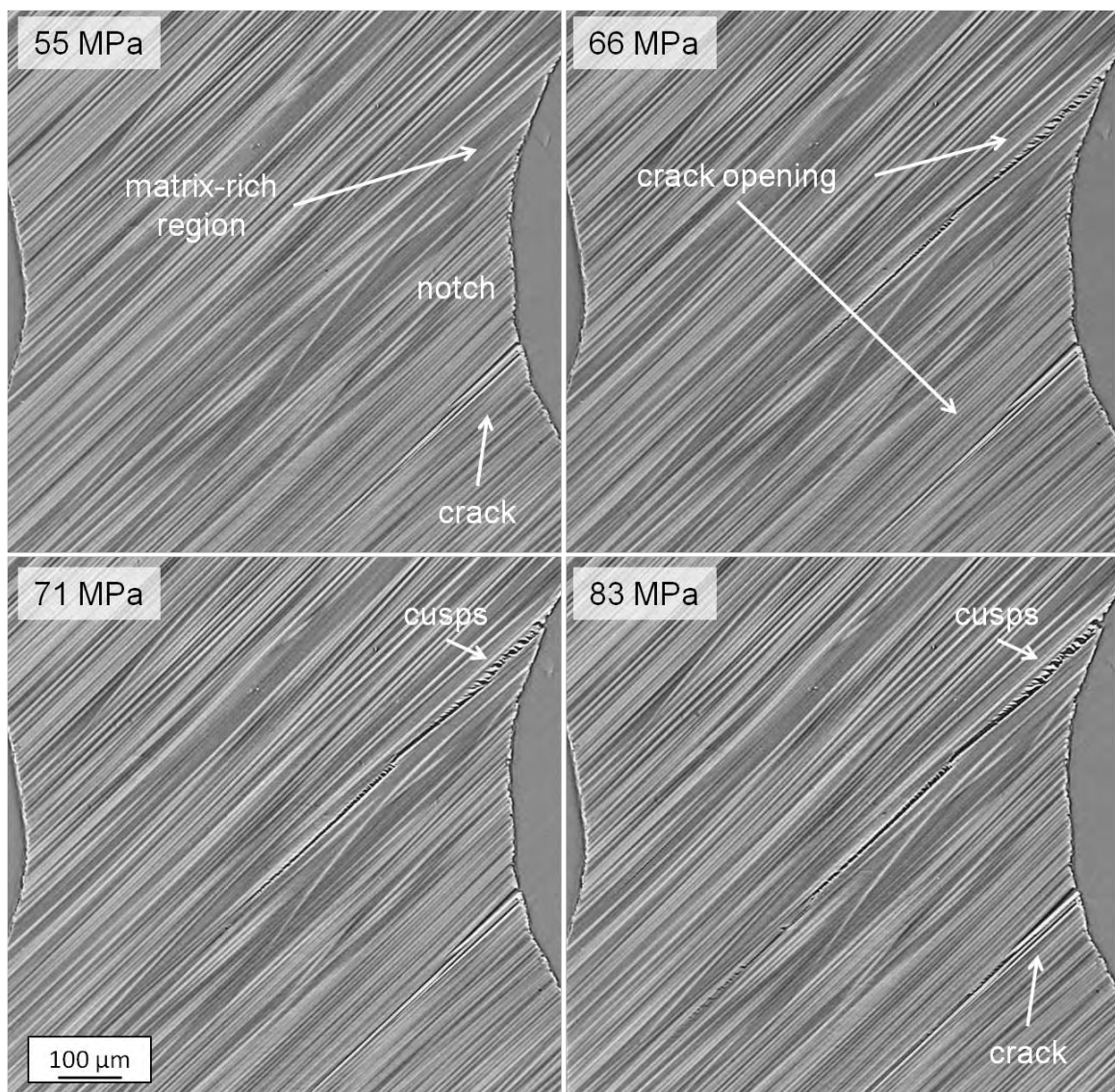
Fig. 223: The sequence of crack opening and the formation of cusps at different load steps, obtained from in-situ synchrotron microtomography (SCT) during tensile test. Voxel size: $(1.2 \ \mu m)^3$.

Fig. 224 shows schematically how cusps are generated during crack growth and the by means of SCT in-situ observed cusps. Fibre break and pull-out are also highlighted.
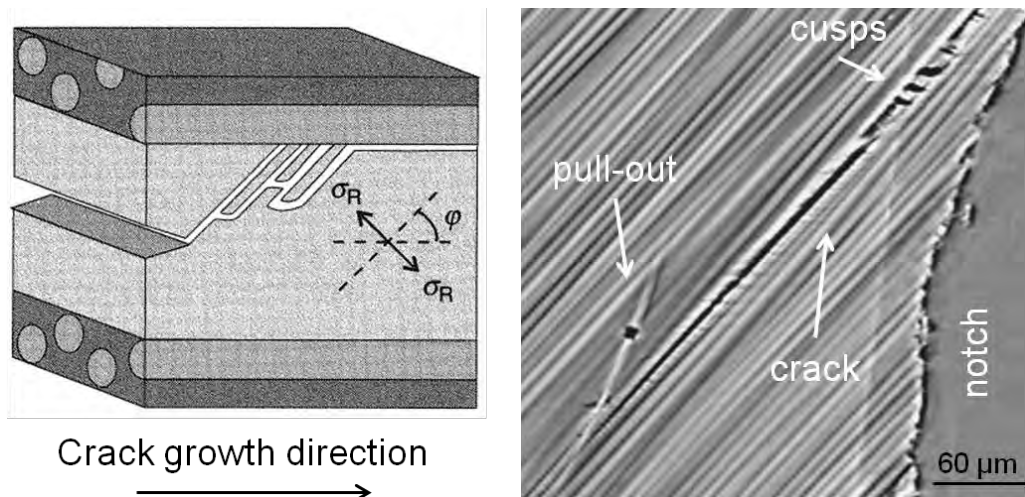
Fig. 224: Crack growth mechanism leading to cusps formation [63] and cusps associated to an opening crack and fibre pull-out as imaged by means of synchrotron microtomography. Voxel size: $(1.2\ \mu m)^3$.

6.7 Classification of defects

At this point it is important to keep in mind what is a defect (definition in the hypothesis, e.g. pore) and what is a failure mode (e.g. fibre splitting, observed in damage analysis section). However some terms are used for both things (e.g. debonding, delamination). For this work: void and pore are synonyms. The defects existing in the samples before testing are characterized and classified. The evaluation of their effect on mechanical properties is presented for the laminates and the pultruded profiles separately.

6.7.1 CFRP Laminates

Typical defects observed in the studied CFRP laminates are summarized in Tab. 36. A classification is made in three subgroups, since defects can be clearly related to single constituents of the composite, i.e. matrix, fibre and their interface. The size of each defect in 2D and 3D is listed, as well as their volumetric content within the composite. Then the supposed origin is indicated, followed by the affected properties. Finally, an assessment of their importance in terms of influence on the component performance is presented by means of a coloured threefold scale: critical(red C), non-critical(yellow M) or insignificant(green L).

Micro cracks, all kinds of porosity, unreinforced or delaminated matrix areas and areas with touching fibres or a local low fibre volume fraction were found to be the most critical defects for this kind of CFRP materials. The surface and edges of a laminate component are also particularly defect rich and therefore weaker regions. A further classification of porosity into different categories regarding the pore size as well as its origin must be made. Laminates always exhibit two kinds of pores: micro pores within a ply/bundle as seen in Fig. 58, and larger pores/voids between plies (seeFig. 55 and Fig. 57). Longitudinal tunnel like pores are also observed in 2D (Fig. 47) and 3D (Fig. 99 and Fig. 100). Regarding its origin we can speak of gas porosity, shrinkage porosity, moisture generated porosity and so on. Voids or pores can be formed either by mechanical entrapment of air or by formation of vapours or gases. The mechanical entrapment could be due to entrained gas bubbles from resin mixing operations, bridging not wetted large particles, voids from wandering tows, broken fibres or air pockets and wrinkles created during the lay-up.

165

Defect	Dimensions 2D or 3D	V_{fract} (%)	Origin	Affected Mech. prop.	Type
Matrix related defects					
micro cracks	L < 10 μm	-	Composite Production Incl. thermal history	strength ↓	C
micro pores	φ < 50-100 μm	<2.7 prepreg		strength ↓	M
macro pores	φ < 1000 μm		strength ↓		C
longitudinal pores	φ < 50 μm V < 101·10³ μm	<9 impreg.		strength ↓ stiffness ↓	C
matrix rich areas	see Fig. 49	-		strength ↓	C
inclusions	L_i < 25 μm	<0.01		strength ↓	L
nonimpregnated areas	see Fig. 54	-		strength ↓ stiffness ↓	M
Interface defects					
fibre-matrix debonding	see Fig. 201	-	Fibre sizing	stiffness ↓	M
delamination	see Fig. 188	-	Composite Production	strength ↓ stiffness ↓	C
Fibre related defects					
fibre/bundle waviness	5°≤ θ ≤ 10°	2-8	Composite Production	stiffness ↓	M
misaligned fibres	θ ≤ 90°	<0.5		stiffness ↓	L
broken fibres	-	<0.5		strength ↓ stiffness ↓	L
different local fibre packing densities	± 5 vol%	-		strength ↓	M-C
touching fibres	2plet-10plet	-		strength ↓	M-C

Tab. 36: Defects observed in studied HexPly8552, Sika CR132 and Hexion L418 CFRP laminates.

Thermal properties are influenced by the thermal history of the matrix, but not by defects. No influence of porosity volume fraction on thermal properties has been observed. Matrix rich areas are observed specially between plies or layers of the laminate (see Fig. 50 and Fig. 57) but also within each bundle/tow there is an inhomogeneous distribution of fibre and matrix (see Fig. 70 and Fig. 71). The eight laminates produced using C-textiles impregnated in liquid epoxy matrix and cured under pressure exhibited some nonimpregnated areas as shown in Fig. 54. Some inclusions of undesired particles were occasionally observed in prepreg based laminates embedded between plies, probably dust particles trapped between prepregs while stacking. Fibre-matrix debonding can only be seen at high magnification, in SEM micrographs, as in Fig. 201. Fibre bundle waviness and single misaligned fibres, as well as broken fibres are observed in all eleven materials, examples are shown in Fig. 46, Fig. 55, Fig. 60 and Fig. 66. The joining edges between textile pieces are also found in the eight impregnated textile laminates, as shown in Fig. 53 and Fig. 75. In general, an inhomogeneous distribution of the constituents is always observed at different length scales within all studied laminates.

6.7.2 Pultruded profiles

Typical defects observed for CFRP pultruded profiles, tubes and rods are summarized in Tab. 37, as well classified with respect to the constituent to which they are associated. The structure of this table is like the one described for Tab. 36.

An inhomogeneous distribution of the constituents within the composite is observed in all three studied pultruded profiles, independently of the magnification used. And a larger number of defects, in the sense of higher deviation from the ideal uniformly UD reinforced composite, was observed at the outer side of the profiles than inside.

Defect	Dimensions 2D or 3D	V_{fract} (%)	Origin	Affected Mech. prop.	Type
Matrix related defects					
micro cracks	L < 10 μm	-	Filler particles	strength ↓	C
micro pores	ϕ < 50 μm $V < 101 \cdot 10^3$ μm^3	<0.1		strength ↓	C
matrix rich areas	see Fig. 93	-	Composite Production	strength ↓	C
filler agglomerations	L_p < 8 μm V_{agg} <120·10^3 μm^3	2.2		stiffness ↓	C
Interface defects					
fibre-matrix debonding	see Fig. 97	-	Fibre sizing	stiffness ↓	M
delamination	see Fig. 196	-	Composite Production	strength ↓ stiffness ↓	C
Fibre related defects					
fibre waviness	5°≤ θ ≤ 20°	5	Composite Production	stiffness ↓	M
misaligned fibres	θ ≤ 90°	<0.5		stiffness ↓	L
different local fibre packing densities	± 5 vol%	-		strength ↓	M-C
touching fibres	2plet-10plet	-		strength ↓	M-C

Tab. 37: Defects observed in studied pultruded CFRP profiles: L20 and Sika CR 141 rods and L20 tubes.

The critical defects of pultruded UD composites are filler particle agglomerations embedded in the matrix and the defects that are associated to them. Failure was observed to occur in the areas with the highest particle agglomeration population. The porosity volume fraction of these materials is very low, the small size of the micro pores make them difficult to detect, but they could be imaged in 2D by means of LOM and SEM and in 3D using high resolution XCT. Matrix rich areas are clearly observed in all specimens, some examples can be seen in Fig. 91, Fig. 92 and Fig. 93. The matrix flow during pultrusion, as well as the fact that the continuous carbon fibres are introduced as fibre bundles can result in local variations of the reinforcement volume fraction, as shown in Fig. 87 and Fig. 91. Micro cracks and fibre-matrix debonding can only be resolved in SEM micrographs, as in Fig. 89 and Fig. 97 due to their small size. Fibre waviness is more noticeable along the sample's edges near to the surface of the composite (see Fig. 92). Misaligned fibres are occasionally observed (Fig. 94). Despite pultrusion, different fibre packing densities are always observed (Fig. 93). In particularly rod samples have higher concentration of one constituent (fibre of filler particles) in the centre/core of the profiles (Fig. 91 and Fig. 112) than near the surface. Although defects such as waviness and misoriented fibres may affect CTE values, due to the natural anisotropy of C-fibres, no significant effect could be observed. The CTE tends to zero in fibre direction and the transverse CTE was reproducible for all specimens in the range as reported in literature [2] [15] [4].

7. Conclusions

<u>Classification of defects:</u>

The defects observed after production of the studied CFRP laminates and pultruded profiles, their size and volume fraction are summarized in Tab. 36 and Tab. 37, respectively. The following statements compare the defects in these two types of CFRP composites:

- **Fibre related defects**: Fibre volume fractions are higher in pultruded profiles than in impregnated textile laminates, with the exception of the laminates produced applying 0.3MPa pressure. While the distribution of the reinforcement is less uniform within the profiles than in the laminates, broken fibres were only observed in the latter. Other fibre related defects, such as waviness, misalignment and touching fibres were observed in both types of materials.

- **Matrix related defects:** The porosity volume fraction in the pultruded composites is markedly (about 30 times) lower than that in the laminates. With regard to the size and morphology, various types of porosity were found in the laminates (longitudinal pores, large interply pores and intraply micro-pores) whilst in the pultruded profiles only spherical micro-pores were observed. The content of inclusions is negligible within the laminates, where they are well distributed. This is in contrast to the intentionally added filler particles in the pultruded materials, which form agglomerations amounting to ~2 vol. % of the composite. Non-impregnated areas were only observed in the laminates. Pultruded profiles, on the other hand, exhibit a larger deviation from the ideal uniform distribution of the constituents than the laminates. A considerable variation in the constituents' volume fraction was observed between the surface and the core of the profiles.

- **Interface defects:** Fibre-matrix debonding was observed in both types of materials at a negligible extent. Delamination was not observed in the as received materials but occurred as a damage mechanism during bending of both, laminates and pultruded profiles.

<u>Effects of defects on properties:</u>

Defects are controlled and determined by the processing conditions (e.g. constituents' flow in pultrusion, compaction pressure, curing cycle) as discussed in section 6.2. The aim should be to reduce those defects, which influence the performance-of the composites most. This is summarized in Tab. 36 and Tab. 37 from where the effects of defects on the strength and/or the stiffness of the studied laminates and pultruded profiles are concluded as follows:

- **Critical defects for strength:** large pores / delaminated areas, matrix-rich areas, filler agglomerations.

- **Insignificant defects for strength:** inclusions with very low volume fraction (< 0.01vol%) in the laminates and rarely observed touching fibres.

- **Critical defects for stiffness:** non-uniform fibre volume fraction, waviness.

- **Insignificant defects for stiffness:** rarely observed misaligned and broken fibres.

- On mechanical properties:

Porosity affects all studied mechanical properties: stiffness, strength and fracture toughness; all these magnitudes decrease substantially with increasing volume fraction of porosity. However, prepreg laminates with porosity <1 vol.% and impregnated laminates with <3 vol.% yield acceptable σ_b, E_b, and F^{SBS} values, as shown in Fig. 215 to Fig.217.

With regard to stiffness most of the critical defects are fibre related defects such as fibre non-uniform volume fraction and fibre waviness. Strength is strongly affected by the matrix type and the contained defects, namely cracks, porosity and fibre-matrix debonding (e.g. Sika CR132 laminates have higher bending strength than Hexion L418 laminates). If a sample contains various defects, the ones with the biggest volume fraction (e.g. longitudinal pores in laminates) determine the damage and its evolution.

Critical defects affecting toughness are micro cracks and porosity present in the matrix, responsible for crack propagation as observed in-situ in the ±45° cross-ply laminates. The matrix system also determines the temperature resistance and load-transfer as observed when comparing the L20 system (which degrades at temperatures above 200°C) with Sika CR141 and HexPly 8552, which can be heated up to 300°C.

Torsion strength is governed by the plasticity of the matrix system. Added filler particle agglomerations reduce it and are responsible for sudden failure. A decrease in shear modulus is observed for all pultruded profiles tested cyclically owing to extensive debonding and matrix crack propagation. Fibre-matrix debonding is favoured by the cyclical nature of the test. Loading deforms the sample and the reinforcement is exposed to high tensile load. During unloading the sample experiences relaxation, particularly at the interface between matrix and fibres. Contrarily, no variations of the bending modulus were observed for the laminates tested in the same manner, even when using consecutive series of loading-unloading cycles.

Regarding the two families of impregnated laminates, of the two different epoxy systems, Sika CR132 and Hexion L418 the latter appears to be less manufacture-friendly, as it yields a higher porosity volume fraction among all four composites. The consequence is a decrease of the bending properties E_b and σ_b, although the fibre volume fraction is higher than in Sika matrix composites. This confirms the detrimental effect of high porosity content. Additionally, it was found, that the support PES-fibres present in the UD C-fibre tape are associated with large pores perpendicular to the carbon bundles (see Fig. 108) deteriorating the mechanical properties.

- On thermal properties:

The glass transition temperature is influenced by the thermal history of the matrix, i.e. its curing degree, but not by the defects present in the microstructure (e.g. porosity content, waviness). Post-curing of the composites by applying thermal treatments resulted in an increase of the glass transition temperature due to supplementary cross-linking. This produces a slight increase of the stiffness, however 100% cured composites are brittle and exhibit poor fibre-matrix adhesion and toughness. For this reason, it can be said that a curing degree above

90%, but less than 100% is preferable. However, it should be noted, that a matrix always undergoes post-curing. Non fully cured composites are temperature sensitive materials, the properties of which change when exposed to temperatures in the range of their glass transition temperature and above.

No significant effect of thermal treatments upon stiffness and strength was observed for the pultruded samples with L20 matrix. For the ones with Sika CR141 matrix, a slight increase of stiffness combined with a loss in strength was observed after heat treatments, especially if the temperature is maintained close to the glass transition temperature interval.

Although defects such as waviness and misoriented fibres may affect the CTE values, due to the natural anisotropy of C-fibres, no significant effect could be observed in the studied materials.

Failure mechanism:

Failure of composites is always a combination of various interacting failure modes, occurring at different length scales: fibre fracture, fibre kinking, fibre pull-out, fibre scissoring, fibre splitting, matrix cracking, fibre-matrix debonding and delamination. Individual fibre fracture takes place in the micrometer range as observed in Fig. 224, whereas degrading delaminations occur over distances ranging from millimetres to the whole dimension of the component (see Fig. 181).

Damage propagation was studied in ±45° cross-ply laminates subjected to in-situ synchrotron tomography during tensile tests. The inner plies developed a higher crack concentration than the outer plies with delamination starting in the outermost ply interface. The growth of existing cracks, the formation of new ones and the evolution of delamination between plies were observed. The volume and area fraction of cracks increases linearly above a threshold stress of 25 MPa as shown in Fig. 176. Initial cracks induced during machining of the tensile notched specimen showed a stronger influence on damage evolution than manufacturing porosity, because the volume fraction of porosity was smaller than that of the initial cracks. Therefore, during tensile test the porosity did not contribute to damage nucleation nor propagation, instead already existing cracks grew and coalesced propagating preferentially in matrix-rich areas (see Fig. 223). It can be said, that the size of the defect influences the on-set of damage, larger defects determine crack path and cause crack orientation changes, being the origin for crack nucleation and promoting damage propagation.

Assessment of methods for detection and quantification of defects:

As the defect size determines the resolution required, different detection and quantification techniques have been used. These were, two methods of 3D computed microtomography, namely laboratory x-ray tomography (XCT) and parallel beam synchrotron tomography (SCT) and two classical materialographic techniques, light optical (LOM) and scanning electron microscopy (SEM).

The smallest features are studied by means of classical 2D materialography (LOM and SEM) and non-invasive 3D visualisation techniques (SCT). The inclusions present in prepreg based laminates can only be detected by high resolution SCT. Large longitudinal features like fibre and bundle waviness can be assessed by means of LOM using panorama modus. XCT covers relatively large volumes, but it cannot resolve the fibres, since their diameter is below the spatial resolution.

3D imaging allows to visualize defects, to quantify their volume fractions and to determine the constituents' distribution and orientation within the composite. It also enables the study of the eventual defects' interaction. The interconnectivity of the cracks was visualized within the ±45° cross-ply laminate tested in-situ. The connexion between the filler particle agglomerations and crack growth was observed in the tubes, which could not have been studied otherwise. SEM fractography is required to get additional information on damage propagation (cusps, riverlines, fibre-break, etc.). Debonding and micro cracks can only be resolved by SEM.

3D XCT is the appropriate method to assess larger features, such as the longitudinal pores in the laminates, or the delaminations in laminates tested by bending, since a large enough volume of the specimen can be imaged. The information gathered is complemented with LOM micrographs for detailed visualisation of the voids' morphology. As pores smaller than three times the voxel size cannot be visualized by means of XCT, 2D LOM or 3D SCT are the methods of choice.

Only non-destructive characterisation of the microstructure of tested samples is not sufficient to analyze damage mechanisms. 3D characterisation prior and after mechanical testing is a fair enough approach, which has proved to yield crucial information about damage propagation in pultruded tubes tested in torsion. But in order to analyze damage evolution during deformation, in-situ destructive methods are required. AE reveals the sequence of failure mechanisms and the relative intensity of events. Crack growth in ±45° cross-ply laminates has been observed during tensile test by in-situ SCT and correlated with SEM fractography, where the micro-structural features were observed post-mortem.

To summarize:

Defects are present in real composites and must be taken into account; idealized models cannot predict the real material in-service response. The information gathered in this work can be used to optimize processing parameters and to provide inputs for virtual processing tools. Furthermore, it can be used to model and predict material performance introducing a relevant distribution of critical defects found. Finally, this study also added some new information about failure mechanisms and damage evolution during deformation, some of which (cusps formation and growth, fibre rotation), to the authors knowledge had not yet been observed in-situ.

8. References

[1] AVK – Industrievereinigung Verstärkte Kunststoffe e. V. (Hrsg.), "Handbuch Faserverbundkunststoffe", Vieweg+Teubner GWV Fachverlage, (2010) 3. Auflage.

[2] G. W. Ehrenstein, "Faserverbund-Kunststoffe", München: Carl Hanser, (2006) 2. Ed..

[3] T. Chou, "Microstructural design of fibre composites", Cambridge University Press, (1992).

[4] D. D. L. Chung, "Carbon Fiber Composites", Butteworth-Heinemann, (1994).

[5] F. C. Campbell, "Structural Composite Materials", ASM International, (2010).

[6] A. McKimmon and N. Fowler, "Shear Strengthening Steel Structures Using FRP Composites," (2007). [Online]. Available: https://sites.google.com/site/frpstrengthening/fibrereinforcedpolymer. [Accessed Dec. 2012].

[7] I. C. Skrna-Jakl, "Leichtbau mit faserverstärkten Werkstoffen", TU Wien, (2010, 2011).

[8] AVK e.V.; Carbon Composites e.V., "Composites-Marktbericht 2012 - Marktentwicklungen, Trends, Ausblicke und Herausforderungen," (2012). [Online]. Available: http://www.carbon-composites.eu/aktuelles/marktberichte. [Accessed Nov. 2012].

[9] "PR Newswire," (2011). [Online]. Available: http://www.prnewswire.com/news-releases/global-and-china-carbon-fiber-industry-report-2010-2011-132038233.html. [Accessed Jan. 2013].

[10] "Acmite Market Intelligence Report July 2010," (2010). [Online]. Available: http://www.acmite.com/market-reports/materials/world-carbon-fiber-composite-market.html. [Accessed Nov. 2012].

[11] "Lucintel Report 2010-2015," (2010). [Online]. Available: http://www.lucintel.com/carbon_fiber_market.aspx. [Accessed Dec. 2012].

[12] R. Stewart, "Carbon fibre market poised for expansion," *Reinforced Plastics,* March (2011).

[13] R. E. H., "Composites-Märkte im Wandel," *K-Zeitung,* no. 20, pp. 1-4, (2012).

[14] "Composite Materials Handbook - Volume 3," (2002). [Online]. Available: http://www.lib.ucdavis.edu/dept/pse/resources/fulltext/HDBK17-3F.pdf. [Accessed May 2012].

[15] P. Morgan, "Carbon Fibers and Their Composites", CRC Press., (2005) 1. Edition.

[16] Neitzel, M.; Breuer, U., "Die Verarbeitungstechnik der Faser-Kunststoff-Verbunde", Carl Hanser, (1997).

[17] R. Schledjewski, "Cost efficient processing of thermoplastic fiber reinforced composite materials for aerospace applications," in *EUCOMAS 2009, 1-2 July*, Augsburg, Germany, (2009).

[18] T. Edwards, "Composite materials revolutionise aerospace engineering," *The Ingenia Magazine. Issue 36,* pp. 24-28, Sept. (2008).

[19] "GW Composites," [Online]. Available: http://gwcomposites.com/production-processes/pultrusion/. [Accessed Sept. (2012)].

[20] "The FRP Pultrusion Information Source," [Online]. Available: http://www.pultrusions.org/. [Accessed Jan. (2013)].

[21] M. F. Ashby, "Materials Selection in Mechanical Design", Butterworth-Heinemann, 4th Ed., (2010).

[22] "Granta CES Selector Software 2012," [Online]. Available: http://www.grantadesign.com/products/ces/. [Accessed Dec. (2012)].

[23] G. Erhard, "Kontruieren mit Kunststoffen", München 4. Ed.: Carl Hanser, (2008).

[24] Foreman, j.; Sauerbrunn, S. R.; Marcozzi, C. L.;, "Exploring the Sensitivity of Thermal Analysis Techniques to the Glass Transition. TA Instruments, Inc.," [Online]. Available: http://www.tainstruments.co.jp/application/pdf/Thermal_Library/Applications_Briefs/TA082.PDF. [Accessed Jan. (2013)].

[25] Seyler, R. J. Ed.;, "Assignment of the Glass Transition", STP 1249. Baltimore: ASTM Intl., (1994).

[26] Busse, G. et al., "Damage and its evolution in fiber-composite materials: Non- Destructive Evaluation (NDE) Part I", Books on demand GmbH, Norderstedt, (2006).

[27] Mook, G.; Pohl, J.; et al, "Non-destructive characterization of smart CFRP structures," *Smart Mater. Struct.,* vol. 12, pp. 997-1004, (2003).

[28] Kapadia, A. (National Composites Network), "Non-Destructive Testing of Composite Materials," (2006). [Online]. Available: http://www.compositesuk.co.uk/LinkClick.aspx?fileticket=14Rxzdzdkjw%3D&. [Accessed Jan. 2013].

[29] Vaara, P.; Leinonen, J.;, "Technology Survey on NDT of Carbon-fiber Composites," (2012). [Online]. Available: http://www3.tokem.fi/kirjasto/tiedostot/Vaara_Leinonen_B_8_2012.pdf. [Accessed Jan. 2013].

[30] Shinyama, Y.; Yamaji, T.; Hatsukade, Y.; et al., "Nondestructive evaluation of braided carbon fiber composites with artificial defect using HTS-SQUID gradiometer," *Physica C,* vol. 471, pp. 1242-1245, (2011).

[31] Aoki, Y.; Kondo, H.; Hatta, H.;, "Effect of Delamination Propagation on Mechanical Behavior in

Compression after Impact," in *16th International Conference on Composite Materials (ICCM 16) 8-13 July*, Kyoto, Japan, (2007).

[32] E. Greenhalgh, C. Meeks, A. Clarke and J. Thatcher, "The effects of defects on the performance of post-bucled CFRP stringer-stiffened panels," *Composites Part A,* vol. 34, no. 7, pp. 623-633, (2003).

[33] Little, J. E.; Yuan, X.; Jones, M. A.;, "Characterisation of voids in fibre reinforced composite materials," *NDT & E International,* vol. Volume 46, pp. 122-127, (2012).

[34] Camanho, P. P.; Matthews, F. L.;, "Stress analysis and strength prediction of mechanically fastened joints in FRP: a review," *Composites Part A,* vol. 27, no. 6, pp. 529-547, (1997).

[35] Irisarri, F. X.; Laurin, F.; Carrere, N.; Maire, J. F.;, "Progressive damage and failure of mechanically fastened joints in CFRP laminates - Part I: Refined Finite element modeling of single-fastener joints," *Composite Structures,* vol. 94, no. 8, pp. 2269-2277, (2012).

[36] Plum, R.; Medgenberg, J.; Merzbacher, M.; Ummenhofer;, "Extended Thermoelastic Stress Analysis Applied to Carbon Steel and CFRP," in *2nd International symposium on NDT in Aerospace, 22.-24.11*, Hamburg, Germany, (2010).

[37] Degenhardt, R.; Kling, A.; Bethge, A.; Orf, J.; Kärger, L.; Zimmermann, R.; Rohwer, K.; Calvi, A.;, "Investigations on imperfection sensitivity and deduction of improved knock-down factors for unstiffened CFRP cylindrical shells," *Composite Structures,* vol. 92, no. 8, pp. 1939-1946, (2010).

[38] R. Talreja, "Damage and failure analysis of composite structures with manufacturing defects," in *15th European Conference on Composite Materials (ECCM 15) 24-28 June*, Venice, Italy, (2012).

[39] Requena, G.; Fiedler, G.; et al., "3D-Quantification of the distribution of continuous fibres in unidirectionally reinforced composites," *Composites Part A,* vol. 40, no. 2, pp. 152-163, (2009).

[40] Sutcliffe, M.P.F.; Lemanski, S.L.; Scott, A. E.; et al., "Measurement of fibre waviness in industrial composite components," *Composites Science and Technology,* vol. 72, no. 16, pp. 2016-2023, (2012).

[41] Kratmann, K.K.; Sutcliffe, M.P.F.; et al., "A novel image analysis procedure for measuring fibre misalignment in unidirectional fibre composites," *Composites Science and Technology,* vol. 69, no. 2, pp. 228-238, (2009).

[42] Hernández, S. et al., "Analysis of curing cycle effect on processing voids distribution and mechanical properties of a polymer composite material," in *15th European Conference on Composite Materials (ECCM 15) 24-28 June*, Venice, Italy, (2012).

[43] Hernández, S.; Sket, F.; et al., "Effect of curing cycle on void distribution and interlaminar shear strength in polymer-matrix composites," *Composites Science and Technology,* vol. 71, no. 10, pp.

1331-1341, (2011).

[44] Sket, F. et al., "Detailed damage mechanisms assesment in composite materials by means of x-ray tomography," in *15th European Conference on Composite Materials (ECCM 15) 24-28 June*, Venice, Italy, (2012).

[45] Lambert, J.; Chambers, A.R.; et al., "3D damage characterisation and the role of voids in the fatigue of wind turbine blade materials," vol. 72, no. 2, p. 337–343, (2012).

[46] Moffat, A. J.; Wright, P.; Buffière, J. Y.; Sinclair, I.; Spearing, S. M.;, "Micromechanisms of damage in 0° splits in a [90/0]s composite material using synchrotron radiation computed tomography," *Scripta Materialia,* vol. 59, no. 10, p. 1043–1046, (2008).

[47] Wright, P.; Fu, X.; Sinclair, I.; Spearing, S. M.;, "Ultra High Resolution Computed Tomography of Damage in Notched Carbon Fiber-Epoxy Composites," *Journal of Composite Materials,* vol. 42, no. 19, pp. 1993-2002, (2008).

[48] Moffat, A. J.; Wright, P.; Helfen, L.; Baumbach, T.; Johnson, G.; Spearing, S. M.; Sinclair, I.;, "In situ synchrotron computed laminography of damage in carbon fibre–epoxy [90/0]s laminates," *Scripta Materialia,* vol. 62, no. 2, p. 97–100, (2010).

[49] Wright, P.; Moffat, A. J.; Sinclair, I.; Spearing, S. M.;, "High resolution tomographic imaging and modelling of notch tip damage in a laminated composite," *Composites Science and Technology,* vol. 70, no. 10, p. 1444–1452, (2010).

[50] Scott, A. E.; Mavrogordato, M.; Wright, P.; Sinclair, I.; Spearing, S. M.;, "In situ fibre fracture measurement in carbon–epoxy laminates using high resolution computed tomography," *Composites Science and Technology,* vol. 71, no. 12, p. 1471–1477, (2011).

[51] Scott, A. E.; Sinclair, I.; Spearing, S. M.; Thionnet, A.; Bunsell, A. R.;, "Damage accumulation in a carbon/epoxy composite: Comparison between a multiscale model and computed tomography experimental results," *Composites Part A,* vol. 43, no. 9, p. 1514–1522, (2012).

[52] HexPly® AS4/8552 RC34 AW194 data sheet, "Hexcel," [Online]. Available: www.hexcel.com. [Accessed June (2012)].

[53] L20 epoxy resin data sheet, "Suter Kunststoffe," [Online]. Available: http://www.swiss-composite.ch. [Accessed June (2012)].

[54] Laminating resin MGS L418 technical information, "Hexion," [Online]. Available: http://www.momentive.com/. [Accessed June (2012)].

[55] Biresin CR132 Compositeharz-System data sheet, "Sika," [Online]. Available: http://toolingandcomposites.sika.com/. [Accessed June (2012)].

[56] Biresin CR 141 Compositeharz-System data sheet, "Sika," [Online]. Available:

http://toolingandcomposites.sika.com/. [Accessed June (2012)].

[57] J. Hatzmann, "Identifizierung von Fehlstellen in Karbonfaser – Epoxidharz – Laminaten und Vergleich zweier Harzsysteme, sowie deren Einfluss auf die mechanischen Eigenschaften", Vienna University of Technology: Diplomarbeit, (2011).

[58] STS40 F13 carbon fiber data sheet, "Toho Tenax GmbH," [Online]. Available: www.tohotenax-eu.com. [Accessed June (2012)].

[59] T700 SC carbon fibre data sheet, "Torayca," [Online]. Available: www.toraycfa.com/contact.html. [Accessed June (2012)].

[60] Sigrafil C40 T024 EPY carbon fibre data sheet, "SGL Group," [Online]. Available: www.sglgroup.com. [Accessed June (2012)].

[61] "Image J," [Online]. Available: http://rsb.info.nih.gov/ij/. [Accessed May (2012)].

[62] "AxioVision," [Online]. Available: http://microscopy.zeiss.com/microscopy/en_de/products/software/axiovision-for-biology.html. [Accessed May (2012)].

[63] Ehrenstein, G. W.; Engel, L.; Klingele, H.; Schaper, H.;, "SEM of Plastics Failure", Hanser, (2010).

[64] E. S. Greenhalgh, "Failure analysis and fractography of polymer composites", Woodhead Publishing Limited and CRC Press LLC, (2009).

[65] Greenhalgh, E. S.; Hiley, M. J.;, "Fractography of polymer composites: current status and future issues," in *13th European conference on composite materials (ECCM 13) 2-5 June*, Stockholm, Sweden, (2008).

[66] M. Rodríguez-Hortalá and D. Salaberger, "The effect of defects in structural composites (DEFCOM Project, FP6-EraNet MATERA)," Vienna University of Technology, (2009).

[67] M. Rodríguez-Hortalá and D. Salaberger, "The effect of defects in structural composites (DEFCOM Project, FP6-EraNet MATERA)," Vienna University of Technology, (2012).

[68] Kastner, J.; Plank, B.; Requena, G.;, "Non-destructive characterisation of polymers and Al-alloys by polychromatic cone-beam phase contrast tomography," *Materials Characterization,* vol. 64, pp. 79-87, (2012).

[69] B. Plank, D. Salaberger and J. Kastner, "High Resolution X-ray CT for Polymer Materials Science," in *Proceedings of NDT in Aerospace Conference*, Hamburg, Germany, (2010).

[70] B. Harrer, "Detektierbarkeit von Heterogenitäten in Fe - Basis - und Aluminiumlegierungen mittels Röntgen - Computertomographie", Vienna University of Technology: Dissertation, (2009).

[71] Koch, T.; Salaberger, D.; et al., "Methods for Characterizing the 3-D Morphology of Polymer Composites," *Macromol. Symp.,* vol. 315, p. 115–124, (2012).

[72] N. Ovsyannikova, "Thermomechanical and Materialographic Characterizations of CFRP", Vienna University of Technology: Master Thesis, (2012).

[73] G. W. Ehrenstein, "Praxis der Thermischen Analyse von Kunststoffen", München-Wien: Carl Hanser Verlag, (2003).

[74] M. Holzmeier, "Characterization of CFRP (Carbon Fiber Reinforced Polymers) – Influence of defects on material properties", Vienna University of Technology: Diplomarbeit, (2011).

[75] James, J.D.; Spittle, J.A.; et al., "A review of measurement techniques for the thermal expansion coefficient of metals and alloys at elevated temperatures," *Measurement Science and Technology,* no. 12, pp. R1-R15, (2001).

[76] DIN EN ISO 53752, "Prüfung von Kunststoffen – Bestimmung des thermischen Längenausdehnungskoeffizienten", (1980).

[77] G. Dieter, "Mechanical Metallurgy", Mcgraw-Hill., (1988) SI Metric 3rd revised ed..

[78] DIN EN ISO 14125, "Faserverstärkte Kunststoffe – Bestimmung der Biegeeigenschaften", (1998).

[79] ASTM D5528-01, "Standard Test Method for Mode I Interlaminar Fracture Toughness of Unidirectional Fiber-Reinforced Polymer Matrix Composites", (2007).

[80] ASTM D2344, "Standard Test Method for Short-Beam Strength of Polymer Matrix Composite Materials and their Laminates", ASTM (American Society for Testing and Materials), (2000).

[81] "IPL Analyzer," Dakel, [Online]. Available: http://www.dakel.cz/index.php?pg=prod/dev/ipl_en. [Accessed Jan. 2013].

[82] "MIDI AE Sensor," Dakel, [Online]. Available: http://www.dakel.cz/index.php?pg=prod/sens/midi_en. [Accessed Jan. 2013].

[83] ASTM E 1067-85, "Standard Practice for Acoustic Emission Examination of Fiberglass Reinforced Plastic Resin", (1985).

[84] D. Tolnai, "3D characterization of microstructure evolution of cast AlMgSi alloys by synchrotron tomography", Vienna University of Technology : Dissertation, (2011).

[85] Labiche, J. C.; Mathon, O.; Pascarelli, S.; Newton, M.A.; Guilera Ferre, G.;, "The fast readout low noise camera as a versatile x-ray detector for time resolved dispersive extended x-ry absorption fine structure and diffraction studies of dynamic problems in materials science, chemistry and catalysis," *Rev. Sci. Instrum.,* vol. 78, no. 091301, (2007).

[86] "MedINRIA," [Online]. Available: http://www-sop.inria.fr/asclepios/software/MedINRIA/. [Accessed May (2012)].

[87] "OrientationJ," [Online]. Available: http://bigwww.epfl.ch/demo/orientation/. [Accessed May (2012)].

[88] "Avizo Fire," [Online]. Available: http://www.vsg3d.com/avizo/fire. [Accessed May (2012)].

[89] ASTM D2734-09, Standard Test Methods for Void Content of Reinforced Plastics, (1994).

[90] Sims, G. D.; Gnaniah, S. J. P. ;, "Improved procedures for the determination of Tg by Dynamic Mechanical Analysis," in *17th International Conference on Composite Materials (ICCM 17) 27-31 July*, Edinburgh, UK, (2009).

[91] ASM International Handbook Committee, "Engineered Materials Handbook. Volume 1. Composites". Section 4, United States of America: ASM International, (1993).

[92] Kelly, A.; Zweben, C. H:;, "Comprehensive Composite Materials. Volume 1: Fiber Reinforcements and General Theory of Composites", UK: Elsevier, (2000).

[93] J. Kaiser, "Untersuchung über das Auftreten von Geräuschen beim Zugversuch", TU München: Dissertation, (1950).

[94] Minak, G.; Abrate, S.; et al., "Residual torsional strength after impact of CFRP tubes," *Composites: Part B,* vol. 41, no. 8, pp. 637-645, (2010).

[95] Gutkin, R.; Green, C. J.; et al., "On acoustic emission for failure investigation in CFRP: Pattern recognition and peak frequency analyses," *Mechanical Systems and Signal Processing,* vol. 25, no. 4, pp. 1393-1407, (2011).

[96] Mei, H.; Cheng, L.;, "Stress-dependence and time-dependence of the post-fatigue tensile behaviour of carbon fiber reinforced SiC matrix composites," *Composites Science and Technology,* vol. 71, no. 11, pp. 1404-1409, (2011).

[97] Brocks, T.; Cioffi, M. O. H.; Voorwald, H. J. C.;, "Effects of interfacial adhesion on thermal and mechanical properties," in *15th European Conference on Composite Materials (ECCM 15) 24-28 June*, Venice, Italy, (2012).

9. Annex A

Method: TGA

Summary TGA:

Sample	W_f %	W_m % W_{part} %	V_f %	V_m %	$V_{porosity}$ %	V_{part} %
HexPly8552 Laminates						
HSAS4/UD58f/0.2MPa/1	65.5±0.4	34.3±0.4	57.9±0.4	41.7±0.5	0.4	-
HSAS4/±45-58f/0.2MPa/2	65.6	34.4	58.2	42.0	n.d.	-
Sika CR132 Laminates						
FT300B/0-90°/1bar/3	55.9	44.1	43.8	52.9	3.3	-
HTA40/UD/1bar/3	62.3	34.7	51.3	43.8	3.2	1.7
HTS5631/UD/1bar/3	68.8	31.2	57.2	40.2	2.6	-
HTS5631/UD/3bar/4	73.3	26.7	63.8	36.0	0.2	-
Hexion L418 Laminates						
FT300/0-90°/1bar/5	66.6	33.4	53.6	41.0	5.4	-
HTA40/UD/1bar/5	69.0	28.2	55.7	34.9	7.9	1.5
HTS5631/UD/1bar/5	77.6	22.4	62.7	27.9	9.5	-
HTS5631/UD/3bar/6	76.0	24.0	65.7	31.9	2.4	-
L20 pultruded tubes						
T/HTSTS/UD65f	62.3±1.6	33.6±2.0 4.7±0.1	53.8±2.8	45.0±1.8	n.d.	2.6±0.1
L20 pultruded rods						
R/HTSTS/UD65f exterior	60.2±0.3	32.1±0.4 7.6±0.6	53.2±0.2	43.6±0.6	n.d.	4.3±0.3
R/HTSTS/UD65f centre	58.4±0.5	34.1±0.6 7.3±0.5	51.6±0.5	46.4±0.7	n.d.	4.2±0.3
Sika CR 141 pultruded rods						
R/Sigrafil-T700SC/UD65f	69.7±0.4	30.2±0.4	62.8±0.4	40.2±0.6	n.d.	-

10.Annex B

Method: DSC

Summary DSC [3K/min (laminates) 5K/min (pultruded)]:

Sample	Tg $_{Beginning}$ (°C)	Tg (°C)	Tg $_{End}$ (°C)
HexPly8552 Laminates			
HSAS4/UD58f/0.2MPa/1	202 ± 6	215 ± 2	221 ± 1
HSAS4/UD58f/0.2MPa/2	199 ± 3	212 ± 2	214 ± 4
<Tg (°C)>	**201 ± 2**	**214 ± 3**	**218 ± 6**
Sika CR132 Laminates			
FT300B/0-90°/1bar/3	117 ± 7	125 ± 4	133 ± 1
HTA40/UD/1bar/3	105 ± 2	117 ± 0	126 ± 1
HTS5631/UD/1bar/3	123 ± 1	129 ± 0	136 ± 0
HTS5631/UD/3bar/4	124 ± 1	129 ± 1	133 ± 1
<Tg (°C)>	**119 ± 8**	**127 ± 5**	**132 ± 3**
Hexion L418 Laminates			
FT300/0-90°/1bar/5	112 ± 2	119 ± 2	124 ± 2
HTA40/UD/1bar/5	108 ± 2	115 ± 1	121 ± 0
HTS5631/UD/1bar/5	98 ± 2	105 ± 3	110 ± 4
HTS5631/UD/3bar/6	100 ± 2	107 ± 2	113 ± 2
<Tg (°C)>	**105 ± 6**	**111 ± 5**	**117 ± 6**
L20 pultruded tubes			
T/L20-T/HTSTS/UD65f	73 ± 1	79 ± 2	90 ± 1
L20 pultruded rods			
R/HTSTS/UD65f – AR-1st	71 ± 3	76 ± 2	84 ± 5
R/HTSTS/UD65f – AR-2nd	101 ± 2	112 ± 3	122 ± 5
<Tg (°C)> 1st	**72 ± 1**	**77 ± 2**	**87 ± 3**
Sika CR 141 pultruded rods			
R/Sig-T700SC/UD65f – AR-1st	60 ± 2	63 ± 2	65 ± 2
R/Sig-T700SC/UD65f – AR-2nd	89 ± 2	100 ± 2	109 ± 2

Single DSC measurements:

Sample code	Heating rate [K/min]	Glass transition temperature interval [°C]	Average glass transition temperature interval <Tg> [°C]
HexPly8552/HSAS4/UD58f/0.2MPa/1			
DSC-01	3	198 – **217** – 221	202 ± 6 – **215 ± 2** – 221 ± 1
DSC-02	3	206 – **214** – 222	
DSC-03	5	197 – **217** – 227	197 ± 0 – **216 ± 1** – 225 ± 2
DSC-04	5	197 – **215** – 224	
DSC-05	10	204 – **211** – 217	191 ± 19 – **208 ± 7** – 220 ± 3
DSC-06	10	179 – **205** – 222	
DSC-07	10	172 – **200** – 223	
DSC-08	10	211 – **217** – 220	
HexPly8552/HSAS4/UD58f/0.2MPa/2			
DSC-01	3	197 – **210** – 216	199 ± 3 – **212 ± 2** – 214 ± 4
DSC-02	3	201 – **213** – 211	
DSC-03	5	191 – **200** – 219	192 ± 1 – **205 ± 7** – 223 ± 5
DSC-04	5	192 – **210** – 226	
DSC-05	10	196 – **214** – 219	193 ± 3 – **208 ± 6** – 217± 3
DSC-06	10	190 – **202** – 213	
DSC-07	10	193 – **207** – 219	

Sample code	Heating rate [K/min]	Glass transition temperature interval [°C]	Average glass transition temperature interval <Tg> [°C]
SikaCR132/FT300B/0-90°/1bar/3			
DSC-01	3	123 – **129** – 132	117 ± 7 – **125 ± 4** – 133 ± 1
DSC-02	3	110 – 1**21** – 134	
SikaCR132/HTA40/UD/1bar/3			
DSC-03	3	106 – **117** – 125	105 ± 7 – **117 ± 0** – 126 ± 1
DSC-04	3	103 – **117** – 127	
SikaCR132/HTS5631/UD/1bar/3			
DSC-05	3	123 – **130** – 136	123 ± 1 – **130 ± 1** – 136 ± 1
DSC-06	3	122 – **129** – 135	
SikaCR132/HTS5631/UD/3bar/4			
DSC-07	3	124 – **130** – 133	124 ± 1 – **129 ± 1** – 133 ± 1
DSC-08	3	125 – **129** – 133	
DSC-09	3	123 – **130** – 133	
DSC-10	3	125 – **129** – 132	
DSC-11	3	121 – **127** – 132	
DSC-12	3	124 – **131** – 134	

Sample code	Heating rate [K/min]	Glass transition temperature interval [°C]	Average glass transition temperature interval <Tg> [°C]
HexionL418/FT300B/0-90°/1bar/5			
DSC-01	3	113 – **117** – 122	112 ± 2 – **119 ± 2** – 124 ± 2
DSC-02	3	114 – 1**21** – 127	
DSC-03	3	110 – 1**18** – 124	
HexionL418/HTA40/UD/1bar/5			
DSC-04	3	109 – **115** – 121	108 ± 2 – **115 ± 1** – 121 ± 1
DSC-05	3	105 – **114** – 122	
DSC-06	3	111 – **115** – 121	
HexionL418/HTS5631/UD/1bar/5			
DSC-07	3	99 – **108** – 115	98 ± 2 – **105 ± 3** – 110 ± 4
DSC-08	3	95 – **101** – 105	
DSC-09	3	99 – **105** – 111	
HexionL418/HTS5631/UD/3bar/6			
DSC-10	3	98 – **105** – 111	100 ± 2 – **107 ± 2** – 113 ± 2
DSC-11	3	103 – **109** – 115	
DSC-12	3	99 – **107** – 112	

T/L20-T/HTSTS/UD65f		
Sample code	Heating rate [K/min]	Glass transition temperature interval [°C]
DSC-01	3	72 – **82** – 90
DSC-02	5	72 – **78** – 89
DSC-03	10	74 – **78** – 91

R/L20-T/HTSTS/UD65f					
Sample code	Cycle	Heating rate [K/min]	$T_{End.}$ [°C]	Glass transition temp. interval [°C]	Heat peak [J/g] [Begin T peak(°C) Max T peak(°C)]
DSC-AR01	1st	5	200	76 – **78** – 79	4.03 [145°C-168°C]
	2nd	5	250	93 – **103** – 111	No peak
	3rd	5	200	103 – **109** – 115	No peak
DSC-AR02	1st	5	250	69 – **74** – 80	4.94 [144°C-168°C]
	2nd	5	250	103 – **113** – 122	No peak
DSC-AR03	1st	5	250	72 – **78** – 89	4.68 [145°C-168°C]
	2nd	5	250	102 – **113** – 121	No peak
DSC-AR04	1st	5	350	69 – **74** – 86	4.75 [145°C-168°C]
	2nd	5	250	97 – **110** – 122	No peak
DSC-AR05	1st	5	350	70 – **77** – 88	4.82 [144°C-168°C]
	2nd	5	250	100 – **117** – 129	No peak

| | | | | | Heat peak [J/g] |
Sample code	Cycle	Heating rate [K/min]	$T_{End.}$ [°C]	Glass transition temp. interval [°C]	[Begin T peak(°C) Max T peak(°C)]
			R/SikaCR141/Sigrafil-T700SC/UD65f		
DSC-AR01	1st	5	250	59 – **61** – 63	0.96 [139°C-160°C]
DSC-AR02	1st	5	250	60 – **62** – 64	1.33 [138°C-162°C]
	2nd	5	250	89 – **100** – 108	No peak
DSC-AR03	1st	5	250	60 – **62** – 65	1.31 [138°C-159°C]
	2nd	5	250	81 – **103** – 112	No peak
DSC-AR04	1st	5	250	65 – **68** – 69	1.60 [138°C-159°C]
	2nd	5	250	86 – **100** – 107	No peak
DSC-AR05	1st	5	300	59 – **61** – 62	0.86 [138°C-160°C]
	2nd	5	300	96 – **107** – 115	No peak
DSC-AR06	1st	5	250	60 – **62** – 65	0.84 [139°C-158°C]
	2nd	5	350	90 – **100** – 111	No peak
DSC-AR07	1st	5	250	57 – **65** – 67	0.95 [139°C-159°C]
	2nd	5	350	89 – **98** – 108	No peak
DSC-AR08	1st	10	250	63 – **65** – 71	0.95 [144°C-172°C]
DSC-AR09	1st	10	250	55 – **57** – 62	2.10 [142°C-175°C]

11. Annex C

Method: DMA

Summary DMA:

Sample	E'_{RT} [GPa]	T_B - T_g - T_E [°C] (Storage modulus)	T_g [°C] (Loss factor)
HexPly8552 Laminates			
HSAS4/UD58f/0.2MPa/1	117 ± 6	$117 - 222 \pm 3 - 225$	225 ± 1
HSAS4/UD58f/0.2MPa/2	119 ± 7	$119 - 217 \pm 3 - 223$	223 ± 4
<Tg (°C)>	**-**	**220 ± 4**	**224 ± 1**
Sika CR132 Laminates			
FT300B/0-90°/1bar/3	35 ± 8	$102 - 119 \pm 3 - 131$	124 ± 3
HTA40/UD/1bar/3	91 ± 5	$101 - 121 \pm 1 - 231$	124 ± 3
HTS5631/UD/1bar/3	101 ± 12	$113 - 123 \pm 1 - 132$	126 ± 1
HTS5631/UD/3bar/4	106 ± 8	$106 - 124 \pm 2 - 134$	127 ± 1
<Tg (°C)>	**-**	**121 ± 3**	**125 ± 2**
Hexion L418 Laminates			
FT300/0-90°/1bar/5	52 ± 10	$116 - 124 \pm 0 - 132$	128 ± 0
HTA40/UD/1bar/5	88 ± 6	$119 - 125 \pm 0 - 133$	129 ± 0
HTS5631/UD/1bar/5	113 ± 12	$113 - 123 \pm 1 - 130$	127 ± 1
HTS5631/UD/3bar/6	117 ± 30	$114 - 122 \pm 0 - 129$	126 ± 0
<Tg (°C)>	**-**	**123 ± 1**	**127 ± 1**
L20 pultruded rods			
R/HTSTS/UD65f – AR-1st	91 ± 6	$84 - 95 \pm 1.5 - 111$	101 ± 1
R/HTSTS/UD65f – AR-2nd	93 ± 5	$93 - 107 \pm 0.8 - 126$	116 ± 2
Sika CR 141 pultruded rods			
R/Sig-T700SC/UD65f – AR-1st	129 ± 6	$91 - 117 \pm 1 - 152$	145 ± 1
R/Sig-T700SC/UD65f – AR-2nd	144 ± 8	$123 - 141 \pm 2 - 175$	161 ± 2

Single DMA measurements:

Sample code	E'_{RT} [GPa]	T_B - T_g - T_E [°C] (Storage modulus)	T_g [°C] (Loss factor)
HexPly8552/HSAS4/UD58f/0.2MPa/1			
HexPlyP1-DMA-01	110	$210 - 226 - 240$	226
HexPlyP1-DMA-02	122	$201 - 221 - 238$	225
HexPlyP1-DMA-03	119	$201 - 220 - 239$	225
HexPly8552/HSAS4/UD58f/0.2MPa/2			
HexPlyP2-DMA-01	111	$210 - 220 - 234$	228
HexPlyP2-DMA-02	120	$198 - 216 - 231$	221
HexPlyP2-DMA-03	125	$194 - 215 - 235$	220

Sample code	E'$_{RT}$ [GPa]	T$_B$ - T$_g$ - T$_E$ [°C] (Storage modulus)	T$_g$ [°C] (Loss factor)
SikaCR132/FT300B/0-90°/1bar/3			
Sika1-DMA-01	37	102 –116 – 129	122
Sika1-DMA-02	26	94 – 117 – 129	122
Sika1-DMA-03	42	110 –124 – 135	127
SikaCR132/HTA40/UD/1bar/3			
Sika2-DMA-01	95	130 – 122 – 132	126
Sika2-DMA-02	88	99 – 119 – 129	122
SikaCR132/HTS5631/UD/1bar/3			
Sika3-DMA-01	109	112 – 122 – 131	126
Sika3-DMA-02	92	115 – 124 – 134	127
SikaCR132/HTS5631/UD/3bar/4			
Sika4-DMA-01	101	119 – 126 – 136	128
Sika4-DMA-02	112	109 – 122 – 131	126

Sample code	E'$_{RT}$ [GPa]	T$_B$ - T$_g$ - T$_E$ [°C] (Storage modulus)	T$_g$ [°C] (Loss factor)
HexionL418/FT300B/0-90°/1bar/5			
Hex1-DMA-01	45	118 –124 – 132	128
Hex1-DMA-02	59	115 – 124 – 132	128
HexionL418/HTA40/UD/1bar/5			
Hex2-DMA-01	92	118 – 125 – 132	129
Hex2-DMA-02	84	120 – 125 – 134	129
HexionL418/HTS5631/UD/1bar/5			
Hex3-DMA-01	122	112 – 123 – 131	127
Hex3-DMA-02	105	114 – 122 – 130	126
HexionL418/HTS5631/UD/3bar/6			
Hex4-DMA-01	90	115 – 122 – 129	126
Hex4-DMA-02	143	113 – 122 – 129	126

Summary DMA as received and after heat treatment:

Sample code	Cycle	E'$_{RT}$ [GPa]	T$_B$ - T$_g$ - T$_E$ [°C] (Storage modulus)	T$_g$ [°C] (Loss factor)
L20 pultruded rods				
DMA-AR	1st	91 ± 6	84 – **95 ± 1.5** – 111	101 ± 1
	2nd	93 ± 5	93 – **107 ± 0.8** – 126	116 ± 2
DMA-HT1(100-2h)	1st	90 ± 2	90 – **101 ± 0.6** – 117	107 ± 0
	2nd	92 ± 1	99 – **111 ± 0.6** – 131	118 ± 1
DMA-HT2(140-2h)	1st	94 ± 3	96 – **107 ± 0.3** – 123	112 ± 2
	2nd	98 ± 1	105 – **116 ± 0.7** – 134	122 ± 3

Single DMA measurements as received and after heat treatment:

Sample code	Cycle	E'$_{RT}$ [GPa]	T$_B$ - T$_g$ - T$_E$ [°C] (Storage modulus)	T$_g$ [°C] (Loss factor)
R/L20-T/HTSTS/UD65f – As Received				
DMA-AR-01	1st	84	87 – 96 – 110	102
	2nd	88	95 – 107 – 125	115
DMA-AR-02	1st	94	85 – 96 – 112	102
	2nd	96	95 – 107 – 126	115
DMA-AR-03	1st	95	80 – 93 – 110	100
	2nd	96	90 – 106 – 128	118
R/L20-T/HTSTS/UD65f – Heat Treatment 1				
DMA-HT1(100°-2h)-01	1st	89	89 – 101 – 118	107
	2nd	91	98 – 111 – 132	120
DMA-HT1(100°-2h)-02	1st	90	90 – 101 – 117	107
	2nd	92	99 – 111 – 131	118
DMA-HT1(100°-2h)-03	1st	86	92 – 102 – 117	107
	2nd	94	98 – 111 – 130	117
DMA-HT1(100°-2h)-04	1st	91	91 – 102 – 116	107
	2nd	94	100 – 112 – 131	119
DMA-HT1(100°-2h)-05	1st	92	89 – 101 – 115	106
	2nd	93	98 – 111 – 129	118
DMA-HT1(100°-2h)-06	1st	90	89 – 100 – 117	106
	2nd	-	-	-
R/L20-T/HTSTS/UD65f – Heat Treatment 2				
DMA-HT2(140°-2h)-01	1st	91	94 – 106 – 124	110
	2nd	97	104 – 115 – 135	119
DMA-HT2(140°-2h)-02	1st	95	97 – 107 – 123	113
	2nd	98	105 – 117 – 134	124
DMA-HT2(140°-2h)-03	1st	97	96 – 107 – 122	113
	2nd	99	105 – 116 – 133	123

Summary DMA as received and after heat treatment:

Sample code	Cycle	E'$_{RT}$ [GPa]	T_B - T_g - T_E [°C] (Storage modulus)	T_g [°C] (Loss factor)
Sika CR 141 pultruded rods				
DMA-AR	1st	129 ± 6	91 – **117 ± 1** – 152	145 ± 1
	2nd	144 ± 8	123 – **141 ± 2** – 175	161 ± 2
DMA-HT(90-4h)	1st	139 ± 2	87 – **123 ± 2** – 163	152 ± 3
	2nd	145 ± 9	118 – **145 ± 2** – 178	165 ± 1
DMA-HT(120-3h)	1st	129 ± 13	106 – **125 ± 0** – 162	153 ± 1
	2nd	141 ± 11	119 – **148 ± 5** – 183	170 ± 6
DMA-HT(120-4h)	1st	128 ± 8	109 – **122 ± 3** – 158	151 ± 1
	2nd	143 ± 6	112 – **139 ± 3** – 174	162 ± 3
DMA-HT(120-5h)	1st	132 ± 14	108 – **123 ± 1** – 162	156 ± 2
	2nd	142 ± 9	114 – **143 ± 1** – 178	165 ± 0
DMA-HT(160-6h)	1st	123 ± 19	113 – **133 ± 1** – 168	154 ± 2
	2nd	136 ± 17	114 – **140 ± 1** – 174	160 ± 2
DMA-HT(190-10h)	1st	124 ± 3	115 – **134 ± 2** – 168	155 ± 6
	2nd	138 ± 3	111 – **139 ± 2** – 175	163 ± 4

Single DMA measurements as received and after heat treatment:

Sample code	Cycle	E'$_{RT}$ [GPa]	T$_B$ - T$_g$ - T$_E$ [°C] (Storage modulus)	T$_g$ [°C] (Loss factor)
R/SikaCR141/Sigrafil-T700SC/UD65f – As Received				
DMA-AR-01	1st	125	94 – **116** – 155	146
	2nd	138	112 – **140** – 174	160
DMA-AR-02	1st	134	88 – **118** – 150	144
	2nd	150	114 – **143** – 176	163
R/SikaCR141/Sigrafil-T700SC/UD65f – Heat Treatment 1				
DMA-HT1(90°-4h)-01	1st	141	94 – **125** – 165	154
	2nd	152	120 – **147** – 180	166
DMA-HT1(90°-4h)-02	1st	138	80 – **122** – 162	150
	2nd	139	117 – **144** – 177	164
R/SikaCR141/Sigrafil-T700SC/UD65f – Heat Treatment 2				
DMA-HT2(120°-3h)-01	1st	138	105 – **125** – 159	154
	2nd	149	122 – **152** – 186	174
DMA-HT2(120°-3h)-02	1st	120	107 – **125** – 165	153
	2nd	134	117 – **145** – 180	166
R/SikaCR141/Sigrafil-T700SC/UD65f – Heat Treatment 3				
DMA-HT3(120°-4h)-01	1st	134	107 – **120** – 157	150
	2nd	148	110 – **137** – 173	160
DMA-HT3(120°-4h)-02	1st	123	111 – **124** – 160	152
	2nd	139	114 – **141** – 176	164
R/SikaCR141/Sigrafil-T700SC/UD65f – Heat Treatment 4				
DMA-HT4(120°-5h)-01	1st	122	111 – **122** – 161	155
	2nd	136	113 – **142** – 178	165
DMA-HT4(120°-5h)-02	1st	142	105 – **124** – 163	158
	2nd	149	115 – **144** – 179	165
R/SikaCR141/Sigrafil-T700SC/UD65f – Heat Treatment 5				
DMA-HT5(160°-6h)-01	1st	112	123 – **134** – 171	156
	2nd	132	114 – **140** – 173	158
DMA-HT5(160°-6h)-02	1st	102	112 – **133** – 168	154
	2nd	113	111 – **140** – 175	161
DMA-HT5(160°-6h)-03	1st	142	111 – **132** – 166	152
	2nd	151	114 – **140** – 174	162
DMA-HT5(160°-6h)-04	1st	137	116 – **134** – 169	155
	2nd	147	117 – **142** – 175	160
R/SikaCR141/Sigrafil-T700SC/UD65f – Heat Treatment 6				
DMA-HT6(190°-10h)-01	1st	122	115 – **135** – 170	157
	2nd	135	108 – **139** – 177	166
DMA-HT6(190°-10h)-02	1st	128	112 – **131** – 165	152
	2nd	139	110 – **139** – 173	160
DMA-HT6(190°-10h)-03	1st	94	114 – **136** – 172	163
	2nd	100	115 – **143** – 179	166
DMA-HT6(190°-10h)-04	1st	122	119 – **133** – 167	150
	2nd	140	112 – **138** – 172	158

12. Annex D

Method: TMA

Summary TMA:

Sample	Direction	1st Cycle			2nd Cycle		
		Tg (°C)	CTE_1 (µm/m·°C)	CTE_2 (µm/m·°C)	Tg (°C)	CTE_1 (µm/m·°C)	CTE_2 (µm/m·°C)
HexPly8552 Laminates							
HSAS4/UD58f/0.2MPa/1	0°	-	-	-	-	0.0 ± 0.2	0.2 ± 0.2
	90°	-	-	-	203	26 ± 1	78 ± 1
HSAS4/UD58f/0.2MPa/2	0°	-	-	-	-	0.4 ± 0.2	0.5 ± 0.2
	90°	-	-	-	200	26	76
Sika CR132 Laminates							
Epoxy Biresin CR132	-	131	71	167	126	71	137
FT300B/0-90°/1bar/3	0°	-	3	2	-	5	2
	90° I	x	x	x	x	x	x
	90° II	117	80	254	119	78	255
HTA40/UD/1bar/3	0°	-	0	0	-	1	0
	90° I	122	39	67	112	37	68
	90° II	128	51	175	117	51	177
HTS5631/UD/1bar/3	0°	-	-1	1	-	0	1
	90° I	130	15	32	122	17	40
	90° II	134	39	103	122	44	114
HTS5631/UD/3bar/4	0°	-	0	0	-	0	1
	90° I	124	28	83	119	34	90
	90° II	131	34	91	117	40	105
L20 pultruded Tubes							
T/HTSTS/UD65f	0°	-	-	-	-	0.8 ± 0.3	0 ± 0.5
	90°	-	-	-	91 ±4	49 ± 3	146 ± 13

13. Annex E

Method: Torsion test

Summary torsion test:

T/L20-T/HTSTS/UD65f				
Sample	**$G_{tangent} \pm 0.1$(GPa)**	**$\tau_u \pm 0.1$(MPa)**	**$M_{T\,max} \pm 0.1$ (Nm)**	**$\theta_{max} \pm 0.001$(°)**
T_{10}_1	2.3	42.2	4.9	49.9°
T_{10}_2	2.4	44.0	5.1	44.5°
N^{er} of cycles	**$G_{secant} \pm 0.1$(GPa)**	**$\tau_u \pm 0.1$(MPa)**	**$M_{T\,max} \pm 0.1$(Nm)**	**$\theta_{max} \pm 0.001$(°)**
T_{10}_h1 - 3c	3.1 - 2.7- 2.4	38.8	4.5	39.3°
T_{10}_h2 - 3c	3.3 - 3.1 - 2.9	interrupted	-	→25°
T_{10}_h3 - 4c	3.4 - 2.9 - 2.7 - 2.6	interrupted	-	→35°
T_{10}_h4 - 3c	2.8 - 2.5 - 2.2	37.9	4.4	53.5°

R/L20-T/HTSTS/UD65f							
Sample	**Strain rate (rad/s)**	**$G_{tangent} \pm 0.1$ (GPa)**	**$1^{st} M_{T\,max} \pm 0.1$ (Nm)**	**$1^{st} \tau_u \pm 0.1$ (MPa)**	**$2^{nd} M_{T\,max} \pm 0.1$ (Nm)**	**$2^{nd} \tau_u \pm 0.1$ (MPa)**	**Δ Elong. ± 0.01 (mm)**
$R_{10}\_L20\_01$	1×10^{-3}	1.4	1.4	55.4	-	-	n.a.
$R_{10}\_L20\_02$	1×10^{-3}	1.4	1.2	48.1	0.8	34.2	-0.06
$R_{10}\_L20\_03$	3×10^{-3}	1.5	1.1	44.8	1.2	49.7	-0.14
$R_{10}\_L20\_04$	3×10^{-3}	1.4	1.4	57.4	1.1	43.6	-0.15
$R_{10}\_L20\_05$	5×10^{-3}	1.5	1.4	58.7	1.5	62.7	-0.40
$R_{10}\_L20\_06$	5×10^{-3}	1.6	1.9	77.4	1.9	78.6	-0.45
$R_{10}\_L20\_07$	7×10^{-3}	1.5	1.2	47.7	1.3	55.0	-0.51
$R_{10}\_L20\_08$	0.01	1.4	1.4	55.4	1.3	53.8	-0.41
Modulated	**Strain rate (rad/s)**	**$G_{tangent} \pm 0.1$ (GPa)**	**$1^{st} M_{T\,max} \pm 0.1$ (Nm)**	**$1^{st} \tau_u \pm 0.1$ (MPa)**	**$2^{nd} M_{T\,max} \pm 0.1$ (Nm)**	**$2^{nd} \tau_u \pm 0.1$ (MPa)**	**Δ Elong. ± 0.01 (mm)**
$R_{10}\_L20\_m1$	5×10^{-3}	1.4	1.0	39.5	1.1-1.2	46.0-50.5	-0.47
Hysteresis	**Strain rate (rad/s)**	**$G_{secant, cycle} \pm 0.1$ (GPa)**				**Δ Elong. (mm)**	
$R_{10}\_L20\_h1$ - 23c	5×10^{-3}	G_1=1.5	G_2=1.3	G_3=0.6	G_4=0.4	-0.20	

R/SikaCR141/Sigrafil-T700SC/UD65f							
Sample	**Strain rate (rad/s)**	$\mathbf{G_{tangent}} \pm 0.1$ **(GPa)**	**1st M_T** $_{max} \pm 0.1$ **(Nm)**	**1st τ_u $\pm$ 0.1 (MPa)**	**2nd M_T** $_{max} \pm 0.1$ **(Nm)**	**2nd τ_u $\pm$ 0.1 (MPa)**	**Δ Elong. (mm)**
R_{10}_Sika_01	1×10^{-3}	2.1	1.5	59.5	1.5	59.5	n.a.
R_{10}_Sika_02	3×10^{-3}	2.2	1.7	68.9	2.1-1.9	85.6-79.0	-1.51
R_{10}_Sika_03	5×10^{-3}	2.0	1.8	74.1	2.4-2.2	99.0-88.4	-1.49
R_{10}_Sika_04	5×10^{-3}	1.9	1.4	57.0	1.8-1.8	74.6-73.7	-1.13
R_{10}_Sika_05	7×10^{-3}	2.1	1.6	63.6	2.0-2.8	83.5-116.1	-2.24
R_{10}_Sika_06	0.01	2.1	1.6	65.6	2.0-2.1	81.5-86.4	-2.25
Modulated	**Strain rate (rad/s)**	$\mathbf{G_{tangent}} \pm 0.1$ **(GPa)**	**1st M_T** $_{max} \pm 0.1$ **(Nm)**	**1st τ_u $\pm$ 0.1 (MPa)**	**2nd M_T** $_{max} \pm 0.1$ **(Nm)**	**2nd τ_u $\pm$ 0.1 (MPa)**	**Δ Elong. ± 0.01 (mm)**
R_{10}_Sika_m1	5×10^{-3}	2.2	1.8	71.7	2.2	89.2	-0.74
R_{10}_Sika_m2	5×10^{-3}	2.1	1.7	70.9	1.9	79.0	-0.40
R_{10}_Sika_m3	5×10^{-3}	2.1	1.5	62.7	1.8	75.4	-0.40
Hysteresis	**Strain rate (rad/s)**	**G** $_{secant, cycle}$ ± 0.1 **(GPa)**				**Δ Elong. (mm)**	
R_{10}_Sika_h1 - 27c	5×10^{-3}	G_1=2.0	G_2=1.7	G_3=1.4	G_4=1.0	-1.1	

14. Annex F

Method: Four-point bending test

Summary four-point bending test:

Sample	E_b (GPa)	σ_u (MPa)	ε_u (%)	ε_f (%)
HexPly8552 Laminates				
HSAS4/UD58f/0.2MPa/P1-4P-0°	126 ± 5	1644 ± 79	1.5 ± 0.1	-
HSAS4/UD58f/0.2MPa/P2-4P-0°	133 ± 4	1956 ± 186	1.7 ± 0.3	-
Sika CR132 Laminates				
Sik/FT300B/0-90°/P3-4P-0°	43 ± 3	544 ± 33	1.27 ± 0.10	-
Sik/HTA40/UD/P3-4P-0°	93 ± 3	794 ± 50	0.87 ± 0.03	-
Sik/HTS5631/UD/P3-4P-0°	103 ± 7	795 ± 39	0.79 ± 0.03	-
Sik/HTS5631/UD/P4-4P-0°	111 ± 8	918 ± 53	0.85 ± 0.03	-
Hexion L418 Laminates				
Hex/FT300/0-90°/P5-4P-0°	48 ± 1	611 ± 35	1.28 ± 0.11	-
Hex/HTA40/UD/P5-4P-0°	98 ± 4	741 ± 36	0.79 ± 0.04	-
Hex/HTS5631/UD/P5-4P-0°	116 ± 3	739 ± 24	0.66 ± 0.03	-
Hex/HTS5631/UD/P6-4P-0°	123 ± 3	973 ± 48	0.80 ± 0.03	-
L20 pultruded rods				
R/L20-T/HTSTS/UD-4P-0°-AR	85 ± 6	1026 ± 76	1.16 ± 0.06	1.32 ± 0.12
R/L20-T/HTSTS/UD-4P-0°-HT1	88 ± 4	994 ± 62	1.12 ± 0.07	1.42 ± 0.17
R/L20-T/HTSTS/UD-4P-0°-HT2	88 ± 7	1046 ± 82	1.16 ± 0.03	1.19 ± 0.03
R/L20-T/HTSTS/UD-4P-0°-HT3	92 ± 5	1070 ± 66	3.14 ± 0.27	1.27 ± 0.02
Sika CR 141 pultruded rods				
R/Sika/Sig-T700/UD-4P-0°-AR	126 ± 9	1256 ± 88	1.07 ± 0.15	2.45 ± 0.62
R/Sika/Sig-T700/UD-4P-0°-HT1	107 ± 14	1150 ± 137	1.11 ± 0.06	2.22 ± 0.48
R/Sika/Sig-T700/UD-4P-0°-HT2	105 ± 19	1142 ± 219	1.35 ± 0.28	1.99 ± 0.53
R/Sika/Sig-T700/UD-4P-0°-HT3	102 ± 6	1111 ± 16	1.10 ± 0.08	1.69 ± 0.34
R/Sika/Sig-T700/UD-4P-0°-HT4	104 ± 17	1135 ± 157	1.09 ± 0.05	1.89 ± 0.51
R/Sika/Sig-T700/UD-4P-0°-HT5	110 ± 6	1218 ± 104	1.21 ± 0.10	2.33 ± 0.31

Single four-point bending test measurements:

Sample	$E_b \pm 8$(GPa)	$\sigma_u \pm 25$(MPa)	$\varepsilon_u \pm 0.01$(%)
HexPly8552/HSAS4/UD58f/0.2MPa/1			
HexPly8552/P1-4P-0°-01	119	1592	1.40
HexPly8552/P1-4P-0°-02	128	1634	1.40
HexPly8552/P1-4P-0°-03	126	(1496)	(0.70)
HexPly8552/P1-4P-0°-04	117	1511	1.58
HexPly8552/P1-4P-0°-05	127	1671	1.44
HexPly8552/P1-4P-0°-06	127	1643	1.45
HexPly8552/P1-4P-0°-07	114	(1392)	(1.41)
HexPly8552/P1-4P-0°-08	127	1704	1.49
HexPly8552/P1-4P-0°-09	124	(1525)	(1.26)
HexPly8552/P1-4P-0°-10	131	(1583)	(1.03)
HexPly8552/P1-4P-0°-11	130	(1475)	(1.07)
HexPly8552/P1-4P-0°-12	129	1755	1.44
HexPly8552/P1-4P-0°-13	128	(1645)	(1.37)
HexPly8552/P1-4P-0°-14	127	(1655)	(1.24)
HexPly8552/P1-4P-0°-15	132	(1437)	(1.09)
HexPly8552/P1-4P-0°-16	132	(1447)	(1.09)
Average values	**126 ± 5**	**1644 ± 79**	**1.5 ± 0.1**
HexPly8552/HSAS4/UD58f/0.2MPa/2			
HexPly8552/P2-4P-0°-01	134	1790	1.37
HexPly8552/P2-4P-0°-02	137	(2039)	(1.65)
HexPly8552/P2-4P-0°-03	138	(2049)	(1.64)
HexPly8552/P2-4P-0°-04	136	(2028)	(1.67)
HexPly8552/P2-4P-0°-05	133	2172	2.08
HexPly8552/P2-4P-0°-06	135	2136	1.90
HexPly8552/P2-4P-0°-07	136	(1276)	(0.92)
HexPly8552/P2-4P-0°-08	134	(1401)	(1.03)
HexPly8552/P2-4P-0°-09	135	(1613)	(1.19)
HexPly8552/P2-4P-0°-10	128	1894	1.50
HexPly8552/P2-4P-0°-11	128	1788	1.40
HexPly8552/P2-4P-0°-12	124	(1608)	(1.3)
Average values	**133 ± 4**	**1956 ± 186**	**1.7 ± 0.3**

Sample	$E_b \pm 8$(GPa)	$\sigma_u \pm 25$(MPa)	$\varepsilon_u \pm 0.01$(%)
SikaCR132/FT300B/0-90°/1bar/3			
Sik/FT300B/0-90°/P3-4P-0°-01	48	515	1.10
Sik/FT300B/0-90°/P3-4P-0°-02	42	522	1.26
Sik/FT300B/0-90°/P3-4P-0°-03	45	595	1.36
Sik/FT300B/0-90°/P3-4P-0°-04	41	560	1.35
Sik/FT300B/0-90°/P3-4P-0°-05	42	513	1.21
Sik/FT300B/0-90°/P3-4P-0°-06	42	559	1.31
Average values	**43 ± 3**	**544 ± 33**	**1.27 ± 0.10**
SikaCR132/HTA40/UD/1bar/3			
Sik/HTA40/UD/P3-4P-0°-01	95	877	0.87
Sik/HTA40/UD/P3-4P-0°-02	93	808	0.90
Sik/HTA40/UD/P3-4P-0°-03	89	728	0.87
Sik/HTA40/UD/P3-4P-0°-04	93	782	0.89
Sik/HTA40/UD/P3-4P-0°-05	95	803	0.86
Sik/HTA40/UD/P3-4P-0°-06	96	766	0.82
Average values	**93 ± 3**	**794 ± 50**	**0.87 ± 0.03**
SikaCR132/HTS5631/UD/1bar/3			
Sik/HTS5631/UD/P3-4P-0°-01	89	714	0.83
Sik/HTS5631/UD/P3-4P-0°-02	93	744	0.80
Sik/HTS5631/UD/P3-4P-0°-03	107	777	0.76
Sik/HTS5631/UD/P3-4P-0°-04	108	821	0.80
Sik/HTS5631/UD/P3-4P-0°-05	105	808	0.79
Sik/HTS5631/UD/P3-4P-0°-06	109	819	0.76
Sik/HTS5631/UD/P3-4P-0°-07	101	799	0.82
Sik/HTS5631/UD/P3-4P-0°-08	105	844	0.83
Sik/HTS5631/UD/P3-4P-0°-09	105	803	0.79
Sik/HTS5631/UD/P3-4P-0°-10	110	821	0.77
Average values	**103 ± 7**	**795 ± 39**	**0.79 ± 0.03**
SikaCR132/HTS5631/UD/3bar/4			
Sik/HTS5631/UD/P4-4P-0°-01	109	942	0.88
Sik/HTS5631/UD/P4-4P-0°-02	115	980	0.89
Sik/HTS5631/UD/P4-4P-0°-03	106	869	0.82
Sik/HTS5631/UD/P4-4P-0°-04	101	840	0.85
Sik/HTS5631/UD/P4-4P-0°-05	123	953	0.82
Sik/HTS5631/UD/P4-4P-0°-06	114	922	0.82
Average values	**111 ± 8**	**918 ± 53**	**0.85 ± 0.03**

Samples four-point bending test tested with hysteresis cycles:

	SikaCR132/FT300B/0-90°/1bar/3	
Sample	**Sik/FT300B/0-90°/P3/ h1-6c**	**Sik/FT300B/0-90°/P3/ h2-10c**
E_b 1 (GPa)	(42.1)	47.2
E_b 2 (GPa)	46.6	45.3
E_b 3 (GPa)	45.6	48.9
E_b 4 (GPa)	45.9	48.7
E_b 5 (GPa)	45.1	48.7
E_b 6 (GPa)	43.4	48.8
E_b 7 (GPa)	-	48.7
E_b 8 (GPa)	-	48.9
E_b 9 (GPa)	-	48.7
E_b 10 (GPa)	-	48.9
	SikaCR132/HTA40/UD/1bar/3	
Sample	**Sik/HTA40/UD/P3/ h1-5c**	**Sik/HTA40/UD/P3/ h2-10c**
E_b 1 (GPa)	88.0	93.9
E_b 2 (GPa)	89.2	93.2
E_b 3 (GPa)	82.3	90.6
E_b 4 (GPa)	86.8	88.1
E_b 5 (GPa)	87.5	86.8
E_b 6 (GPa)	-	84.1
E_b 7 (GPa)	-	82.4
E_b 8 (GPa)	-	81.8
E_b 9 (GPa)	-	81.3
E_b 10 (GPa)	-	80.7

	SikaCR132/HTS5631/UD/1bar/3		
Sample	**Sik/HTS5631/UD/P3/ h1-3c**	**Sik/HTS5631/UD/P3/ h2-10c**	**Sik/HTS5631/UD/P3/ h3-11c**
E_b 1 (GPa)	89	714	0.83
E_b 2 (GPa)	93	744	0.80
E_b 3 (GPa)	107	777	0.76
E_b 4 (GPa)	108	821	0.80
E_b 5 (GPa)	105	808	0.79
E_b 6 (GPa)	109	819	0.76
E_b 7 (GPa)	101	799	0.82
E_b 8 (GPa)	105	844	0.83
E_b 9 (GPa)	105	803	0.79
E_b 10 (GPa)	110	821	0.77
E_b 11 (GPa)			

Sample	$E_b \pm 8$(GPa)	$\sigma_u \pm 25$(MPa)	$\varepsilon_u \pm 0.01$(%)
HexionL418/FT300B/0-90°/1bar/5			
Hex/FT300/0-90°/P5-4P-0°-01	48	547	1.08
Hex/FT300/0-90°/P5-4P-0°-02	49	611	1.30
Hex/FT300/0-90°/P5-4P-0°-03	47	642	1.38
Hex/FT300/0-90°/P5-4P-0°-04	47	600	1.23
Hex/FT300/0-90°/P5-4P-0°-05	47	628	1.31
Hex/FT300/0-90°/P5-4P-0°-06	47	640	1.38
Average values	**48 ± 1**	**611 ± 35**	**1.28 ± 0.11**
HexionL418/HTA40/UD/1bar/5			
Hex/HTA40/UD/P5-4P-0°-01	98	741	0.75
Hex/HTA40/UD/P5-4P-0°-02	100	765	0.78
Hex/HTA40/UD/P5-4P-0°-03	89	677	0.85
Hex/HTA40/UD/P5-4P-0°-04	97	740	0.81
Hex/HTA40/UD/P5-4P-0°-05	102	783	0.76
Hex/HTA40/UD/P5-4P-0°-06	100	739	0.78
Average values	**98 ± 4**	**741 ± 36**	**0.79 ± 0.04**
HexionL418/HTS5631/UD/1bar/5			
Hex/HTS5631/UD/P5-4P-0°-01	117	758	0.67
Hex/HTS5631/UD/P5-4P-0°-02	117	766	0.65
Hex/HTS5631/UD/P5-4P-0°-03	115	732	0.66
Hex/HTS5631/UD/P5-4P-0°-04	111	705	0.65
Hex/HTS5631/UD/P5-4P-0°-05	119	719	0.61
Hex/HTS5631/UD/P5-4P-0°-06	117	757	0.70
Average values	**116 ± 3**	**739 ± 24**	**0.66 ± 0.03**
HexionL418/HTS5631/UD/3bar/6			
Hex/HTS5631/UD/P6-4P-0°-01	128	1041	0.83
Hex/HTS5631/UD/P6-4P-0°-02	122	960	0.78
Hex/HTS5631/UD/P6-4P-0°-03	120	899	0.77
Hex/HTS5631/UD/P6-4P-0°-04	122	954	0.79
Hex/HTS5631/UD/P6-4P-0°-05	126	995	0.80
Hex/HTS5631/UD/P6-4P-0°-06	121	990	0.82
Average values	**123 ± 3**	**973 ± 48**	**0.80 ± 0.03**

Single four-point bending test measurements:

Sample	$E_b \pm 8$(GPa)	$\sigma_u \pm 25$(MPa)	$\varepsilon_u \pm 0.01$(%)	$\varepsilon_f \pm 0.01$(%)
R/L20-T/HTSTS/UD65f – As Received				
R/L20-T/HTSTS/UD-4P-0°-AR-01	87	1114	1.27	1.48
R/L20-T/HTSTS/UD-4P-0°-AR-02	93	1036	1.13	1.28
R/L20-T/HTSTS/UD-4P-0°-AR-03	90	1066	1.12	1.43
R/L20-T/HTSTS/UD-4P-0°-AR-04	81	902	1.13	1.35
R/L20-T/HTSTS/UD-4P-0°-AR-05	84	1064	1.17	1.22
R/L20-T/HTSTS/UD-4P-0°-AR-06	77	976	1.14	1.18
Average values	**85 ± 6**	**1026 ± 76**	**1.16 ± 0.06**	**1.32 ± 0.12**
R/L20-T/HTSTS/UD65f – Heat Treatment 1				
R/L20-T/HTSTS/UD-4P-0°-HT1-1	86	1084	1.22	1.52
R/L20-T/HTSTS/UD-4P-0°-HT1-2	86	987	1.07	1.23
R/L20-T/HTSTS/UD-4P-0°-HT1-3	95	952	1.10	1.60
R/L20-T/HTSTS/UD-4P-0°-HT1-4	86	953	1.09	1.34
Average values	**88 ± 4**	**994 ± 62**	**1.12 ± 0.07**	**1.42 ± 0.17**
R/L20-T/HTSTS/UD65f – Heat Treatment 2				
R/L20-T/HTSTS/UD-4P-0°-HT2-1	89	1002	1.14	1.16
R/L20-T/HTSTS/UD-4P-0°-HT2-2	96	1166	1.17	1.18
R/L20-T/HTSTS/UD-4P-0°-HT2-3	79	986	1.20	1.21
R/L20-T/HTSTS/UD-4P-0°-HT2-4	89	1028	1.14	1.22
Average values	**88 ± 7**	**1046 ± 82**	**1.16 ± 0.03**	**1.19 ± 0.03**
R/L20-T/HTSTS/UD65f – Heat Treatment 3				
R/L20-T/HTSTS/UD-4P-0°-HT3-1	96	1117	3.33	1.29
R/L20-T/HTSTS/UD-4P-0°-HT3-2	89	1024	2.96	1.26
Average values	**92 ± 5**	**1070 ± 66**	**3.14 ± 0.27**	**1.27 ± 0.02**

Sample	$E_b \pm 8$(GPa)	$\sigma_u \pm 25$(MPa)	$\varepsilon_u \pm 0.01$(%)	$\varepsilon_f \pm 0.01$(%)
R/SikaCR141/Sigrafil-T700SC/UD65f − As Received				
R/Sika/Sig-T700/UD-4P-0°-AR-01	126	1219	1.16	2.26
R/Sika/Sig-T700/UD-4P-0°-AR-02	114	1130	0.95	1.57
R/Sika/Sig-T700/UD-4P-0°-AR-03	121	1316	1.01	3.12
R/Sika/Sig-T700/UD-4P-0°-AR-04	133	1260	0.93	2.35
R/Sika/Sig-T700/UD-4P-0°-AR-05	137	1355	1.28	2.96
Average values	**126 ± 9**	**1256 ± 88**	**1.07 ± 0.15**	**2.45 ± 0.62**
R/SikaCR141/Sigrafil-T700SC/UD65f − Heat Treatment 1				
R/Sika/Sig-T700/UD-4P-0°-HT1-1	126	1377	1.22	1.82
R/Sika/Sig-T700/UD-4P-0°-HT1-2	119	1208	1.11	1.47
R/Sika/Sig-T700/UD-4P-0°-HT1-3	113	1231	1.07	2.64
R/Sika/Sig-T700/UD-4P-0°-HT1-4	120	1261	1.14	2.75
R/Sika/Sig-T700/UD-4P-0°-HT1-5	92	1057	1.05	2.70
R/Sika/Sig-T700/UD-4P-0°-HT1-6	96	1028	1.06	2.20
R/Sika/Sig-T700/UD-4P-0°-HT1-7	94	1013	1.05	1.80
R/Sika/Sig-T700/UD-4P-0°-HT1-8	92	1025	1.16	2.38
Average values	**107 ± 14**	**1150 ± 137**	**1.11 ± 0.06**	**2.22 ± 0.48**
R/SikaCR141/Sigrafil-T700SC/UD65f − Heat Treatment 2				
R/Sika/Sig-T700/UD-4P-0°-HT2-1	128	1440	1.17	1.50
R/Sika/Sig-T700/UD-4P-0°-HT2-2	109	1151	1.05	1.57
R/Sika/Sig-T700/UD-4P-0°-HT2-3	97	1051	1.54	2.42
R/Sika/Sig-T700/UD-4P-0°-HT2-4	84	925	1.62	2.48
Average values	**105 ± 19**	**1142 ± 219**	**1.35 ± 0.28**	**1.99 ± 0.53**
R/SikaCR141/Sigrafil-T700SC/UD65f − Heat Treatment 3				
R/Sika/Sig-T700/UD-4P-0°-HT3-1	102	1090	1.02	1.32
R/Sika/Sig-T700/UD-4P-0°-HT3-2	110	1117	1.06	1.61
R/Sika/Sig-T700/UD-4P-0°-HT3-3	95	1127	1.21	2.13
R/Sika/Sig-T700/UD-4P-0°-HT3-4	99	1112	1.13	1.72
Average values	**102 ± 6**	**1111 ± 16**	**1.10 ± 0.08**	**1.69 ± 0.34**
R/SikaCR141/Sigrafil-T700SC/UD65f − Heat Treatment 4				
R/Sika/Sig-T700/UD-4P-0°-HT4-1	127	1345	1.02	1.38
R/Sika/Sig-T700/UD-4P-0°-HT4-2	103	1094	1.10	2.54
R/Sika/Sig-T700/UD-4P-0°-HT4-3	85	966	1.13	2.02
R/Sika/Sig-T700/UD-4P-0°-HT4-4	100	1136	1.12	1.61
Average values	**104 ± 17**	**1135 ± 157**	**1.09 ± 0.05**	**1.89 ± 0.51**
R/SikaCR141/Sigrafil-T700SC/UD65f − Heat Treatment 5				
R/Sika/Sig-T700/UD-4P-0°-HT5-1	113	1235	1.10	2.37
R/Sika/Sig-T700/UD-4P-0°-HT5-2	113	1182	1.21	2.03
R/Sika/Sig-T700/UD-4P-0°-HT5-3	103	1100	1.14	2.78
R/Sika/Sig-T700/UD-4P-0°-HT5-4	105	1189	1.29	2.05
R/Sika/Sig-T700/UD-4P-0°-HT5-5	118	1383	1.34	2.42
Average values	**110 ± 6**	**1218 ± 104**	**1.21 ± 0.10**	**2.33 ± 0.31**

15.Annex G

Method: Interlaminar fracture toughness (Mode I&II)

Summary interlaminar fracture toughness:

Sample	Modus I Interlaminar fracture toughness G_{Ic} (J/mm²)	Modus II Interlaminar fracture toughness G_{IIc} (J/mm²)
HexPly8552 Laminates		
HSAS4/UD58f/0.2MPa/P1-IFT	0.31 ± 0.03	0.67 ± 0.01
HSAS4/UD58f/0.2MPa/P2-IFT	0.34 ± 0.03	0.88 ± 0.06

Single interlaminar fracture toughness measurements:

Sample	Modus I Interlaminar fracture toughness G_{Ic} (J/mm²)
HexPly8552/HSAS4/UD58f/0.2MPa/1	
HexPly8552/P1-IFT-ModI-01	0.312
HexPly8552/P1-IFT-ModI-02	0.349
HexPly8552/P1-IFT-ModI-03	0.284
HexPly8552/P1-IFT-ModI-04	0.296
Average values	**0.31 ± 0.03**
HexPly8552/HSAS4/UD58f/0.2MPa/2	
HexPly8552/P2-IFT-ModI-01	0.379
HexPly8552/P2-IFT-ModI-02	0.347
HexPly8552/P2-IFT-ModI-03	0.318
HexPly8552/P2-IFT-ModI-04	0.318
Average values	**0.34 ± 0.03**

Sample	Modus II Interlaminar fracture toughness G_{IIc} (J/mm²)
HexPly8552/HSAS4/UD58f/0.2MPa/1	
HexPly8552/P1-IFT-ModII-01	0.662
HexPly8552/P1-IFT-ModII-02	0.667
HexPly8552/P1-IFT-ModII-03	0.688
HexPly8552/P1-IFT-ModII-04	0.655
Average values	**0.67 ± 0.01**
HexPly8552/HSAS4/UD58f/0.2MPa/2	
HexPly8552/P2-IFT-ModII-01	0.876
HexPly8552/P2-IFT-ModII-02	0.810
HexPly8552/P2-IFT-ModII-03	0.888
HexPly8552/P2-IFT-ModII-04	0.943
Average values	**0.88 ± 0.06**

16. Annex H

Method: Short beam shear strength (SBS)

Summary short beam shear strength:

Sample	F_{max} (N)	F^{sbs} (MPa)
Sika CR132 Laminates		
Sik/FT300B/0-90°/P3-SBS	5044 ± 311	54.4 ± 3.3
Sik/HTA40/UD/P3-SBS	3625 ± 208	51.1 ± 1.4
Sik/HTS5631/UD/P3-SBS	3312 ± 181	53.1 ± 0.9
Sik/HTS5631/UD/P4-SBS	3118 ± 74	61.7 ± 1.3
Hexion L418 Laminates		
Hex/FT300/0-90°/P5-SBS	4160 ± 153	53.0 ± 1.1
Hex/HTA40/UD/P5-SBS	4102 ± 51	55.9 ± 1.1
Hex/HTS5631/UD/P5-SBS	2360 ± 18	39.6 ± 0.5
Hex/HTS5631/UD/P6-SBS	2616 ± 111	53.0 ± 2.2

Single short beam shear strength measurements:

Sample	F_{max} (N)	F^{sbs} (MPa)
SikaCR132/FT300B/0-90°/1bar/3		
Sik/FT300B/0-90°/P3-SBS-01	5317	57.82
Sik/FT300B/0-90°/P3-SBS-02	5185	55.16
Sik/FT300B/0-90°/P3-SBS-03	5289	56.98
Sik/FT300B/0-90°/P3-SBS-04	4807	51.70
Sik/FT300B/0-90°/P3-SBS-05	4625	50.23
Average values	**5044 ± 311**	**54.4 ± 3.3**
SikaCR132/HTA40/UD/1bar/3		
Sik/HTA40/UD/P3-SBS-01	3837	52.21
Sik/HTA40/UD/P3-SBS-02	3763	52.64
Sik/HTA40/UD/P3-SBS-03	3279	51.20
Sik/HTA40/UD/P3-SBS-04	3605	50.78
Sik/HTA40/UD/P3-SBS-05	3505	48.53
Sik/HTA40/UD/P3-SBS-06	3760	51.25
Average values	**3625 ± 208**	**51.1 ± 1.4**
SikaCR132/HTS5631/UD/1bar/3		
Sik/HTS5631/UD/P3-SBS-01	3071	52.14
Sik/HTS5631/UD/P3-SBS-02	3322	53.50
Sik/HTS5631/UD/P3-SBS-03	3428	52.99
Sik/HTS5631/UD/P3-SBS-04	3505	52.03
Sik/HTS5631/UD/P3-SBS-05	3112	53.68
Sik/HTS5631/UD/P3-SBS-06	3434	54.42
Average values	**3312 ± 181**	**53.1 ± 0.9**
SikaCR132/HTS5631/UD/3bar/4		
Sik/HTS5631/UD/P4-SBS-01	3034	59.72
Sik/HTS5631/UD/P4-SBS-02	3075	61.16
Sik/HTS5631/UD/P4-SBS-03	3066	62.27
Sik/HTS5631/UD/P4-SBS-04	3221	62.71
Sik/HTS5631/UD/P4-SBS-05	3191	63.41
Sik/HTS5631/UD/P4-SBS-06	3119	60.93
Average values	**3118 ± 74**	**61.7 ± 1.3**

Sample	F_{max} (N)	F^{sbs} (MPa)
HexionL418/FT300B/0-90°/1bar/5		
Hex/FT300/0-90°/P5-SBS-01	4361	54.65
Hex/FT300/0-90°/P5-SBS-02	4054	52.54
Hex/FT300/0-90°/P5-SBS-03	4015	52.10
Hex/FT300/0-90°/P5-SBS-04	4168	53.08
Hex/FT300/0-90°/P5-SBS-05	4035	51.77
Hex/FT300/0-90°/P5-SBS-06	4330	53.82
Average values	**4160 ± 153**	**53.0 ± 1.1**
HexionL418/HTA40/UD/1bar/5		
Hex/HTA40/UD/P5-SBS-01	4090	57.08
Hex/HTA40/UD/P5-SBS-02	4087	55.30
Hex/HTA40/UD/P5-SBS-03	4073	55.19
Hex/HTA40/UD/P5-SBS-04	4041	54.48
Hex/HTA40/UD/P5-SBS-05	4145	56.11
Hex/HTA40/UD/P5-SBS-06	4180	57.32
Average values	**4102 ± 51**	**55.9 ± 1.1**
HexionL418/HTS5631/UD/1bar/5		
Hex/HTS5631/UD/P5-SBS-01	2345	39.09
Hex/HTS5631/UD/P5-SBS-02	2359	39.36
Hex/HTS5631/UD/P5-SBS-03	2391	39.84
Hex/HTS5631/UD/P5-SBS-04	2345	39.45
Hex/HTS5631/UD/P5-SBS-05	2355	40.37
Hex/HTS5631/UD/P5-SBS-06	2370	39.62
Average values	**2360 ± 18**	**39.6 ± 0.5**
HexionL418/HTS5631/UD/3bar/6		
Hex/HTS5631/UD/P6-SBS-01	2511	51.29
Hex/HTS5631/UD/P6-SBS-02	2575	52.90
Hex/HTS5631/UD/P6-SBS-03	2653	53.56
Hex/HTS5631/UD/P6-SBS-04	2802	56.72
Hex/HTS5631/UD/P6-SBS-05	2507	50.28
Hex/HTS5631/UD/P6-SBS-06	2653	53.31
Average values	**2616 ± 111**	**53.0 ± 2.2**

Personal information

Name: Marta Rodríguez-Hortalá
Title: Licenciada en ciencias químicas (Master of Science)
Date of birth: April 17th, 1979
Place of birth: Madrid, Spain
Nationality: Spanish
Languages: Spanish (native language), German (C1 ÖSD), English (advanced), Norwegian (basic knowledge).

Education and studies

2009-2013: PhD studies, Vienna University of Technology
2007-2008: Erasmus Grant, University of Vienna
1997-2008: Degree in Chemistry, Universidad Complutense de Madrid
1993-1997: High School, Instituto Cervantes (Madrid)
1985-1993: Grammar School, Colegio Luz Casanova (Madrid)

Professional experience

October 2007-August 2008: Student Assistant
Department of Inorganic Chemistry/Materials Chemistry, University of Vienna
November2008-March2009: Project Assistant
Institute of Materials Science and Technology, Vienna University of Technology
Since April 2009: University Assistant
Institute of Materials Science and Technology, Vienna University of Technology
Project management DEFCOM Project (ERA-Net MATERA, 6th Framework Programme)

Other

Drachenboot Cup Ost - Wien 2009: Team Technische Drachen, 1st Price (fun class).

Research interests

Materials Science, Materials Characterisation, High-resolution X-ray Tomography, Carbon Fibre Reinforced Polymers, Light weight Alloys.

Publications

Paper:

C. Poletti, M. Rodríguez-Hortalá, M. Hauser, C. Sommitsch: *"Microstructure development in hot deformed AA6082"*; Materials Science and Engineering A, A (2010), 528; S. 2413 - 2430. DOI: http://dx.doi.org/10.1016/j.msea.2010.11.048

Selected contributions to conferences:

(09.2012) M. Rodríguez-Hortalá, G. Requena, F. Sket, J. Molina-Aldareguia, E. Maire, L. Salvo, M. Scheel: *"In-situ synchrotron microtomography during tensile deformation of a ± 45° cross-ply carbon fibre reinforced epoxy laminate",* Poster: iCT2012 - Conference on Industrial Computed Tomography, FHOÖ Campus Wels; 19.09.2012 - 21.09.2012.

(06.2012) M. Rodríguez-Hortalá, Judith Hatzmann, H.P. Degischer: *"Structural characterisation of defects in CFRP laminates produced with different epoxy resin systems and their influence on the mechanical properties".* In proceedings: 15th European Conference on Composite Materials, Venezia (Italy); 24.06.2012 - 28.06.2012;

(12.2011) M. Rodríguez-Hortalá, D. Salaberger, P. Dobron, M. Holzmeier, H.P. Degischer: *"Charakterisierung der Schädigung in CFK-Verbundwerkstoffen mittels Computertomographie und in-situ Schallemission Messungen".* In proceedings: "DVM Bericht 643 Tagung Werkstoffprüfung 2011"; W. Grellmann (Hrg.); DVM, (2011), ISBN: 978-3-9814516-1-0; S. 207 - 212. Berlin (Deutschland); 01.12.2011 - 02.12.2011.

(11.2011) M. Rodríguez-Hortalá, G. Requena, F. Sket, J. Molina-Aldareguia, E. Maire, L. Salvo, M. Scheel: *"In-situ synchrotron microtomography during tensile deformation of a multidirectional carbon fibre reinforced epoxy laminate".* In Proceedings: "3D Microstructure Meeting 2011", MatInfo Werkstoffinformationsgesellschaft mbH, Frankfurt (2011), ISBN: 978-3-88355-388-7; S. 14 - 15. 3D Microstructure Meeting 2011, Saarbrücken (Deutschland); 02.11.2011 - 04.11.2011.

(04.2011) M. Rodríguez-Hortalá, D. Salaberger, S. Hernández, M. Holzmeier, H.P. Degischer, J. Kastner: *"Characterisation of defects in carbon fibre reinforced polymers (CFRP)".* In proceedings: "Tagungsband zum 18. Symposium Verbundwerkstoffe und Werkstoffverbunde", TU Chemnitz, Schriftenreihe Werkstoffe und Werkstofftechnische Anwendungen, Band 41 (2011), ISBN: 978-3-00-033801-4; S. 208 - 215. 18. DGM Symposium Verbundwerkstoffe und Werkstoffverbunde, Chemnitz (Deutschland); 30.03.2011 - 01.04.2011.

(11.2010) M. Rodríguez-Hortalá, P. Dobroň, H.P. Degischer: *"Acoustic emission signals produced during deformation of carbon fibre reinforced polymers (CFRP)"*; 5th Seminar for PhD students "Research in progress on metallic materials", Graz (invited); 08.11.2010 - 09.11.2010.

(09.2010) M. Rodríguez-Hortalá, D. Salaberger, S. Hernández, H.P. Degischer: *"Mechanical and structural characterisation of defects in CFRP materials"*; Poster: Fachtagung für Industrielle Computertomografie, FHOÖ Campus Wels; 27.09.2010 - 29.09.2010.

(05.2010) M. Rodríguez-Hortalá: *"Microstructure and mechanical properties of CFPR materials"*; Seminar "Physics of Materials", Charles University in Prague, Prague (Czech Republic) (invited); 19.05.2010.

(07.2009) M. Rodríguez-Hortalá, G. Requena, B. Seiser, H.P. Degischer, M. Di Michiel, T. Buslaps: *"3D-Characterization of continuous reinforced composites".* In proceedings: "17th International Conference on Composite Materials", (2009), S. 1 - 9. 17th International Conference on Composite Materials, Edinburgh, Scotland, UK; 27.07.2009 - 31.07.2009.